

**ISTANBUL TECHNICAL UNIVERSITY ★ GRADUATE SCHOOL OF SCIENCE**  
**ENGINEERING AND TECHNOLOGY**

**DETERMINATION OF THE INELASTIC DISPLACEMENT DEMAND  
AND RESPONSE CONTROL OF STEEL FRAME TYPE STRUCTURES  
BY SEISMIC ENERGY EQUATIONS**

**Ph.D. THESIS**

**Ahmet GÜLLÜ**

**Department of Civil Engineering**  
**Structural Engineering Programme**

**NOVEMBER 2018**



**ISTANBUL TECHNICAL UNIVERSITY ★ GRADUATE SCHOOL OF SCIENCE**  
**ENGINEERING AND TECHNOLOGY**

**DETERMINATION OF THE INELASTIC DISPLACEMENT DEMAND  
AND RESPONSE CONTROL OF STEEL FRAME TYPE STRUCTURES  
BY SEISMIC ENERGY EQUATIONS**

**Ph.D. THESIS**

**Ahmet GÜLLÜ  
(501122012)**

**Department of Civil Engineering  
Structural Engineering Programme**

**Thesis Advisor: Prof. Dr. Ercan YÜKSEL**

**NOVEMBER 2018**



**İSTANBUL TEKNİK ÜNİVERSİTESİ ★ FEN BİLİMLERİ ENSTİTÜSÜ**

**SİSMİK ENERJİ DENKLEMLERİ İLE  
ÇELİK ÇERÇEVE TÜRÜ SİSTEMLERİN İNELASTİK YERDEĞİŞTİRME  
İSTEMLERİNİN BELİRLENMESİ VE DAVRANIŞ KONTROLÜ**

**DOKTORA TEZİ**

**Ahmet GÜLLÜ  
(501122012)**

**İnşaat Mühendisliği Anabilim Dalı**

**Yapı Mühendisliği Programı**

**Tez Danışmanı: Prof. Dr. Ercan YÜKSEL**

**KASIM 2018**



Ahmet Güllü, a Ph.D. student of ITU Graduate School of Science Engineering and Technology student ID 501122012, successfully defended the thesis entitled “DETERMINATION OF THE INELASTIC DISPLACEMENT DEMAND AND RESPONSE CONTROL OF STEEL FRAME TYPE STRUCTURES BY SEISMIC ENERGY EQUATIONS”, which he prepared after fulfilling the requirements specified in the associated legislations, before the jury whose signatures are below.

**Thesis Advisor :**      **Prof. Dr. Ercan YÜKSEL** .....  
Istanbul Technical University

**Jury Members :**      **Prof. Dr. Engin ORAKDÖĞEN** .....  
Istanbul Technical University

**Prof. Dr. Konuralp GİRGIN** .....  
Istanbul Technical University

**Doç. Dr. Cem YALÇIN** .....  
Boğaziçi University

**Prof. Dr. Bülent AKBAŞ** .....  
Gebze Technical University

**Date of Submission** : 16 August 2018

**Date of Defense** : 07 November 2018





*To my charming daughter Betül,*



## FOREWORD

Primarily, I can proudly say that being a student of Prof. Dr. Ercan Yüksel is an honor for me. I heartily thank my advisor for his endless support, encouragement and inspiration.

I would also like to thank Prof. Dr. Engin Orakdöğen and Assoc. Prof. Dr. Cem Yalçın for their guidance and support during the thesis.

My family also has played an important role in maintaining my motivation and encouraging me to submit this thesis in time. I offer my best regards and blessings to my father Veysel Güllü, my mother Fatma Güllü, my sister Ayşe Güllü, my brother Muhammet Güllü and his wife Nebe Güllü. Finally, I would like to express my gratitude to my dearest wife Zeynep Güllü for her patience during the preparation of this thesis. Beyond them, my daughter Betül Güllü, who was born during the very last days of writing this thesis, was the biggest motivation of all for me.

I also give thanks to MSc. Civil Engineer Tansu Gökçe, who helped me anytime I needed during the experimental phase of the study. Last but not least, I would like to express my warm thanks to ITU Structural and Earthquake Engineering Laboratory staff members Hakan Saruhan, Mehmet Fatih Şahin, Mahmut Şamlı and Turgay Özgünay.

Finally, I would like to thank the staff of the Materials Laboratory of ITU.

The study was funded by research project *BAP 39305* of ITU. The grant by ITU BAP is gratefully appreciated.

August 2018

Ahmet Güllü  
(Civil Engineer, MSc)



## TABLE OF CONTENTS

	<u>Page</u>
<b>FOREWORD</b> .....	<b>ix</b>
<b>TABLE OF CONTENTS</b> .....	<b>xi</b>
<b>LIST OF TABLES</b> .....	<b>xiii</b>
<b>LIST OF FIGURES</b> .....	<b>xv</b>
<b>SUMMARY</b> .....	<b>xxi</b>
<b>ÖZET</b> .....	<b>xxiii</b>
<b>1. INTRODUCTION</b> .....	<b>1</b>
1.1 Purpose of Thesis .....	1
1.2 Literature Review .....	2
1.3 Hypothesis .....	11
<b>2. EXPERIMENTAL STUDIES</b> .....	<b>13</b>
2.1 Testing Facility and the Preparatory Works.....	13
2.1.1 Testing facility. ....	13
2.1.2 Selected ground motions.....	14
2.1.3 Measuring system. ....	17
2.1.4 Application of the vision-based measuring system.....	17
2.1.5 Material tests .....	21
2.1.6 Development of software to compute seismic energy components .....	23
2.2 Single Degree of Freedom Systems .....	24
2.2.1 Definition of specimens and testing system.....	24
2.2.2 Tests in the elastic range .....	30
2.2.3 Tests in the inelastic range .....	32
2.2.4 The effect of mass tuning on the seismic energy components.....	34
2.3 Multi Degree of Freedom Systems.....	35
2.3.1 Definition of specimens and testing system.....	35
2.3.2 Bare frame #1 (BF1): weak column – strong beam .....	44
2.3.2.1 Free vibration tests .....	44
2.3.2.2 Tests in the elastic range .....	45
2.3.2.3 Tests in the inelastic range .....	49
2.3.3 Bare frame #1 retrofitted with metallic damper (BF1-D1) .....	50
2.3.3.1 Free vibration tests .....	51
2.3.3.2 Tests in the elastic range .....	52
2.3.3.3 Tests in the inelastic range .....	55
2.3.4 Bare frame #2 (BF2): strong column –weak beam .....	59
2.3.4.1 Free vibration tests .....	60
2.3.4.2 Tests in the elastic range .....	60

2.3.4.3 Tests in the inelastic range .....	63
2.3.5 Bare frame #2 retrofitted with metallic damper (BF2-D1) .....	65
2.3.5.1 Free vibration tests .....	66
2.3.5.2 Tests in the elastic range .....	67
2.3.5.3 Tests in the inelastic range .....	70
2.3.6 The effect of structural configuration on seismic energy components .....	75
2.3.7 Supplementary damping effect on the seismic input energy components ..	79
2.4 Representation of MDOF response through SDOF system responses .....	87
<b>3. NUMERICAL MODELS .....</b>	<b>91</b>
3.1 Modelling Strategy .....	91
3.2 Comparison of Response Parameters .....	94
3.2.1 Response of the SDOF specimens .....	94
3.2.2 Response of the MDOF specimens .....	97
3.3 Comparison of the Seismic Energy Components .....	101
3.3.1 Energy components of the SDOF specimens .....	101
3.3.2 Energy components of the MDOF specimens .....	105
3.4 The Response Control of MDOF Systems by Alternative Implementation of SCs .....	110
<b>4. ESTIMATION OF THE SEISMIC INPUT ENERGY .....</b>	<b>117</b>
4.1 The Existing Seismic Input Energy Equations vs. Experimental Results. ....	117
4.2 New Seismic Input Energy Relation Proposals .....	119
4.2.1 A novel spectral prediction equation .....	119
4.2.2 The closed form equation based on a piece-wise exact method to calculate seismic input energy .....	130
4.3 Representation of Damping Effect on the Seismic Input Energy .....	136
4.4 Seismic Input Energy as an Earthquake Intensity Measure .....	145
<b>5. PREDICTION OF THE CRITICAL DISPLACEMENT .....</b>	<b>153</b>
5.1 A Demonstrative Example. ....	154
5.2 Discussion on the Results .....	161
<b>6. CONCLUSIONS AND RECOMMENDATIONS .....</b>	<b>163</b>
6.1 Conclusions .....	163
6.1.1 General .....	163
6.1.2 Experimental study .....	164
6.1.3 Numerical study. ....	165
6.1.4 Measurement and others .....	165
6.2 Recommendations. ....	166
<b>REFERENCES .....</b>	<b>167</b>
<b>CURRICULUM VITAE .....</b>	<b>175</b>

## LIST OF TABLES

	<u>Page</u>
<b>Table 2.1</b> : Some properties of the EQ records. ....	15
<b>Table 2.2</b> : Result of the coupon tests. ....	23
<b>Table 2.3</b> : Effective height of the specimens and corresponding periods.....	25
<b>Table 2.4</b> : Measured maximum relative response and seismic energy components for elastic tests. ....	31
<b>Table 2.5</b> : The measured maximum relative response and seismic energy terms for inelastic range. ....	33
<b>Table 2.6</b> : Dynamic properties of specimen BF2 with and without the displacement transducers positioned at the floor levels.....	42
<b>Table 2.7</b> : Free vibration test results of BF1.....	45
<b>Table 2.8</b> : The maximum lateral storey accelerations in mm/s <sup>2</sup> . ....	47
<b>Table 2.9</b> : The floor acceleration ratios. ....	48
<b>Table 2.10</b> : The ultimate strains recorded in the elastic tests ( $\mu$ strain $\times 10^6$ ). ....	48
<b>Table 2.11</b> : Dominant frequencies of BF1-D1.....	51
<b>Table 2.12</b> : Maximum floor accelerations in mm/s <sup>2</sup> . ....	53
<b>Table 2.13</b> : Acceleration ratios between adjacent floors. ....	54
<b>Table 2.14</b> : Measured strains in the elastic tests ( $\mu$ strain $\times 10^6$ ). ....	54
<b>Table 2.15</b> : Dominant frequencies of BF2. ....	60
<b>Table 2.16</b> : The measured maximum absolute accelerations in mm/s <sup>2</sup> . ....	62
<b>Table 2.17</b> : Acceleration ratios between the storeys.....	63
<b>Table 2.18</b> : The ultimate strains measured in the elastic tests ( $\mu$ strain $\times 10^6$ ). ....	63
<b>Table 2.19</b> : The dominant frequencies of BF2-D1. ....	66
<b>Table 2.20</b> : The absolute peak accelerations of BF2-D1 in mm/s <sup>2</sup> . ....	68
<b>Table 2.21</b> : Acceleration ratios between adjacent storeys. ....	69
<b>Table 2.22</b> : Measured strains in the elastic tests ( $\mu$ strain $\times 10^6$ ). ....	69
<b>Table 3.1</b> : Natural vibration periods of the alternative MDOF systems. ....	111
<b>Table 3.2</b> : The energy components of the retrofitted frames. ....	111
<b>Table 4.1</b> : B and k parameters, Dindar et al. (2015). ....	121
<b>Table 4.2</b> : The EQ records utilized for numerical comparisons. ....	123
<b>Table 4.3</b> : Parameters utilized for the proposed spectra. ....	124
<b>Table 4.4</b> : The selected ground motions for the evaluation of damping effect.....	139
<b>Table 4.5</b> : The parameter a, b and c provided by Alici and Sucuoğlu (2016). ....	144
<b>Table 4.6</b> : The sub-groups for intensity measures. ....	149
<b>Table 4.7</b> : The comparisons of various intensity measures. ....	151
<b>Table 5.1</b> : Selected EQ records. ....	156

**Table 5.2** : The dynamic properties of 9- and 20- story SAC LA buildings..... **156**  
**Table 5.3** : Input energy and top displacement predictions for 9-story frame. .... **160**  
**Table 5.4** : Input energy and top displacement predictions for 20-story frame. .... **161**



## LIST OF FIGURES

	<u>Page</u>
<b>Figure 1.1</b> : Energy equivalent velocity comparisons of MDOF and equivalent SDOF systems, (Uang and Bertero, 1990). .....	2
<b>Figure 1.2</b> : Energy based evaluation procedure steps of Leelataviwat et al. (2009). .....	8
<b>Figure 1.3</b> : Testing specimen of the Benavent-Climent (2011). .....	9
<b>Figure 1.4</b> : Energy balance of equivalent SDOF system and design parameters. ...	10
<b>Figure 2.1</b> : ARI-1 shake table of ITU. ....	13
<b>Figure 2.2</b> : Plan and elevation views of the ARI-1 shake table. ....	14
<b>Figure 2.3</b> : Selected EQ records. ....	14
<b>Figure 2.4</b> : Acceleration and input energy spectra of the selected records. ....	15
<b>Figure 2.5</b> : Selected EQ records for MDOF specimens. ....	16
<b>Figure 2.6</b> : 3% elastic acceleration spectra of the selected EQ records. ....	16
<b>Figure 2.7</b> : Application of vision based measuring systems to SDOF specimens. ...	20
<b>Figure 2.8</b> : Strain measurements by vision based algorithm. ....	20
<b>Figure 2.9</b> : Evaluation of the strain measurements. ....	21
<b>Figure 2.10</b> : Coupon dimensions and tested specimen. ....	21
<b>Figure 2.11</b> : Testing set up in MTS C40. ....	22
<b>Figure 2.12</b> : Coupon test results. ....	22
<b>Figure 2.13</b> : Flow chart of developed algorithm. ....	23
<b>Figure 2.14</b> : SDOF specimens and mass tuning. ....	24
<b>Figure 2.15</b> : Hole configuration of Part 3. ....	25
<b>Figure 2.16</b> : SDOF specimens with diverse lateral stiffnesses. ....	26
<b>Figure 2.17</b> : In-plane and out-of-plane top accelerations of the SDOF specimens. ..	26
<b>Figure 2.18</b> : Measuring system of SDOF specimens. ....	27
<b>Figure 2.19</b> : Effect of LPT utilized for measuring top displacement on damping. .	27
<b>Figure 2.20</b> : Top acceleration vs. top displacement. ....	28
<b>Figure 2.21</b> : Comparison of strain and accelerometer based accelerations. ....	29
<b>Figure 2.22</b> : Applied and measured accelerations on the table. ....	30
<b>Figure 2.23</b> : Mass normalized $E_I$ values for second group SDOF specimens. ....	32
<b>Figure 2.24</b> : Specimens tested in the inelastic range. ....	32
<b>Figure 2.25</b> : Acceleration and $E_I/m$ spectra of the El Centro NS record. ....	34
<b>Figure 2.26</b> : Seismic input energy vs. frequency content of the EQs. ....	35
<b>Figure 2.27</b> : Schematic views of the MDOF specimens. ....	36
<b>Figure 2.28</b> : Floor plans of MDOF specimens. ....	37
<b>Figure 2.29</b> : The effect of steel strips on the response. ....	38
<b>Figure 2.30</b> : Alteration of the dynamic response by adding the steel strips. ....	38

<b>Figure 2.31</b> : Tested MDOF specimens. ....	<b>39</b>
<b>Figure 2.32</b> : Steel cushions utilized in the literature. ....	<b>39</b>
<b>Figure 2.33</b> : Geometric dimensions of the designed steel cushion. ....	<b>40</b>
<b>Figure 2.34</b> : Measuring equipment for MDOF specimens. ....	<b>41</b>
<b>Figure 2.35</b> : Definition of half-power bandwidth method. ....	<b>43</b>
<b>Figure 2.36</b> : Damping ratio calculations by using the logarithmic decrement method. ....	<b>43</b>
<b>Figure 2.37</b> : Free vibration test results of BF1. ....	<b>44</b>
<b>Figure 2.38</b> : Acceleration increments between the storeys. ....	<b>45</b>
<b>Figure 2.39</b> : Acceleration increments between table and 1 <sup>st</sup> storey levels. ....	<b>46</b>
<b>Figure 2.40</b> : The representative strain histories for 0.20×SS-CIG record. ....	<b>48</b>
<b>Figure 2.41</b> : Frequency characteristic of the BF1 before and after the inelastic tests. .....	<b>49</b>
<b>Figure 2.42</b> : Strains occurred on the structural members during the inelastic tests. ....	<b>49</b>
<b>Figure 2.43</b> : The observed damage in the inelastic tests. ....	<b>50</b>
<b>Figure 2.44</b> : Floor acceleration histories of BF1 for the inelastic tests. ....	<b>50</b>
<b>Figure 2.45</b> : The placement of SCs. ....	<b>51</b>
<b>Figure 2.46</b> : Frequencies of BF1-D1 and comparison with BF1. ....	<b>51</b>
<b>Figure 2.47</b> : Acceleration histories of BF1-D1. ....	<b>52</b>
<b>Figure 2.48</b> : Acceleration ratios between floor levels of BF1 and BF1-D1. ....	<b>54</b>
<b>Figure 2.49</b> : Frequency characteristic of the BF1-D1. ....	<b>55</b>
<b>Figure 2.50</b> : Strains on structural members of BF1-D1. ....	<b>55</b>
<b>Figure 2.51</b> : Strain history comparisons of specimens BF1 and BF1-D1. ....	<b>57</b>
<b>Figure 2.52</b> : Comparison for floor accelerations of BF1 vs. BF1-D1. ....	<b>58</b>
<b>Figure 2.53</b> : Observed damages on the structural members. ....	<b>58</b>
<b>Figure 2.54</b> : Horizontal and vertical displacements of metallic dampers. ....	<b>59</b>
<b>Figure 2.55</b> : Deformed shape of metallic dampers. ....	<b>59</b>
<b>Figure 2.56</b> : Frequencies of BF2 obtained by diverse free vibration tests. ....	<b>60</b>
<b>Figure 2.57</b> : Acceleration increments between table and 1 <sup>st</sup> floor levels. ....	<b>61</b>
<b>Figure 2.58</b> : Dominant frequencies of BF2 in inelastic tests. ....	<b>63</b>
<b>Figure 2.59</b> : Strain histories at members of BF2. ....	<b>64</b>
<b>Figure 2.60</b> : The observed welding cracks after the tests. ....	<b>64</b>
<b>Figure 2.61</b> : Storey accelerations measured during the inelastic tests. ....	<b>65</b>
<b>Figure 2.62</b> : The placement of steel cushions. ....	<b>65</b>
<b>Figure 2.63</b> : The frequency content of free vibration data for BF2-D1. ....	<b>66</b>
<b>Figure 2.64</b> : Comparison of the frequency content of free vibration data for BF2 and BF2-D1. ....	<b>66</b>
<b>Figure 2.65</b> : The accelerations histories of the table and 1 <sup>st</sup> floor of the specimen. ....	<b>67</b>
<b>Figure 2.66</b> : Acceleration ratios between floor levels of BF2 and BF2-D1. ....	<b>69</b>
<b>Figure 2.67</b> : Frequency characteristic of BF2-D1 in inelastic tests. ....	<b>70</b>
<b>Figure 2.68</b> : Strains on structural members of BF2-D1. ....	<b>71</b>
<b>Figure 2.69</b> : The comparison of strain histories of specimens BF2 and BF2-D1. ....	<b>72</b>
<b>Figure 2.70</b> : The comparison of floor accelerations for BF2 vs. BF2-D1. ....	<b>73</b>
<b>Figure 2.71</b> : The welding damage at beam-to-column connections. ....	<b>73</b>

<b>Figure 2.72</b> : The views of the SCs after the tests.....	<b>74</b>
<b>Figure 2.73</b> : Horizontal and vertical displacements of the SCs.....	<b>74</b>
<b>Figure 2.74</b> : Total input energies imparted into specimens BF1 and BF2. ....	<b>75</b>
<b>Figure 2.75</b> : The mass normalized floor input energy histories. ....	<b>76</b>
<b>Figure 2.76</b> : Comparison of the mass normalized kinetic energy histories of BF1 and BF2.....	<b>77</b>
<b>Figure 2.77</b> : Comparison of the normalized elastic strain energy of BF1 and BF2. ....	<b>78</b>
<b>Figure 2.78</b> : Comparison of the damping energy histories for BF1 and BF2.....	<b>79</b>
<b>Figure 2.79</b> : Comparison of the plastic energy histories of BF1 and BF2.....	<b>79</b>
<b>Figure 2.80</b> : Total seismic input energy comparisons for BF1 and BF1-D1.....	<b>80</b>
<b>Figure 2.81</b> : Total seismic input energy comparisons for BF2 and BF2-D1.....	<b>80</b>
<b>Figure 2.82</b> : Distribution of the seismic input energies of BF1 and BF1-D1 among the storeys. ....	<b>81</b>
<b>Figure 2.83</b> : Comparison for normalized kinetic energies of BF1 and BF1-D1. ....	<b>82</b>
<b>Figure 2.84</b> : Comparison for elastic strain energies of BF1 and BF1-D1. ....	<b>83</b>
<b>Figure 2.85</b> : Comparison for damping energies of BF1 and BF1-D1. ....	<b>83</b>
<b>Figure 2.86</b> : Comparison for plastic strain energies of BF1 and BF1-D1. ....	<b>84</b>
<b>Figure 2.87</b> : Distribution of the seismic input energies of BF2 and BF2-D1 among the storeys. ....	<b>84</b>
<b>Figure 2.88</b> : Comparison for normalized kinetic energies of BF2 and BF2-D1. ....	<b>85</b>
<b>Figure 2.89</b> : Comparison for elastic strain energies of BF2 and BF2-D1. ....	<b>86</b>
<b>Figure 2.90</b> : Comparison for damping energies of BF2 and BF2-D1. ....	<b>86</b>
<b>Figure 2.91</b> : Comparison for plastic energies of BF2 and BF2-D1. ....	<b>87</b>
<b>Figure 2.92</b> : Testing specimen of the Uang and Bertero (1990).....	<b>87</b>
<b>Figure 2.93</b> : The relative seismic input energy comparisons for MDOF and SDOF specimens.....	<b>88</b>
<b>Figure 3.1</b> : The generated numeric models.....	<b>91</b>
<b>Figure 3.2</b> : Material models used for the tested elements.....	<b>92</b>
<b>Figure 3.3</b> : Definition of the sectional properties in Perform 3D. ....	<b>93</b>
<b>Figure 3.4</b> : Modelling the SCs in Perform 3D. ....	<b>94</b>
<b>Figure 3.5</b> : Experimental and numerical comparisons for 0.25×SS-CIG.....	<b>95</b>
<b>Figure 3.6</b> : Experimental and numerical comparisons for 0.25×CH-N10E. ....	<b>95</b>
<b>Figure 3.7</b> : Comparisons of the relative response components. ....	<b>96</b>
<b>Figure 3.8</b> : Comparisons of the relative response components. ....	<b>96</b>
<b>Figure 3.9</b> : Comparison of the storey responses of BF1 for 0.75×SS-CIG. ....	<b>97</b>
<b>Figure 3.10</b> : Comparisons of the storey responses of BF1 for 1.00×SS-CIG.....	<b>97</b>
<b>Figure 3.11</b> : Comparisons of the storey responses of BF1-D1 for 0.75×SS-CIG. ..	<b>98</b>
<b>Figure 3.12</b> : Comparisons of the storey responses of BF1-D1 for 1.00×SS-CIG. ..	<b>98</b>
<b>Figure 3.13</b> : Comparisons of the storey responses of BF2 for 0.75×SS-CIG.....	<b>99</b>
<b>Figure 3.14</b> : Comparisons of the storey responses of BF2 for 1.00×SS-CIG.....	<b>99</b>
<b>Figure 3.15</b> : Comparisons of the storey responses of BF2-D1 for 0.75×SS-CIG. ....	<b>100</b>
<b>Figure 3.16</b> : Comparisons of the storey responses of BF2-D1 for 1.00×SS-CIG. ....	<b>100</b>
<b>Figure 3.17</b> : Energy comparisons for SDOF specimen having 0.385 s period.....	<b>102</b>
<b>Figure 3.18</b> : Energy comparisons for SDOF specimen having 0.526 s period.....	<b>103</b>

<b>Figure 3.19</b> : Energy comparisons for SDOF specimen having 0.667 s period.....	<b>104</b>
<b>Figure 3.20</b> : Seismic energy plots for SDOF specimen tested in the inelastic range. .....	<b>105</b>
<b>Figure 3.21</b> : Energy comparisons for BF1.....	<b>106</b>
<b>Figure 3.22</b> : Energy comparisons for BF1-D1.....	<b>107</b>
<b>Figure 3.23</b> : Energy comparisons for BF2.....	<b>108</b>
<b>Figure 3.24</b> : Energy comparisons for BF2-D1.....	<b>109</b>
<b>Figure 3.25</b> : Some alternative SC implementations for the response control.....	<b>110</b>
<b>Figure 3.26</b> : $E_p$ distribution of the strong beam - weak column type frames.....	<b>112</b>
<b>Figure 3.27</b> : $E_p$ distribution of the weak beam - strong column type frames.....	<b>114</b>
<b>Figure 3.28</b> : The storey displacement histories of the bare frames.....	<b>115</b>
<b>Figure 3.29</b> : Plastic energy to input energy ratios.....	<b>115</b>
<b>Figure 4.1</b> : Comparison of the existing equation with the experimental results....	<b>118</b>
<b>Figure 4.2</b> : The proposed mass normalized relative input energy spectrum.....	<b>119</b>
<b>Figure 4.3</b> : Proposed seismic input energy spectra vs. the experimental results. ..	<b>121</b>
<b>Figure 4.4</b> : Spectra of the selected records. ....	<b>122</b>
<b>Figure 4.5</b> : Input energy spectra comparisons. ....	<b>125</b>
<b>Figure 4.6</b> : Frequency content of some records. ....	<b>126</b>
<b>Figure 4.7</b> : Correlation analyses for the suggested input energy spectra.....	<b>127</b>
<b>Figure 4.8</b> : Weightiness of the parameters on the seismic input energy.....	<b>128</b>
<b>Figure 4.9</b> : Effect of moment magnitude on the seismic input energy. ....	<b>128</b>
<b>Figure 4.10</b> : Effect of PGV on the seismic input energy. ....	<b>129</b>
<b>Figure 4.11</b> : Effect of intensity on the spectral shape. ....	<b>129</b>
<b>Figure 4.12</b> : Comparison of relative responses obtained by experiment and piece- wise exact method.....	<b>133</b>
<b>Figure 4.13</b> : Comparison for the spectra of the record and piece-wise exact method. .....	<b>133</b>
<b>Figure 4.14</b> : Comparison of the mass normalized input energies obtained from experiment and piece-wise method.....	<b>134</b>
<b>Figure 4.15</b> : Comparison of $E_I/m$ spectrum with elastic experimental results. ....	<b>134</b>
<b>Figure 4.16</b> : Comparison of $E_I/m$ spectrum with inelastic experimental results. ..	<b>135</b>
<b>Figure 4.17</b> : Comparison of the proposed piece-wise method and MDOF specimen results. ....	<b>135</b>
<b>Figure 4.18</b> : Velocity and acceleration spectra of the Erz-EW.....	<b>136</b>
<b>Figure 4.19</b> : Experimental and numerical responses of a SDOF system for 0.25×SS- CIG.....	<b>137</b>
<b>Figure 4.20</b> : Seismic energy components of a SDOF system for 0.25×SS-CIG. ..	<b>138</b>
<b>Figure 4.21</b> : Comparisons of experimentally obtained energy terms for the specimens. ....	<b>139</b>
<b>Figure 4.22</b> : $E_I/m$ intensities and power spectra for the selected EQ records.....	<b>140</b>
<b>Figure 4.23</b> : Comparison of the damping modification factors with the spectral equation. ....	<b>142</b>
<b>Figure 4.24</b> : The comparisons of the DMFs. ....	<b>143</b>

<b>Figure 4.25</b> : Comparison of the input energy spectra constructed by using PSV values and proposed damping modification factor. ....	<b>144</b>
<b>Figure 4.26</b> : Engineering demand parameter and proposed intensity measure results. ....	<b>150</b>
<b>Figure 4.27</b> : Correlation coefficients of the existing and proposed intensity measures.....	<b>152</b>
<b>Figure 5.1</b> : Application of the proposed method. ....	<b>154</b>
<b>Figure 5.2</b> : 9-Story SAC LA frame.....	<b>155</b>
<b>Figure 5.3</b> : 20-Story SAC LA frame.....	<b>155</b>
<b>Figure 5.4</b> : Seismic input energy predictions for 9- and 20-story SAC frames.....	<b>157</b>
<b>Figure 5.5</b> : Determination of the spectral displacement (SD) for 9 (red) and 20 (blue) SAC LA buildings. ....	<b>157</b>





# **DETERMINATION OF THE INELASTIC DISPLACEMENT DEMAND AND RESPONSE CONTROL OF STEEL FRAME TYPE STRUCTURES BY SEISMIC ENERGY EQUATIONS**

## **SUMMARY**

Energy-based seismic design has several advantages over force- or displacement-based design methodologies. Firstly it takes into account frequency content and duration of the earthquake record. Moreover hysteretic behavior of the structural members can be considered in the analyses rather than envelope curves. Additionally, energy is a scalar value whereas force and displacement are vector terms. Hence using energy for evaluating the structures is a more rational approach.

Since energy procedures have effective features, an energy-based procedure to compute inelastic top displacement of the *MDOF* systems under the effect of a given earthquake record is developed in the content of the thesis. At the outset existing equations to predict seismic input energy are evaluated through elastic *SDOF* specimen tests and their correlation with the experimental results was found to be weak. Therefore, a new formulation is developed, which considers the duration, frequency content and intensity of the earthquake, spectral acceleration and velocity, damping ratio of the structure and soil type. The product of the proposed relation satisfactorily matched with the experimental and numerical results. Correlation of the proposed equation with the experimental results are found to be strong (0.75).

The proposed spectral input energy equation considers the damping ratio, whereas the damping effect on the input energy has been considered insignificant in the current literature. However, the performed experimental and numerical works showed that the damping ratio may have a significant effect around the dominant frequencies of the earthquake record. Therefore it should be considered in a precise design equation.

Even though the proposed spectral equation satisfactorily envelopes the experimental results, a more precise calculation of the relative seismic input energy is required to obtain more accurate top displacement predictions. Therefore, a piece-wise exact method is developed in close form. Results of the piece-wise method are compared with the experimental and numerical results. The predictions of the piece-wise method were significant.

Since the relative seismic input energy is predicted and computed satisfactorily, an energy-based intensity measure is also proposed in the thesis. The efficiency, sufficiency and the predictability of the proposed intensity measure is evaluated through several shake table tests and compared with almost all of the available intensity measures. The proposed intensity measure suitably predicts the severity order of the earthquake records. The correlation of the proposed intensity measure with the experimental results was found to be very strong for all of the dynamic tests.

Finally a hybrid spectrum that consists of spectral input energy and displacement is proposed to predict top displacement of a *MDOF* system. The proposed procedure is

applied to two frame type structures which have 9- and 20-storeys. Average of the relative error in the prediction of top displacement occurred was around 20%.



# SİSMİK ENERJİ DENKLEMLERİ İLE ÇELİK ÇERÇEVE TÜRÜ SİSTEMLERİN İNELASTİK YERDEĞİŞTİRME İSTEMLERİNİN BELİRLENMESİ VE DAVRANIŞ KONTROLÜ

## ÖZET

Mevcut yönetmeliklerde yapıların sismik tasarımı için kuvvet veya yerdeğiştirme esaslı yöntemler önerilmektedir. Kuvvet esaslı yöntemlerde deprem etkisi fiktif yatay yükler ile temsil edilmektedir. Hesaplanan deprem kuvvetleri sistem sünekliği ve malzeme dayanım fazlalığı katsayısına bağlı bir azaltma çarpanı ile küçültülmektedir. Tasarlanan sistemin etkilenen azaltılmış yükleri güvenle taşıması hedeflenir. Bu yöntemde oluşacak yerdeğiştirmeler, hasar derecesi ve dağılımı belirsizdir. Alternatif olarak önerilen yerdeğiştirme esaslı yöntemlerde itme analizinden elde edilen kapasite eğrisi ve tasarım ivme spektrumu kullanılarak sistemin performans noktası belirlenir. Performans noktasına bağlı olarak yapısal elemanlar üzerindeki şekildeğiştirmeler hesaplanır ve yönetmeliklerde verilen limit değerler ile karşılaştırılır. Bu yöntemlerde her ne kadar hasar izlenebilir olsa da depremin türü (yakın fay, uzak fay vb.), süresi ve frekans içeriği gibi önemli özellikler göz ardı edilmektedir. Bunlara bağlı olarak süreye bağlı yığılımlı hasar durumu da gözden kaçırılmaktadır.

Enerji esaslı tasarım yöntemleri ise kuvvet ve yerdeğiştirme esaslı yöntemlerinin olumlu özelliklerini kapsamakla beraber, bu yöntemlerin dikkate alamadığı parametreleri de hesaba katabilmektedir. Yapıya giren sismik enerji ve terimlerinin hesaplanması için önerilen ifadeler tek serbestlik dereceli bir sistemin hareket denkleminde dayanmaktadır. İlk olarak hareket denklemini oluşturan her bir terim hız arttırmaları ile çarpılıp toplam deprem süresi üzerinde integre edilmiştir. Daha sonra hız terimi yerine yerdeğiştirme ile zaman çarpımı kullanılarak zaman tanım alanında enerji ifadelerinin hesaplanması mümkün olmuştur.

Kuvvet ve yerdeğiştirme terimleri vektörel büyüklüklerken enerji skaler bir büyüklüktür. Vektörel büyüklükler ile yüksek modların etkisinin dikkate alınması vb. gibi durumlarda kullanılan birleştirme yöntemlerinde vektör yönüne bağlı işaret farklılıkları sorun oluşturmaktadır. Skaler bir büyüklük olan enerji yöntemlerinde ise böyle bir sorun oluşmamaktadır. Bu nedenle yapıların tasarımında ve değerlendirilmesinde enerji yaklaşımlarının kullanılmasının daha gerçekçi sonuçlar üretmesi beklenmektedir.

Enerji esaslı yöntemlerinin belirgin üstünlüklerine rağmen farklı malzemelerden oluşan yapısal elemanların enerji kapasitelerinin belirlenmesine yönelik bir bağıntı mevcut olmadığı için tam anlamıyla enerji esaslı bir tasarım yönteminin önerilmesi mümkün olmamaktadır. Bunun yerine literatürde genel olarak enerji esaslı yöntemler ile yerdeğiştirme esaslı yöntemler birleştirilmektedir. Bu nedenle yapısal elemanların enerji kapasitelerinin belirlenmesine yönelik çalışmalara ihtiyaç vardır.

Önerilen tez kapsamında da yapıya giren sismik enerji kullanılarak çok serbestlik dereceli bir sistemin tepe yerdeğiřtirmesinin tahmini için bir yöntem geliřtirilmiřtir. Önerilen yöntemle elde edilen tepe yerdeğiřtirmeleri literatürdeki modal statik itme analizi yöntemlerine uygulanabilir. Bu yöntemler önce zaman tanım alanında dođrusal olmayan analizlerle tepe yerdeğiřtirmesi hesaplanıp daha sonra bu yerdeğiřtirme deđeri geliřtirilen itme analizi yöntemlerinde kullanılmaktadır. Zaten dođrusal olmayan analizler yapılmıř olduđu için bu yöntemlerin uygulanabilirliđi tartıřılmaktadır. Tez kapsamında önerilen yöntem ile bulunan yerdeğiřtirmelerin bu yöntemlerde kullanılması ile hızlı dođrusal olmayan hesapların ve deđerlendirmelerin yapılması mümkün olabilecektir.

Önerilen yöntemle tahmin edilen yerdeğiřtirmelerin daha dođru olabilmesi için giren sismik enerjinin dođruya olabildiđince yakın tahmin edilmesi gerekmektedir. Bu nedenle tez kapsamında deneysel ve numerik çalıřmalar gerçekteřtirilmiřtir.

Tezin birinci bölümünde tezin amacı ve hipotezle birlikte literatürde enerji esaslı yöntemler hakkında yapılan çalıřmalar özetlenmiřtir.

İkinci bölümde tez kapsamında yapılan deneysel çalıřmalar anlatılmıřtır. İlk olarak İTÜ Yapı ve Deprem Mühendisliđi Laboratuvarında bulunan deneysel olanaklar ve ARI-1 sarsma masası özellikleri anlatılmıřtır. Deneylerde kullanılan ölçüm aletleri ve sarsma masasına uygulanan deprem kayıtları yine bu bölümde özetlenmiřtir. Mevcut ölçüm aletlerinin deney numunelerinin sönüm oranları üzerinde önemli bir etkisi olabileceđi deneysel olarak gösterilmiřtir. Bu nedenle mevcut görüntü işleme yöntemleri bir miktar geliřtirilerek kamera tabanlı bir ölçüm sistemi de geliřtirilmiřtir. Deneysel çalıřmalarda kullanılan yapısal elemanlardan çıkarılan kupon numuneleri İTÜ Yapı Malzemeleri Laboratuvarında çekme deneylerine tabi tutulmuřtur. Buradan elde edilen sonuçlar numerik analizlerde kullanılmıřtır.

Deneysel çalıřmalarda ilk olarak farklı titreřim periyotlarına sahip elastik tek serbestlik dereceli sistemler elastik ivme spektrumları neredeyse aynı olan iki farklı deprem kaydına maruz bırakılmıřtır. Bu deprem kayıtlarından biri 9.02 sn iken diđer 116.345 sn'dir. Deneysel sonuçlar elde edilen enerji büyüklüklerinin çok farklı olduđunu göstermiřtir. Daha sonra benzer numuneler plastik bölgede deneyerek enerji terimleri elde edilmiřtir. Bunlara ek olarak aynı titreřim periyotuna sahip farklı boylarda alüminyum ve çelikten yapılmıř benzer tek serbestlik dereceli numuneler 3 farklı zemin türüne ait 3 farklı deprem kaydına maruz bırakılmıřtır. Elde edilen sonuçlar kütleye göre normalize edilmiř rölatif sismik enerjinin yapının yatay rijitliđinden bađımsız olduđunu kanıtlamıřtır.

Çok serbestlik dereceli sistem deneyleri için ise 3 katlı, her yönde bir açıklıđı bulunan çerçeve türü yapılar tasarlanmıřtır. Yalın çerçevelerin biri eski tip yapıları temsil ederken (zayıf kolon güçlü kiriř) diđer modern tasarım anlayıřını yansıtmaktadır (güçlü kolon zayıf kiriř). Bunlara ek olarak yalın çerçeveler literatürde mevcut bir metalik sönümleyici kullanılarak güçlendirilmiřtir. Yalın numunelerin titreřim periyotlarına çok fazla etki edip spektral ifadelerde çok farklı noktalarda bulunmalarını engellemek için sönümleyiciler birinci kat kiriřleri ile deney yapısından bađımsız olarak masaya sabitlenen ikincil çerçeve arasına yerleřtirilmiřtir. Metalik sönümleyicilerin eklenmesi ile yapıların sönüm oranları %2-3 mertebelerinden %5-6 mertebelerine kadar arttırılmıřtır. Yapıların periyotları hedeflendiđi gibi birbirine oldukça yakındır. Çok serbestlik dereceli sistemlere ilk olarak elastik bölgede 7 farklı

deprem kaydı etkilmiştir. Daha sonra seçilen 7 kayıt arasından bir tanesi kullanılarak plastik deneyler gerçekleştirilmiştir. Periyotları birbirine çok yakın olduğu için kayma ve eğilme türü çerçevelerde giren enerjiler birbirine oldukça yakın elde edilmiştir. Ancak enerjinin dağılımı oldukça farklıdır. Özellikle plastik enerji kayma türü yapılarda daha büyüktür. Deney yapılarının metalik sönümleyicilerle güçlendirilmesi ile toplam plastik enerji önemli oranda azaltılmış ve böylece giren enerjide büyük oranda azaltılmıştır.

Tezin üçüncü bölümünde deneyler Perform 3D ile oluşturulan sayısal modellerle benzeştirilmiştir. Tek serbestlik dereceli ve çok serbestlik dereceli sistemlerde hem tepe/kat tepkileri hem de enerji terimleri deneyler ile karşılaştırılmıştır. Sonuçlar birbirine oldukça yakın elde edilmiştir. Yalnızca çok serbestlik dereceli numunelerin birinci katında kullanılan ivme ölçer verilerine çok fazla gürültü karıştığı için bazı durumlarda yerdeğiştirmelerin ivmenin türevi olarak hesaplanabilmesi mümkün olmamıştır. Numerik modeller deneylerle doğrulandıktan sonra yalın çerçevelere daha fazla yastığın yerleştirildiği modeller oluşturulmuştur. Bu modeller kullanılarak yeterli sayıda yastık kullanımı ile yapısal elemanlardaki plastik enerjinin sifıra indirilebileceği gösterilmiştir.

Tezin dördüncü bölümünde ise deneysel ve numerik modeller kullanılarak giren enerjinin tahminine yönelik çalışmalar gerçekleştirilmiştir. Bu bölümde ilk olarak deneysel sonuçlar ile literatürdeki mevcut giren enerji formülleri karşılaştırılmıştır. Mevcut ifadelerin deneylerle korolasyonu oldukça zayıf olduğu için öncelikle yeni bir spektral ifade önerilmiştir. Bu ifadeye depremin süresi, yoğunluğu ve frekans içeriği ile yapının sönüm oranı, titreşim periyodu ve zemin özellikleri dikkate alınmaktadır. Önerilen giren enerji spektrumu lineer artan, plato ve parabolik azalan olmak üzere üç bölümden oluşmaktadır. Seçilen herhangi bir kayıt için plato bölgesi deprem kaydının köşe periyodundan başlatılmaktadır. Daha sonra literatürdeki öneri göz önüne alınarak plato bölgesi köşe periyodun  $1/1.2$  değerine kadar uzatılıp başlangıç noktası ile lineer olarak birleştirilmektedir. Parabolik azalan kol ise kaydın köşe periyodundan başlayıp zemin sınıfına göre değişen bir katsayıyla azaltılmaktadır. Önerilen spektral ifade deneysel ve sayısal sonuçlarla karşılaştırılarak aralarındaki korolasyonun oldukça yüksek olduğu gösterilmiştir.

Önerilen spektral ifadeye yapının sönüm oranı dikkate alınmasına karşılık, literatürde genel olarak giren enerjinin sönüm oranından bağımsız olduğu savunulmuştur. Ancak yapılan deneysel ve sayısal sonuçlar deprem kaydının baskın periyotlarında sönüm oranının önemli bir etkisi olabileceği gösterilmiştir. Bu nedenle literatürdeki mevcut giren enerji ifadelerinin farklı sönüm oranlarında da kullanılabilmesi için yeni bir sönüm düzeltme çarpanı önerilmiştir. Önerilen düzeltme çarpanının başarılı bir şekilde uygulanabileceği gösterilmiştir.

Her ne kadar önerilen spektral ifade deneysel ve sayısal sonuçları oldukça başarılı tahmin etse de önerilen yöntemde tepe yerdeğiştirmesinin daha doğru tahmin edilmesi için giren enerjinin daha kesin hesaplanması gerekmektedir. Bu nedenle giren enerji ve enerji bileşenlerinin oldukça hızlı hesaplanabileceği sabit adım aralıklı kesin bir çözüm yöntemi kapalı ifade olarak verilmiştir. Önerilen kapalı ifade hem tek serbestlik dereceli hem de çok serbestlik dereceli sistemler için oldukça etkin sonuçlar üretmiştir.

Giren enerji önerilen yöntemlerle kesine yakın hesaplanabildiği için enerji esaslı bir deprem şiddet ölçütü tanımlanmıştır. Önerilen şiddet ölçütünün etkinliği, yeterliliği ve

tahmin edebilirliđi farklı dinamik deneyler ile kanıtlanmıřtır. Tüm deneylerde uygulanan deprem kayıtlarının yapı üzerinde oluřturacađı etki sırası oldukça dođru olarak tahmin edilmiřtir. Deneysel sonuřlar ile önerilen řiddet ölçütü arasındaki korelasyon oldukça yüksektir.

Tezin beřinci bölümünde çok serbestlik dereceli sistemlerin tepe yerdeđiřtirmesinin enerji esaslı olarak hesaplanabilmesi için bir yöntem önerilmiřtir. Dördüncü bölümde verilen kapalı ifadeler ve göz önüne alınan 9 ve 20 katlı çelik çerçevelerin ilk 3 modu dikkate alınarak, yapılara giren enerji deđerleri büyük dođrulukta hesaplanabilmiřtir. 9 ve 20 katlı çerçevelere uygulanan 19 deprem kaydı sonucunda elde edilen sayısal giren enerji deđerleri ile hesaplanan enerji deđerleri karşılařtırıldıđında ortalama hata sırasıyla %6.7 ve %9.9 olarak elde edilmiřtir. Tepe yerdeđiřtirmesinin tahminindeki ortalama rölatif hata ise sırasıyla %10.0 ve %20.1 olarak gerçekleřmiřtir.



## 1. INTRODUCTION

Force and displacement-based methodologies are generally proposed by modern seismic design codes. In the force-based analyses, the equivalent earthquake loads are reduced by a factor “ $R$ ”, which relies on the ductility and over-strength factor of the structure. At the end of the design procedure, the structural members are expected to carry those reduced loads safely. However, the deformation intensities and their distribution on the structural system are not clear. The displacement-based methods use the structural capacity curve to compute the displacement demand of the structure. Member deformations are determined and classified by comparing these against some reference values. However, the effective duration and frequency content of the earthquake ( $EQ$ ) and the hysteretic behavior of structural members are disregarded in this methodology. It was also stated that displacement-based procedures have difficulty in accounting for the duration-related damage, in a similar manner to force-based methodologies (Chou and Uang, 2000). In another study, the same authors mentioned that seismic damage of  $MDOF$  systems may not be caused by only maximum responses of force and displacement, Chou and Uang (2003). Hence, a more comprehensive design methodology named as “*Energy Based Seismic Design*” ( $EBSD$ ) was proposed, originally by Housner (1956).  $EBSD$  combines not only the features of the former design procedures, but also includes some critical parameters of earthquake and structural systems.

### 1.1 Purpose of Thesis

This PhD thesis aims to generate some crucial data to be used in the  $EBSD$ . The study combines intensive experimental and numerical works. The experimental part consisting of steel  $SDOF$  and  $MDOF$  system tests aimed to generate an elastic input energy spectrum and to define the distribution of energy components between the structural members. The purpose of the numerical part is not only to reproduce the experimental results but also to produce some formulations to estimate the seismic

input energy through the spectral and closed-form formulations, as well as the determination of the seismic top displacement demand.

## 1.2 Literature Review

The energy terms, namely kinetic ( $E_k$ ), damping ( $E_d$ ), strain ( $E_s$ ) and input energy ( $E_I$ ), can be derived from the equation of motion of a *SDOF* system, equation (1.1). Strain energy can be divided into two parts, namely elastic strain energy ( $E_{es}$ ) and plastic strain energy ( $E_{ps}$ ).  $E_{ps}$  is related to the damage on the structural members; subsequently its computation is the most important step in the *EBS*, (Akiyama, 1985).

$$M \int_0^{t_0} \ddot{u} du + C \int_0^{t_0} \dot{u} du + \int_0^{t_0} F(u) du = -M \int_0^{t_0} \ddot{u}_g du \quad (1.1)$$

Since displacement “ $du$ ” is the first derivative of velocity; “ $du$ ” can be replaced with “ $\dot{u} dt$ ” and equation 1.1 can be rewritten in the time domain as given by (Akiyama, 1985), equation (1.2).

$$M \int_0^t \ddot{u} \dot{u} dt + C \int_0^t \dot{u} \dot{u} dt + \int_0^t F(u) \dot{u} dt = -M \int_0^t \ddot{u}_g \dot{u} dt \quad (1.2)$$

Akiyama (1985) proposed an approach that involves the coefficients to distribute the seismic input energy between storeys of the structure. Moreover, it was shown that the energy terms of a *MDOF* system could be estimated through the equivalent *SDOF* systems. The effectiveness of equivalent *SDOF* system usage was experimentally proved by Uang and Bertero (1990). They performed dynamic tests on 6-storey, 1/3 scale, concentrically braced steel frames and compared the results with the numerical ones those obtained from the equivalent *SDOF* system, Figure 1.1. The point (0.62 s, 104 in/sec) that corresponds to experimental results shown on Figure 1.1 is consistent with the analytical prediction.

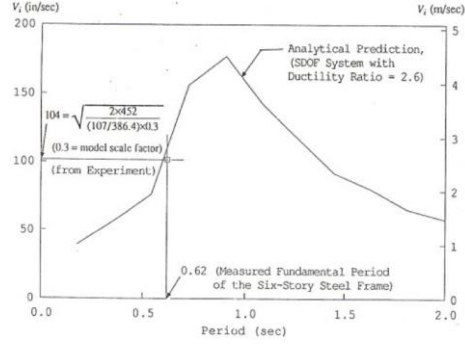


**Figure 1.1 :** Energy equivalent velocity comparisons of *MDOF* and equivalent *SDOF* systems, (Uang and Bertero, 1990).

Since the efficiency of the equivalent *SDOF* system usage has been proved by the experimental and numerical studies, several mass normalized input energy spectra have been proposed in the literature (Akiyama 1985, Kuwamura and Galambos 1989, Fajfar et al. 1989, Uang and Bertero 1990, Kuwamura et al. 1994, Chai et al. 1998, Chou and Uang 2000, Decanini and Mollaioli 2001, Benavent-Climent et al. 2002, Lopez-Almansa et al. 2013, Dindar et al. 2015, Mezgebo and Lui 2016).

Akiyama (1985) assumed that the damping ratio of a system may reach up to 10% after generation of the damage on the structural members. So, the 10% damped spectral velocity was proposed for the prediction of the bilinear  $E_I$  spectrum. The breaking point on the spectrum is obtained by dividing the corner period ( $T_C$ ) of *EQ* record by a scalar value of 1.2, equation (1.3).

$$\left( \frac{E_I}{m} \right)_{\max} = \frac{V_E^2}{2} \quad (1.3)$$

Kuwamura and Galambos (1989) proposed a similar equation to predict  $E_I$ . However, the intensity of *EQ* record ( $I_e$ ) is also considered by the variable of  $T_C$ , equation (1.4).  $I_e$  is calculated by equation (1.5). The study also mentioned that  $E_I$  is independent of the lateral stiffness of the structure and barely affected by the damping. Additionally,  $V_E$  vs. period ( $T$ ) relation is quite similar to that of pseudo velocity spectrum of *EQ* record.

$$V_E = \begin{cases} \frac{\sqrt{T_C I_e}}{2} \frac{1.2T}{T_C} & T \leq T_C \\ \frac{\sqrt{T_C I_e}}{2} & T > T_C \end{cases} \quad (1.4)$$

$$I_e = \int_0^t \ddot{u}_g^2(t) dt \quad (1.5)$$

Fajfar et al. (1989) computed the mass normalized input energy ( $E_I/m$ ) for diverse velocity controlled *SDOF* systems and proposed an empirical relation, equation (1.6). The corner period ( $T_c$ ) was calculated by using equation (1.7).

$$\left(\frac{E_I}{m}\right)_{\max} = 2.2t_d^{0.5} PGV^2 \quad (1.6)$$

$$T_c = 4.3 \frac{PGV}{PGA} \quad (1.7)$$

Uang and Bertero (1990) proposed a relationship based on the significant duration ( $t_d$ ) of *EQ* to predict  $E_I/m$  of a structure with a damping ratio of 5%, equation (1.8). They stated that maximum energy is realized on corner period ( $T_c$ ) of *EQ*.

$$\left(\frac{E_I}{m}\right)_{\max} = \frac{1}{2}(1+0.12t_d)^2 PGV^2 \quad (1.8)$$

Kuwamura et al. (1994) performed some numerical analyses and proved that the Fourier spectrum of an acceleration record is almost identical with  $V_E$  spectrum of the undamped elastic *SDOF* system.

Chai et al. (1998) suggested a formulation for  $V_E$  based on the results of Akiyama (1985) and Kuwamura and Galambos (1989). The study considers the peak ground acceleration ( $PGA$ ), peak ground velocity ( $PGV$ ),  $t_d$  and  $T_c$ , equation (1.9).

$$V_E = \Omega_v PGV \quad (1.9)$$

where  $\Omega_v$  is calculated as given in equation (1.10).

$$\Omega_v = \begin{cases} 1.2 \times 0.69 \left(\frac{PGA}{PGV} t_d\right)^{3/8} \frac{T}{T_c} & T \leq \frac{T_c}{1.2} \\ 0.69 \left(\frac{PGA}{PGV} t_d\right)^{3/8} & T > \frac{T_c}{1.2} \end{cases} \quad (1.10)$$

Chou and Uang (2000) tried to predict absorbed energy through the attenuation relations for inelastic systems, equation (1.11).  $Y$  is the response value,  $M$  is moment magnitude,  $D$  is closest distance from station in km,  $G_{ci}$  and  $G_{di}$  are parameters related to soil type. Relations are obtained for source-to-site distance, local soil type and displacement ductility by means of various acceleration records. The study demonstrated that absorbed energy is a stable index for the prediction of  $E_I$ , whereas pseudo-velocity is a weak one for inelastic damped systems.

$$\log_{10}(Y) = a + b(M - 6) + c(M - 6)^2 + d \log \sqrt{r^2 + h^2} + eG_1 + fG_2 + \varepsilon \quad (1.11)$$

Decanini and Mollaioli (2001) proposed a spectral equation to estimate  $E_I$  in both linear and nonlinear stages. The study considers moment magnitude ( $M_w$ ), soil type and source-to-site distance to compute  $E_I$ . An elastic perfectly plastic (*EPP*) model is adopted and compared with some others.

Benavent-Climent et al. (2002) proposed an  $E_I$  spectra that is applicable to structures located in low-to-moderate seismicity regions. The spectra were generated by the dynamic response analyses of historical records gathered from 48 *EQs* in Spain, equation (1.12).

$$\begin{aligned} T \leq T_C &\rightarrow V_E / (PGA \times K) = 1.25(T / K) \\ T > T_C &\rightarrow V_E / (PGA \times K) = 1.25T_C \end{aligned} \quad (1.12)$$

Lopez-Almansa et al. (2013) proposed an  $E_I$  spectrum for the regions having a design acceleration of 0.3g or higher by means of linear and nonlinear dynamic analyses of the selected Turkish *EQ* records. Since the inelastic energy is higher than the elastic energy for a short-period range, nonlinear analyses were performed in this range. Conversely, as elastic energy is higher than the inelastic energy for the mid- and high-period range, elastic time history analyses were accommodated for this range. The selected *EQ* records were grouped according to soil type, severity of *EQ* and source-to-site distance. It was stated that the proposed spectrum generates similar results with the existing spectra.

Cheng et al. (2014) proposed an empirical ground motion prediction equation to estimate absolute and relative input energy equivalent velocities by using a large set of *EQ* records, equation (1.13). It was concluded that absolute and relative input energy are good alternatives against to the standard intensity measures utilized in the performance-based design.

$$\begin{aligned} \ln(IM_{ij}) &= a + b(M_i - 6) + c(M_i - 6)^2 + (d + fM_i) \ln \sqrt{R_{ij}^2 + h^2} + \dots \\ &\dots + e \ln(V_{s30ij} / 1130) + m_1 NR_i + m_2 RS_i + \eta_i + \xi_i \end{aligned} \quad (1.13)$$

Dindar et al. (2015) proposed spectra for  $E_I$  and  $E_P$  by using the results of extensive nonlinear time history analyses. The spectra account for soil type, *EPP* restoring force characteristics, displacement ductility, *PGA* of the record and a 5% damping ratio. The

study concluded that the developed spectra should be modified and/or redeveloped for the dissimilar cases.

Mezgebo and Lui (2016) also proposed spectra for  $E_I$  and  $E_P$ . The spectra were generated by considering constant ductility to decrease the scattering of the numerical results. The researchers concluded that the proposed equations produced conservative results comparing to others.

Alicı and Sucuoğlu (2016) proposed attenuation models to predict seismic input energy by using a large number of records, equation (1.14). In the equation,  $R$  is epicentral distance,  $M$  is moment magnitude,  $S$  is a coefficient related with soil type,  $F_N$  and  $F_R$  are the coefficients related with the fault types. They also proposed a velocity scaling method in their study, equation (1.15).

$$\log(V_e) = b_1 + b_2M + b_3M^2 + (b_4 + b_5M) \log \sqrt{R^2 + b_6^2} + b_7S + b_8F_N + b_9F_R \quad (1.14)$$

$$\frac{V_{eq}}{PSV} = ae^{-bT} + c \quad (1.15)$$

Most of the existing literature claims that seismic input energy ( $E_I$ ) spectra is scarcely affected by the variation of damping (Bertero and Uang 1988, Bruneau and Wang 1996, Zahrah 1998, Sütçü et al. 2006, Benavent-Climent and Zahran 2010). The available input energy spectra were produced mostly for a 5% damping ratio.

Khashaee et al. (2003) performed some numerical analyses for the inelastic systems with constant displacement ductility of  $\mu=3$  and variable stiffness ratios. Different acceleration records, as well as damping ratios ( $\xi=0, 2, 5, 10, 20$  and  $40\%$ ), were evaluated in the study. It was concluded that although the effect of damping ratio less than 5% is a minor effect, damping ratios greater than 5% have a significant effect on  $E_I$ . Additionally, it was stated that as the damping ratio increases this results in higher  $E_I$  for longer periods.

In a similar way, Ye et al. (2009) proposed an energy-based seismic design framework by considering the damping ratio. The damping modification factor is suggested in the study, equations (1.16) and (1.17).

$$\zeta = \frac{E_{I_{max,\xi,\mu}}}{E_{I_{max,\xi=0.02,\mu=1}}} = \left( 0.6845 - \frac{0.6393}{\mu} - 0.0882 \ln \xi - \frac{0.1517}{\mu} \ln \xi \right) \mu^{-0.57} \quad (1.16)$$

$$NE_{1max,\xi,\mu} = (\zeta + 0.05) \times NE_{1max,\xi=0.02,\mu=1} \quad (1.17)$$

The study concludes that seismic input energy  $E_I$  is decreasing by the increment of damping ratio and ductility.

The spectra of input energy ( $E_I$ ) and plastic energy ( $E_P$ ) that were proposed by several researchers could be utilized to evaluate the severity of any earthquake data in terms of efficiency, sufficiency and sensitivity. Specifically, Mollaioli et al. (2013) utilized the energy equations as an alternative intensity measure for base isolated structures.

For the time being; although several equations exist to predict  $E_I$ , only a small number of studies aimed at *EBS*D procedures are available. Moreover, there are no studies that were performed on the energy capacities of the structural members (Fardis 2018). Fardis (2018) also mentioned that being scalar and having a solid base (energy balance) are the basic advantages of *EBS*D. The study concluded that if earthquake engineering research re-engages with the very promising and appealing concept of seismic energy, it is feasible to formulate a full-fledged new paradigm of seismic design in time for the third generation of Eurocodes, after 2030.

Akbaş et al. (2001) proposed an energy-based design methodology for performance-based earthquake resistant design. The seismic energy was expressed by hysteretic energy and its distribution along the building's height. The energy distribution model along the height of the frame was believed to represent the energy distribution very well in special moment-resisting frames. The energy dissipation capacity of structural members were determined by cumulative plastic rotation capacity of the element under cyclic loading.

Leelataviwat et al. (2002) derived seismic design forces through the energy balance concept for *SDOF* systems and extended it to multi-storey moment frames. Ultimate design forces are derived directly from input energy for a selected design pseudo-velocity spectrum, plastic yield mechanism and target deformation. The proposed procedure is evaluated by means of 2-, 6- and 10-storey moment frames for 2% target drift. The results of generated numerical models indicated that deriving the design forces through the energy balance concept may lead to design structures with controllable seismic response. However, the results obtained were in the conservative side when compared to the nonlinear time history analyses.

Sütçü et al. (2006) proposed an energy-based damper design procedure that assumes an uniform inter-storey displacement distribution to determine viscous damping coefficient. Inter-storey displacements were reduced by means of the viscous dampers positioned according to the suggested procedure.

Leelataviwat et al. (2009) proposed a seismic evaluation procedure through the modified energy balance concept, (Lee and Goel, 2001). The force-displacement curve obtained from push-over analyses is converted into an energy capacity diagram. The energy demand curve is obtained by using the modified energy balance equation given in equation (1.18), where  $\gamma$  is the modification factor provided by Lee and Goel (2001),  $M_n^*$  modal mass for  $n^{th}$  mode and  $S_v$  is pseudo spectral velocity.

$$E_{demand} = \gamma \frac{1}{2} M_n^* S_v^2 \quad (1.18)$$

Details of the method is shown schematically in Figure 1.2. The point reached from the intersection of the energy demand and capacity curves is considered as the performance point. The method was applied to a three-storey moment resisting frame for the selected acceleration record applied in the incremental form. The obtained storey displacements were compared with the results of the nonlinear time history analyses. Differences between the results are obtained in the range of 1.39 to 44.32%.

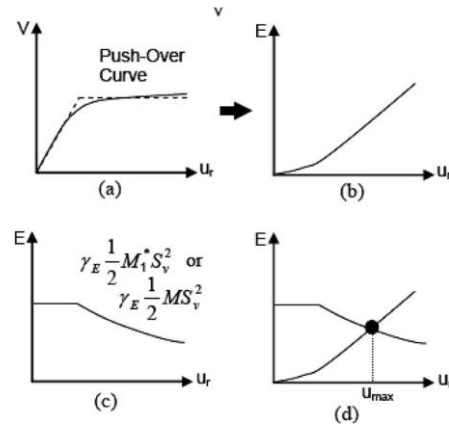


**Figure 1.2** : Energy based evaluation procedure steps of Leelataviwat et al. (2009).

Benavent-Climent and Zahran (2010) developed a methodology to evaluate the existing frames in terms of their seismic energy components. The methodology combines push-over and some modal analyses. The frequency content of  $EQ$  and dynamic properties of the frames are considered in the procedure. The methodology was applied to five- and eight-storey frames numerically. The predicted hysteretic energy are compared with the results of nonlinear time history analyses. The

comparisons indicate acceptable consistency for the five-storey frame. However, differences in the hysteretic energy reached almost 45-50% for the eight-storey frame. Benavent-Climent (2011) applied their procedure to frames retrofitted with the metallic dampers. He tested a one-storey frame on the shake table to evaluate his procedure, Figure 1.3. The experimentally obtained top displacement of the specimen was 15.5 mm while the prediction of the methodology is 16.2 mm. The procedure was also applied to 3, 6 and 9-storey moment resisting frames, numerically. By application of the procedure, the storey drifts of the retrofitted frames were obtained smaller than the allowable limits.



**Figure 1.3 :** Testing specimen of the Benavent-Climent (2011).

Manoukas et al. (2011) proposed a static push-over analysis methodology by using the energy equivalent *SDOF* system. The methodology assumes that performance point corresponds to the point where the works done by internal and external forces are equal to each other. The methodology was applied to specific moment-resisting frames with 3, 6, 9 and 12-storeys. It was concluded that the proposed push-over analysis methodology mostly predicted floor displacements of the frames with a  $\pm 25\%$  error margin when compared with the nonlinear time history analyses.

Habibi et al. (2013) suggested a step-wise multi-mode energy based design method to retrofit existing structures by means of passive energy dissipaters. Modal push-over analyses were applied to compute modal yield force and ductility factor of an equivalent *SDOF* system. The contribution of the passive energy dissipaters was taken into account by using the parameters of the effective damping ratio and effective stiffness of the devices. Storey drifts were computed through the suggested procedure. Location of the dampers was decided by considering the dissipated energy and the storey drifts. The results of the procedure were compared with the results of nonlinear time history analyses for a nine-storey building. Maximum disagreement between the results was found to be about 6%.

Ke and Chen (2014) developed a design and evaluation procedure for steel frames with steel slit walls. The proposed concept, which was based on modified energy-balance, was applied to full-scale test and numerical models developed for three- and nine-storey frames. The fundamental vibration modes were considered in the analyses by neglecting the effect of higher modes. Additionally, mode shapes of the frames were considered invariable in the nonlinear range. The energy balance is represented by the equation (1.19) where  $\gamma_s$ ,  $M_1^*$  and  $S_v$  are energy factor, effective mass acting on fundamental period and pseudo spectral velocity, respectively.

$$\gamma_s \left( \frac{1}{2} M_1^* S_v^2 \right) = E_e + E_p \quad (1.19)$$

Since the dynamic response of the system is controlled by the fundamental mode, the energy balance of the equivalent *SDOF* system is able to represent the response of the *MDOF* system. Dependently, the energy factor is computed through equation (1.20).

$$\gamma_s = \frac{E_e + E_p}{\left( \frac{1}{2} M_1^* S_v^2 \right)} = \frac{\frac{1}{2} V_{pw} \delta'_{pwr} + \frac{1}{2} (V_{pw} + V_b) (\delta' - \delta'_{pwr})}{\frac{1}{2} V_e \delta'_e} \quad (1.20)$$

The general meanings of the terms existing in equation 1.20 are illustrated in Figure 1.4.

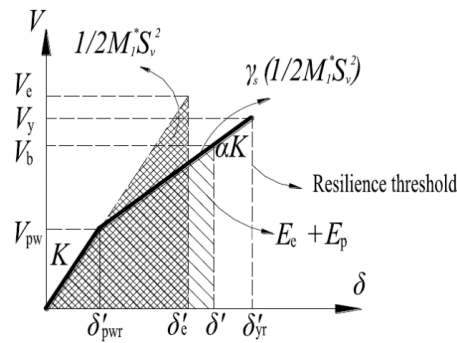


**Figure 1.4 :** Energy balance of equivalent SDOF system and design parameters

Predictions of the proposed energy based procedure displayed attractive similarity with the results of nonlinear time history analyses. However, it should be noted that the procedure can only be applied to low- and mid-rise structures because of the assumptions.

D'Ambrissi and Mezzi (2015) developed a nonlinear static analyses methodology in which the energy capacity and energy demand were utilized. The methodology does

not require an iterative process. It was applied to a six-storey frame. It produced more reliable results in terms of the lateral displacements comparing with the *EC8* method. However, the scattering of the predictions gets higher values for the plastic hinge rotations.

Mezgebo and Lui (2016) suggested a new design methodology for *EBS* of steel moment frames. Energy demand of the *MDOF* systems are extracted from the equivalent *SDOF* systems. Moreover, push-over analyses were necessary similar to the formerly proposed methodologies. The procedure was applied to moment resisting frames with 3, 5, 7 and 9-storeys. The input energies were determined in two independent ways. These were the nonlinear time history analyses and the usage of equivalent *SDOF* systems. Maximum input energy differences between those methods were obtained about 20%.

### **1.3 Hypothesis**

Storey displacements of an inelastic frame type steel *MDOF* system can be predicted by means of the seismic input energy and vibrational characteristics of the structural system. Essentially, success of the displacement prediction is dependant on the accuracy of the seismic input energy.

The distribution of the plastic energy between the structural members could be controlled via the energy equations. Hence, the disposable members (i.e. metallic dampers) could be utilized in the proper locations to diminish the damage in the structural members.



## 2. EXPERIMENTAL STUDIES

Shake table tests on diverse steel *SDOF* and *MDOF* specimens were performed to investigate intensity and variation of seismic energy terms. The *SDOF* and *MDOF* specimens, having similar natural periods, were exposed to the same historical *EQ* records to check the relationship of their modal seismic input energies.

The definitions of testing facilities and specimens, the properties of the historical *EQs*, details of the tests and the results will be presented in this chapter.

### 2.1 Testing Facility and the Preparatory Works

#### 2.1.1 Testing facility

The real dynamic tests of *SDOF* and *MDOF* systems were performed on ARI-1 shake table of ITU Structural and Earthquake Engineering Laboratory (STEELab), Figure 2.1. The uni-axial shake table has 2.35×2.35 m plan dimensions and  $\pm 2$  g acceleration,  $\pm 1000$  mm/s piston velocity and  $\pm 325$  mm displacement stroke capacities. The overturning moment capacity of the table is 320 kNm and the friction lost is around 1.5%.



**Figure 2.1** : ARI-1 shake table of ITU.



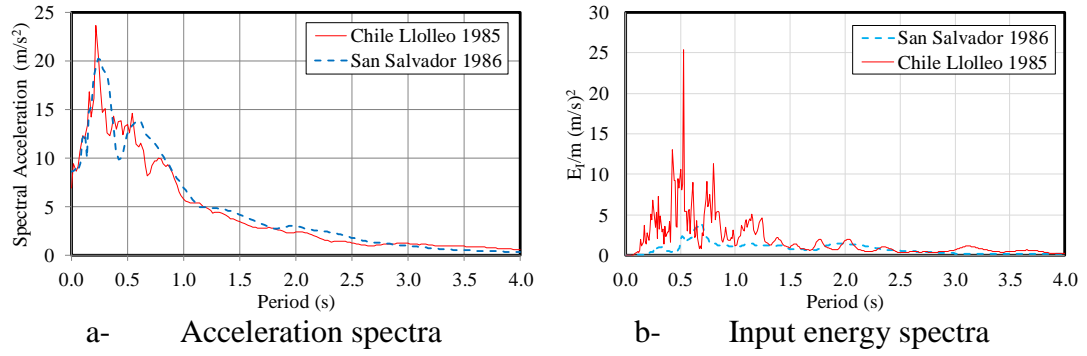


**Figure 2.4 :** Acceleration and input energy spectra of the selected records.

Loma Prieta and Erzincan  $EQs$  were also utilized in the part of this study to evaluate lateral stiffness effect on the seismic input energy. The same data were also used in another research study to obtain a scaling factor for seismic input energy, (Okuyan 2017).

Six additional records were selected to use in the experimental and numerical studies of  $MDOF$  systems. Some important features of the records are gathered in Table 2.1.  $M_s$  and  $d$  stand for surface moment magnitude and epicentral distance, respectively.

**Table 2.1 :** Some properties of the  $EQ$  records.

#	Record	Symbol	$M_s$	$d$ [km]	PGA [cm/s <sup>2</sup> ]	PGV [cm/s]	Test
1	Chile Llleleo 1985	CH-N10E	7.80	6.70	693.7	38.4	S
2	San Salvador 1986	SS-CIG	5.40	16.00	858.3	59.3	S, M
3	Erzincan 03/13/1992 Erzincan S.	ERZ-EW	6.90	8.97	486.6	64.3	S, M
4	Loma Prieta 10/18/1989 Hollister Diff. Array S.	HDA165	7.10	45.10	263.9	43.9	S, M
5	Superstition Hills 11/24/1987 USGS 9400 Poe Road S.	POE360	6.60	11.20	294.3	32.8	M
6	Superstition Hills 11/24/1987 USGS 5051 P. Test Site S.	PTS315	6.60	15.99	369.8	43.9	M
7	Duzce 12/11/1999 Bolu S.	BOL090	7.14	12.02	790.4	65.9	M
8	Chi-Chi, Taiwan 09/20/1999 CWB 99999 TCU067 S.	TCU067	7.62	28.70	318.8	66.6	M

In the last column of the table, the abbreviations of  $S$  and  $M$  represent the types of systems ( $SDOF$  or  $MDOF$ ). Acceleration time histories of the additional records were plotted in Figure 2.5.

Elastic spectral accelerations of the records for a 3% damping ratio, as well as their mean spectra, are presented in Figure 2.6. A plateau is observed between 0.3 and 0.9 seconds.

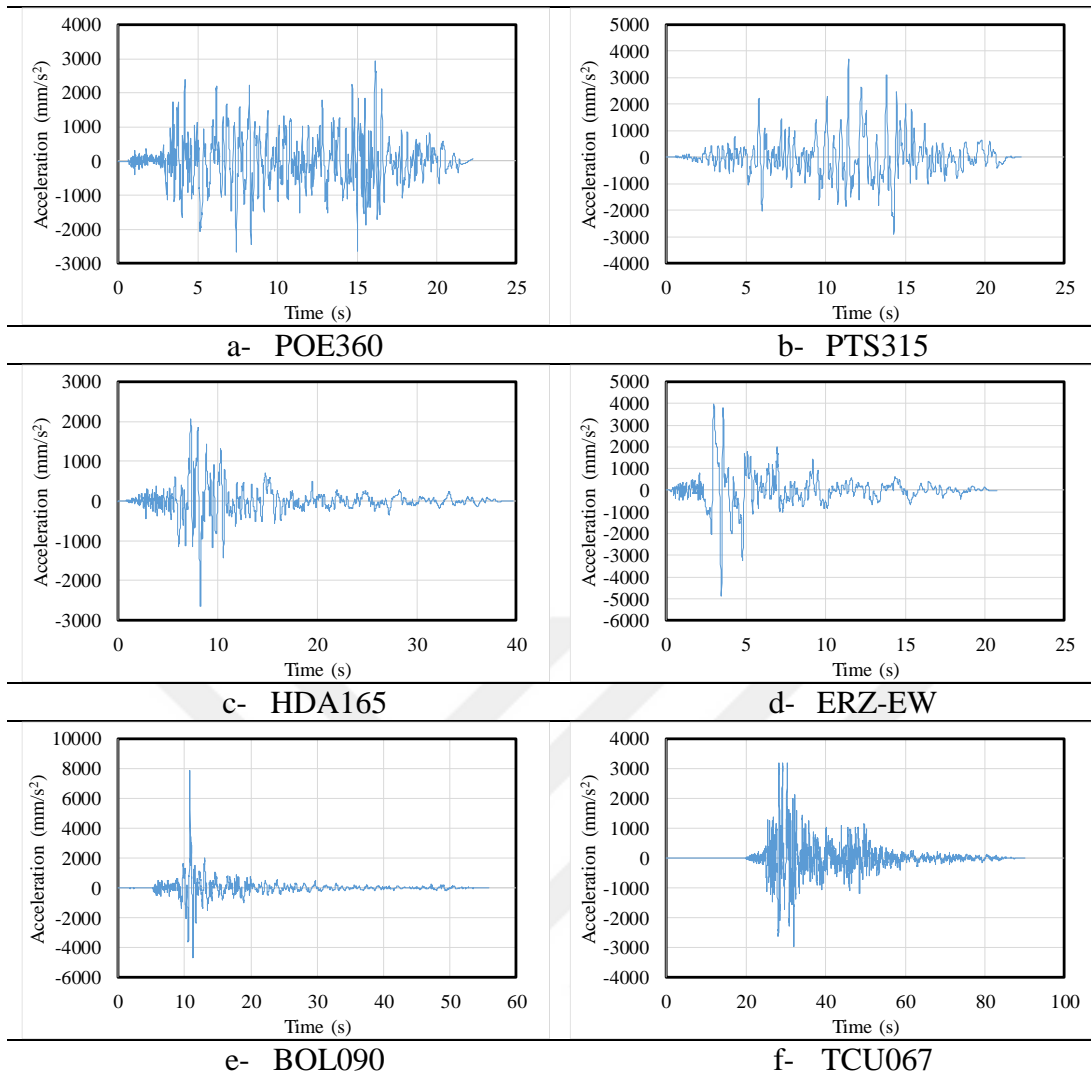


**Figure 2.5 :** Selected *EQ* records for *MDOF* specimens.

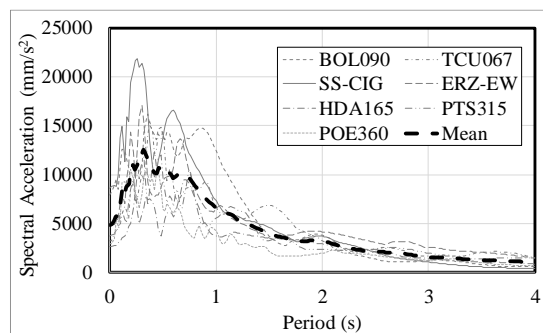


**Figure 2.6 :** 3% damped elastic acceleration spectra of the *EQ* records.

The minimum and maximum spectral accelerations are obtained as 9500 and 22000  $\text{mm/s}^2$  in the plateau range for *POE360* and *SS-CIG* records, respectively.

### 2.1.3 The measuring system

The measuring system employed in the performed tests consists of accelerometers, strain gauges, linear potentiometric transducers (*LPTs*) and linear variable differential transformers (*LVDTs*). *MEMS* type tri-axial accelerometers having  $\pm 2g$  capacity were utilized in *SDOF* tests and at the first storey of *MDOF* specimens. Besides, *MEMS* type accelerometers with  $\pm 8g$  capacity were employed at 2<sup>nd</sup> and 3<sup>rd</sup> floors of *MDOF* specimens. Additionally, three strain based accelerometers with  $\pm 2g$  capacity were used to collate with the *MEMS* type accelerometers. The raw acceleration data received from the accelerometers was filtered by using a *Butterworth bandpass filter* with cut-off frequencies of 0.1 and 18 Hz.

*LPTs* were utilized to measure the displacements of shake table and floors of the specimens at the beginning of the study. However, once aware of their damping effect on the specimen, it was decided to cancel their usage for the measurement of floor displacements.

*LVDTs* were mostly utilized to measure smaller displacements of the components of the specimens. TML type displacement transducers (CDP5, CDP10 and CDP25) that are suitable for both static and dynamic measurements were used in various locations of the specimens (Url-1).

Several strain gauges were pasted in different sections of the specimens. Post-yield type (*YF* series) strain gauges that have a deformation capacity of 15-20% were selected for this purpose. The strain gauges can operate in a temperature range of -20 to +80°C (Url-2).

### 2.1.4 Application of the vision-based measuring system

The vision-based measuring systems are preferred as an alternative to the conventional systems due to their cost-effective application. The basic component in the measurements is linear displacement. Strain, angular displacement, velocity and acceleration histories are able to be generated through the post-processing procedures. The vision-based measuring systems applied with medium and high quality equipments are relatively free from noise problems. The other important advantages of the vision-based measuring system are as follows: it is a cable-free and non-contact system, there is no practical limitation for the number of channels. Some of these features are relatively important, especially for small and flexible specimens.

A video-based algorithm was developed in an accompanying study (Karameşe 2018) and used in this thesis. The developed algorithm was tested by using the video records taken by personal mobile phones and professional cameras with specific lenses.

The video-based sensing methods are applied in the literature for different purposes. Chang and Ji (2007) proposed a method to monitor 3D structural vibration response through images supplied by two diverse recorder. The algorithm is tested by sinusoidal movement of a single point, wind tunnel test of a small bridge model and earthquake simulation of a three-storey small scaled structure. Measuring errors show increasing values at the higher vibration frequency exposed to the specimens.

Morlier et al. (2007) devoped software to figure out the dynamic characteristics of a bridge by means of high speed cameras that based on optical flow algorithm, (Lukas-Kanade 1980). Even though the study was aimed at damage identification on the bridge, the noise became a major concern to overcome in field experiments.

Nogueria et al. (2009) proposed a methodology to determine in-plane spatial displacement and natural frequencies of the structure by using video records. A noticeable marker (black circle on white background) was utilized. Location of the center of circles were traced during the experiments. Since cameras with relatively high frame per second (fps) were preferred in the study, satisfactory results were obtained in a certain frequency interval. They concluded that insufficient illumination and reflection on the image directly effect the result.

Choi et al. (2010) suggested a *dynamic displacement vision system* that focuses on a specific target, the so-called *range of interest (ROI)* in the evaluation stage. The presented system resizes each frame in each step and re-compute the coefficients to obtain real size of each pixel in *ROI*. The comparison of the theoretical results and video-based experimental data exhibited a good consistency.

Park et al. (2010) developed a video-based methodology to detect the behavior of flexible high-rise structures. Two simple web-cams located with diverse angles were utilized to compute displacements of particular points on a simple flexible column specimen. Horizontal displacements were computed through not only spatial variation of the positions but also the rotations. The results of the proposed methodology were compared with the laser displacement sensors. The maximum difference was obtained less than 0.5%.

Nayyerloo et al. (2011) utilized high-speed line-scan type cameras to obtain the spatial displacements. Edges of the specimens were spotted as a continues line to identify certain position of the specimen. The study concluded that the proposed method can compute displacement of the targets without regarding the magnitude of motion. A calibration method to reduce the measurement errors was also proposed.

Vision-based measuring systems have also some defects, however, such as dependency on lighting, resolution and sampling rate (*fps*).

The applied algorithm was based on *template matching methods* (Karameşe 2018). The template matching method has been mostly used for tracking a specific target in the video record rather than to measure a specific displacement component. Two base images should be supplied as source and template. The template image can be obtained by cropping the source image. At the initial stage, the pixels matched with the template exist in the source image. All matching points can be found perfectly if the ideal conditions are satisfied. However, daylight, contrast and reflection may effect achievement of the method.

The Normalized Cross Correlation (*NCC*) method is selected for the algorithm. The main equation representing *NCC* method is shown in equation (2.1).

$$R(x, y) = \frac{\sum_{x', y'} (T'(x', y') I'(x+x', y+y'))}{\sqrt{\sum_{x', y'} (T'(x', y'))^2 \sum_{x', y'} (I'(x+x', y+y'))^2}} \quad (2.1)$$

Where  $T$  and  $I$  stand for template image and source image, respectively.  $T'$  and  $I'$  are determined from equations (2.2) and (2.3).

$$T'(x', y') = T(x', y') - \frac{1}{wh} \sum_{x'', y''} T(x'', y'') \quad (2.2)$$

$$I'(x+x', y+y') = I(x+x', y+y') - \frac{1}{wh} \sum_{x'', y''} I(x+x'', y+y'') \quad (2.3)$$

A GaussianBlur type of filtering operation is utilized to reduce the effect of lighting and reflection on the pixels. Besides, Savitzky-Golay type filtering was adopted to the generated algorithm for smoothing the data.

The vision-based measuring algorithm is utilized in the *SDOF* and *MDOF* tests performed in this thesis. Some demonstrative results obtained for the *SDOF* specimens are presented in Figure 2.7. It can be seen that the vision-based displacement data gathered on the table and specimen show good consistency with the conventional methods, detail of the tests is given in Chapter 2.2.

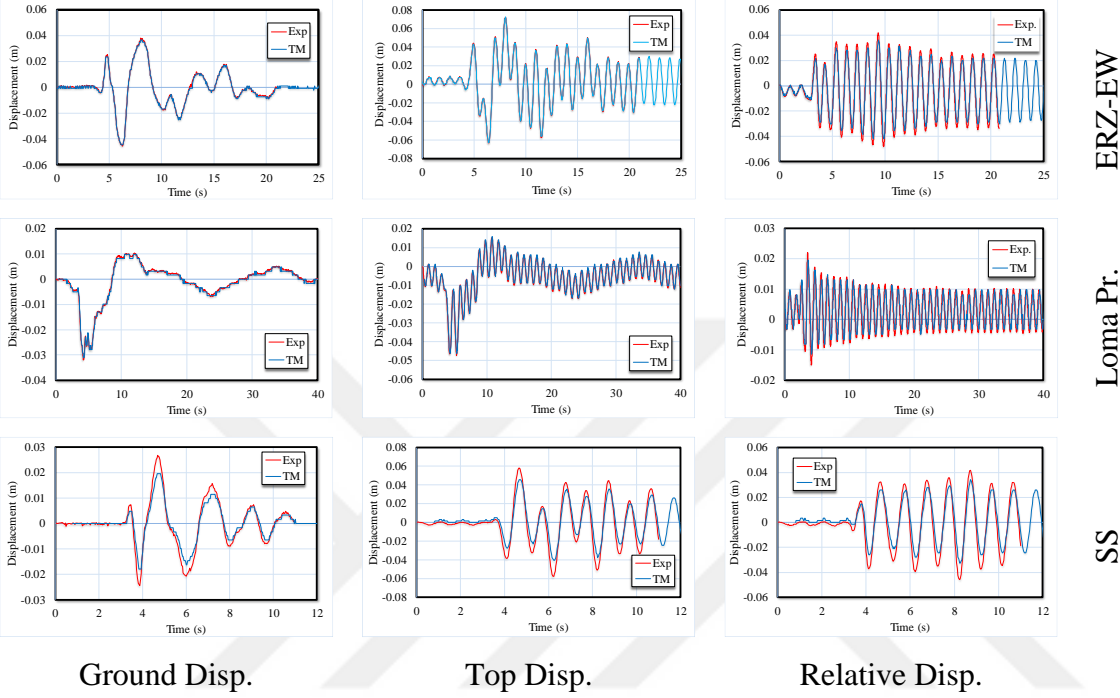


**Figure 2.7 :** Application of vision based measuring systems to *SDOF* specimens.

The algorithm is applied to measure longitudinal strains at the critical section. Six white circles enclosed by black squares (templates) are fixed to the critical section of the member, Figure 2.8.

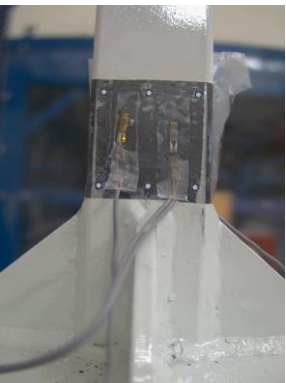


**Figure 2.8 :** Strain measurements by vision based algorithm.

Since the linear displacement components are determined by means of the developed vision-based algorithm, the strains in two perpendicular directions can be computed

by dividing the difference of movement to the initial length between the reference points. Since the linear replacement of pixels at the section is lesser, the filtering operation may cause the loss of some data. Frame rate and resolution quality are key parameters to overcome the issue.

To evaluate the vision quality of the existing cameras on the strain measurements, the video records taken by cameras with 4K (3840 × 2160 pixels) resolution - 30 fps and 2K (1920 × 1920 pixels) resolution - 100 fps were compared with the conventional strain gauge measurements, Figure 2.9. Both cameras produced acceptable results.

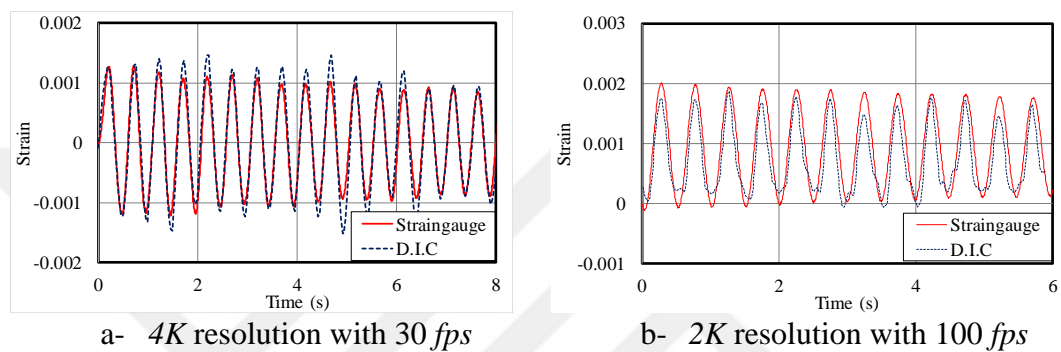


**Figure 2.9 :** Evaluation of the strain measurements.

### 2.1.5 Material tests

Standard coupon tests were performed to define the material characteristics. The dimensions of the coupons are compatible with TS 138 EN 10002-1, Figure 2.10. The coupons were notched at every 5 mm interval. The tests were performed at the ITU Material Engineering Laboratory.

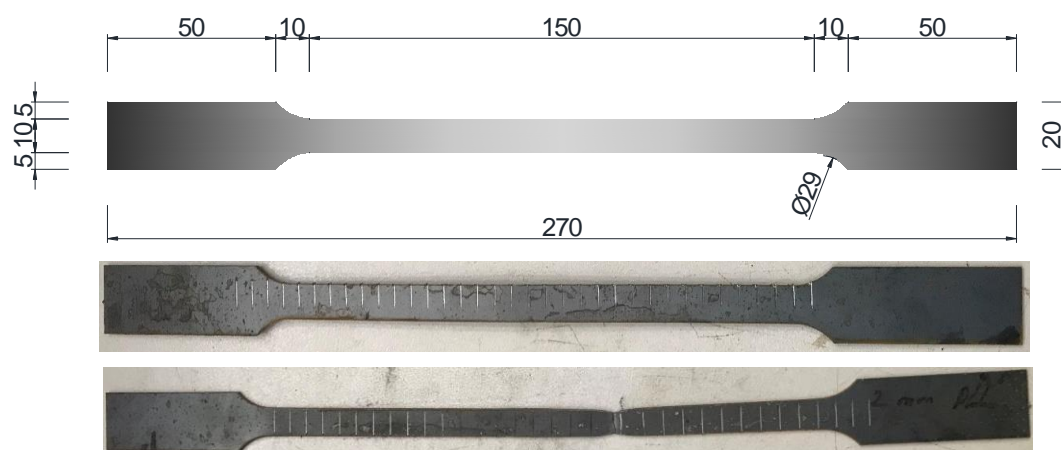


**Figure 2.10 :** Coupon dimensions and tested specimen.

A MTS C40 testing machine was utilized in the coupon tests, Figure 2.11. The extensometer of the device was utilized up to a strain level of 8-10%. Additionally, a couple of strain gauges were used for each specimen.

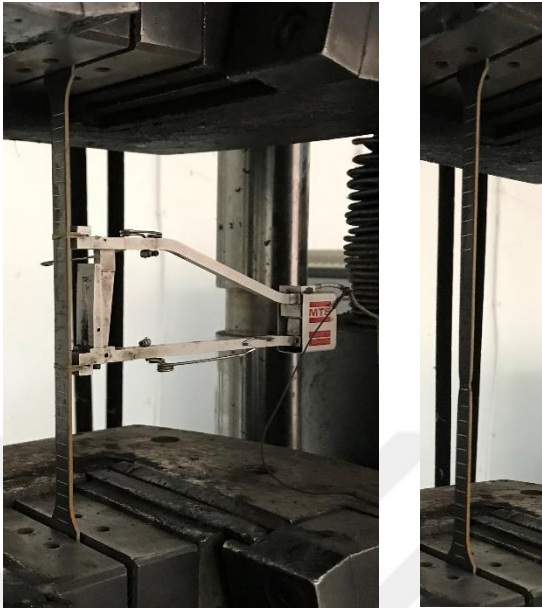


Figure 2.11 : Testing set-up in MTS C40.

A total of eleven tensile tests were performed for the plates taken from four different cross-sections. The test results are presented in Figure 2.12. The response curves of the coupons taken from the same member are quite consistent with each other.

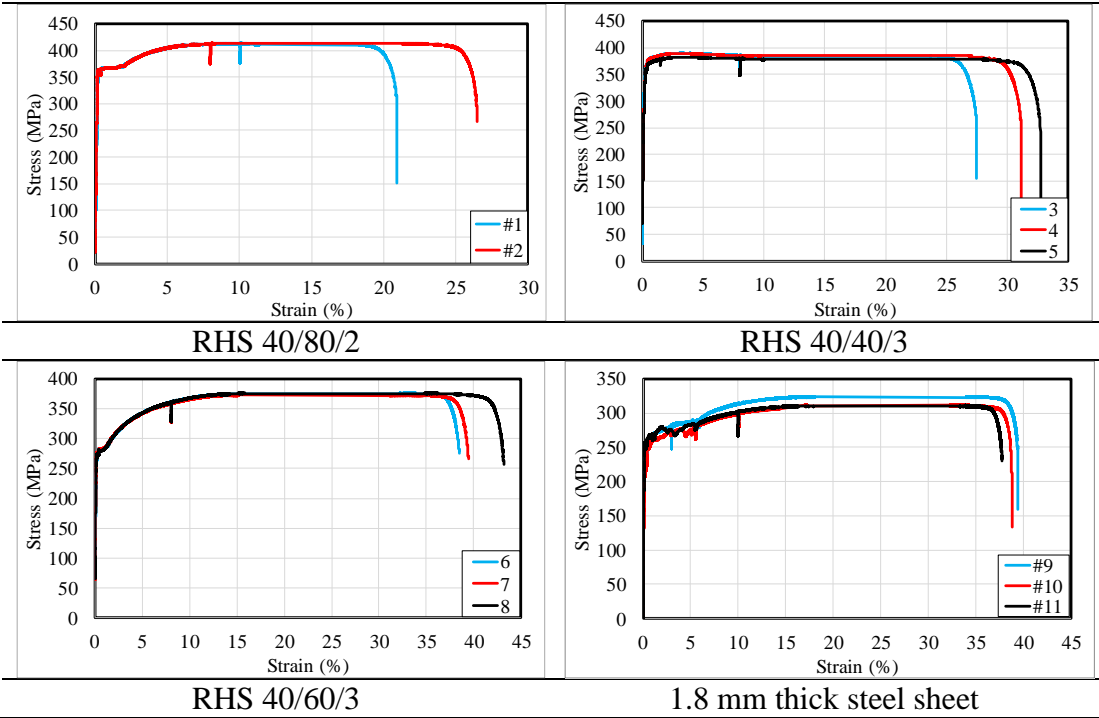


Figure 2.12 : Coupon test results.

Different yield strengths were obtained for the specimens. The minimum value was 205 MPa for 1.8 mm thick steel sheets and the maximum one was 350 MPa for 40/80/2 mm box section. However, the yield strains are quite close to each other. The strain corresponding to the end of the yield plateau is about 2% for all specimens. Some extend of hardening was observed, except for the 40/40/3 box sections. The results of the coupon test are summarized in Table 2.2.

**Table 2.2 :** Results of the coupon tests.

Section	#	$\sigma_y$ (MPa)	$\varepsilon_y$ (%)	E (MPa)	$\sigma_u$ (MPa)	$\varepsilon_{@ \sigma_u}$ (%)	$\varepsilon_u$ (%)
40/80/2	1	350	0.16	1930	414	11.8	22.0
	2	350	0.16	2042	414	12.0	25.0
	3	330	0.13	2052	390	9.2	25.5
40/40/3	4	330	0.14	2064	390	9.6	27.6
	5	330	0.15	2002	383	11.2	29.4
	6	260	0.10	1977	376	19.2	37.6
40/60/3	7	260	0.10	2068	374	22.4	37.8
	8	260	0.11	2090	376	21.6	41.0
1.8 mm Plate	9	205	0.10	2001	299	19.8	37.4
	10	205	0.14	1464	312	21.2	38.6
	11	250	0.13	1946	311	21.6	36.0

### 2.1.6 Development of an algorithm to compute the seismic energy components

An algorithm was developed to compute the seismic energy components. General flow chart of the algorithm is depicted in Figure 2.13. A Matlab based code based on this algorithm was generated for the post-processing of the test data.

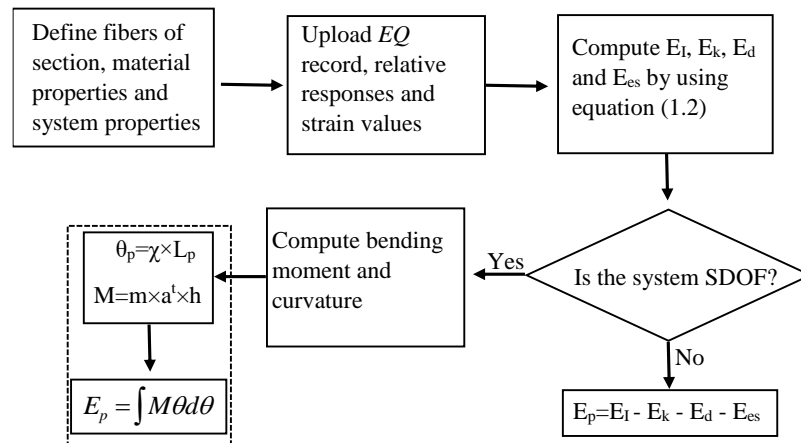


**Figure 2.13 :** Flow chart of the developed algorithm.

Important steps of the algorithm are listed as follows:

- 1- Recieving of the fiber data to generate the critical sections of the system.

- 2- Computation of the sectional properties i.e. area and moment of inertia.
- 3- Receiving of the system characteristics such as damping ratio, natural vibration period and the material properties.
- 4- Receiving of the input acceleration data and the storey response histories.
- 5- Computation of seismic input energy and the other components in the energy balance equation, equation (2.2).
- 6- Computation of plastic energy ( $E_p$ ) by subtracting elastic and damping energy terms from seismic input energy. In the current version of the software, for *SDOF* systems,  $E_p$  can also be calculated by integration of moment-rotation relations in the critical sections.

## 2.2 Single Degree of Freedom Systems

### 2.2.1 Definition of specimens and testing system

The steel cantilever specimens consist of three parts called as Part 1, Part 2 and Part 3. Part 2 is a test column that has a rectangular box section with 40 mm in depth, 80 mm in width and 2 mm in thickness. The height of the column is 1500 mm. The identical parts of #1 and #3 are utilized to connect the columns to the shake table and the supplementary mass, Figure 2.14. The parts are connected to each other with the steel plates having 10 mm thickness and 150×150 mm plan dimensions. Four 8.8 quality M8 bolts were used for the connection.

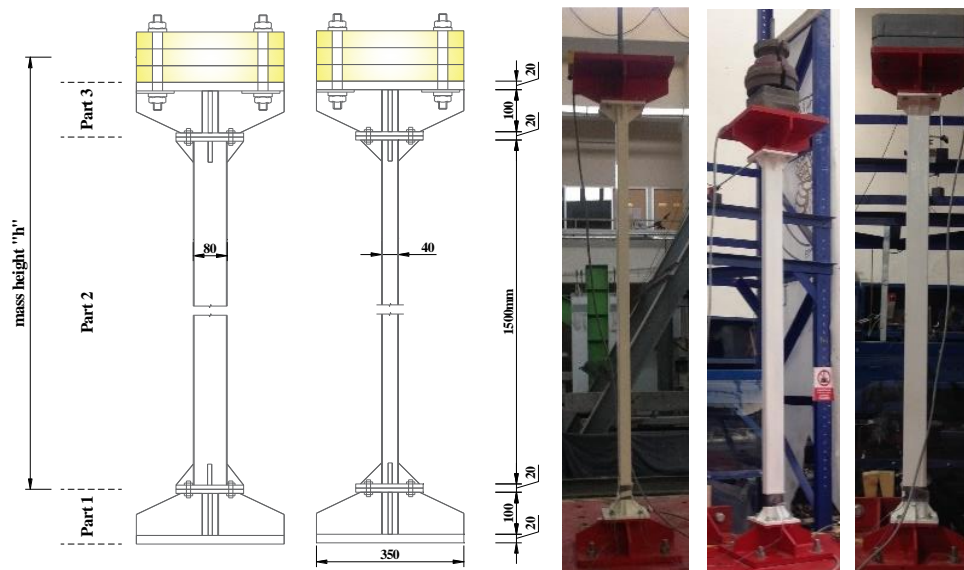


**Figure 2.14 :** *SDOF* specimens and mass tuning.

The hole configuration of Part 3 gives an opportunity to utilize diverse types of supplementary masses, Figure 2.15.

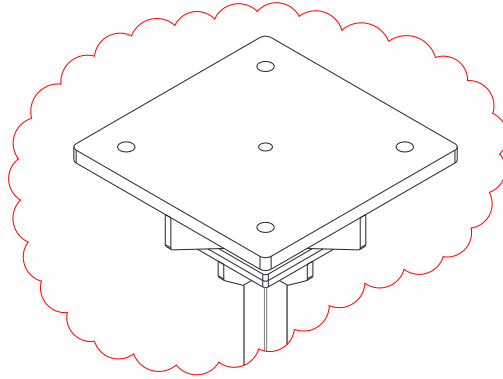


**Figure 2.15 :** Hole configuration of the Part 3.

The effective height ( $h$ ) of the specimens is arranged to represent the proper position of mass center. The properties of the specimens, i.e. cross-sectional dimensions, effective heights, supplementary masses and the measured vibration periods, are listed in Table 2.3.

**Table 2.3 :** Effective height of the specimens and corresponding periods.

Specimen #	Cross-Section mm	Eff. height (h) m	Mass (W) $\text{Ns}^2/\text{m}$	Period (T) s
1	40/80/2	1.690	31.59	0.277
2	40/80/2	1.725	43.75	0.333
3	40/80/2	1.725	57.26	0.385
4	40/80/2	1.775	74.09	0.455
5	40/80/2	1.775	84.69	0.500
6	40/80/2	1.775	98.09	0.526
7	40/80/2	1.795	152.75	0.667
8	40/80/2	1.940	272.66	1.000
9	40/80/2	1.955	390.71	1.250
10	40/80/2	2.200	519.56	1.667
11	20/40/1	0.940	42.73	0.500
12	20/40/1	0.990	76.68	0.667
13	20/40/1	1.125	136.53	1.000

The specimens tagged #11, #12 and #13 correspond to half-scaled specimens, which have 20/40/1 mm rectangular box cross-sections with 750 and 1500 mm height. Steel and aluminum versions of specimens #11, #12 and #13 were produced, Figure 2.16. Comprehensive information about these specimens can be found in the work of Okuyan (2018).



**Figure 2.16 :** *SDOF* specimens with diverse lateral stiffness.

All *SDOF* specimens were tested in the ‘weak’ direction of the cross-section. Consequently, during the uni-axial shaking tests, very low intensity of vibrations were recorded in the perpendicular direction. A representative graphic to evaluate the intensities of in-plane and out-of-plane accelerations is presented in Figure 2.17.

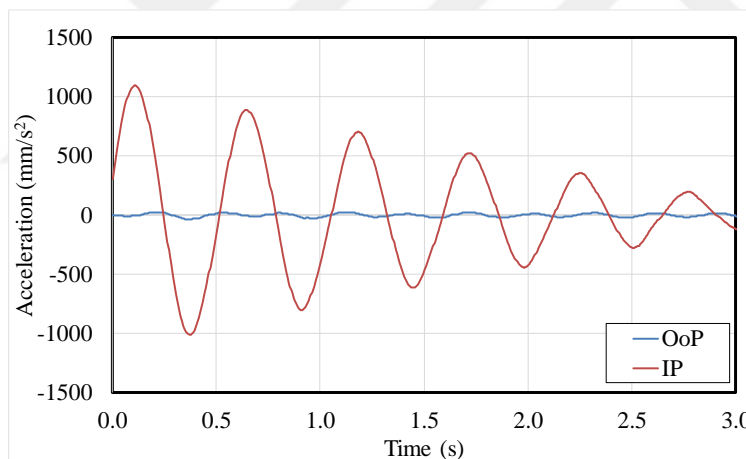


**Figure 2.17 :** In-plane and out-of-plane top accelerations of the *SDOF* specimens.

Two strain gauges on both faces of the bottom-most section of Part 2 are utilized to capture longitudinal strain histories. The material test results were used to evaluate the measured strains. All the measuring system used in *SDOF* tests are illustrated in Figure 2.18.

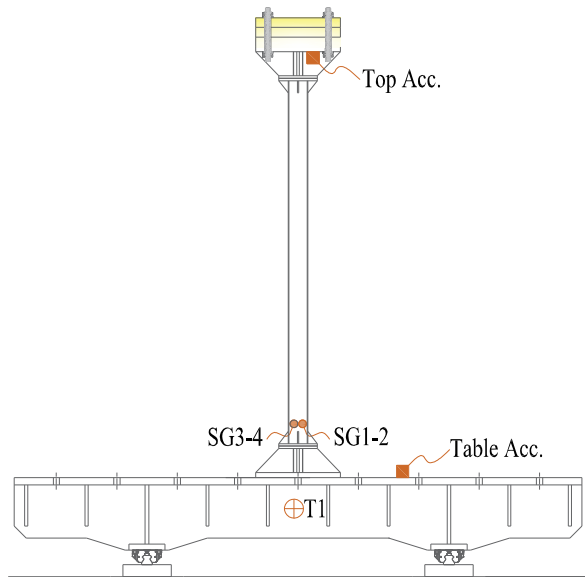


**Figure 2.18 :** Measuring system of *SDOF* specimens.

It was pointed out that the displacement transducer (LPT-1250) positioned at the top of the specimen caused some additional damping to the specimen. The measurements showed that global damping of the system, as calculated with equation (2.4), increased to 3% from 0.3%, Figure 2.19. In the figure, blue lines represent the free vibration response of the specimen without the displacement transducer after the *EQ* excitation is over. The red line illustrates the response of the specimen with the top displacement transducer.

$$\xi = \frac{1}{2\pi n} \ln \frac{\ddot{u}_i}{\ddot{u}_{i+j}} \quad (2.4)$$

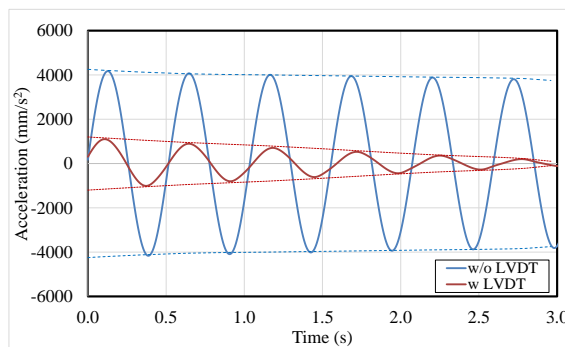


**Figure 2.19 :** Effect of LPT utilized for measuring top displacement on damping.

It is notable that the envelope connecting the peaks of the blue curve is almost horizontal, whereas the slope is greater for the red curve. Not only is the damping ratio influenced by the existing of displacement transducer, but acceleration amplitudes is

also changed. A similar experience was discussed in the literature by Deniz et al. (2017). They stated that the unexpected damping because of inherent friction and spring stiffness of the displacement transducer may have an effect on the results, especially for relatively flexible specimens. Hence, it was decided not to use the displacement transducer at top of the specimen.

One of the indirect methods that can be used to elucidate the top displacement history of the specimen is the integration of acceleration data measured at the same location. However, the noise effect in the acceleration data is the main disadvantage of the method. The error propagation in the calculated displacement may be getting larger in the time domain, Figure 2.20. In the figure, the direct measured displacement history (dashed black line) is not consistent with the acceleration based displacement history (solid red line) beyond 4 s.

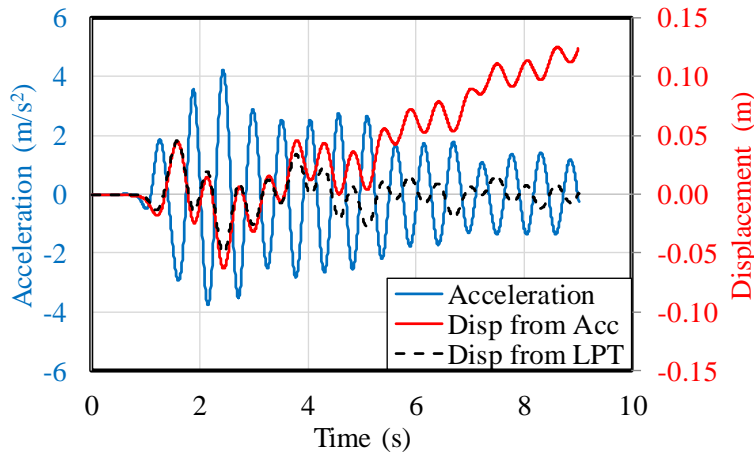


**Figure 2.20 :** Top acceleration vs. top displacement.

To overcome these drawbacks, a simple procedure that can be applied in the elastic range is generated to obtain top displacement history through the longitudinal strain measurements. The essential steps of the procedure are explained as follows:.

*Step 1:* The column cross-section is divided into small fibers. Stresses of each fiber is computed by assuming *plane sections remain plane* after bending. In equation (2.5)  $F_{fiber}$ ,  $A_{fiber}$  and  $\varepsilon_{fiber}$  is force, area and strain of fibers, respectively.

$$F_{fiber} = E \times \varepsilon_{fiber} \times A_{fiber} \quad (2.5)$$

*Step 2:* The corresponding sectional moment is computed by multiplying the fiber forces ( $F_{fiber}$ ) with distance of the fiber to neutral axis ( $d_{fiber}$ ), equation (2.6).

$$M_{bottom} = \sum F_{fiber} \times d_{fiber} \quad (2.6)$$

Step 3: Virtual lateral force acting at the mass center can be calculated by equation (2.7) where “h” is mass height.

$$F_{top} = \frac{M_{bottom}}{h} \quad (2.7)$$

Step 4: Lateral stiffness of the column “k” is calculated by equation (2.8). The second term in equation 2.8 represents second-order effects, (Wilson and Habibullah 1987, Aydinoglu and Fahjan 2003).

$$k = \frac{3EI}{h^3} - \frac{W}{h} \quad (2.8)$$

Step 5: Lateral top displacement of the specimen is calculated by dividing the virtual lateral force to lateral stiffness of k, equation (2.9).

$$u_{top} = \frac{F_{top}}{k} \quad (2.9)$$

Velocity and acceleration histories at the point can also be computed by derivation of the displacement history. One of the significant advantages of this method is that strain measurements are noise-free. Hence, the derive operator may be used more reliably. A representative acceleration history measured by two independent systems are illustrated in Figure 2.21. There exists full consistency between two measuring systems except for some of the peaks.

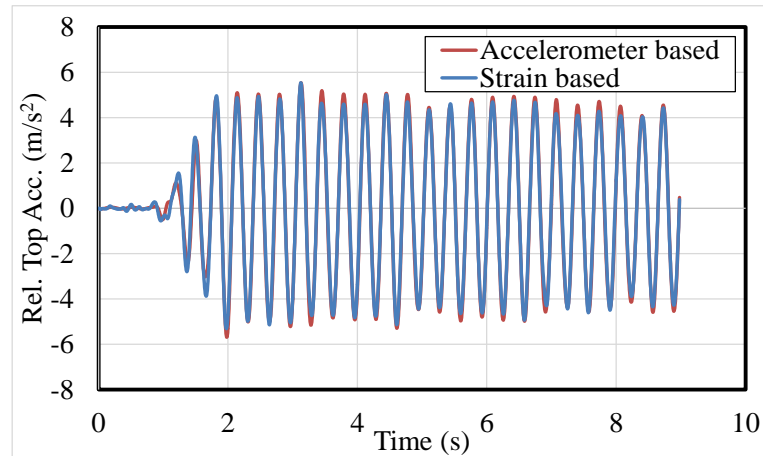


**Figure 2.21 :** Comparison of strain and accelerometer based accelerations.

### 2.2.2 Tests in the elastic range

The effects of natural period variations and  $EQ$  properties on the seismic input energy ( $EI$ ) and its components has been investigated in the elastic range. Two diverse group of specimens were utilized in the elastic tests of  $SDOF$  specimens, see Chapter 2.2.

In the first group, two specific  $EQ$  records (San Salvador 1986 and Chile 1985) were exposed to the steel cantilever columns with ten different natural frequencies. The commanded and the measured acceleration histories on the shake table are given for two acceleration records in Figure 2.22. The comparison displays that the loading and measuring systems are more successful in the case of the  $SS-CIG$  record.

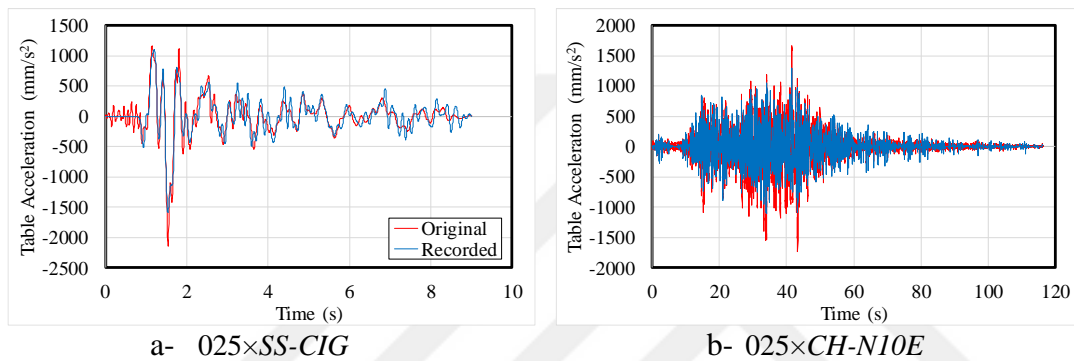


**Figure 2.22 :** Applied and measured accelerations on the table.

The results of elastic tests performed for  $SDOF$  specimens with 10 different vibration periods are presented in Table 2.4 for two specific  $EQs$ . The experimentally obtained maximum top acceleration, velocity, displacement responses and the longitudinal strains at the bottom section, as well as the corresponding seismic energy components that are calculated by the developed algorithm (Chapter 2.1.6), are given in the columns of the table.

From the evaluation of the results given in Table 2.4, a direct relationship was not found between the intensities of mass and seismic input energy. As an example, for  $SS-CIG$  record, the seismic input energies are obtained as 1.79 and 27.33 kNmm for the specimens having the vibration periods of 0.667 and 0.526 s, respectively. The same condition is also true for the other response parameters given in the table.

**Table 2.4 :** Measured maximum relative responses and seismic energy components for the elastic tests.

EQ	T	Top	Bottom	E <sub>I</sub>	E <sub>k</sub>	E <sub>s</sub>	E <sub>D</sub>		
	(s)	Acc.	Vel.					Disp.	Strain
		(mm/s <sup>2</sup> )	(mm/s)	(mm)	(×10 <sup>-6</sup> )	kNmm			
025×SS-CIG	0.277	4979	189.4	9.52	212.6	0.76	0.59	0.74	0.21
	0.333	5686	285.1	15.39	310.4	2.48	1.78	1.80	0.68
	0.385	5186	404.9	34.43	234.0	11.83	8.04	8.56	3.36
	0.455	3332	243.3	18.53	357.3	2.63	2.19	2.44	0.45
	0.500	3815	270.3	22.18	451.4	4.05	3.09	3.32	0.97
	0.526	5186	404.9	34.43	689.4	27.33	23.86	23.39	7.20
	0.667	3256	223.4	11.03	235.5	1.79	1.10	1.02	0.35
	1.000	3422	732.3	64.48	970.6	17.74	14.77	15.31	3.36
	1.250	2226	368.9	54.55	1142.3	33.29	26.61	29.57	5.31
	1.667	2026	359.5	88.60	1118.4	23.15	20.16	17.41	1.68
025×CH-N10E	0.277	10708	472.6	20.96	635.9	6.64	3.53	3.58	5.17
	0.333	5378	294.6	15.65	444.5	3.10	1.90	1.94	1.82
	0.385	4616	287.6	18.70	521.0	4.30	2.37	2.68	3.81
	0.455	7691	546.9	39.23	810.8	16.27	11.09	10.90	9.45
	0.500	11388	912.8	71.17	1297.2	53.71	35.30	34.11	43.26
	0.526	8700	667.9	54.55	1121.2	53.65	29.45	29.39	50.37
	0.667	3360	799.3	30.97	1185.3	9.33	7.33	7.28	6.01
	1.000	2290	300.4	48.53	1364.3	18.91	12.30	12.67	13.66
	1.250	3511	522.3	99.02	1520.9	89.35	53.36	48.52	81.18
	1.667	4391	555.5	107.28	1079.1	83.74	60.28	56.52	62.07

The *dominant periods* of *CH-N10E* and *SS-CIG* records were determined as 0.500 and 0.526 s, respectively, see Chapter 2.2.4. The specimens were exposed to resonance at these periods, so the response parameters as well as the seismic input energy are getting substantially larger.

In the second group test, it was aimed to verify the relation between seismic input energy and lateral stiffness, as described in Kuwamura and Galambos (1989). There are four diverse specimens (two different cross-section and two different column heights for two discrete materials) in this group, see Chapter 2.2.1. The vibration frequencies of the specimens in this group are 1.0, 1.5 and 2.0 Hz. *EQ* records #2, #3 and #4 listed in Table 2.1 were utilized in the tests. Seismic input energy was calculated by equation 2.2. The input energy was normalized respect to mass to express it in a spectral form, (Housner 1956, Akiyama 1985). Mass normalized seismic input energies for the tested specimens are plotted in Figure 2.23.

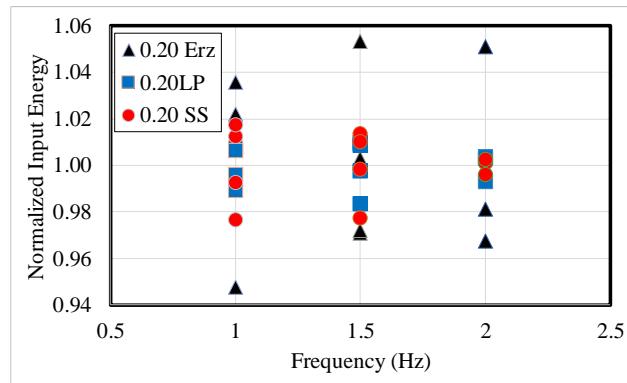


**Figure 2.23 :** Mass-normalized  $E_I$  values for second group  $SDOF$  specimens.

The ultimate variation between mass-normalized seismic input energies for specific frequency levels is less than 10%, which is perhaps related to the sensitivity of the loading and measuring equipment. It is found that mass normalized seismic input energy is free from the lateral stiffness of the system as defined by Kuwamura and Galambos (1989).

### 2.2.3 Tests in the inelastic range

The dimensions of the specimens are the same as those used with the previous group, Figure 2.14. Natural periods of inelastic  $SDOF$  specimens are 0.500, 0.526, 0.667, 1.000 and 1.250 s, Figure 2.24. A safety rope was attached to the specimens to avoid a potential accident. The *SS-CIG* record was utilized for all specimens of this group with a factor of 1.0. Results of the tests were also shared with Börekçi (2018) to compute the damping ratio in the inelastic range.

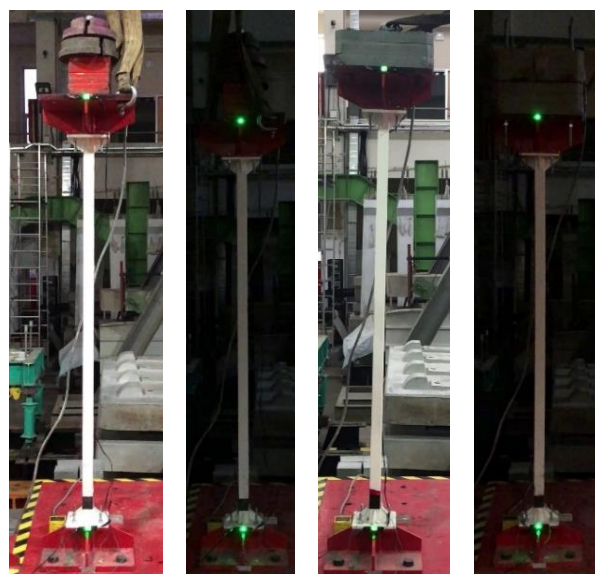


**Figure 2.24 :** Specimens tested in the inelastic range.

The procedure regarding displacement determination given in Chapter 2.2.1 could not be applied for this group of specimens because of their inelastic response. For this reason, a vision-based measuring technique was applied to these specimens, see Chapter 2.1.4. Velocity response is produced from the vision-based displacement data. Conversely, acceleration and strain responses of the specimens were determined directly by the measurements made by the proper transducers.

Seismic energy terms, namely  $E_k$ ,  $E_d$ ,  $E_s$ ,  $E_I$  and  $E_{es}$ , given in equation 2.2. are computed directly from the data gathered from the experiments. Nevertheless,  $E_p$  is also able to be obtained as the area enclosed by the moment-rotation curve. The equivalent force acting on the top of the specimen can be calculated simply by equation (2.10) where  $m$  is mass and  $a^t$  is absolute top acceleration. Then, overturning moment is determined through multiplication of the equivalent force with the mass height defined in Table 2.3.

$$F = ma^t \quad (2.10)$$

Strain measurements on the bottommost section of the specimens are utilized to calculate the sectional curvature ( $\chi$ ). The sectional rotation is determined by equation (2.11) where  $L_p$  is the plastic hinge length. It is assumed as cross-section height.

$$\theta_p = \chi_p L_p \quad (2.11)$$

The ultimate experimental data i.e. acceleration, velocity, displacement and strain and the corresponding energy components of the specimens that are tested in inelastic range are given in Table 2.5.

**Table 2.5 :** The measured ultimate relative responses and seismic energy terms for inelastic range.

T (s)	Acc. (mm/s <sup>2</sup> )	Top	Bottom Strain (×10 <sup>-6</sup> )	E <sub>I</sub>	E <sub>k</sub>	E <sub>s</sub>	E <sub>d</sub>	E <sub>p</sub>	E <sub>p</sub> /E <sub>I</sub> %	
		Vel. (mm/s)								Disp. (mm)
0.500	13125	1089	79.07	1650	56.7	23.8	23.7	15.0	1.4	2.47
0.526	10607	981	76.67	1800	58.8	8.0	8.0	9.0	40.0	68.03
0.667	11703	1038	137.99	2525	232.9	54.5	39.6	15.2	184.6	79.26
1.000	6675	1024	170.09	3810	259.2	166.2	42.7	9.1	212.1	81.83
1.250	8101	1027	220.89	6751	354.3	206.1	128.1	24.0	205.1	57.89

From the table, it can be seen that the seismic input energy and its components are affected by variations of the predominant period. Especially, the ratio between plastic energy and seismic input energy is getting larger by the increment of the vibrational period.

#### 2.2.4 The effect of mass tuning on seismic energy components

Mass tuning is one of the applied techniques used to reduce the seismic effect on the structures. Therefore, several mass tuning systems were developed for the practical aim to elongate the vibration periods of the structural system. Although the spectral accelerations are getting smaller in the long period range, the seismic input energy may be larger depending on the frequency content of *EQ* record. A demonstrative example in which spectral acceleration and mass normalized input energy are compared, is presented in Figure 2.25 for *El Centro NS* record (Aydinoğlu and Fahjan 2003).

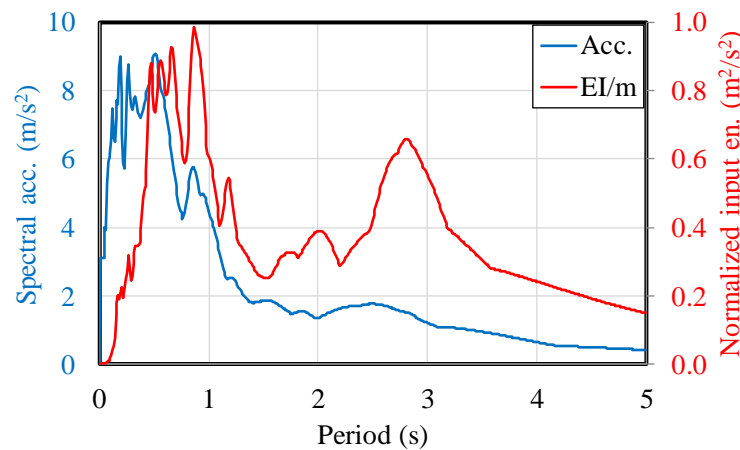


**Figure 2.25 :** Acceleration and mass normalized  $E_I/m$  spectra of *El Centro NS* record.

If the natural period of a structure is increased from 1.10 s to 2.83 s by means of mass tuning; the spectral acceleration decreases to 1.50 m/s<sup>2</sup> from 3.25 m/s<sup>2</sup>, Figure 2.25. However for the same structure, the seismic input energy increases almost 1.6 times. Hence, it is true to state that the energy-based seismic design is more robust for correctly deciding the amount of elongation for a mass-tuning system.

The experimental results for a group of mass tuned systems are presented in Figure 2.26. The mass-normalized seismic input energies of the systems are illustrated, together with power spectrum of the records. From the graphics, it is clearly seen that

the seismic input energy has a good correlation with the power spectrum shape of the  $EQ$  record.

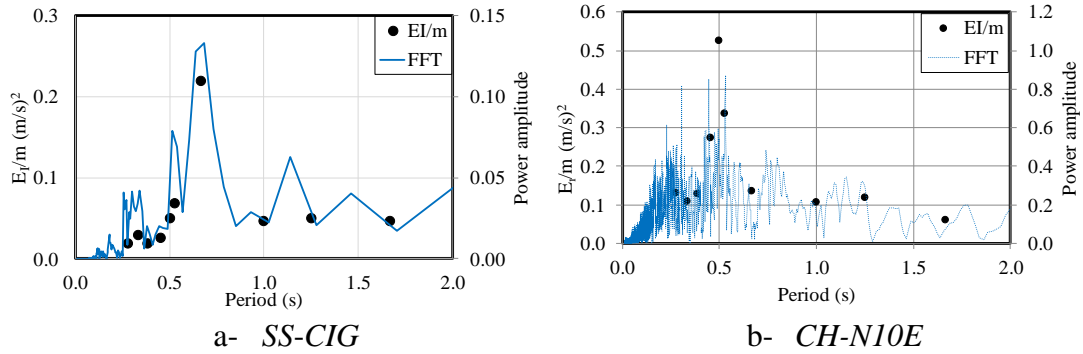


**Figure 2.26** : Seismic input energy vs. frequency content of the  $EQ$ s.

Moreover, the relatively larger input energies are reached for the peaks of the power spectrum of  $EQ$  records.

Depending on the comparisons made in Figures 2.25 and 2.26, one can conclude that the seismic response of a structural system may be controlled more correctly by considering the frequency content of  $EQ$  records.

## 2.3 Multi Degree of Freedom Systems

### 2.3.1 Definition of specimens and testing system

Four spatial skeleton type steel frames with three-storeys and 1-span in each direction were designed and constructed to test on the shake table. The specimens are nearly 1/3 geometric scale and their storey heights and span lengths are 0.9 m and 1.0 m, respectively.

Two of the specimens were produced to represent *weak column-strong beam* type systems ( $BF1$ ) as well as the others, which were produced as *strong column-weak beam* type ( $BF2$ ). Moreover, one specimen from each group was instrumented with a special damper placed in the first storey. Those specimens are called  $BF1-D1$  and  $BF2-D1$ . The comprehensive information about the damper called *Steel Cushion (SC)* can be found elsewhere Yüksel et al. 2018, Özkaynak et al. 2018, Güllü et al. 2017, Güllü et al. 2016, Güllü et al. 2015, Smyrou et al. 2014, Özkaynak et. al. 2014. The schematical views of the skeleton type steel frame specimens are illustrated in Figure 2.27. A supporting rigid frame is also utilized to support the damper for specimens of  $BF1-D1$  and  $BF2-D1$ . The supporting frame consists of 40/60/3 mm rectangular box

sections. Additionally, the frame was strengthened in the loading direction with a L80/80/8 angle.

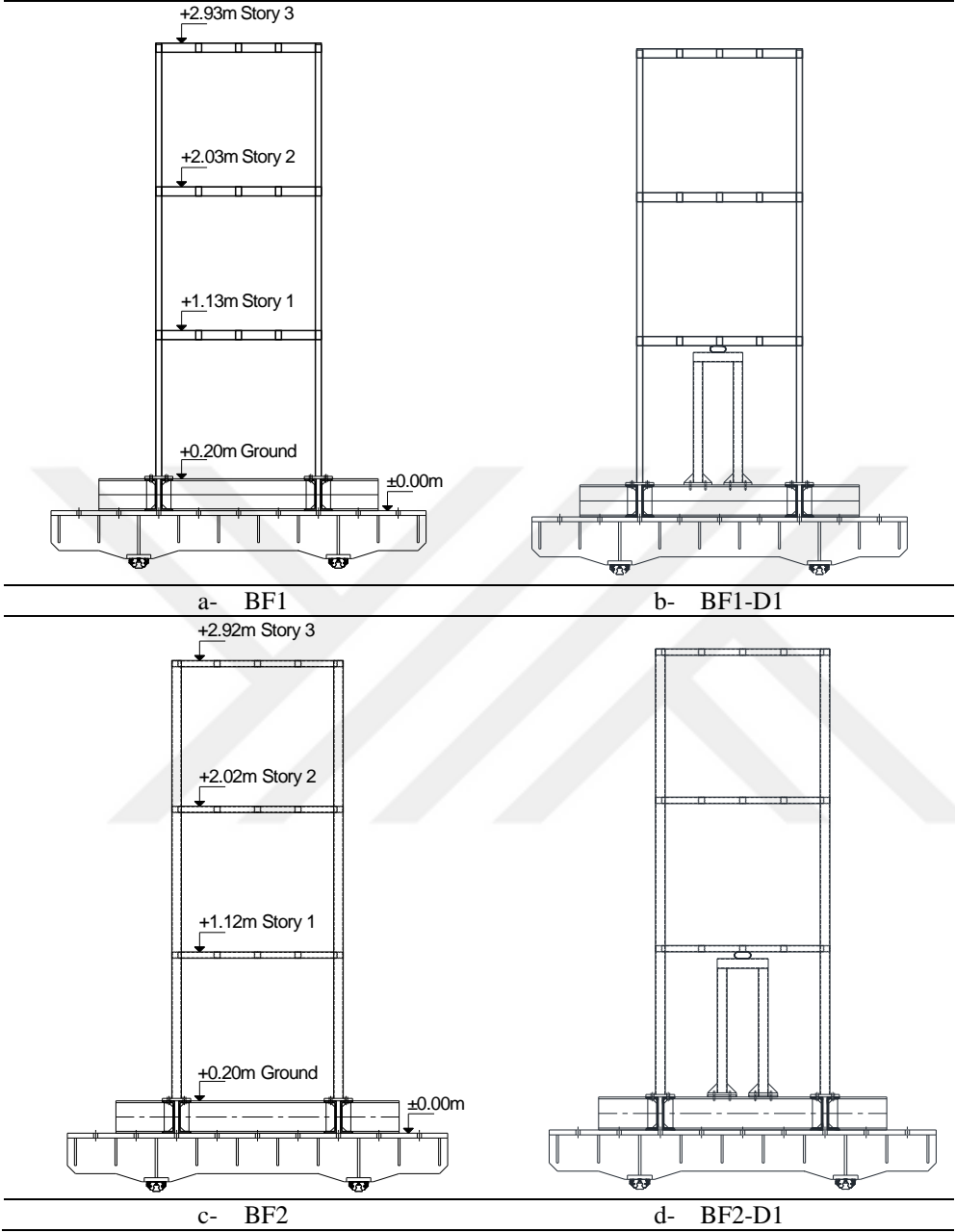


**Figure 2.27** : Schematic views of the *MDOF* specimens.

The columns have 40/40/3 mm square box cross-section for specimens of *BF1* and *BF1-D1*, whereas columns of *BF2* and *BF2-D1* have 40/60/3 mm rectangular box cross-sections. The primary and secondary beams of *BF1* and *BF1-D1* have 40/60/3 mm rectangular box cross-section, whereas *BF2* and *BF2-D1* have beams with 40/40/3 mm square box cross-section. A special rigid frame utilized to support the metallic dampers has 40/60/3 mm rectangular box cross-sections. The specimens were fixed to the shake table by means of a special beam grid made of UNP200 profiles. The special

beam grid was connected to the shake table by 8.8 quality 4 M24 bolts. The test specimens were connected to the beam grid by 8.8 quality 4 M16 bolts at each column base. Dimension of the column base plates was  $175 \times 175 \times 15$  mm. Five mm thick triangular stiffeners ( $50 \times 50$  mm) were utilized between the column base plate and column section. All beam-to-column and beam-to-beam connections were produced by fully penetrated welding with 3 mm thickness.

In-plane floor stiffness of the skeleton type steel frame specimens was provided by the secondary beam system. A special steel plate with dimensions of  $700 \times 700 \times 6$  mm was welded onto the secondary beams to fix the supplementary masses to the specimen, Figure 2.28.

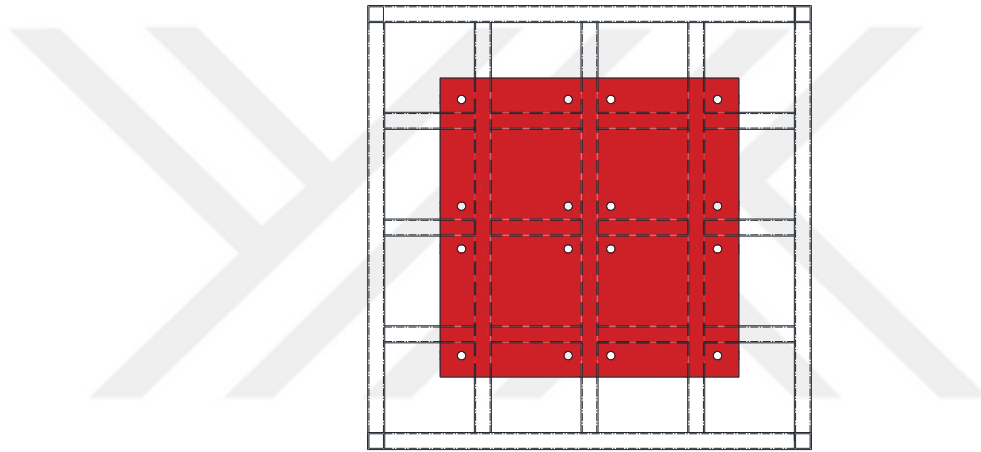


**Figure 2.28 :** Floor plans of *MDOF* specimens.

The supplementary mass was formed by steel blocks, which were available in the laboratory. The steel blocks with 945 kg in weight were fixed to each floors by 8.8 quality M12 bolts. A uniform mass distribution was supplied on the floor levels.

In the preliminary uni-axial shaking table tests, relatively high out-of-plane vibrations were recorded on the floor levels of the specimens. The graphics in Figure 2.29a gives an opportunity to compare the intensities of in-plane and out-of-plane vibrations. To accomplish the undesired condition, it was resolved to use steel strips with dimensions of  $50 \times 3$  mm. The strips were placed diagonally in the perpendicular direction to the motion. They were welded to the specimens at the beam-to-column connections. The effectiveness of the strips can be evaluated through the graphics given in Figure 2.29b, where the intensity of the out-of-plane vibrations are reasonably smaller than the in-plane vibrations.

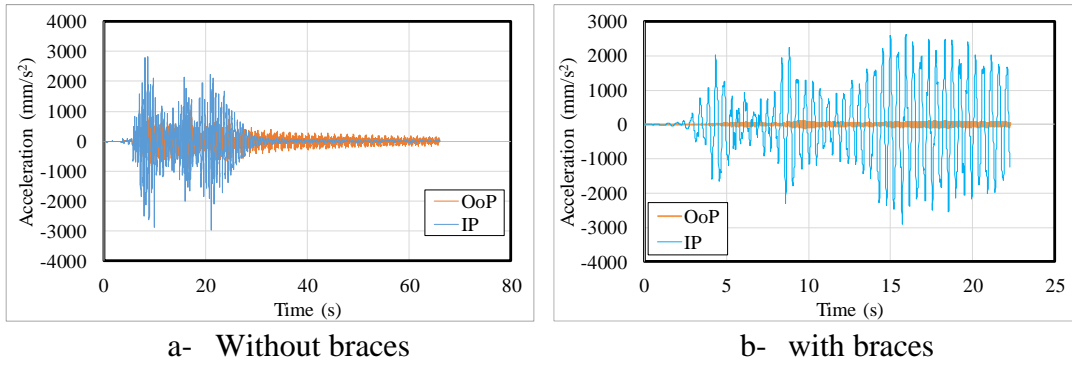


**Figure 2.29 :** The effect of steel strips on the response.

The effect of the steel strips on the dynamic response of the specimen can be traced from Figure 2.30. The torsional mode observed around 7 Hz disappears after the addition of the strips. Moreover, the secondary peaks around the main peak (~2.3 Hz) vanished with the usage of the steel strips. It can be observed that the operation did not change the dominant frequency of the system.

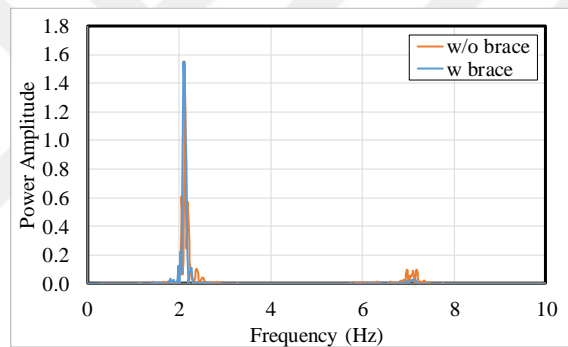


**Figure 2.30 :** Alteration of the dynamic response by adding the steel strips.

Photographs of the specimens placed on the shake table are presented in Figure 2.31. The specimens were attached lightly to the laboratory crane by cloth ropes for occupational safety. The special markers that are used in the vision-based measuring system were attached to the shake table and floor levels of the specimens.

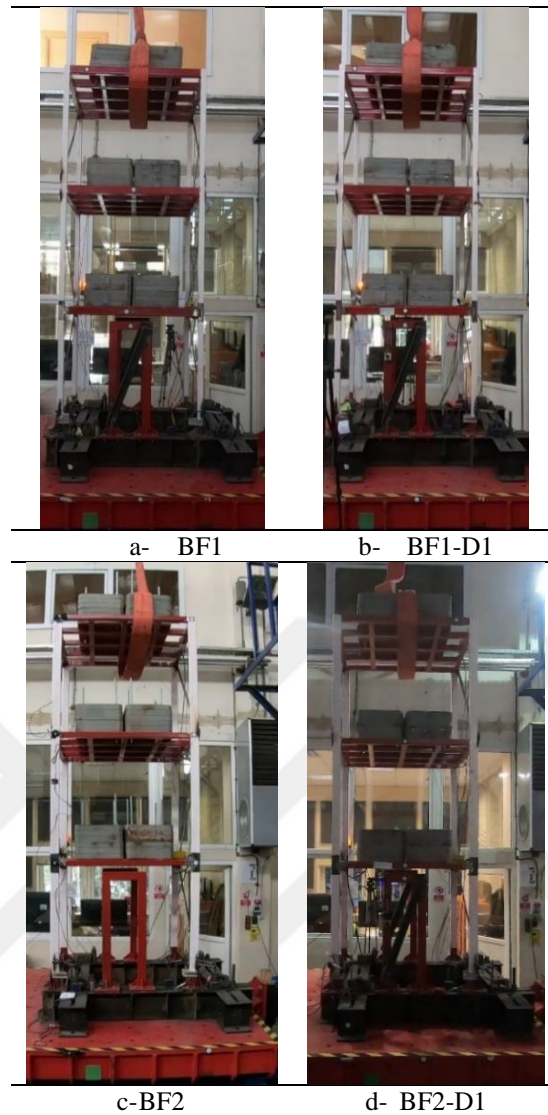


**Figure 2.31 :** Tested *MDOF* specimens.

*SC* is a kind of metallic damper that uses the advantages of its geometric shape and the ductile behavior of steel to dissipate the seismic energy, Figure 2.32.

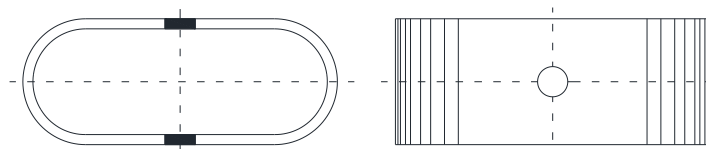


**Figure 2.32 :** Steel cushions utilized in the literature.

The comprehensive experimental, numerical and analytical studies about *SC* with different geometries and loading conditions have been accomplished and published in the literature, Güllü et al. (2015), Yüksel et al. (2018), Özkaynak et al. (2018). Although one bolt is utilized at each face of the *SCs* in the above literature, it was decided to use double bolts to supply additional torsional stiffness, Figure 2.33.

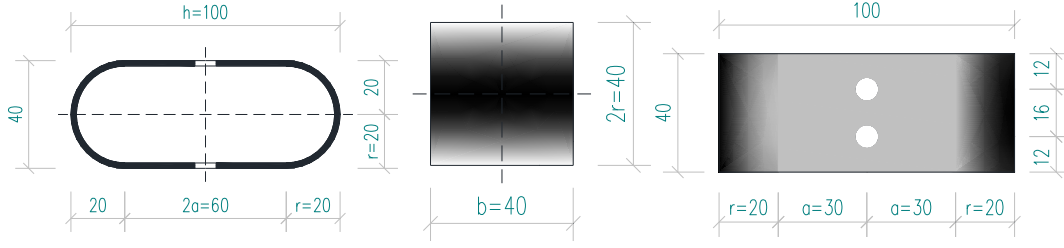


**Figure 2.33 :** Geometric dimensions of the designed steel cushion.

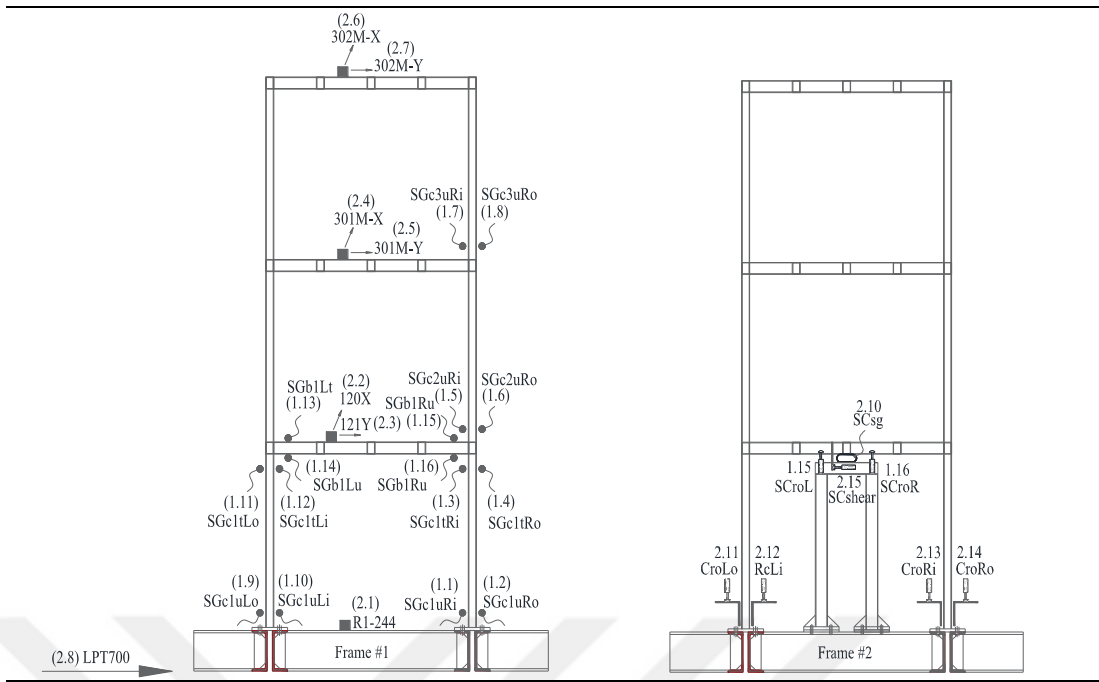
The SCs utilized for retrofitting to the bare frames are designed by using the equations (2.12) and (2.13), which are derived for maximum loading capacity and yielding displacement, respectively (Yüksel et al. 2018, Özkaynak et al. 2018). The elastic perfectly plastic (*EPP*) constitutive model is suitable for the SCs. Hence,  $P_u$  is also corresponding to yielding force. Other terms in equations 2.12 and 2.13 are the yield strength of steel plate ( $f_{yd}$ ), thickness of steel sheet ( $t$ ), half length of the straight part ( $a$ ), radius of the half circles ( $r$ ), width of the device ( $b$ ), the angle between straight line and plastic hinge position on the half circle ( $\varphi$ ), modulus of elasticity ( $E$ ) and moment of inertia ( $I$ ).

$$P_u = \frac{f_{yd}bt^2}{D} = \frac{f_{yd}bt^2}{2r \cos \varphi} \quad (2.12)$$

$$\delta_h = \frac{Pr^2}{EI} \left( \frac{5a^4 + 9\pi a^3 r + (36 + 1.5\pi^2)a^2 r^2 + 12\pi a r^3 + (2.25\pi^2 - 12)r^4}{4a^3 + 6\pi a^2 r + 24a r^2 + 3\pi r^3} \right) \quad (2.13)$$

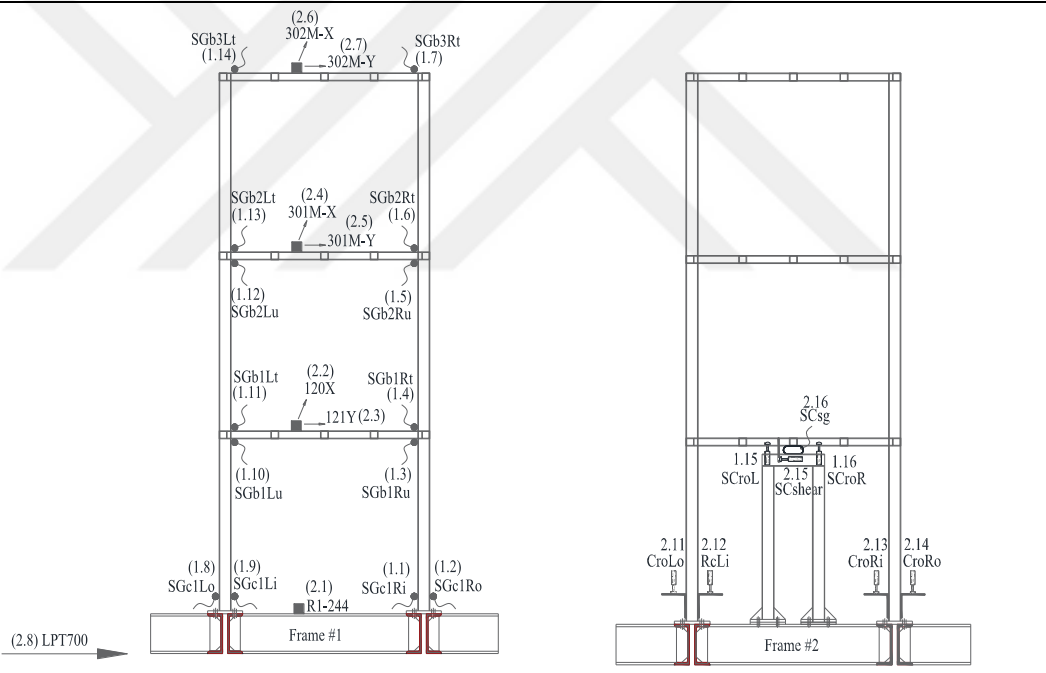
The dimensions of the SCs used in the experimental study are illustrated in Figure 2.33. Specifically, the height and width of the device are 100 and 40 mm, respectively. Yielding force and displacement of the SCs are determined from equations 2.12 and 2.13 are 1.50 kN and 0.4 mm, respectively.

Rotation of column base section, horizontal and vertical displacements of SCs are also measured by using *LVDTs*. Location of the measuring equipments i.e. accelerometers, *LVDTs* and strain gauges are depicted in Figure 2.34. The numbers shown in parenthesis stands for data logger and channel ID. For instance, (2.6) represents sixth channel of the second datalogger. Channel names are shown at the positions of the related instruments as well as the abbreviation is offered in Figure 2.34e.



a- BF1 and BF1-DI Frame #1

b- BF1 and BF1-DI Frame #2

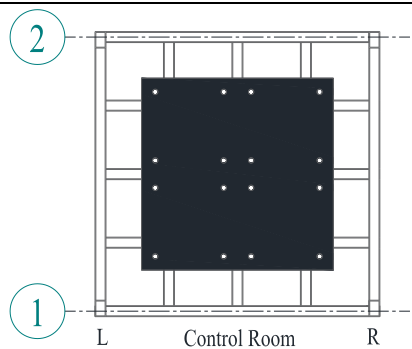


c- BF2 and BF2-DI Frame #1

d- BF2 and BF2-DI Frame #2

- L: Left      R: Right  
u: under     t: top  
c: Column    b: Beam  
o: outside    i: inside  
ro: rotation   SC: Steel cushion  
SG: Strain gauge  
LPT: Disp. Transducer  
■ : Accelerometer

e- Abbreviations utilized in the figure



f- Definition of the frames

**Figure 2.34 : Measuring equipments for MDOF specimens.**

The unexpected damping because of the presence of some displacement transducers was also encountered for the *MDOF* systems. LPT-1250 and LPT-700 type displacement transducers that were used at the floor levels to measure the lateral displacements are extracted from the measuring system after the completion of the preliminary tests. The effect of the transducers can be traced from Table 2.6. Although they have no effect on the frequencies, some amount of additional damping (about 2-3%) occurred due to their presence.

**Table 2.6 :** Dynamic properties of specimen *BF2* with and without the displacement transducers positioned at the floor levels.

Loading	with LPT			without LPT		
	Damping Ratio (%)	Frequency		Damping Ratio (%)	Frequency	
		Shaking Direction	Transverse Direction		Shaking Direction	Transverse Direction
Sinus	5.5	2.051	1.660	2.4	2.026	1.660
	5.8	7.105	5.029	3.0	7.055	5.005
Step Function	5%		1.660	2.8% 2.6%		1.642
			5.005			4.974
		7.080	10.352		7.050	10.333
		13.696	16.406			16.077

The damping ratio of all the specimens was determined by using the methods of *logarithmic decrement* and *half-power bandwidth*. The *logarithmic decrement* is described as the decrement rate of damped free-vibration amplitudes. Equation (2.14) is utilized for the calculation of damping. Where  $u_i$  and  $u_{i+j}$  are arbitrary two adjacent amplitudes in *time domain*,  $n$  is the number of cycles and  $\ln$  is the natural logarithm.

$$\xi = \frac{1}{2\pi n} \ln \frac{u_i}{u_{i+j}} \quad (2.14)$$

The *half-power bandwidth* method is a tool to compute damping ratio in the *frequency domain*. In this method, the *Frequency Response Function (FRF)* amplitude of the signal is obtained to elucidate the natural frequencies of the system, Figure 2.35.

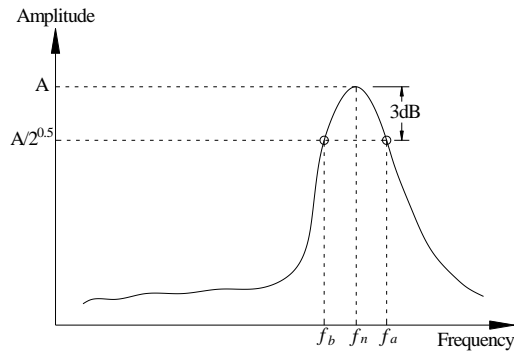


**Figure 2.35** : Definition of half-power bandwidth method.

In the method, the intersection points of the horizontal line ( $f_a$  and  $f_b$ ) with  $FRF$  are determined with two alternative techniques. In the first technique, the horizontal line is assigned at 3 dB lower than the peak corresponding to  $f_n$ . In the second one, the peak frequency is divided by  $\sqrt{2}$  to decide the horizontal line level. After assignment of the horizontal line, damping ratio is calculated from equation (2.15).

$$\xi = \frac{f_b - f_a}{2f_n} \quad (2.15)$$

The practice of the logarithmic decrement method for the  $MDOF$  specimens are presented in Figure 2.36. Although the bare frames ( $BF1$  and  $BF2$ ) have a damping ratio of 2.4-3.0%, the specimens with metallic dampers have about 5.0% damping.

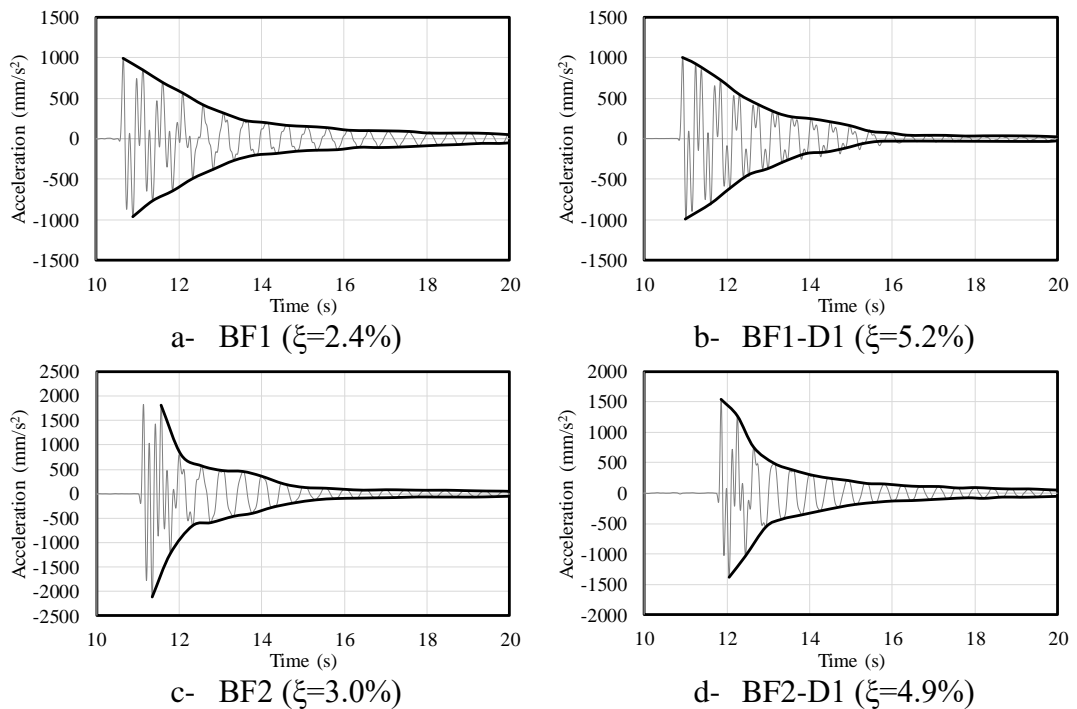


**Figure 2.36** : Damping ratio calculations by using the logarithmic decrement method.

Application of the half power band width method yields 2.3% for the bare frames (*BF1* and *BF2*) and 5.4% for the retrofitted specimens (*BF1-D1* and *BF2-D1*).

The contribution of *SCs* to the damping properties of the system might be improved by using additional *SCs* in the proper positions.

The alternative free vibration tests namely *hammer*, *sinus*, *step function* and *white noise* were performed to determine the frequency characteristics of the specimens at each test stage. The amplitude and frequency of *sinus tests* were 2 mm and 1 Hz, respectively. The amplitude of the applied step function was 4 mm.

All the specimens were tested initially in their elastic range, for which the *EQ* records given in Table 2.1 were applied to the shake table with the coefficients of 0.10 and 0.20.

The *SS-CIG* record with 0.75 and 1.00 multipliers was used in the inelastic tests of all specimens.

### 2.3.2 Bare frame #1 (BF1): weak column – strong beam

*BF1* is a typical strong beam - weak column type structural system. Plastic deformations are mostly expected on the columns, so most of the strain gauges were attached to the column sections, see Figure 2.34 a-b.

#### 2.3.2.1 Free vibration tests

The free vibration test results of *BF1* is given in Figure 2.37. There are three peaks in the frequency content around 2, 6 and 10 Hz. Findings from the alternative methods are quite close to each other.

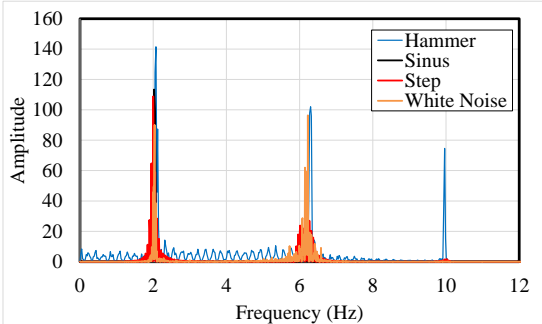


Figure 2.37 : Free vibration test results of *BF1*.

The third peak in the frequency content disappears in the results of the *sinus* and *white noise* techniques. Table 2.7 consists of the results of the alternative tests methods. The average frequencies are calculated as 2.036, 6.261 and 9.964 Hz, respectively.

**Table 2.7 :** Free vibration tests results of *BF1*.

Test	Hammer	Sinus	Step			White Noise		
			Initial	0.1	0.2	Initial	0.1	0.2
$f_1$	2.075	2.026	2.002	2.002	2.002	2.039	2.014	2.002
$f_2$	6.299	6.299	6.219	6.116	6.116	6.226	6.226	6.226
$f_3$	9.961	N.A.	9.967	9.961	9.961	N.A.	N.A.	N.A.

The successive free vibration tests resulted same frequencies. Hence, no unexpected plastic deformation arose in the elastic tests.

### 2.3.2.2 Tests in the elastic range

*BF1* was exposed to *EQ* records of #2, #3, #4, #5, #6, #7 and #8 given in Table 2.1. All of the records except *TCU067* were multiplied with the scale factors of 0.1 and 0.2. However, the scale factor for *TCU067* was selected as 0.15 to keep the specimen in the elastic range.

The lateral accelerations at floor levels as well as on the shake table are compared in Figure 2.38 for the 0.1 scaled *POE360* record. The maximum increment in the amplitudes of vibration was observed at the first floor (*ST1*), Figure 2.38a.

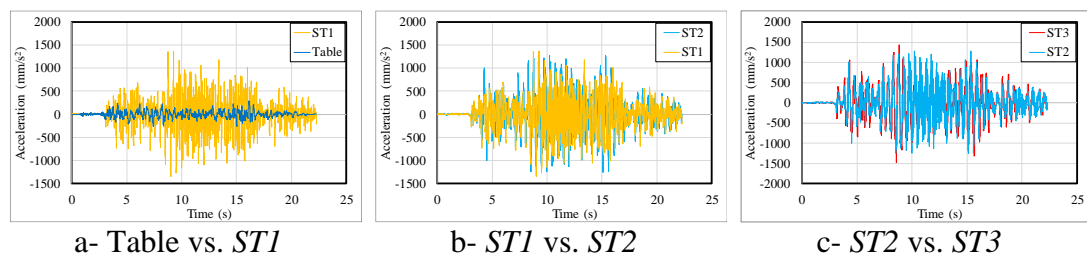


**Figure 2.38 :** Acceleration increments between the storeys.

The comparisons of the acceleration data measured on the shake table and at first floor (*ST1*) are presented in Figure 2.39 for all of the records.

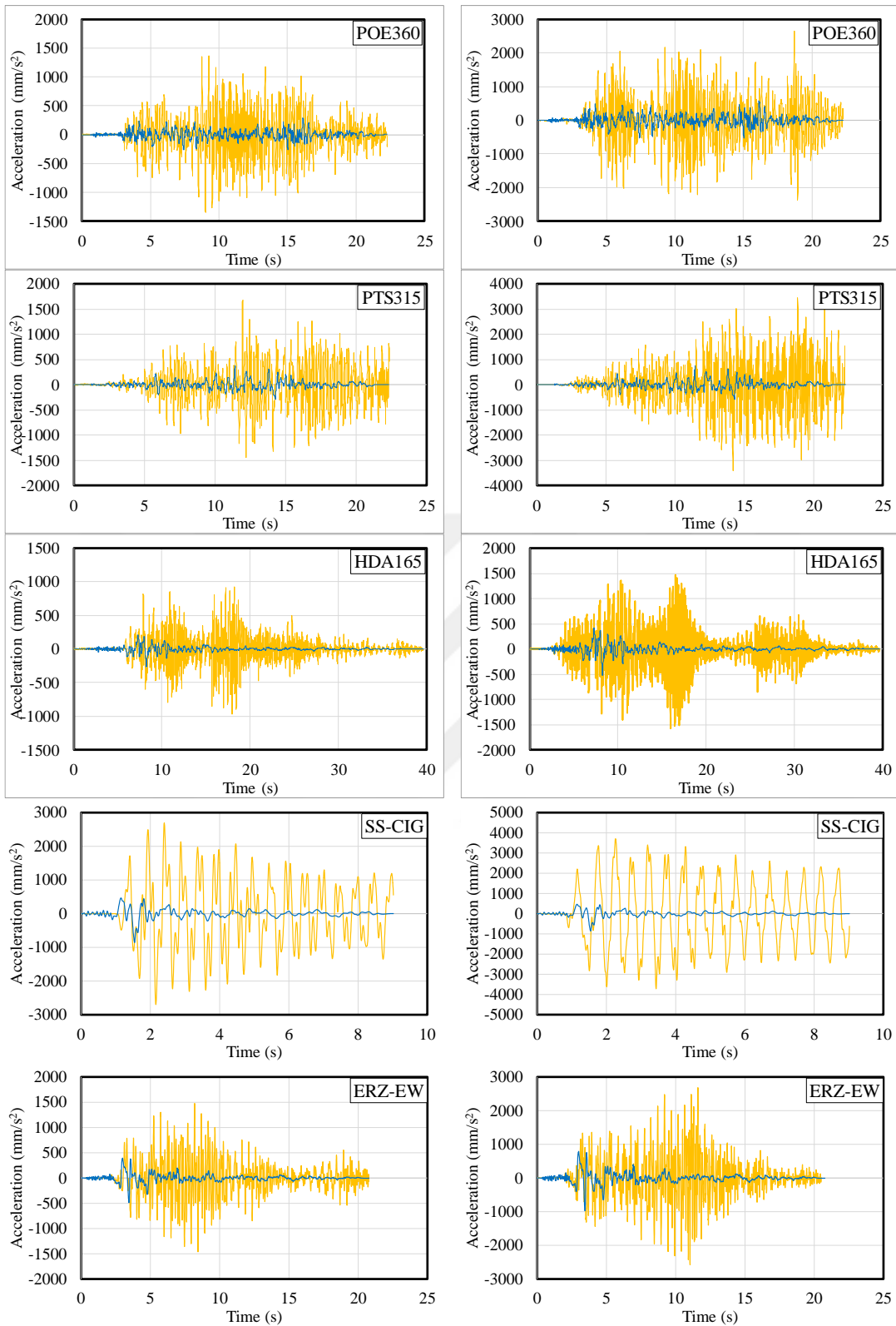


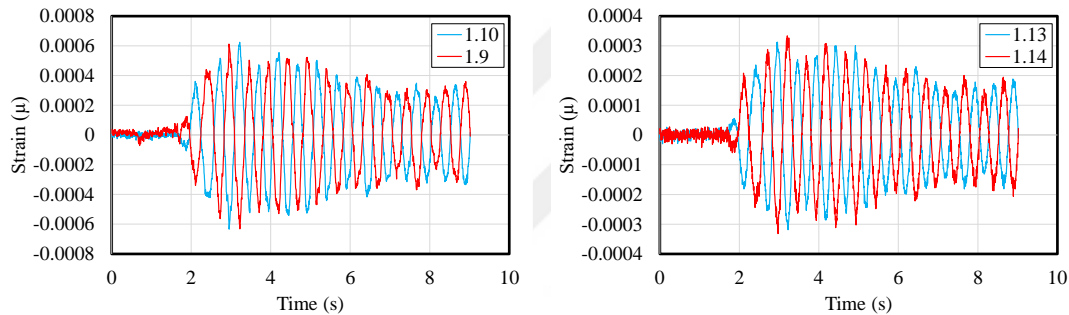
**Figure 2.39 :** Acceleration increments between table and 1<sup>st</sup> storey levels.



**Table 2.9** : The floor acceleration ratios.

Record	ST1/Table		ST2/ST1		ST3/ST2	
	SF=0.1	SF=0.2	SF=0.1	SF=0.2	SF=0.1	SF=0.2
POE360	4.65	4.50	0.93	0.88	1.16	0.97
PTS315	4.51	4.64	0.96	0.96	1.09	0.92
HDA165	3.66	2.98	0.99	1.06	1.38	1.03
SS-CIG	2.72	2.05	0.93	1.19	1.25	0.89
ERZ-EW	3.04	2.76	1.03	0.96	1.10	0.95
BOL090	2.77	1.98	0.88	1.22	1.52	0.97
TCU067	10.40	8.94	1.00	0.95	1.06	1.28
Average	<b>4.54</b>	<b>3.98</b>	<b>0.96</b>	<b>1.03</b>	<b>1.22</b>	<b>1.00</b>

One representative longitudinal strain history recorded at the column base and the beam end are presented in Figure 2.40. Blue and red lines correspond to the strains measured at the rear and front faces of the column section and the top and bottom faces of the beam section. Blue and red lines are asymmetric due to homogeneous behavior of the cross-sections.

**Figure 2.40** : The representative strain histories for the 0.2 *SS-CIG* record.

The ultimate strains recorded at different cross-sections are shown in Table 2.10. The values in the table correspond to average of absolute strains recorded at the same section.

**Table 2.10** : The ultimate strains recorded in the elastic tests ( $\mu$  strain $\times 10^6$ ).

<i>EQ</i> Record	ST1-Col-bot		ST1-Col-top		ST2-Col-bot		ST3-Col-bot		ST1-Beam	
	SF=0.1	SF=0.2	SF=0.1	SF=0.2	SF=0.1	SF=0.2	SF=0.1	SF=0.2	SF=0.1	SF=0.2
POE360	250	377	240	429	210	366	143	207	125	197
PTS315	300	483	281	499	268	492	165	273	153	236
HDA165	178	243	154	214	156	226	109	152	87	125
SS-CIG	404	634	389	653	345	589	214	310	202	325
ERZ-EW	272	389	255	474	214	341	153	219	128	203
BOL090	303	606	287	615	365	512	220	292	191	316
TCU067*	611	776	566	766	556	694	307	421	344	428

The maximum strain recorded at the beam ends is  $428 \times 10^{-6}$ , which is smaller than the yield strain of  $1033 \times 10^{-6}$ . However, the maximum strain obtained for the columns was  $776 \times 10^{-6}$  and the value was smaller than the yield strain of  $1400 \times 10^{-6}$ .

### 2.3.2.3 Tests in the inelastic range

*BFI* was tested in the inelastic range by using the *SS-CIG* record multiplied by the coefficients of 0.75 and 1.00. Free vibration tests (*step function* and *white noise*) were conducted between the successive test steps. The plastification of the structural members are traced by strain gauge and vibration measurements.

Variation in the peaks' locations was negligible in the successive test stages, Figure 2.41. Although a changing for the first and third modes was not observed, a minor alteration ( $\sim 0.1$  Hz) was recorded for the second mode. Consequently, one can conclude that the intensity of the inelastic deformations is relatively low.

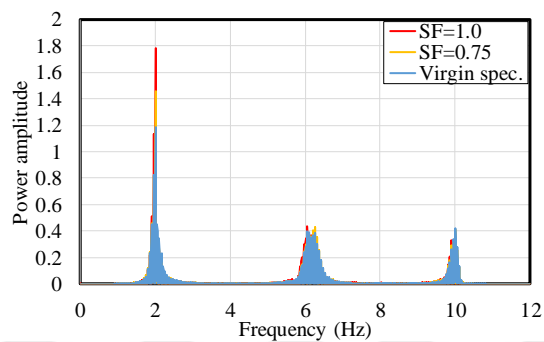


**Figure 2.41** : Frequency characteristic of *BFI* before and after inelastic tests.

The results of longitudinal strain measurements are given in Figure 2.42 for column base and first storey beam, respectively. Yield deformation of the material is also shown on the graphics with red lines. Although yielding is observed for the column section, the beam end is in the elastic range.

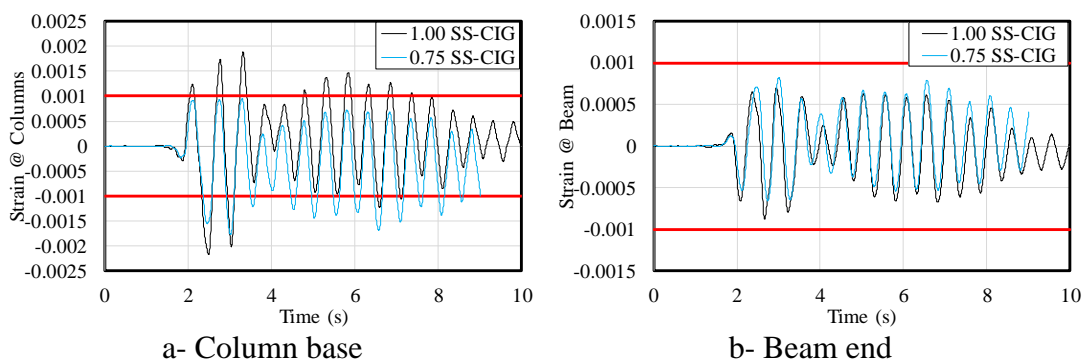


**Figure 2.42** : Strains occurred on the structural members during the inelastic tests.

The observed damage in the inelastic range is in welding cracks at the column base and first storey beam-to-column connections, as well as surface deformations at the ends of the first storey members, Figure 2.43. Some extent of residual lateral

displacement is recorded at the end of the tests. It was about a 10 mm at top of the specimen.



**Figure 2.43 :** The observed damage in inelastic tests.

The floor acceleration histories for *SS-CIG* scaled by 0.75 and 1.00 multipliers are presented in Figure 2.44. The recorded peak accelerations on the shake table were 6437 and 8583 mm/s<sup>2</sup> for the 0.75 and 1.00 multipliers. The recorded maximum floor accelerations were 6555, 7136 and 10098 mm/s<sup>2</sup> for 1<sup>st</sup>, 2<sup>nd</sup> and 3<sup>rd</sup> floors, respectively for 0.75 multiplier. The maximum floor accelerations were recorded as 9311, 8724 and 11604 mm/s<sup>2</sup> for the multiplier of 1.00.

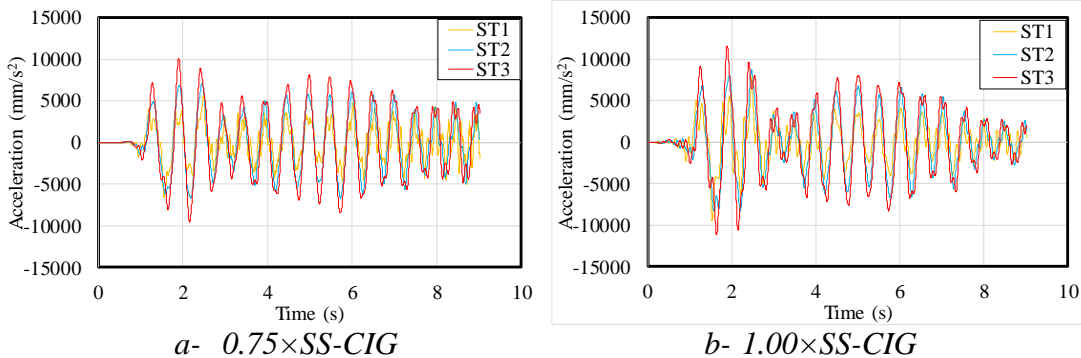


**Figure 2.44 :** Floor acceleration histories of *BF1* for the inelastic tests.

**2.3.3 Bare frame #1 retrofitted with metallic damper (*BF1-D1*)**

The virgin *BF1* is retrofitted with *Steel Cushions (SCs)*, Chapter 2.3.1. Two *SCs* were placed between the supporting frame and the first storey beams in the loading direction, Figure 2.45. The location of *SCs* corresponds to the mid-point of the beam span.



**Figure 2.45 :** The placement of SCs.

### 2.3.3.1 Free vibration tests

The results of free vibration tests that were obtained by using distinct free vibration test methods are given in Table 2.11. The dominant frequencies obtained after the elastic tests are also inserted in this table. If one compare Tables 2.7 and 2.11, it concludes that the effect of metallic dampers on free vibration characteristics of the specimen is very limited.

**Table 2.11 :** Dominant frequencies of *BF1-D1*.

Test	Hammer	Sinus	Step			White Noise		
	Initial	Initial	Initial	0.1	0.2	Initial	0.1	0.2
f <sub>1</sub>	2.271	2.148	2.148	2.209	2.209	2.185	2.172	2.172
f <sub>2</sub>	6.665	6.543	6.421	6.427	6.476	6.586	6.580	6.580
f <sub>3</sub>	10.205	N.A.	10.059	N.A.	N.A.	N.A.	N.A.	N.A.

Average frequencies of the retrofitted specimen are obtained as 2.188 and 6.554 Hz.

The comparison of the results of distinct free vibration test methods is given in Figure 2.46a. All of the methods resulted similar peaks. The peaks corresponding to *BF1-D1* are shifted slightly in frequency domain, Figure 2.46b. Additionally, the third peak at around 10 Hz did not observed.

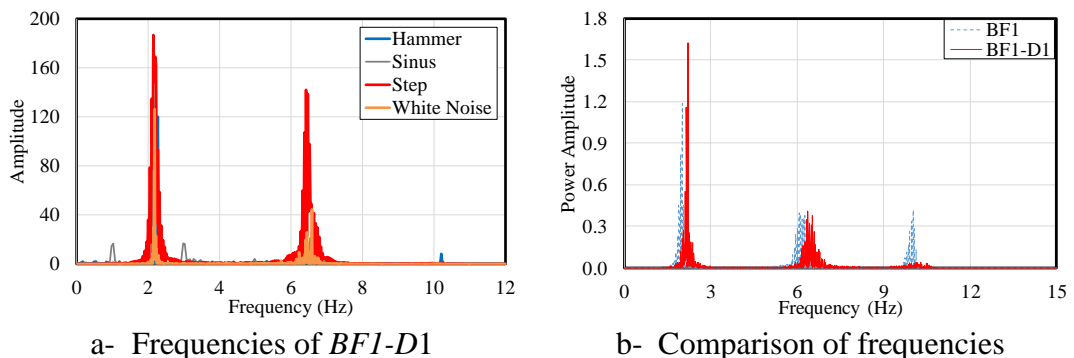


**Figure 2.46 :** Frequencies of *BF1-D1* and comparison with *BF1*.

**2.3.3.2 Tests in the elastic range**

The specimen *BF1-D1* was tested in the elastic range similar to *BF1*. *EQ* records #2, #3, #4, #5, #6, #7 and #8 given in Table 2.1 are utilized with scale factors of 0.1 and 0.2.

The acceleration magnification between the shake table and 1<sup>st</sup> floor level is considerably higher than the other floors similar to *BF1*. The acceleration histories for different *EQs* and scale factors are presented in Figure 2.47.

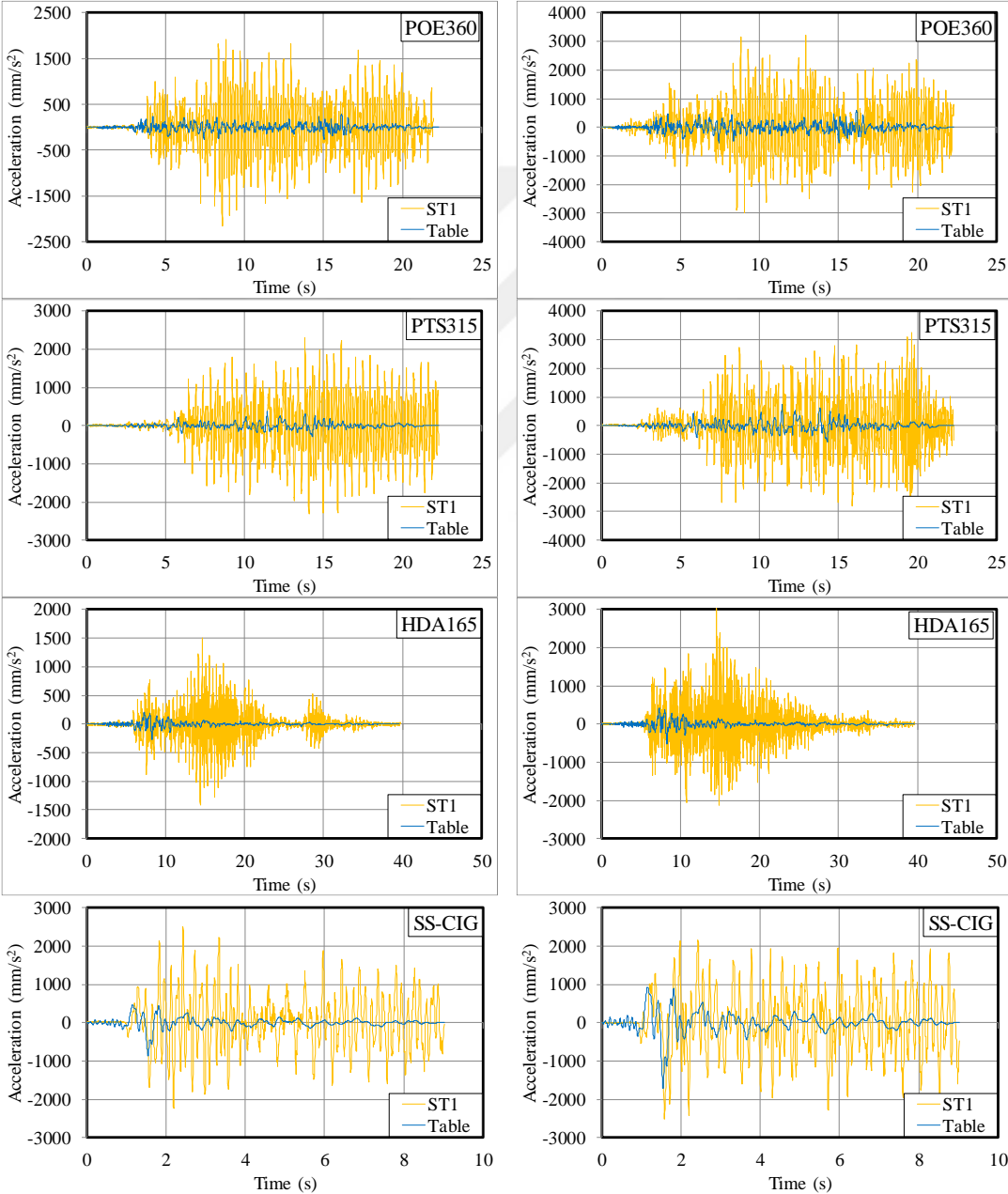


**Figure 2.47 : Acceleration histories of *BF1-D1*.**

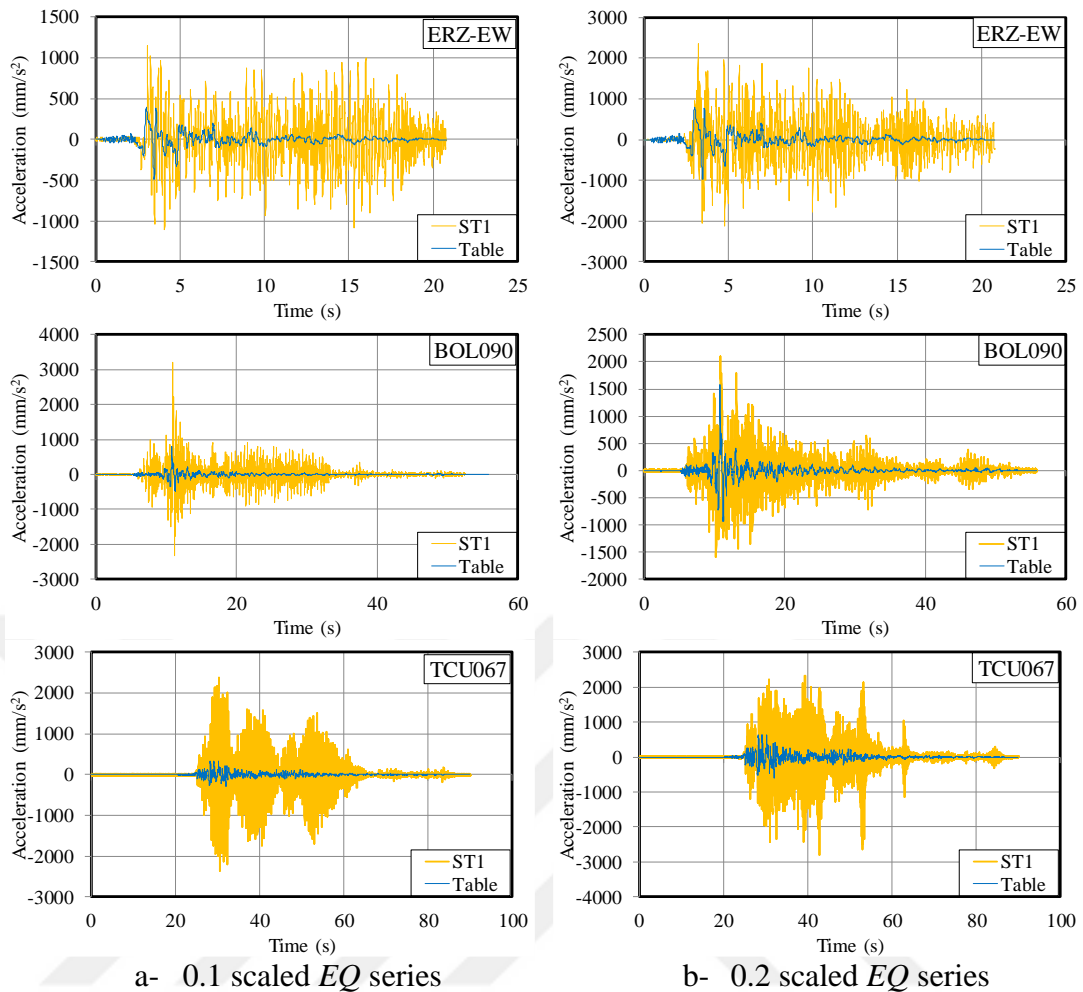


**Figure 2.47 (continued) :** Acceleration histories of *BF1-D1*.

The ultimate floor accelerations are summarized in Table 2.12. It realized that the accelerations recorded on 2<sup>nd</sup> and 3<sup>rd</sup> floors are quite close to accelerations of the 1<sup>st</sup> floor.

**Table 2.12 :** Maximum floor accelerations in  $\text{mm/s}^2$ .

Record	Table		Storey 1		Storey 2		Storey 3	
	SF=0.1	SF=0.2	SF=0.1	SF=0.2	SF=0.1	SF=0.2	SF=0.1	SF=0.2
POE360	294.6	589.2	2150.3	3215.1	2585.3	3226.5	2304.5	3477.4
PTS315	370.0	740.0	2317.3	3256.8	2750.8	3309.2	2736.6	3950.6
HDA165	263.6	527.1	1503.1	3027.1	1820.0	2647.4	1666.7	2098.8
SS-CIG	858.3	1716.6	2233.8	2505.2	2026.9	2812.8	2407.4	2983.6
ERZ-EW	486.1	972.2	1148.2	2359.1	1096.2	2213.0	1707.9	2592.6
BOL090	790.4	1580.7	3215.1	2108.6	2874.9	2978.3	3950.6	3868.3
TCU067*	319.2	474.8	2380.0	2797.5	3143.8	2978.3	3127.6	3703.7

\* TCU067 record is multiplied by 0.15 instead of 0.20.

Acceleration ratios between floor levels are given in Table 2.13. Maximum acceleration ratio reached to 7.46 for  $0.1 \times \text{TCU067}$  record. However, the ratio is around the unity for the upper storeys.

**Table 2.13 :** Acceleration ratios between adjacent floors.

Record	ST1/Shake Table		ST2/ST1		ST3/ST2	
	SF=0.1	SF=0.2	SF=0.1	SF=0.2	SF=0.1	SF=0.2
POE360	7.30	5.46	1.20	1.00	0.89	1.08
PTS315	6.26	4.40	1.19	1.02	0.99	1.19
HDA165	5.70	5.74	1.21	0.87	0.92	0.79
SS-CIG	2.60	1.46	0.91	1.12	1.19	1.06
ERZ-EW	2.36	2.43	0.95	0.94	1.56	1.17
BOL090	4.07	1.33	0.89	1.41	1.37	1.30
TCU067	7.46	5.89	1.32	1.06	0.99	1.24
Average	<b>5.11</b>	<b>3.82</b>	<b>1.10</b>	<b>1.06</b>	<b>1.13</b>	<b>1.12</b>

The lateral floor acceleration ratios of specimens *BF1* to *BF1-D1* are presented in Figure 2.48. The obtained maximum ratio is 2.02. Average of the floor ratios for each *EQs* are 1.55, 1.32, 1.58, 0.83, 0.89, 1.14 and 0.78. For *EQs* #4, #5 and #7, the floor accelerations increased after retrofitting. The possible reason of this increment is the acceleration spectrum shape of the records.

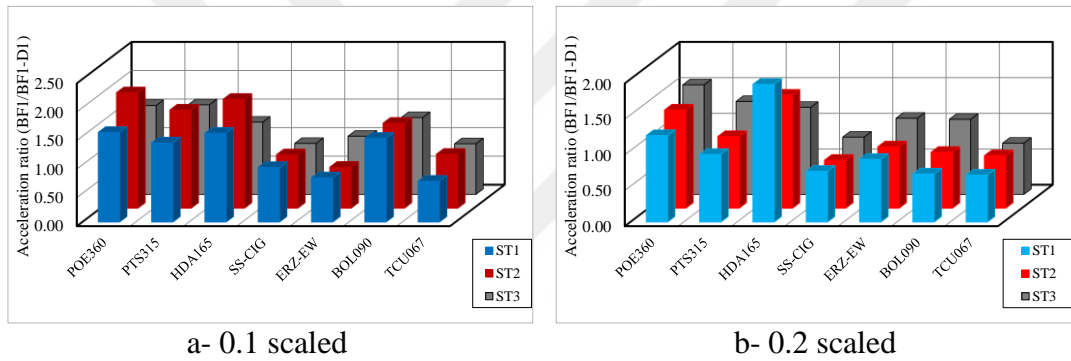


**Figure 2.48 :** Acceleration ratios between floor levels of *BF1* and *BF1-D1*.

The position of the strain gauges are identical with *BF1*. An additional strain gauge was glued on to the *SC*. The maximum strains obtained from the strain gauges are listed in Table 2.14. Some decrement in the ultimate strains was obtained by using *SCs* in columns (776 to 534 micro strain) and beams (428 to 262 micro strain). The obtained maximum strain for *SCs* was 857 micro strain.

**Table 2.14 :** Measured strains in the elastic tests ( $\mu$  strain $\times 10^6$ ).

Record	ST1-Col-bot		ST1-Col-top		ST2-Col-bot		ST3-Col-bot		ST1-Beam		SC	
	SF=0.1	SF=0.2	SF=0.1	SF=0.2	SF=0.1	SF=0.2	SF=0.1	SF=0.2	SF=0.1	SF=0.2	SF=0.1	SF=0.2
POE360	331	540	263	416	276	465	200	285	156	233	741	822
PTS315	393	517	303	361	394	515	229	327	190	234	779	810
HDA165	237	302	188	255	248	286	157	174	128	134	540	616
SS-CIG	322	448	221	310	334	418	207	256	169	193	713	792
ERZ-EW	188	317	162	235	177	305	150	201	91	147	336	540
BOL090	403	534	295	369	469	556	304	312	203	262	728	754
TCU067*	482	512	321	362	442	496	258	292	233	240	857	829

The strain distribution between the members of the 1<sup>st</sup> and 2<sup>nd</sup> storeys are affected by the existence of *SCs*. The beam strains are relatively low compared with *BF1*.

However, the strains measured at bottom of 2<sup>nd</sup> storey columns are relatively larger than for *BF1*.

### 2.3.3.3 Tests in inelastic range

*SS-CIG* was used in the shake table tests of *BF1-D1*. The scale factors applied to the record were 0.75 and 1.00. A slight variation in the first frequency was observed in the inelastic tests, Figure 2.49.

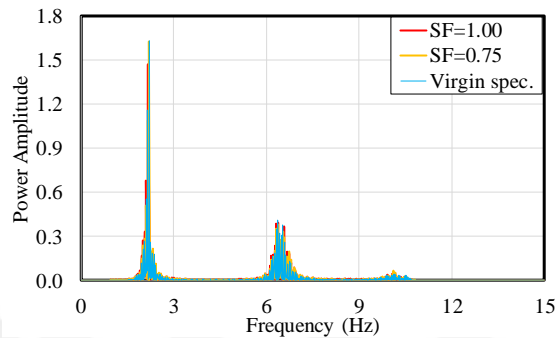


**Figure 2.49 :** Frequency characteristic of *BF1-D1*.

The strain histories recorded at various cross-sections are presented in Figure 2.50 for both scale factors. First and second storey columns, as well as the *SCs*, experienced some extent of nonlinear deformations.

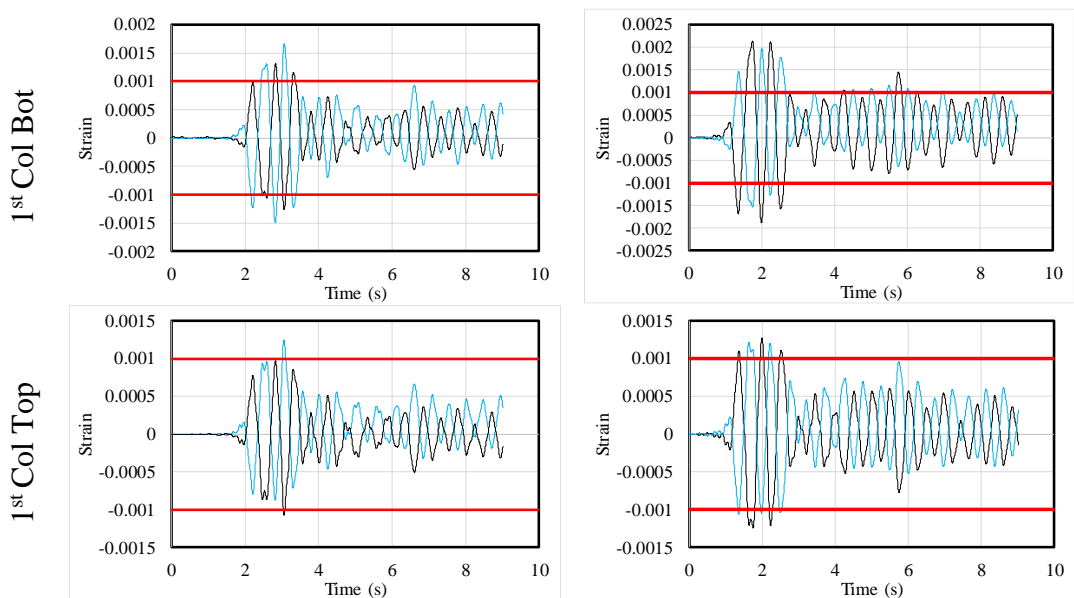


**Figure 2.50 :** Strains on structural members of *BF1-D1*.

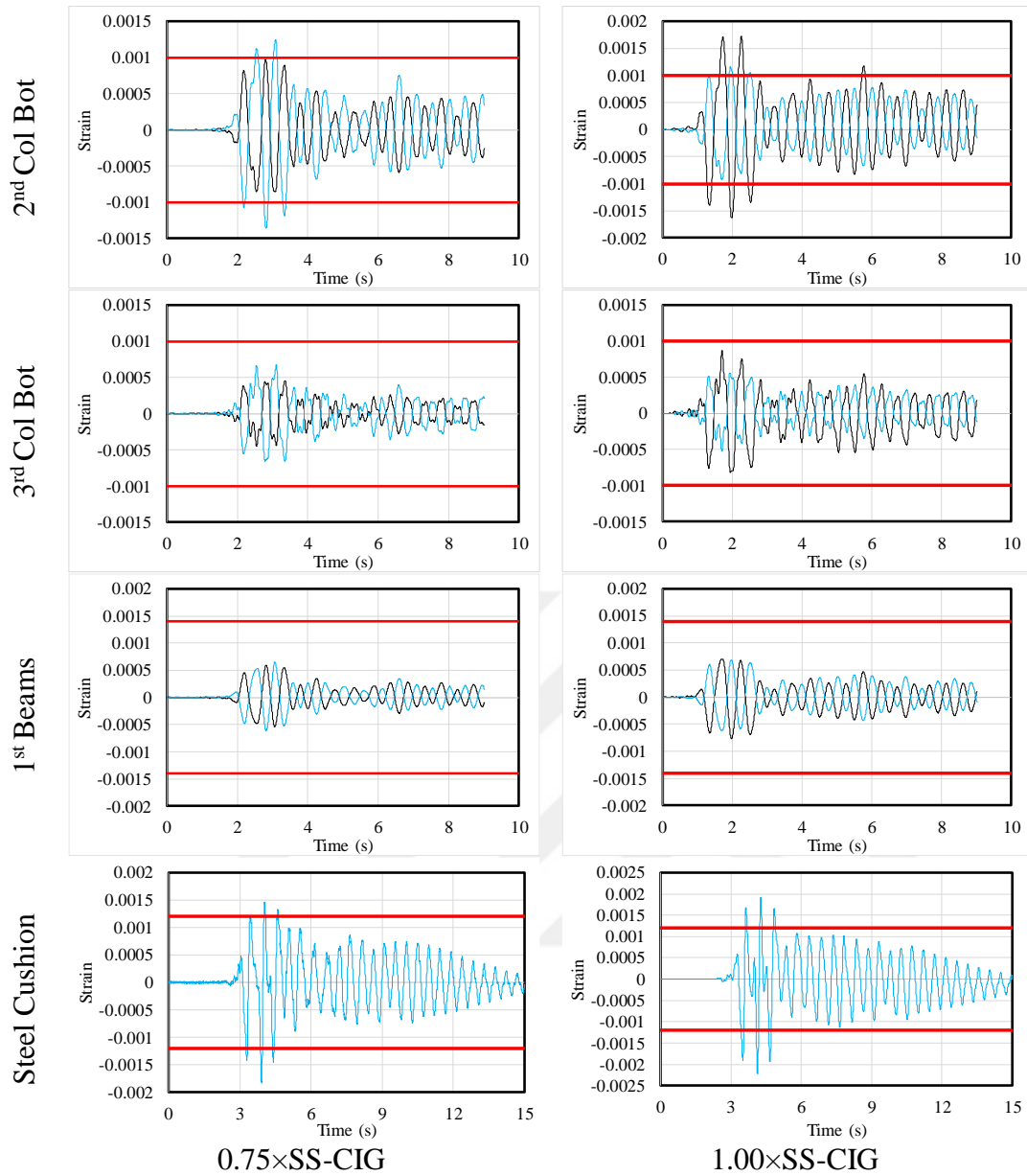


**Figure 2.50 (continued) :** Strains on structural members of *BF1-D1*.

The strain comparisons between *BF1* and *BF1-D1* are made in Figure 2.51. Due to the additional damping supplied by *SCs*, the intensities of the vibration peaks have evidently been reduced.

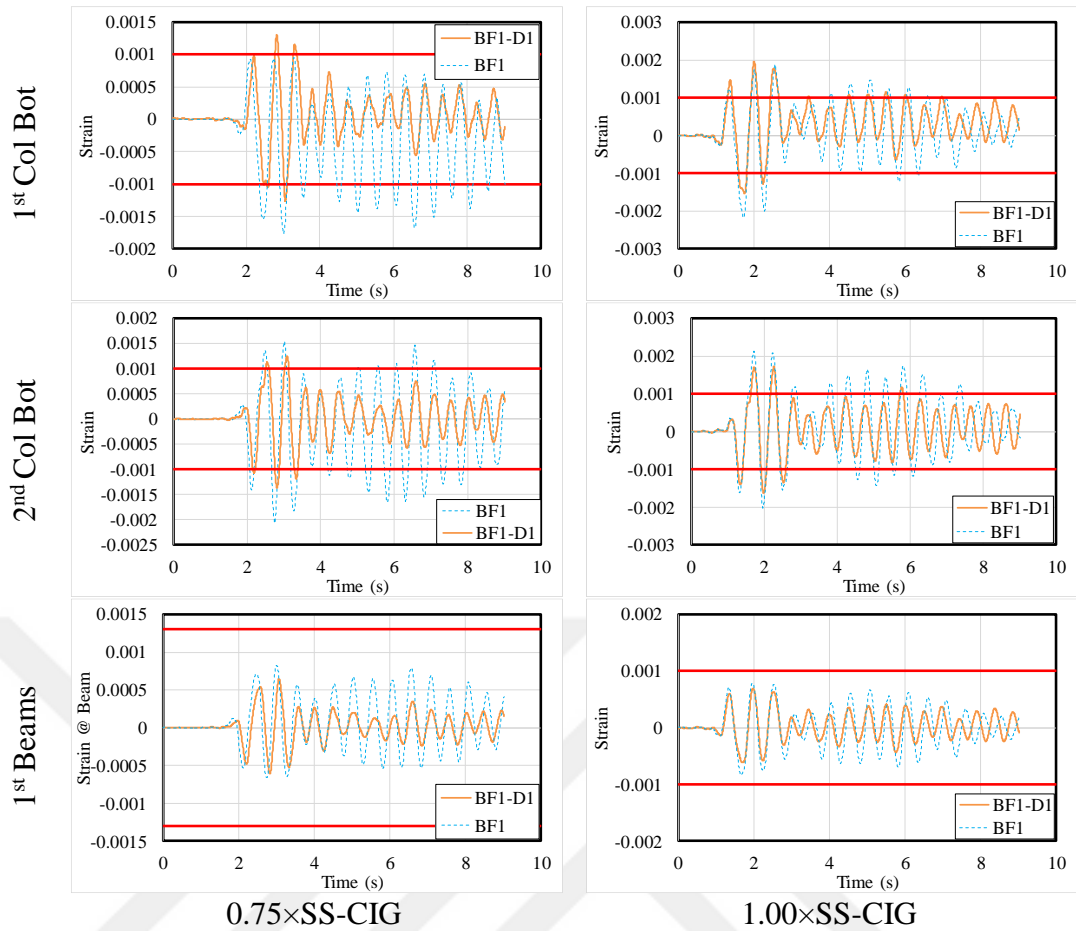


**Figure 2.51** : Strain history comparisons of specimens *BF1* and *BF1-D1*.

The comparison of floor accelerations is presented in Figure 2.52. The floor accelerations are also effected from the existency of *SCs*. In the existing configuration of *SCs*, the ultimate floor accelerations are reduced by about 20-25% for the first storey and 10-18% for the upper storeys.

Some minor damage was observed in the inelastic tests. They are the welding cracks at the column base and beam-to-column connection joints, Figure 2.53.

The longitudinal and transversal displacement histories of *SCs* are given in Figure 2.54. Although transversal displacements are very limited ( $\sim 0.1$  mm), the longitudinal displacement varies in the range of  $\pm 4$  mm.

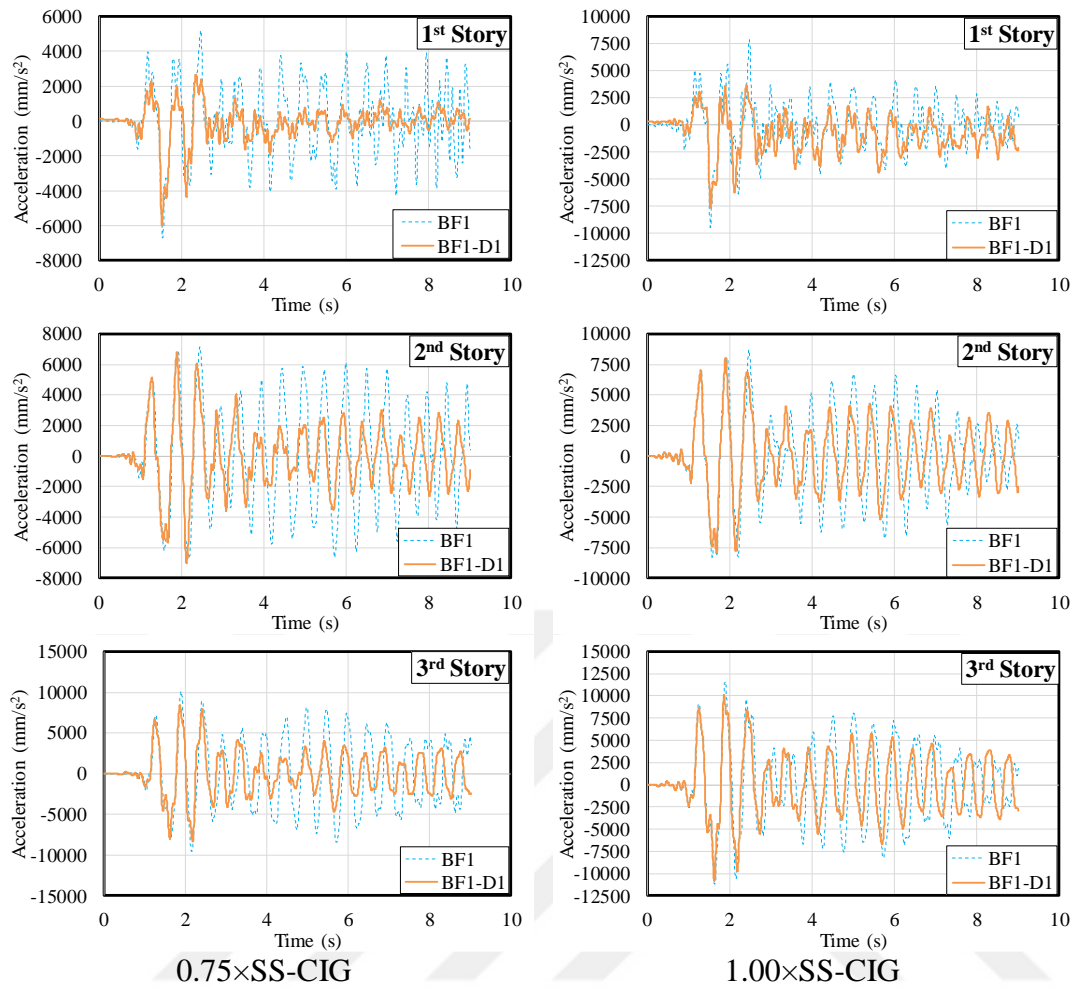


**Figure 2.52 :** Comparison for floor accelerations of *BF1* vs. *BF1-D1*.



**Figure 2.53 :** Observed damage on the structural members.

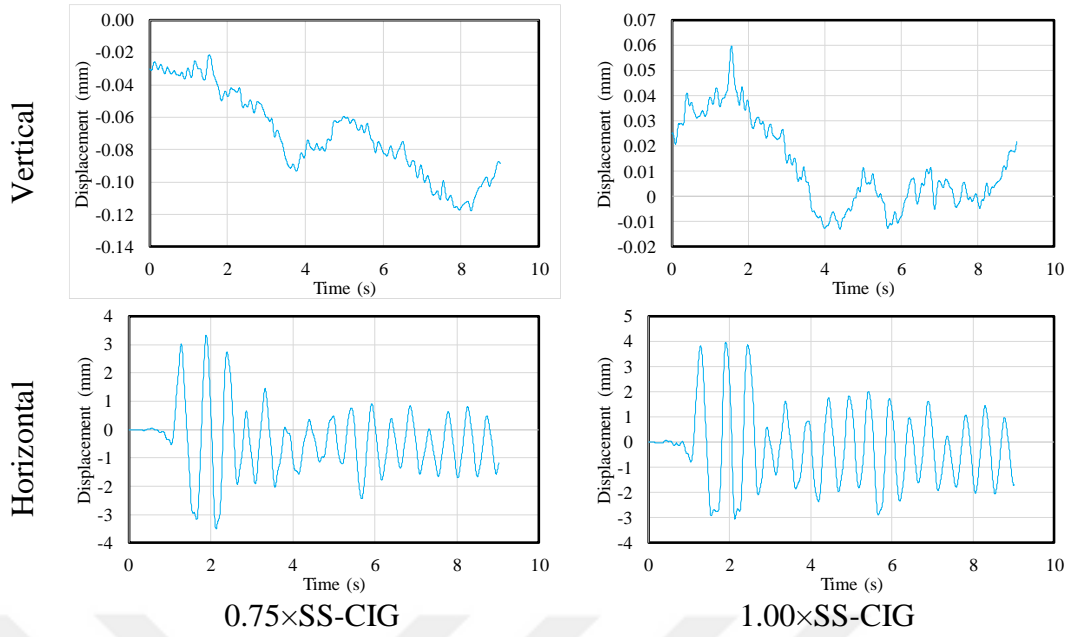


**Figure 2.54 :** Horizontal and vertical displacements of metallic dampers.

The transversal yield displacement of the *SCs* was estimated as 1.25 mm by using the equation (2.16), (Yüksel et al. 2018, Özkaynak et al. 2018, Güllü et al. 2016)

$$\delta_{v,compression} = \frac{Nr}{2EI} \left( \frac{\pi a^3 + 8a^2 r + 2\pi a r^2 + (\pi^2 - 8)r^3}{2(2a + \pi r)} \right) \quad (2.16)$$

A considerable amount of residual displacement was recorded after the completion of the tests, Figure 2.55.



**Figure 2.55 :** Deformed shape of metallic dampers.

### 2.3.4 Bare frame #2 (*BF2*): strong column – weak beam

*BF2* is designed as strong column - weak beam type frame that represents the philosophy of modern seismic codes. Since it is expected that the plastic deformations will be accumulated on the beam ends, strain gauges are mostly attached to the beams, see Figure 2.34 c-d.

**2.3.4.1 Free vibration tests**

Three dominant peaks in the frequency content are obtained in free vibration tests of *BF2*, Table 2.15. The average frequencies were obtained as 2.077, 7.123 and 14.191 Hz.

**Table 2.15 :** Dominant frequencies of *BF2*.

Test	Hammer	Sinus	Step			White Noise		
	Initial	Initial	Initial	0.1	0.2	Initial	0.1	0.2
f <sub>1</sub>	2.124	2.051	2.057	2.057	2.057	2.075	2.075	2.075
f <sub>2</sub>	7.251	7.007	7.153	7.153	7.153	7.080	7.080	7.178
f <sub>3</sub>	13.672	14.160	14.074	14.074	14.020	14.191	14.191	14.105

The results of the alternative free vibration test methods are given together in the frequency domain in Figure 2.56. All the results are consistent with each other.

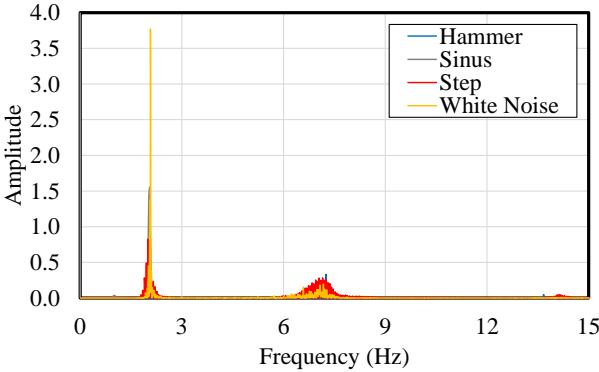


**Figure 2.56 :** Frequencies of *BF2* obtained by diverse free vibration tests.

**2.3.4.2 Tests in the elastic range**

The specimens were exposed to *EQ* records #2, #3, #4, #5, #6, #7 and #8 given in Table 2.1 with scale factors of 0.1 and 0.2 except *TCU067*. It was scaled by a multiplier of 0.175 instead of 0.2.

Similar to the previous tests, maximum acceleration increments were observed between the table level and first floor, Figure 2.57. The data are given for all *EQs*.

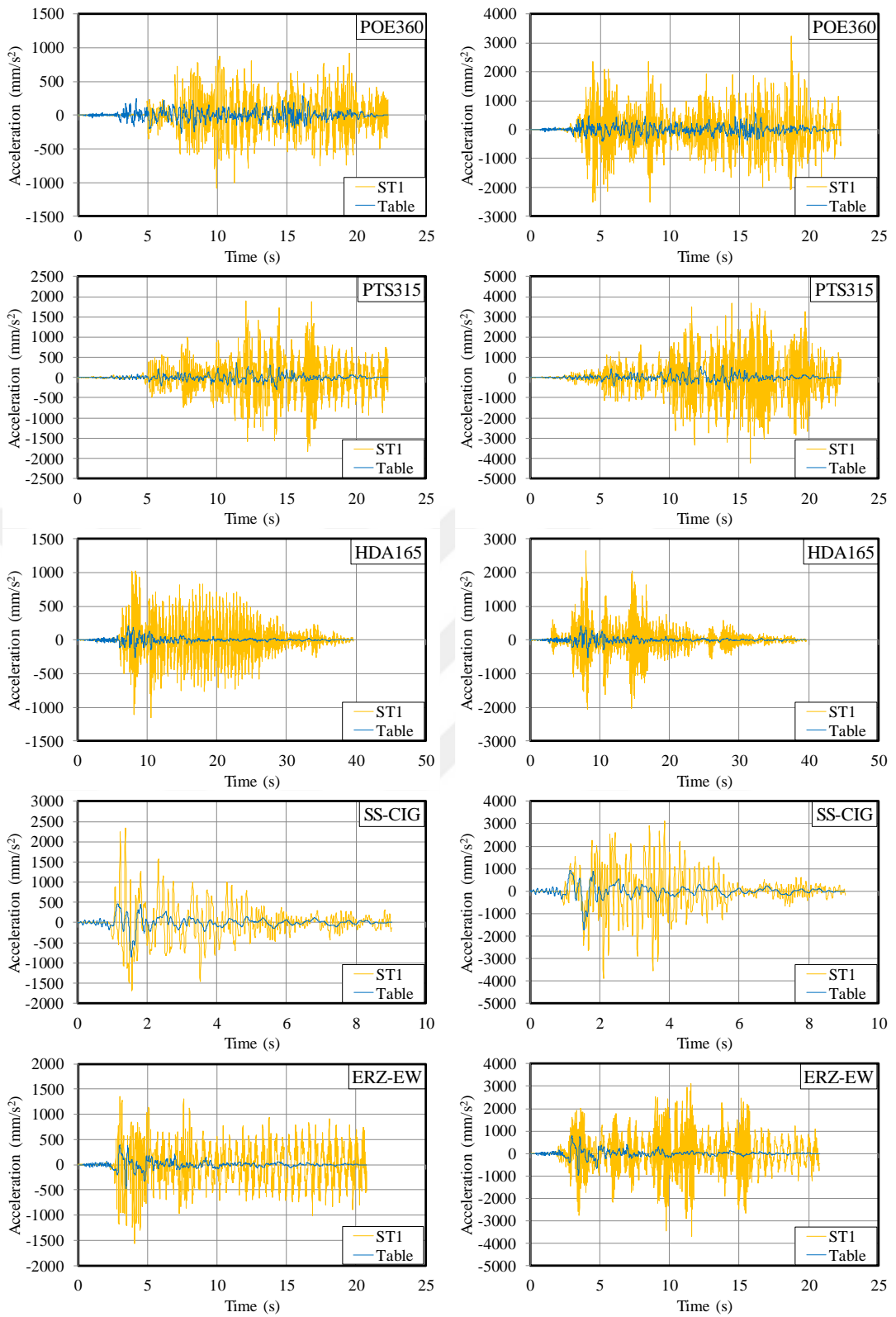


**Figure 2.57 :** Acceleration increments between the table and 1<sup>st</sup> floor levels.

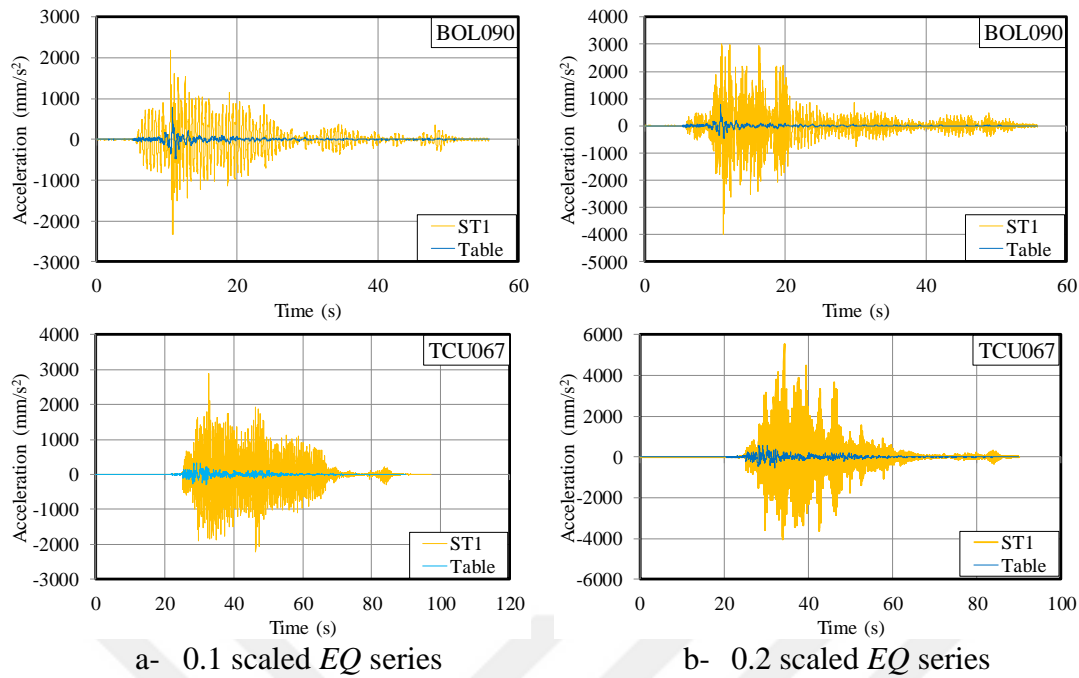


**Figure 2.57 (continued)** : Acceleration increments between table and 1<sup>st</sup> storey levels

The ultimate absolute accelerations recorded at the shake table and floor levels are shown in Table 2.16. The maximum accelerations, of about 0.6g, were obtained from TCU067.

**Table 2.16** : The measured maximum absolute accelerations in mm/s<sup>2</sup>.

Record	Table		Storey 1		Storey 2		Storey 3	
	SF=0.1	SF=0.2	SF=0.1	SF=0.2	SF=0.1	SF=0.2	SF=0.1	SF=0.2
POE360	294.6	589.2	1086.5	3226.4	1387.9	2923.8	1408.6	3127.0
PTS315	370.0	740.0	1898.4	4223.2	2407.0	4356.6	2186.3	4512.1
HDA165	263.6	527.1	1155.3	2644.8	1503.5	2377.9	1341.7	2171.1
SS-CIG	858.3	1716.6	2341.0	3883.7	2240.5	3987.9	2734.3	4465.1
ERZ-EW	486.1	972.2	1561.7	3962.6	1745.3	3620.7	1860.9	3037.9
BOL090	790.4	1580.7	2382.5	3993.5	2106.3	4296.2	2340.9	4675.6
TCU067*	319.2	474.8	2896.8	5516.4	3792.3	6197.5	4233.4	5437.8

\* TCU067 record is multiplied by 0.175 instead of 0.20.

The acceleration ratios between the successive floor levels are calculated and given in Table 2.17. The maximum ratio is about 11.62 and it corresponds to the first storey. The ratio obtained is near unity on the upper floors.

The ultimate strains measured at various locations of the specimen are given in Table 2.18. The maximum strain is 748 micro strain, that is, smaller than the yield strain.

**Table 2.17** : Acceleration ratios between the storeys.

Record	ST1/Shake Table		ST2/ST1		ST3/ST2	
	SF=0.1	SF=0.2	SF=0.1	SF=0.2	SF=0.1	SF=0.2
POE360	3.69	5.48	1.28	0.91	1.01	1.07
PTS315	5.13	5.71	1.27	1.03	0.91	1.04
HDA165	4.38	5.02	1.30	0.90	0.89	0.91
SS-CIG	2.73	2.26	0.96	1.03	1.22	1.12
ERZ-EW	3.21	4.08	1.12	0.91	1.07	0.84
BOL090	3.01	2.53	0.88	1.08	1.11	1.09
TCU067	9.08	11.62	1.31	1.12	1.12	0.88
Average	<b>4.46</b>	<b>5.24</b>	<b>1.16</b>	<b>1.00</b>	<b>1.05</b>	<b>0.99</b>

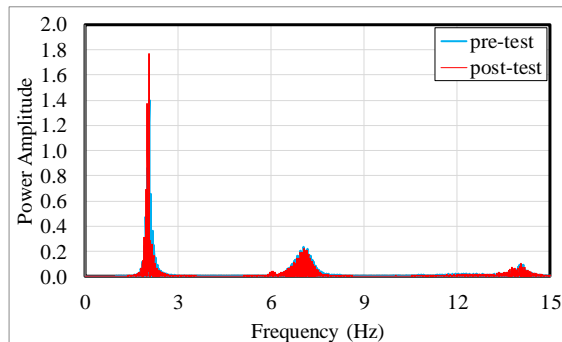
**Table 2.18** : The ultimate strains measured in the elastic tests ( $\mu$  strain $\times 10^6$ ).

Record	ST1-Col-bot		ST1- Beam		ST2-Beam		ST3-Beam	
	SF=0.1	SF=0.2	SF=0.1	SF=0.2	SF=0.1	SF=0.2	SF=0.1	SF=0.2
POE360	192	373	186	350	185	349	66	136
PTS315	310	624	291	587	273	572	101	200
HDA165	194	233	183	211	178	224	66	89
SS-CIG	294	497	275	477	262	500	96	212
ERZ-EW	261	439	245	400	242	377	86	140
BOL090	282	625	258	582	252	577	98	210
TCU067*	562	748	537	734	543	707	201	274

The strain intensities at first storey column base and first and second storey beam ends are in the same range. *TCU067* imposed relatively high strains compared with the other records.

### 2.3.4.3 Tests in the inelastic range

*BF2* was tested in the inelastic range by subjecting it to scaled *SS-CIG*. The frequency response of the specimen was determined by free vibration tests (*step function* and *white noise*). Even some members of the specimen experienced nonlinear deformations, the peaks corresponding to vibration modes moved slightly ( $\sim 0.1$  Hz) in frequency domain, Figure 2.58.

**Figure 2.58** : The dominant frequencies of *BF2* in inelastic tests.

The strain histories at four different cross sections are depicted in Figure 2.59. The yield deformations are shown by red lines on the graphics.

The bottommost section of columns and the ends of first storey beams are exposed to nonlinear deformation, whereas the remaining members are in the elastic range for *SS-CIG* record scaled with 0.75. Moreover, the ends of second storey beams are also plasticized in the application of *SS-CIG* scaled with 1.00.

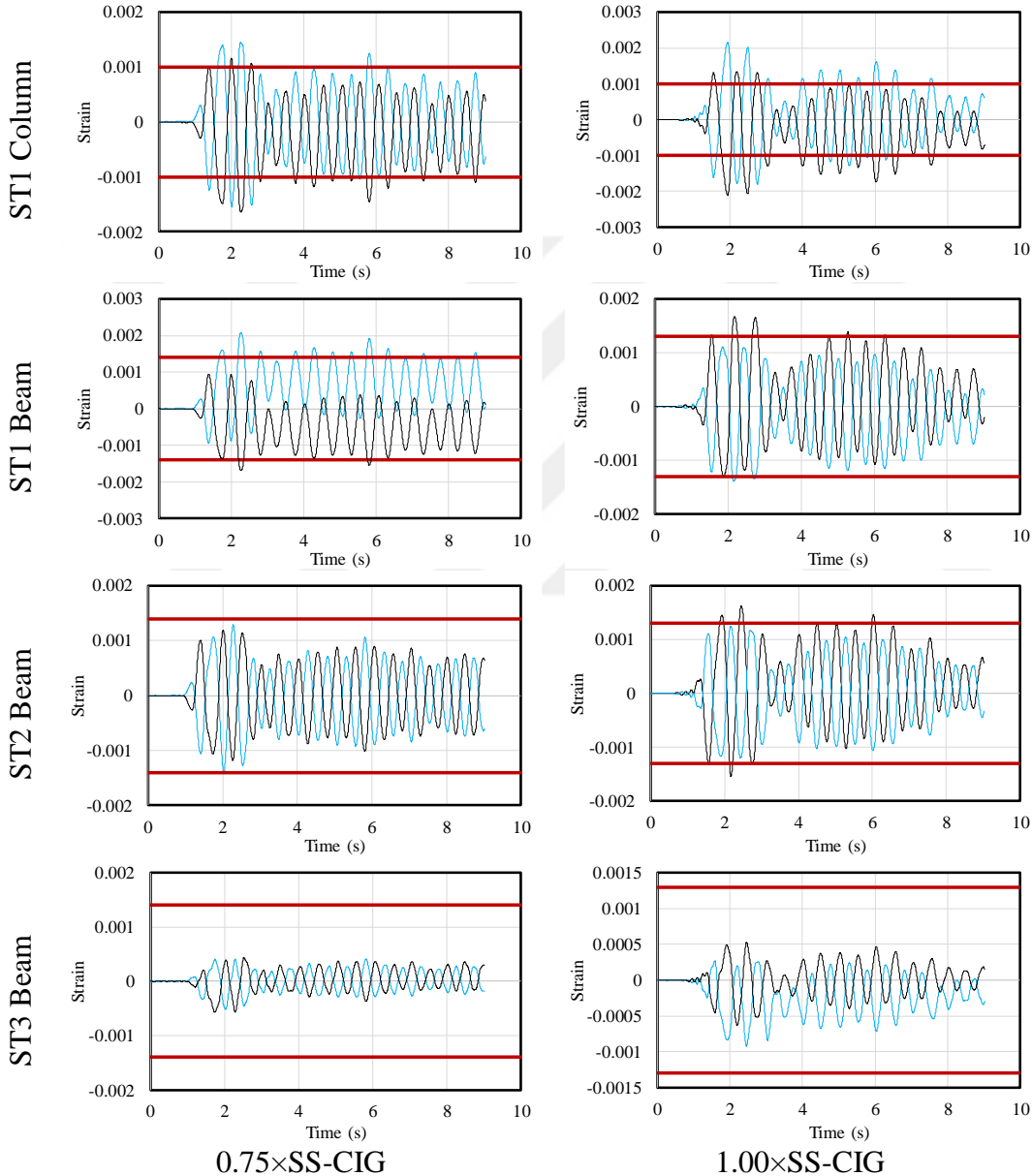


**Figure 2.59 :** Strain histories at members of *BF2*.

Some welding cracks at the beam-to-column connections were observed at the end of the tests. The specimen also had some residual displacements after the tests. The residual top displacement was about 4 mm.



**Figure 2.60 :** The observed welding cracks after the tests.

The floor acceleration histories obtained for the *EQs* are presented in Figure 2.61. The peak accelerations recorded on the shake table were 6437 and 8583 mm/s<sup>2</sup> for 0.75 and 1.00 scaled *SS-CIG*, respectively. However, the peak accelerations recorded at the floor levels were 4804, 6716 and 10181 for 0.75× *SS-CIG* and 5536, 7738 and 11732 for 1.00× *SS-CIG*.

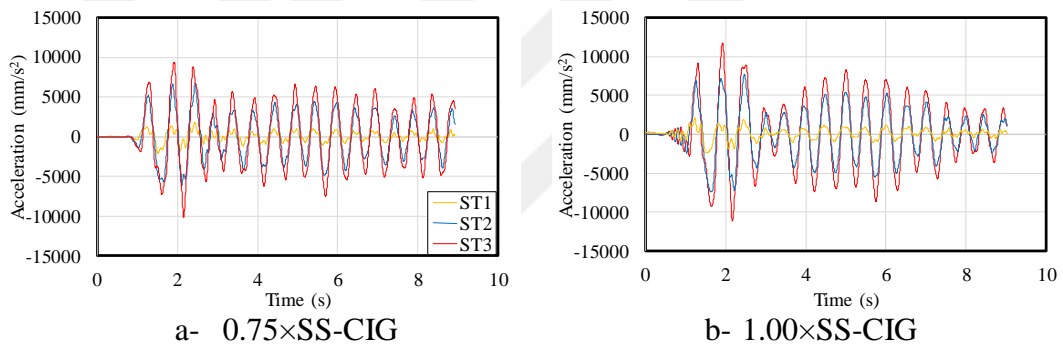


**Figure 2.61 :** Story accelerations measured during the inelastic tests.

### 2.3.5 Bare Frame #2 retrofitted with metallic damper (*BF2-D1*)

*BF2* is retrofitted by means of *SCs* that were placed between the first floor beams and the supporting frame, Figure 2.62. Two bolts (8.8 quality M8) were used at both faces of the cushions.

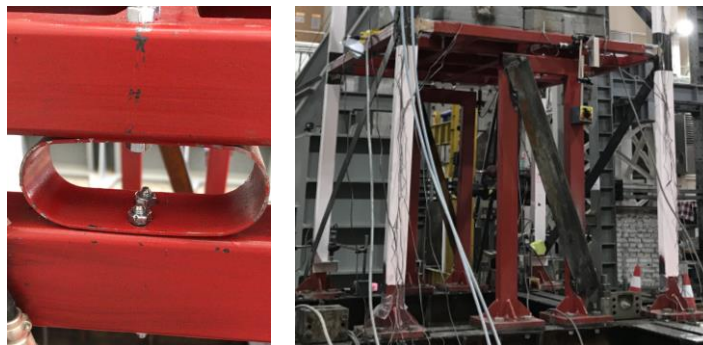


**Figure 2.62 :** The placement of the steel cushions.

**2.3.5.1 Free vibration tests**

Similar to the previous specimens, *hammer*, *sinus*, *step* and *white noise* tests were applied to determine the free vibration characteristics. The obtained frequency contents of the records are summarized in Table 2.19. The averages of the findings were 2.284 and 7.826 s.

**Table 2.19 :** The dominant frequencies of BF2-D1.

Test	Hammer	Sinus	Step			White Noise		
	Initial	Initial	Initial	0.1	0.2	Initial	0.1	0.2
$f_1$	2.319	2.271	2.264	2.264	2.264	2.283	2.289	2.283
$f_2$	7.983	7.641	7.831	7.830	7.880	7.849	7.910	7.434

The frequency distributions obtained from the alternative methods are given in Figure 2.63. The peaks at 2.284 Hz and 7.826 Hz are the dominant peaks.

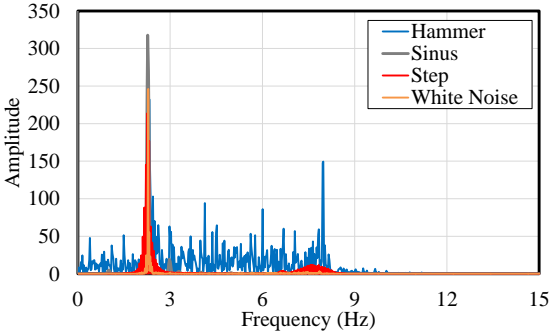


**Figure 2.63 :** The frequency content of free vibration data for *BF2-D1*.

The damping device has a limited effect on the frequency characteristics of the specimen. By comparing the specimens of *BF2* and *BF2-D1*, the first mode shifted from 2.077 Hz to 2.284 Hz, Figure 2.64. Apparently, *SCs* impact not only to revise the shape of second dominant peak but also to eliminate the third peak of *BF2*.

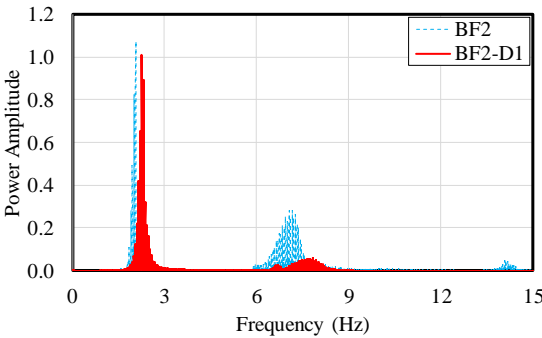


**Figure 2.64 :** Comparison of the frequency content of free vibration data for *BF2* and *BF2-D1*.

### 2.3.5.2 Tests in the elastic range

*BF2-D1* was tested in the elastic range, similar to the aforementioned specimens. The specimen were subjected to *POE360*, *PTS315*, *HDA165*, *SS-CIG*, *ERZ-EW*, *BOL090* and *TCU067* records (see Table 2.1) scaled by coefficients of 0.1 and 0.2. The acceleration histories in the loading direction recorded at the table and the first floor of the specimen are presented in Figure 2.65.

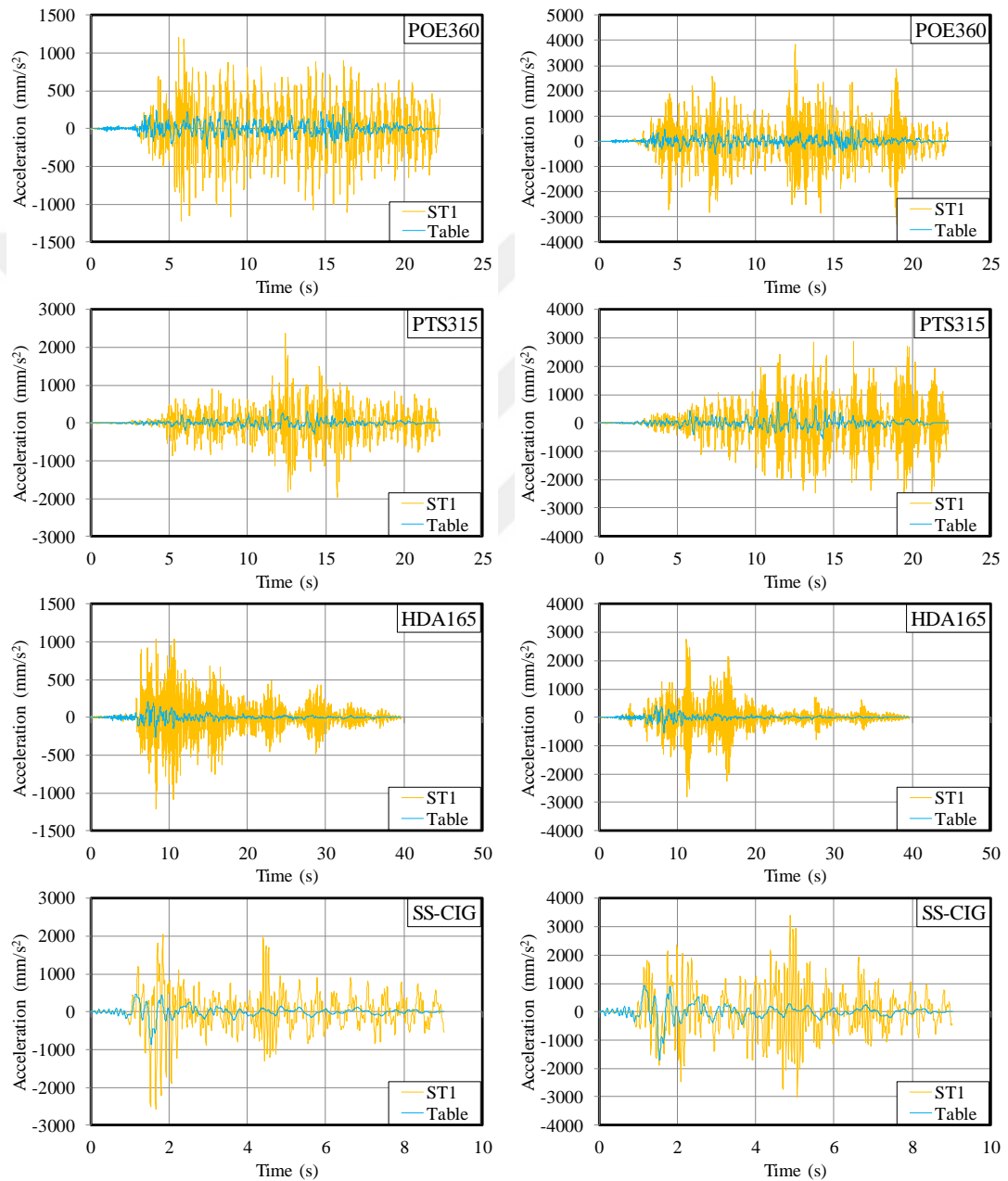


**Figure 2.65** : The acceleration histories of the table and first floor of the specimen.

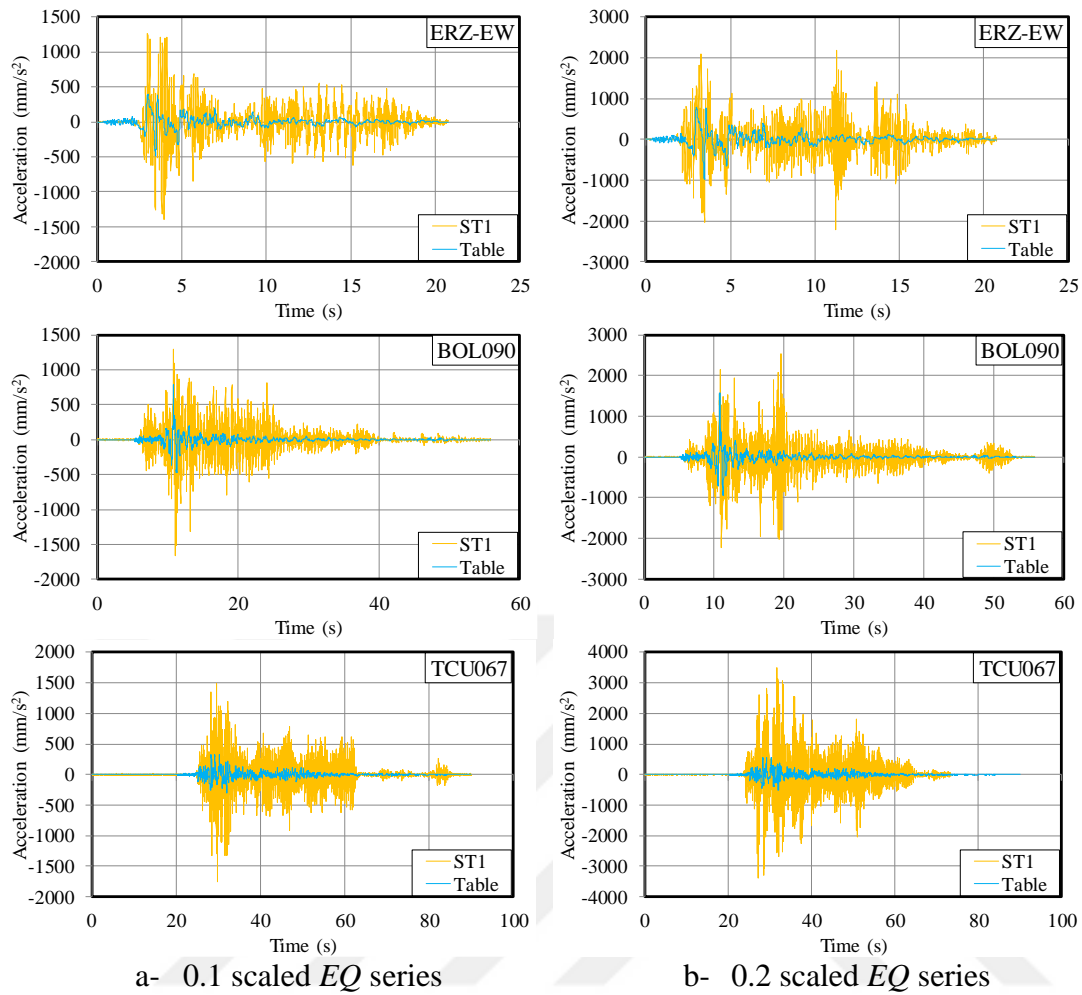


**Figure 2.65 (continued) :** The acceleration histories of the table and first floor of the specimen.

The absolute peak accelerations are gathered in Table 2.20. The major acceleration magnification was observed at the first floor of the specimen.

**Table 2.20 :** The absolute peak accelerations of *BF2-D1* in mm/s<sup>2</sup>.

Record	Table		Storey 1		Storey 2		Storey 3	
	SF=0.1	SF=0.2	SF=0.1	SF=0.2	SF=0.1	SF=0.2	SF=0.1	SF=0.2
POE360	294.6	589.2	1220.9	3834.2	1619.7	3770.7	2012.6	3645.9
PTS315	370.0	740.0	2363.4	2892.3	2434.1	3436.0	2758.0	4158.7
HDA165	263.6	527.1	1206.8	2800.5	1391.2	2719.3	1206.4	1838.9
SS-CIG	858.3	1716.6	2584.3	3408.4	2360.8	3864.7	2168.4	3869.0
ERZ-EW	486.1	972.2	1400.9	2215.5	1733.3	2566.9	1603.9	2176.3
BOL090	790.4	1580.7	1658.0	2530.1	1490.2	3249.2	2082.4	3673.8
TCU067*	319.2	474.8	1748.3	3476.8	2356.6	4387.4	2526.1	3555.8

The acceleration ratios between the successive floor levels are calculated and given in Table 2.21. The major increment is obtained as 7.32 for *TCU067* scaled by 0.175. The average increments are obtained about 4.0, 1.0 and 1.0 from bottom to top.

**Table 2.21** : Acceleration ratios between adjacent storeys.

Record	ST1/Shake Table		ST2/ST1		ST3/ST2	
	SF=0.1	SF=0.2	SF=0.1	SF=0.2	SF=0.1	SF=0.2
POE360	4.14	6.51	1.33	0.98	1.24	0.97
PTS315	6.39	3.91	1.03	1.19	1.13	1.21
HDA165	4.58	5.31	1.15	0.97	0.87	0.68
SS-CIG	3.01	1.99	0.91	1.13	0.92	1.00
ERZ-EW	2.88	2.28	1.24	1.16	0.93	0.85
BOL090	2.10	1.60	0.90	1.28	1.40	1.13
TCU067*	5.48	7.32	1.35	1.26	1.07	0.81
Average	<b>4.08</b>	<b>4.13</b>	<b>1.13</b>	<b>1.14</b>	<b>1.08</b>	<b>0.95</b>

Ratio of the storey accelerations ( $BF2/BF2-D1$ ) are presented in Figure 2.66. Maximum and minimum values are obtained as 1.79 at 1<sup>st</sup> storey for 0.2×ERZ-EW and 0.70 at 3<sup>rd</sup> storey for 0.1×POE360. Although the ratio is less than 1.0 for the EQs with relatively lower input energy (POE360, PTS315, HDA165), it is greater than 1.0 for the EQs with relatively high input energy (SS-CIG, ERZ-EW, BOL090, TCU067).

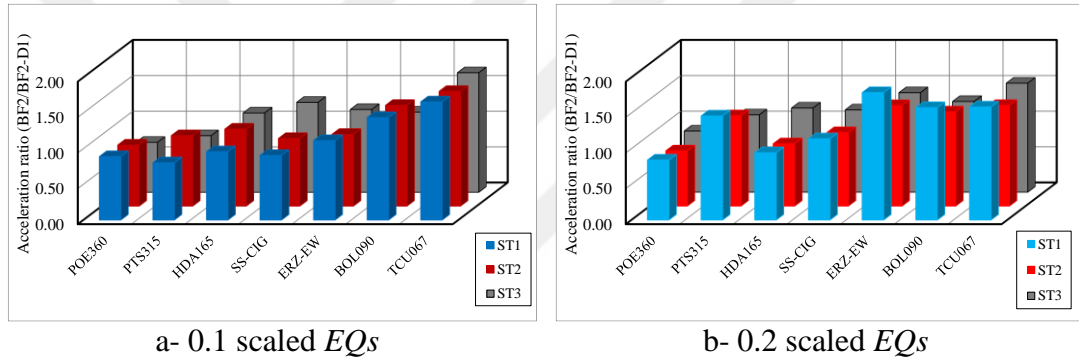


**Figure 2.66** : Acceleration ratios between floor levels of  $BF2$  and  $BF2-D1$ .

The ultimate strain values captured by the strain gauges at various sections are listed in Table 2.22. It is considered that the sections remained in the elastic range. Although large longitudinal displacements were encountered in the SCs, it was not possible to collect data from the strain gauges.

**Table 2.22** : Measured strains in the elastic tests ( $\mu$  strain $\times 10^6$ ).

Record	ST1-Col-bot		ST1-Beam		ST2-Beam		ST3-Beam	
	SF=0.1	SF=0.2	SF=0.1	SF=0.2	SF=0.1	SF=0.2	SF=0.1	SF=0.2
POE360	205	343	216	374	236	380	138	193
PTS315	237	426	239	486	280	523	178	266
HDA165	116	192	115	211	122	225	65	111
SS-CIG	194	324	199	350	210	368	108	188
ERZ-EW	122	194	120	220	154	240	82	129
BOL090	188	369	210	402	243	434	126	230
TCU067*	249	350	245	356	269	366	143	180

If one compares Table 2.22 and Table 2.14, it can be considered that the strains of first storey columns were getting relatively smaller after the placement of SCs. However, the strains of the first storey beams increased in *BF2-D1*.

### 2.3.5.3 Tests in the inelastic range

Similar to the other specimens, *SS-CIG* was used in the shaking tests of *BF2-D1* with the scale factors of 0.75 and 1.00. The results of free vibration tests performed pre- and post- inelastic tests yielded the results shown in Figure 2.67. The frequency corresponding to the first peak is reduced for the inelastic case.

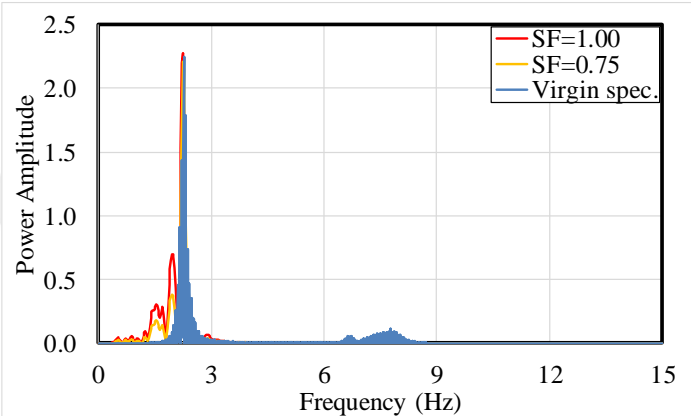


**Figure 2.67 :** Frequency characteristic of the BF2-D1 in inelastic tests.

Strain histories for the specific sections are presented in Figure 2.68. Blue and black colors represent the front and rear faces of the sections. The experimentally obtained yield strains are also added to the graphics as solid red lines.

Minor plastification is recorded at the bottommost section of the columns and all of the other sections remained in the elastic range.

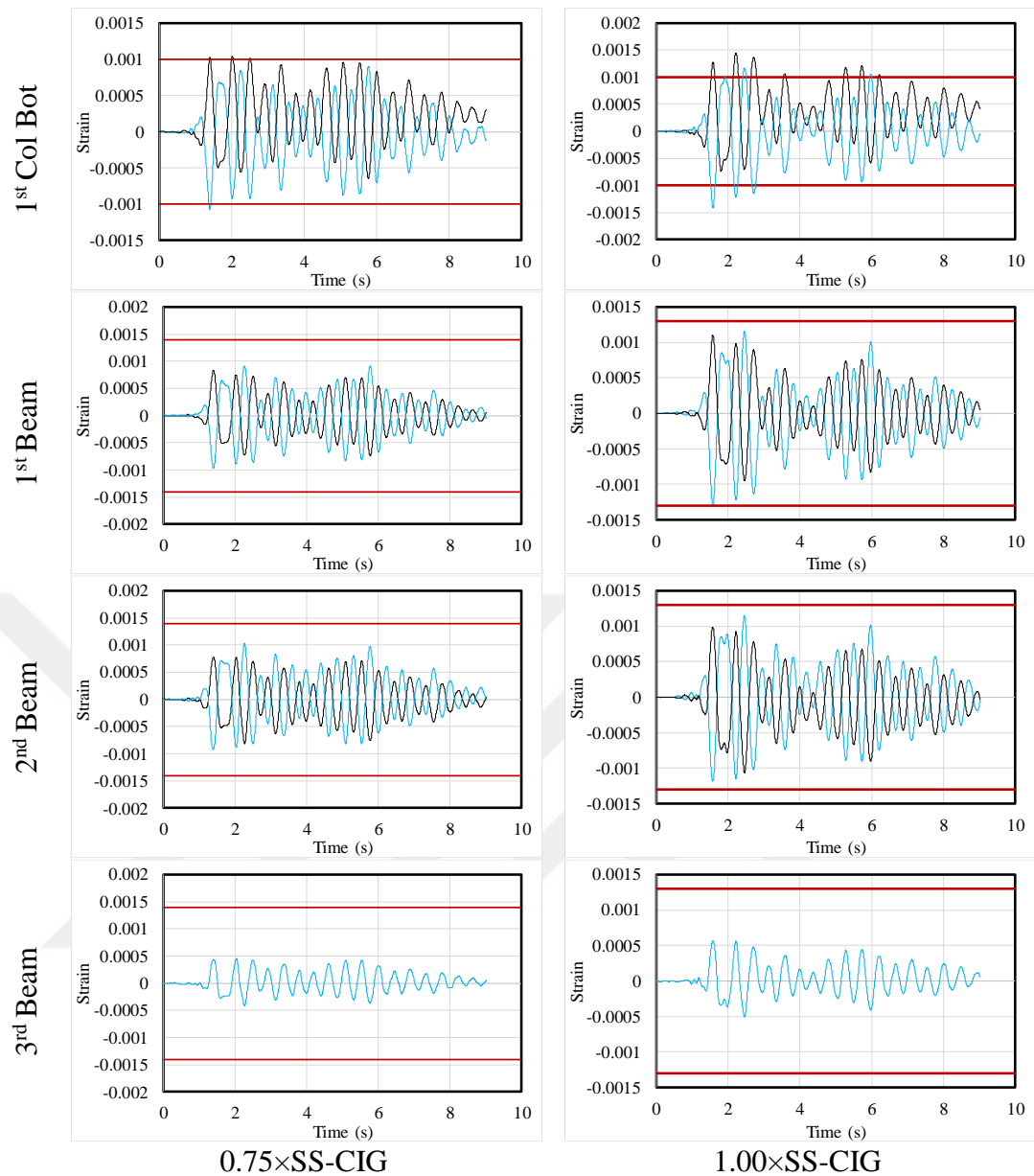


**Figure 2.68 :** Strains on structural members of *BF2-D1*.

The strain comparison between *BF2* and *BF2-D1* specimens is accomplished through the graphics given in Figure 2.69. In the retrofitted specimen (*BF2-D1*), the strain intensities at the first storey columns and beams are almost half of the ones of the bare frame (*BF2*). The effect of the steel cushion on the deformations of members is reducing from the first to the third storeys. So, different metallic damper configurations may be more effective to diminish the strain intensities of members of the upper floors.

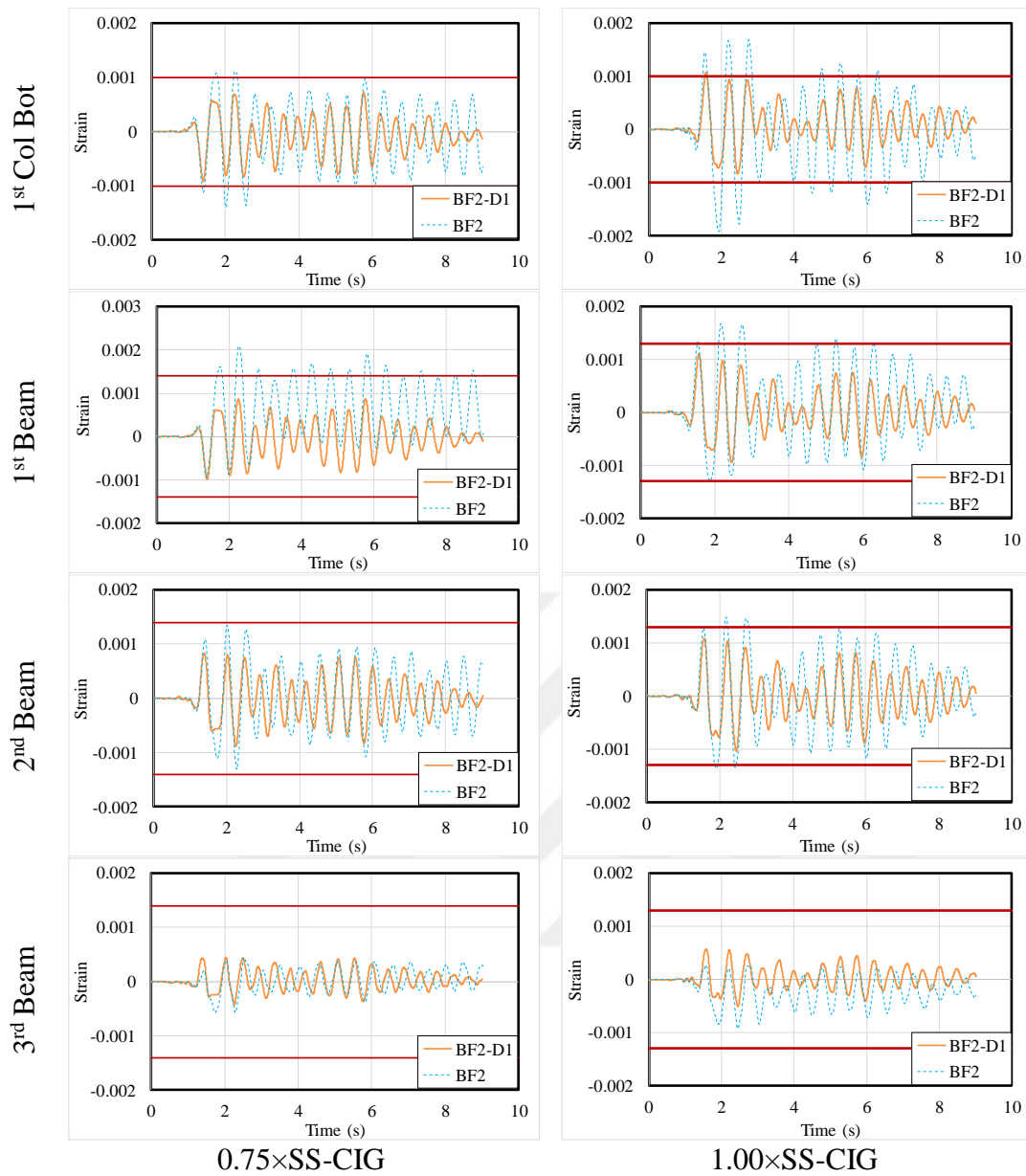


**Figure 2.69 :** The comparison of strain histories of *BF2* and *BF2-D1*.

The comparison of the floor accelerations of *BF2* and *BF2-D1* specimens is given Figure 2.70. The floor accelerations decreased through 18%, 22% and 30% for the 1<sup>st</sup>, 2<sup>nd</sup> and 3<sup>rd</sup> floors of the specimens.

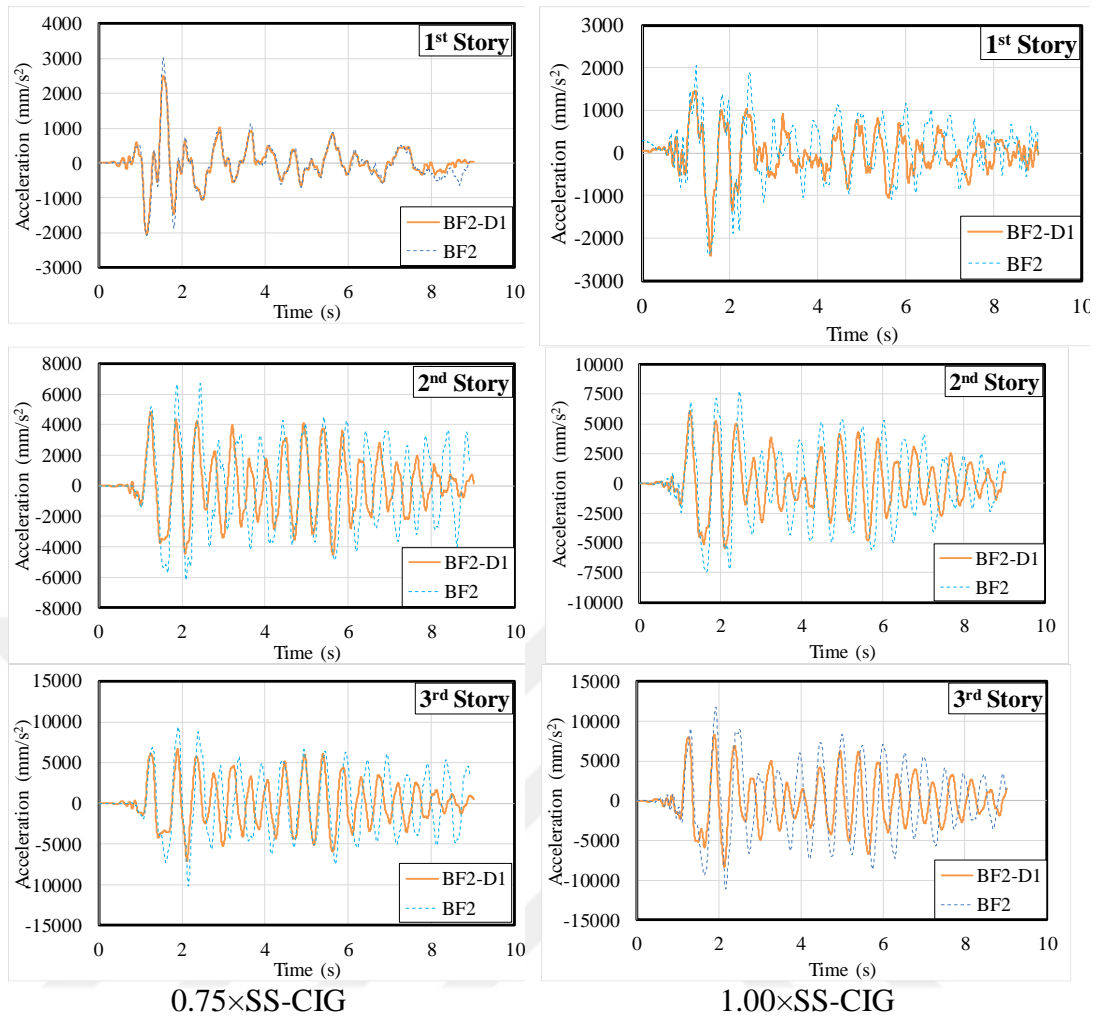


**Figure 2.70 :** The comparison of floor accelerations for *BF2* and *BF2-D1*.

The typical sites of damage were welding cracks at the beam-to-column connections of the specimen, Figure 2.71.



**Figure 2.71 :** The welding damage at the beam-to-column connection.

On the other hand, *SCs* experienced larger plastic deformations that were mostly concentrated on the circular parts of the device. The residual displacement in the longitudinal direction was measured as 4.00 mm after the completion of tests, Figure 2.72.



**Figure 2.72 :** The views of the *SCs* after the tests.

The relative longitudinal and transversal displacements histories of *SCs* are presented in Figure 2.73. The maximum relative longitudinal and transversal displacements were 4.0 and 0.3 mm, respectively. As was expected, the transversal displacement is relatively smaller than the longitudinal one.

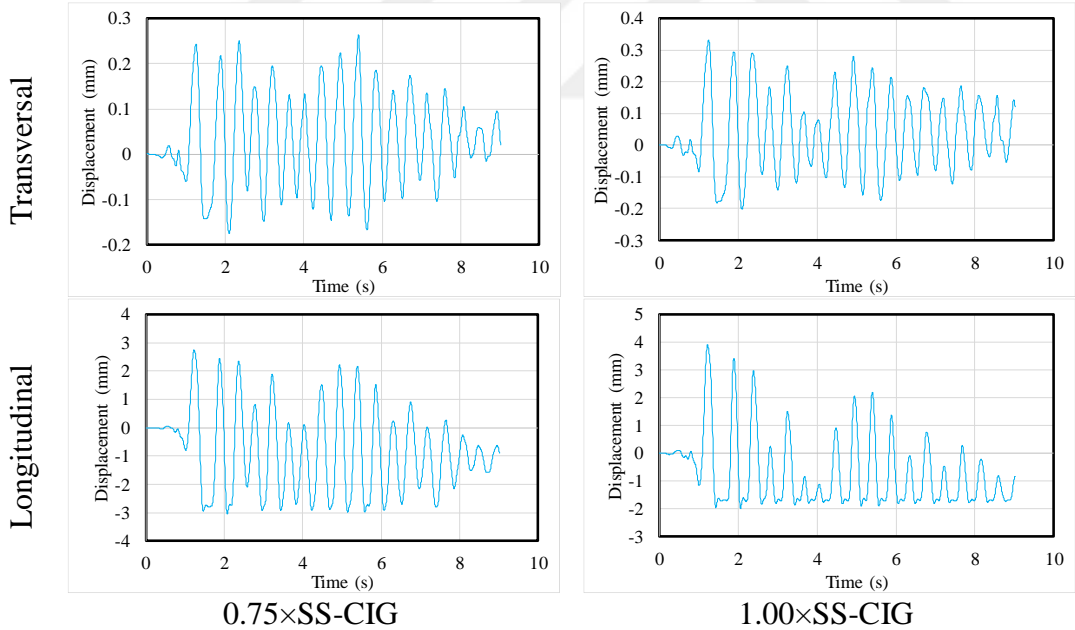


**Figure 2.73 :** Horizontal and vertical displacements of the *SCs*.

The residual longitudinal displacement was about 1.0 mm for *SS-CIG* scaled with 0.75. Hence the displacement history at the succeeding step was not symmetric.

### 2.3.6 The effect of structural configuration on seismic energy components

The seismic energy components defined in Chapter 1.1 are computed through the methodology given in Chapter 2.1.6. The quantities utilized in the equations are all experimental data. The structural responses of *BF1* (weak column – strong beam type structure) and *BF2* (weak beam – strong column type structure) are compared in terms of the energy components.

The dominant frequencies of the specimens were 2.036 Hz and 2.077 Hz. The mass-normalized input energy histories obtained for 0.75×SS-CIG and 1.00×SS-CIG are given in Figure 2.74. The input energy demand of *BF1* (weak column – strong beam type structure) is larger than for *BF2* (weak beam – strong column type structure). The seismic input energies were obtained as 1.55 and 1.27 m<sup>2</sup>/s<sup>2</sup> for 0.75×SS-CIG record; and 2.66 and 2.20 m<sup>2</sup>/s<sup>2</sup> for 1.00×SS-CIG record for *BF1* and *BF2*, respectively.

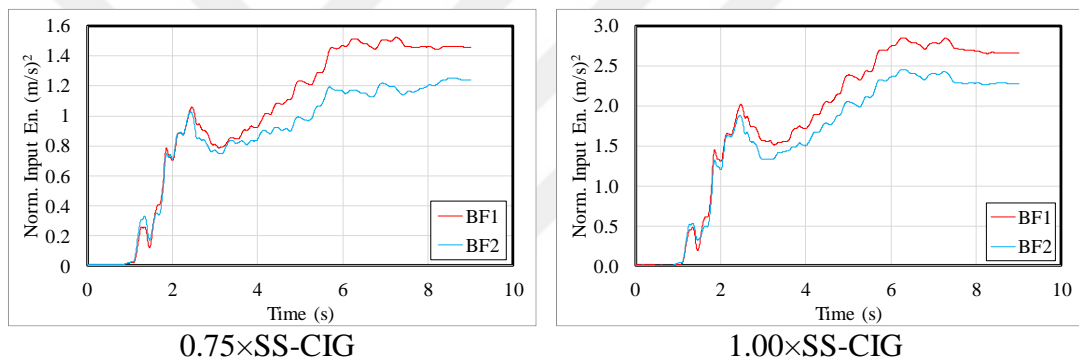


**Figure 2.74 :** Total input energies imparted into specimens *BF1* and *BF2*.

The mass-normalized storey input energy histories are presented in Figure 2.75. Although some extent of differences present between *BF1* (weak column – strong beam type structure) and *BF2* (weak beam – strong column type structure) results at the first and second floors, the difference is negligible for the third floor.

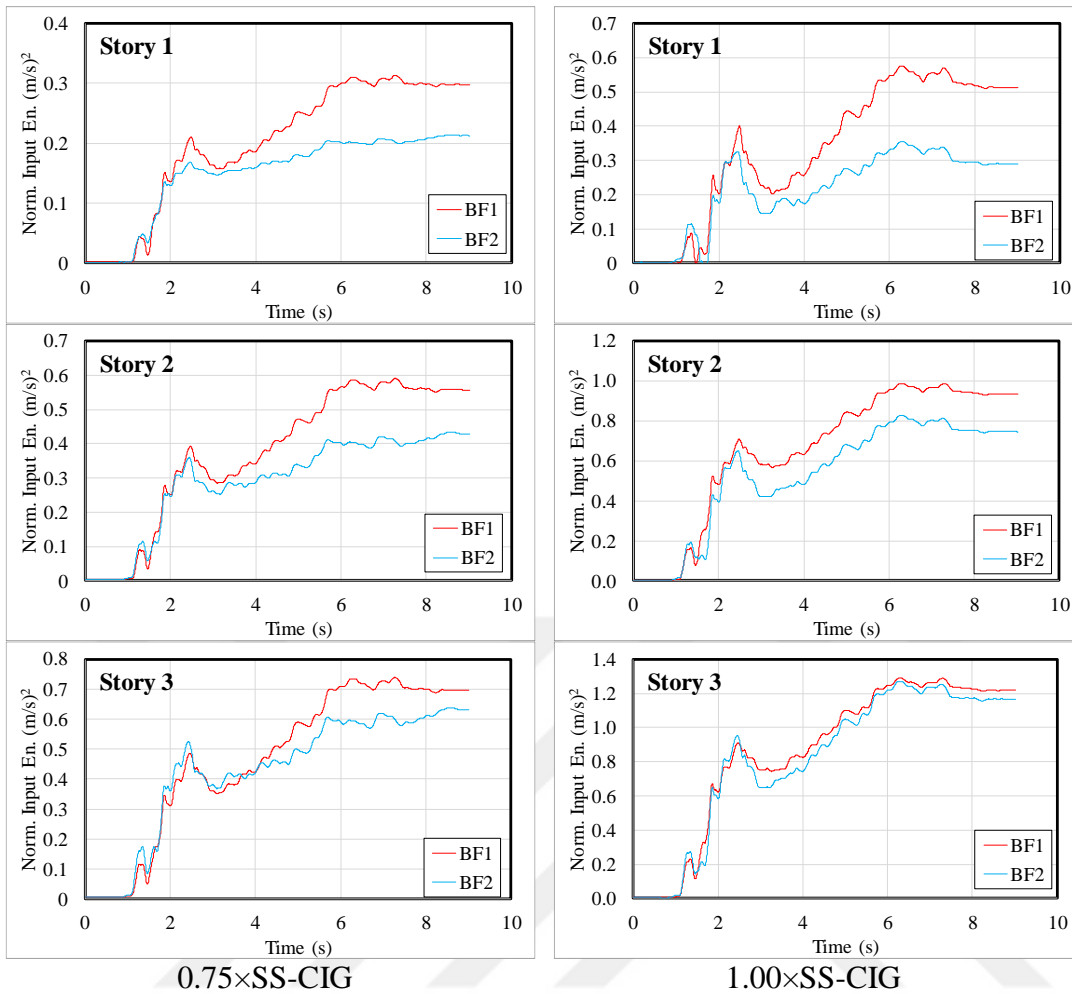


**Figure 2.75 :** The mass-normalized floor input energy histories.

The mass normalized kinetic energy histories are given together for *BF1* and *BF2* in Figure 2.76. As the term is velocity dependent (see Chapter 1.1), the shape of the histories are strongly affected by the velocity profile.

The mass-normalized elastic strain energy histories are given in Figure 2.77. The ratios between the peaks of elastic strain energy and input energy are determined as 0.15 and 0.47 for *BF1* and *BF2*, respectively.

The damping energy histories that are a function of the damping ratio and velocity content are very close for the specimens, Figure 2.78.

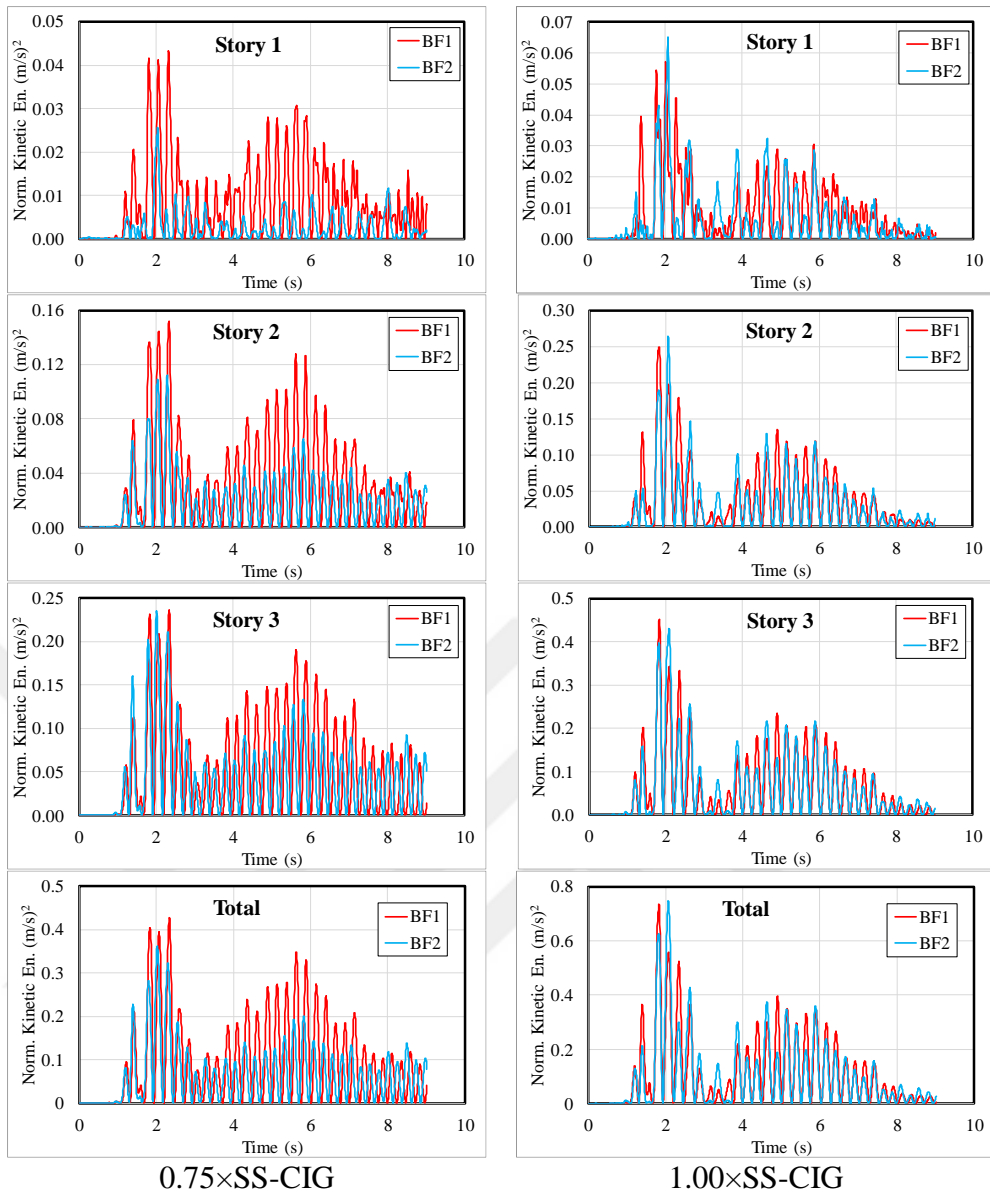


**Figure 2.76 :** Comparison of the mass normalized kinetic energy histories of *BF1* and *BF2*.

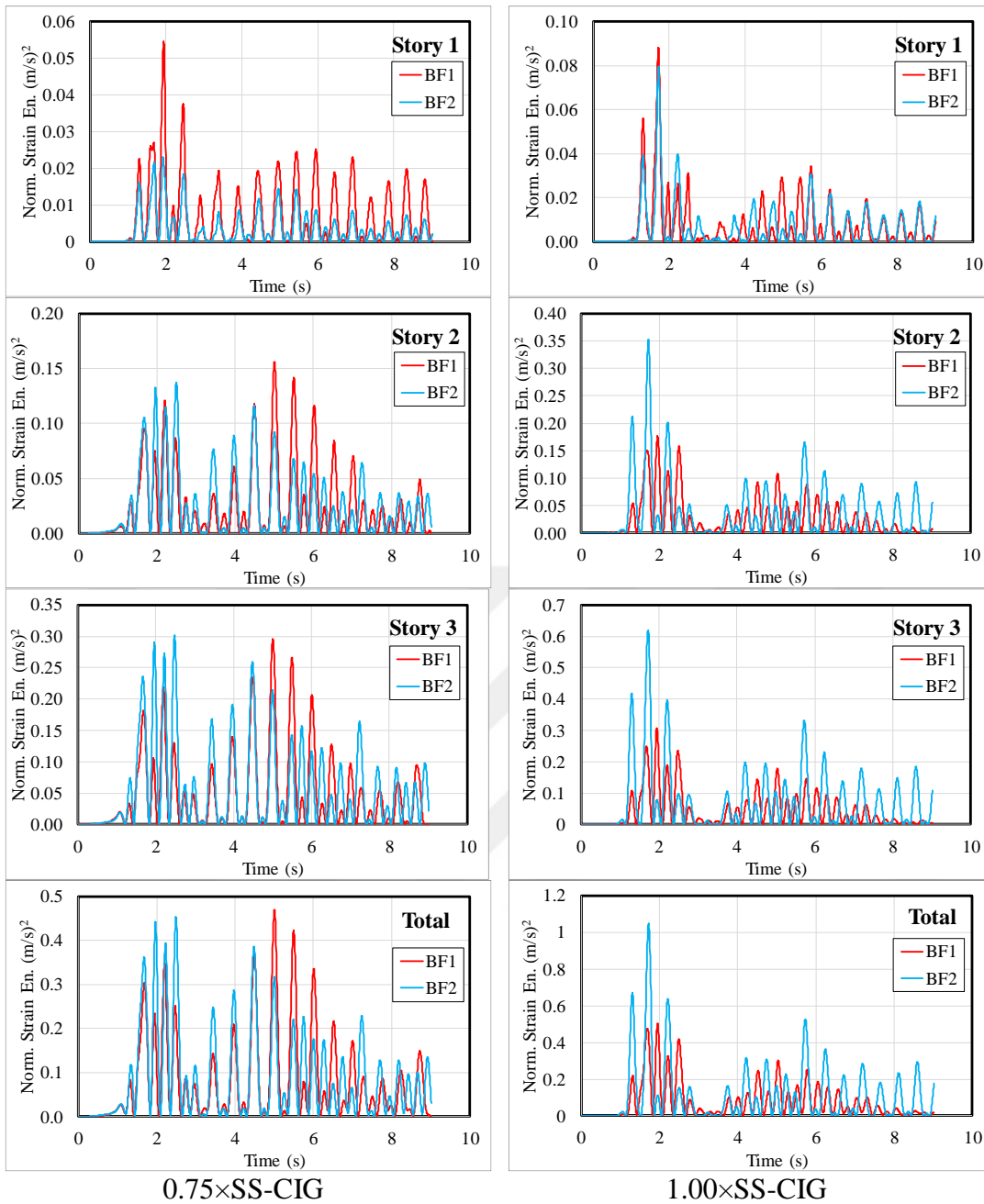


**Figure 2.77** : Comparison of the normalized elastic strain energy of *BF1* and *BF2*.

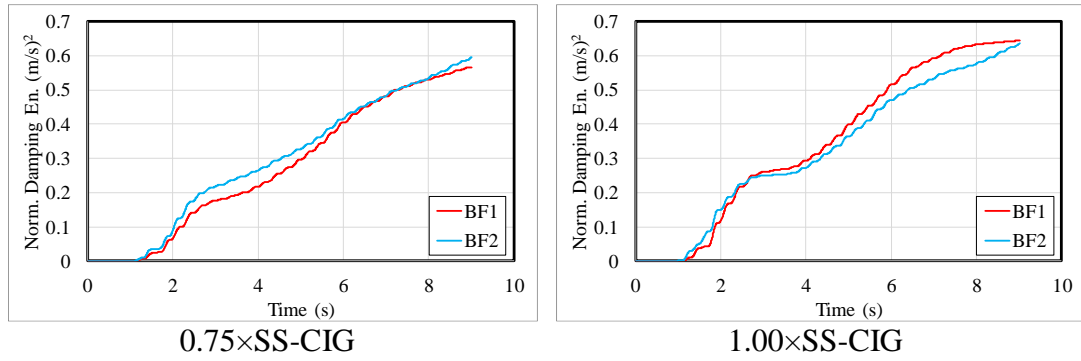


**Figure 2.78 :** Comparison of the damping energy histories for *BF1* and *BF2*.

Plastic energy, that is a reliable indicator for the plastic damage is obtained by subtracting the elastic and damping energies from the total seismic input energy. Even though the seismic input energies of the specimens are close to each other, the plastic energy of *BF1* is considerably larger than for *BF2*, Figure 2.79.

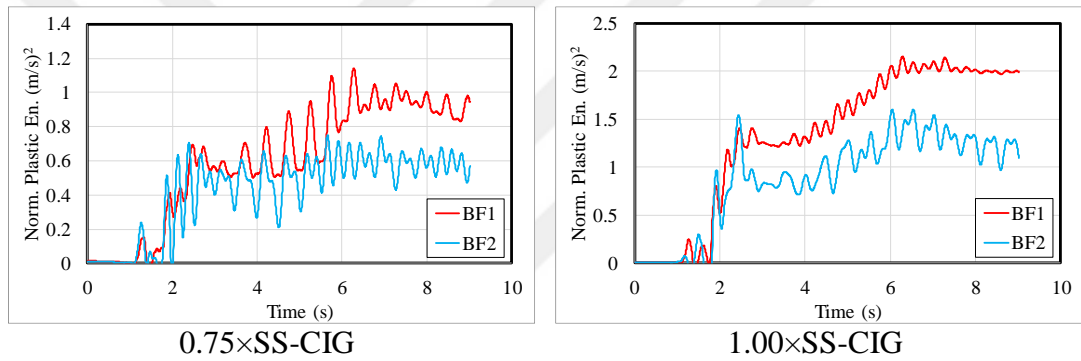


**Figure 2.79 :** Comparison of the plastic energy histories of *BF1* and *BF2*.

Although the seismic input energies of *BF1* and *BF2* are similar to each other, *BF2*, which represents the structures designed according to modern seismic codes, has lower plastic and higher elastic energies.

### 2.3.7 Supplementary damping effect on the seismic input energy components

The comparisons of *BF1* vs. *BF1-D1* and *BF2* vs. *BF2-D1* that were performed in terms of seismic input energy components validate the effect of supplementary damping on the general response of the systems. Although minor frequency alteration between the bare and retrofitted frames was experienced, mass normalized input energy terms are relatively effected from the retrofitting.

For *BF1* and its retrofitted version; the mass-normalized seismic input energy decreased from 1.55 to 1.06  $\text{m}^2/\text{s}^2$  (31.6%) for 0.75xSS-CIG and from 2.662 to 2.226  $\text{m}^2/\text{s}^2$  (16.4%) for 1.00xSS-CIG, Figure 2.80.

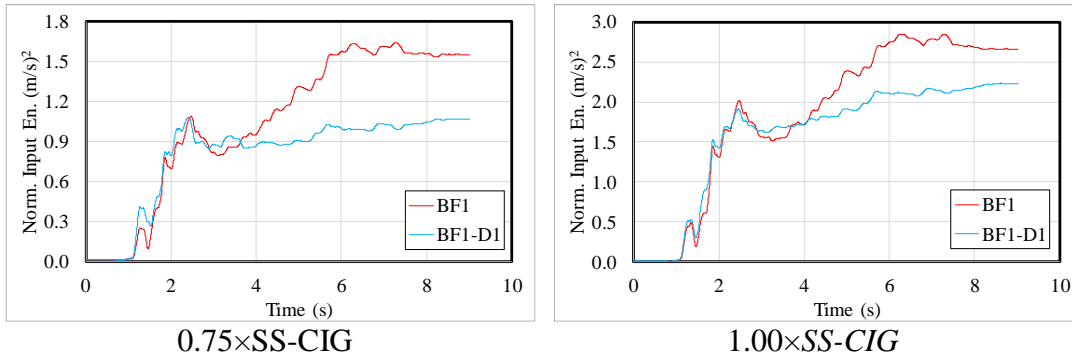


**Figure 2.80** : Total seismic input energy comparisons for *BF1* and *BF1-D1*.

For *BF2* and its retrofitted version; mass normalized seismic input energy decreased from 1.27 to 0.80  $\text{m}^2/\text{s}^2$  (37%) for  $0.75 \times \text{SS-CIG}$  and from 2.20 to 1.51  $\text{m}^2/\text{s}^2$  (31%) for  $1.00 \times \text{SS-CIG}$ , Figure 2.81.

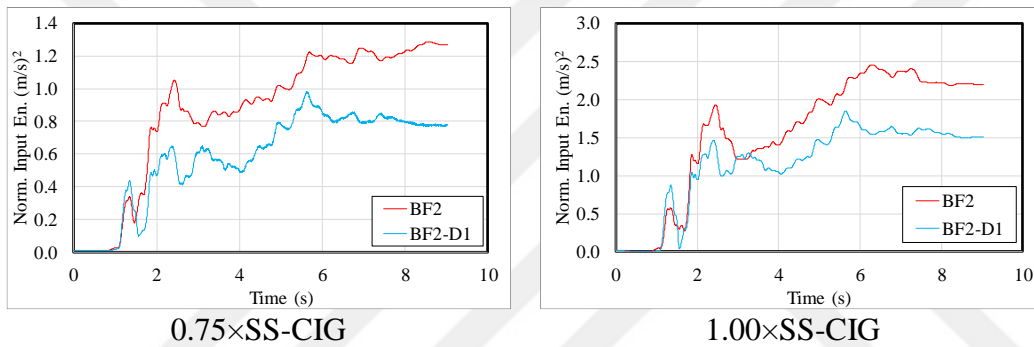


**Figure 2.81** : Total seismic input energy comparisons for *BF2* and *BF2-D1*.

The distribution of seismic input energy between the storeys of *BF1* and *BF1-D1* is presented in Figure 2.82. It is clear that the forms of the graphics are quite different for Storey 1. Normalized input energy is relatively larger for *BF1-D1* exposed to  $1.00 \times \text{SS-CIG}$ .

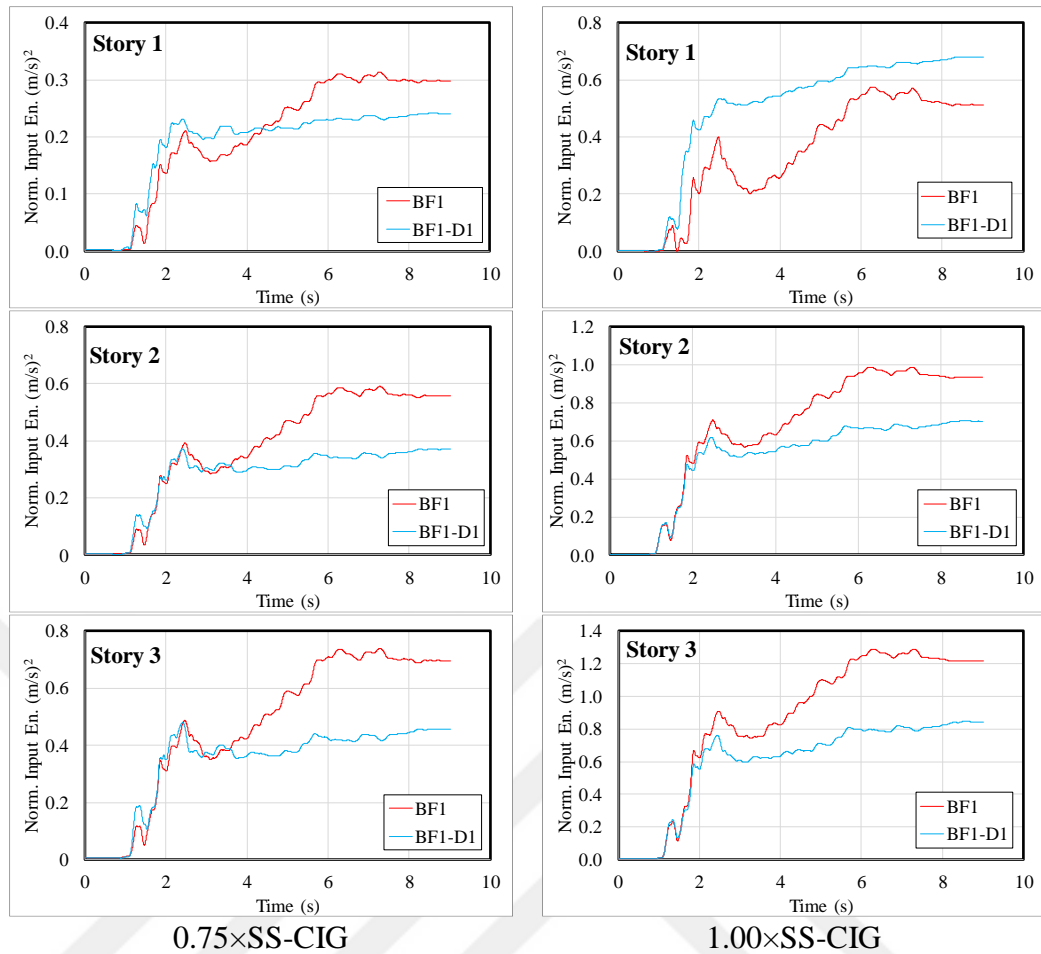


**Figure 2.82** : Distribution of the seismic input energies of *BF1* and *BF1-D1* among the storeys.

Elastic energy terms (kinetic and elastic strain energies) were reduced considerably by adding supplementary damping, Figures 2.83 and 2.84. While elastic strain energy was reduced largely for  $0.75 \times SS-CIG$ , the reduction ratio was relatively smaller for  $1.00 \times SS-CIG$ .

Damping ratios of the retrofitted specimens were determined to be 2-3% higher than those for the bare frames. However, in contradiction, the calculated damping energy is lower for  $1.00 \times SS-CIG$ , Figure 2.85. A possible reason is the decrement of storey velocities for the case, see equation 1.2.

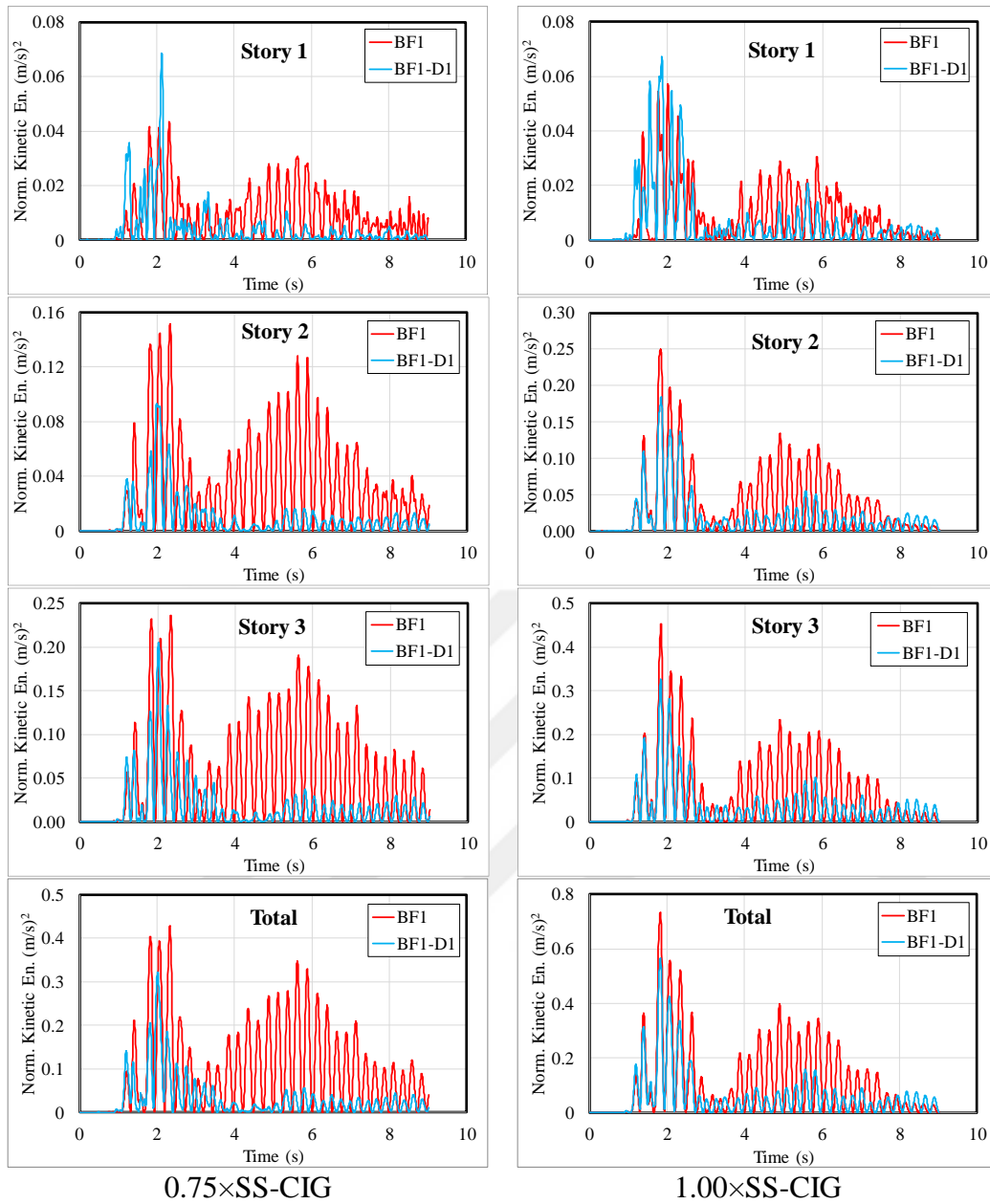


**Figure 2.83** : Comparison for normalized kinetic energies of *BF1* and *BF1-D1*.

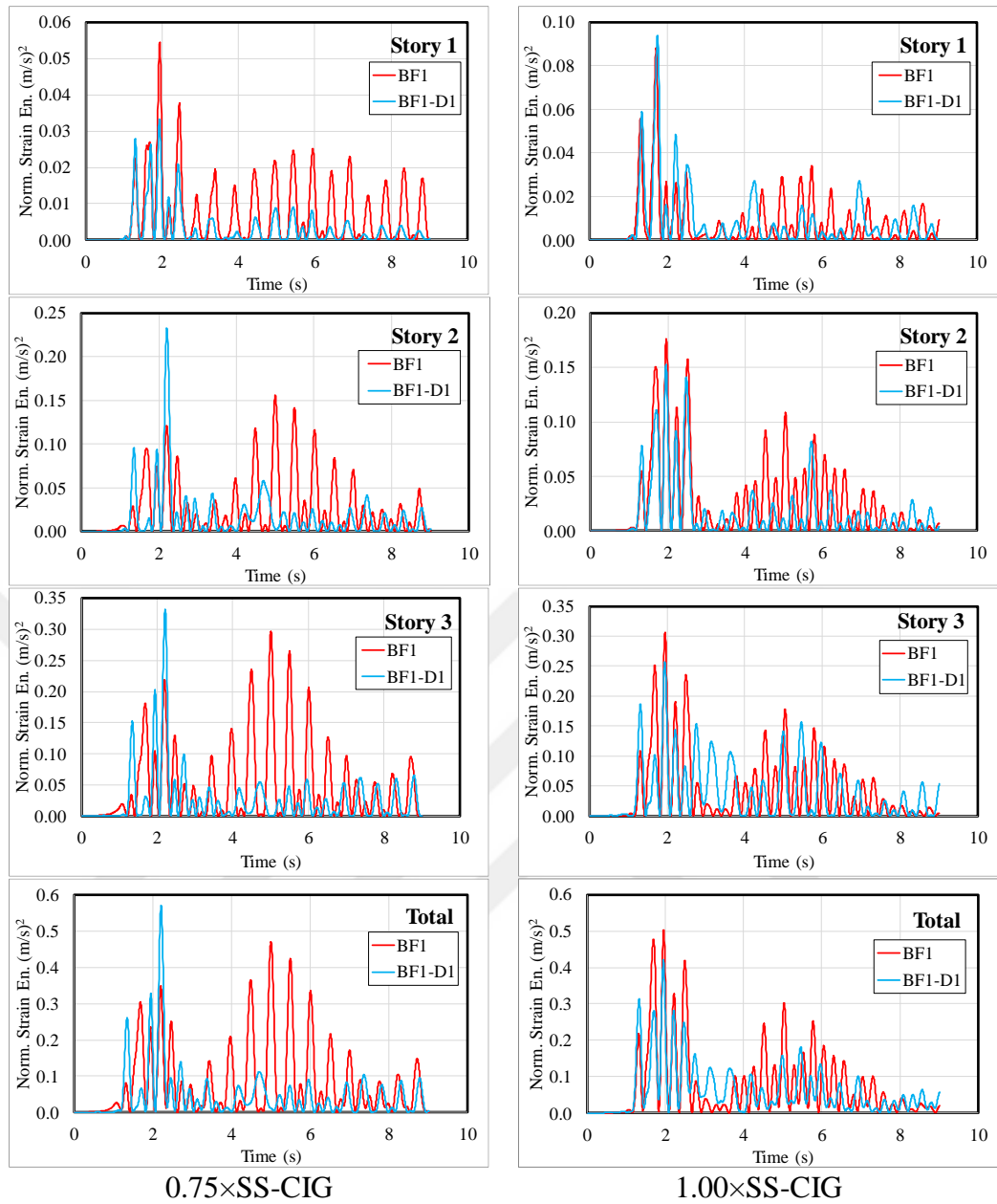


**Figure 2.84 :** Comparison for elastic strain energies of *BF1* and *BF1-D1*.

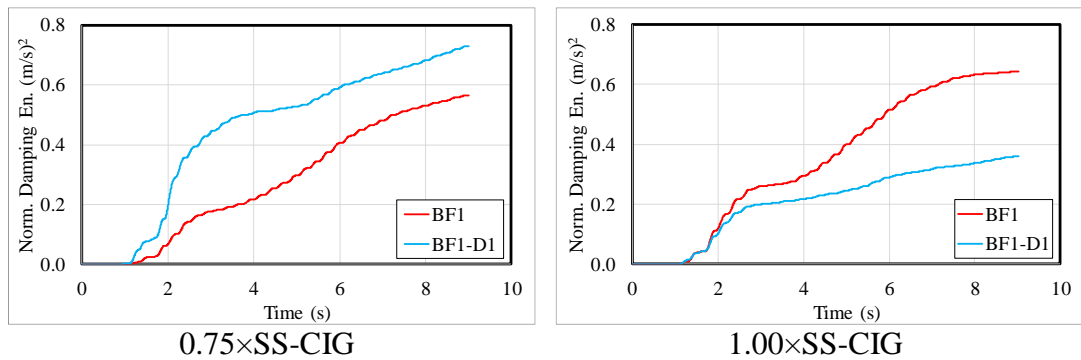


**Figure 2.85 :** Comparison for damping energies of *BF1* and *BF1-D1*.

The plastic energy distributions are given in Figure 2.86 to allow the comparison of the responses of bare and retrofitted specimens. In the retrofitted specimens, plastic energy distributions are given separately for the frame and dampers. It is seen that most part of the plastic energy is generated by the damper.

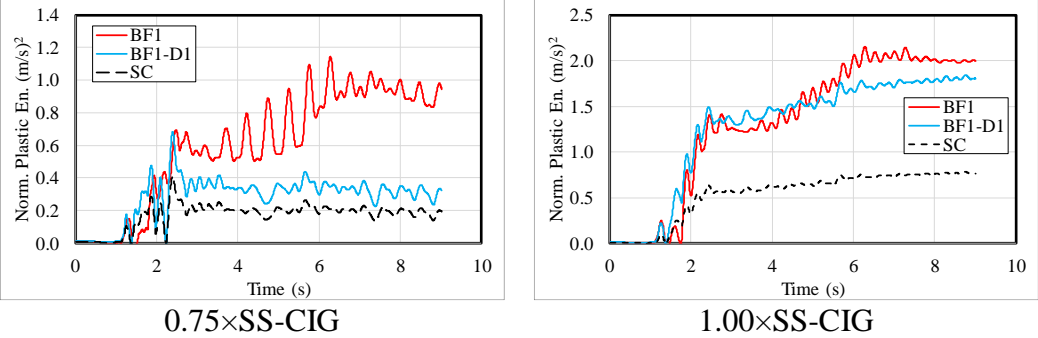


**Figure 2.86 :** Comparison for plastic energies of *BF1* and *BF1-D1*.

Similarly, distribution of seismic input energy between storeys of the specimens *BF2* and *BF2-D1* is depicted in Figure 2.87. The input energy history is larger for the bare frame at each storey.

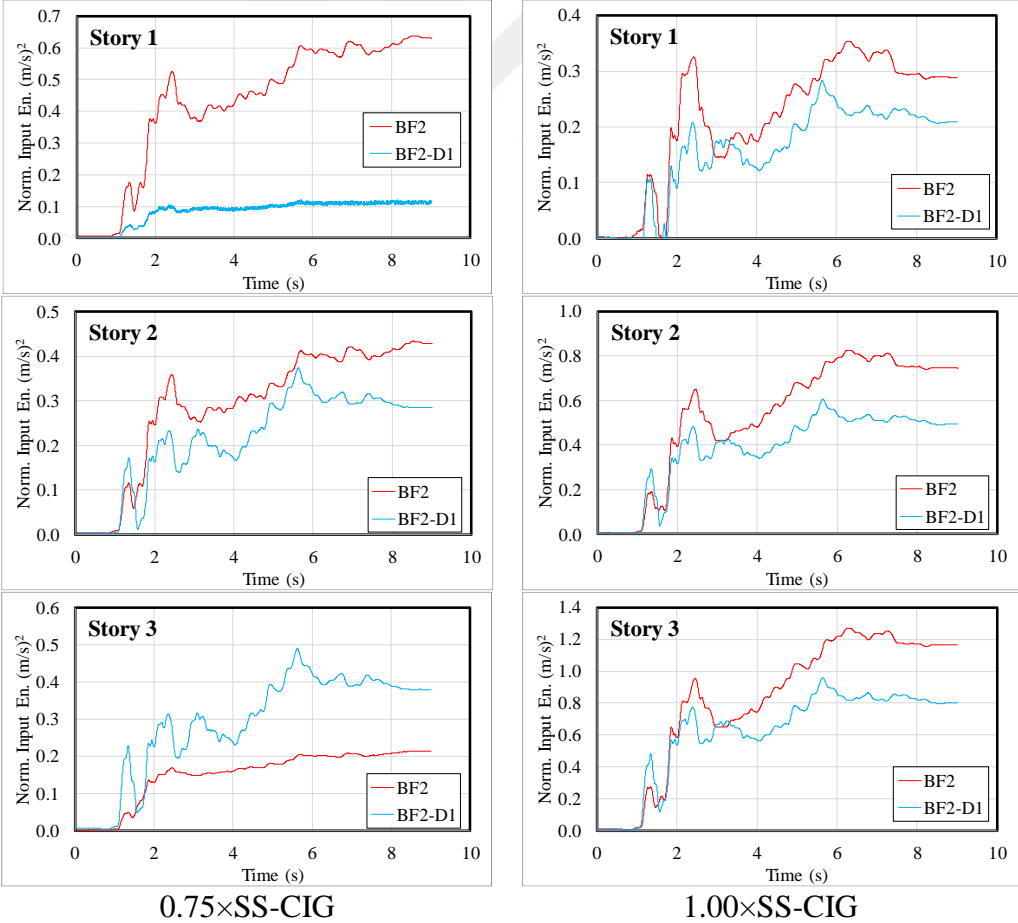


**Figure 2.87 :** Distribution of the seismic input energies of *BF2* and *BF2-D1* among the storeys.

The normalized kinetic energy that is one of elastic energy terms was decreased significantly (~50%) for the retrofitted specimen at each storey, Figure 2.88.

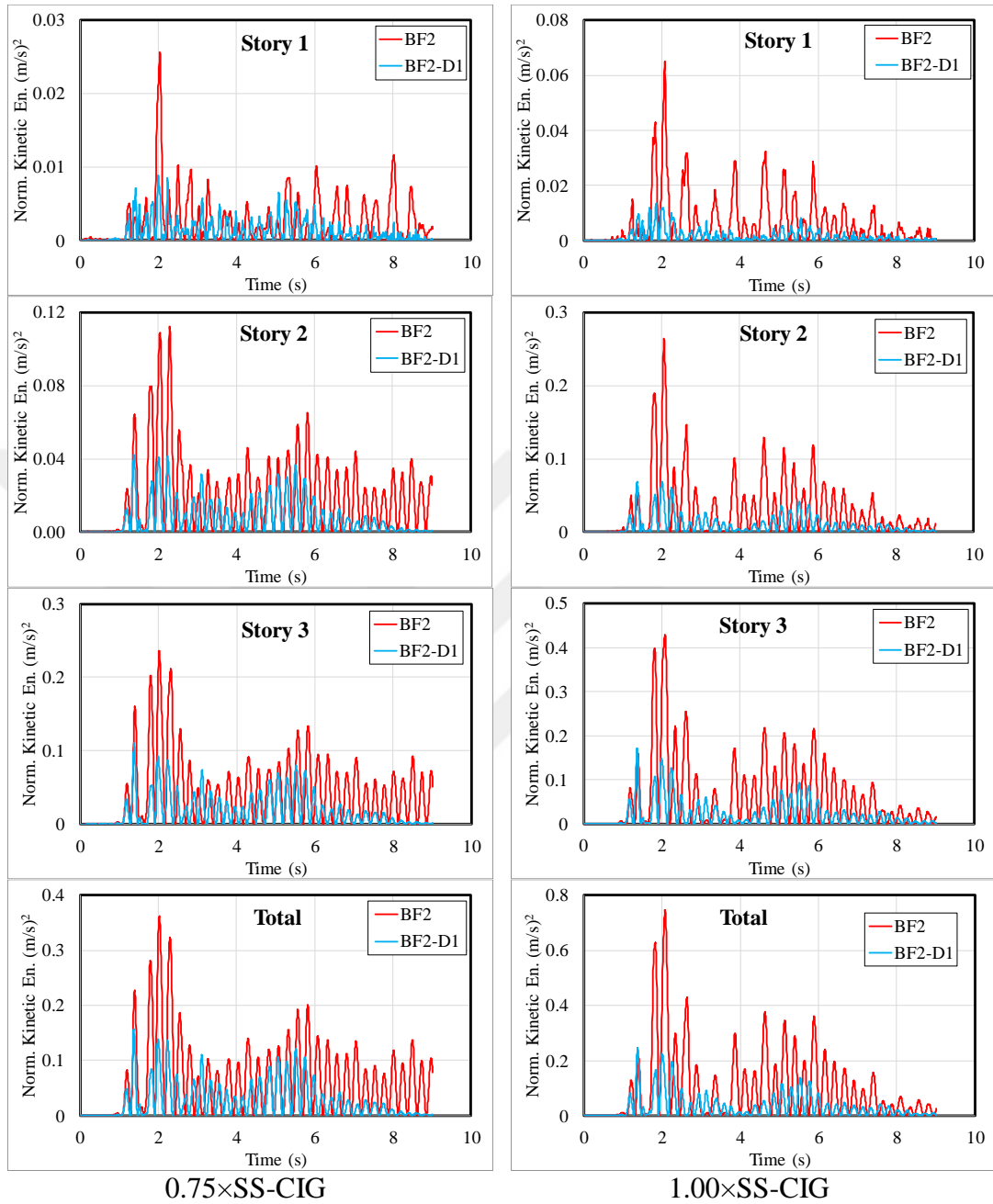


**Figure 2.88 :** Comparison for normalized kinetic energies of *BF2* and *BF2-D1*.

The normalized elastic strain energy that is another elastic energy term is compared between the bare and retrofitted cases in Figure 2.89. It is obvious that the damper also decreased the elastic strain energy.

The normalized damping energy of *BF2-D1* is relatively low compared with *BF2* and that is similar to the previous case, Figure 2.90. It may be attributed to the decrement of storey velocities, equation 1.2.

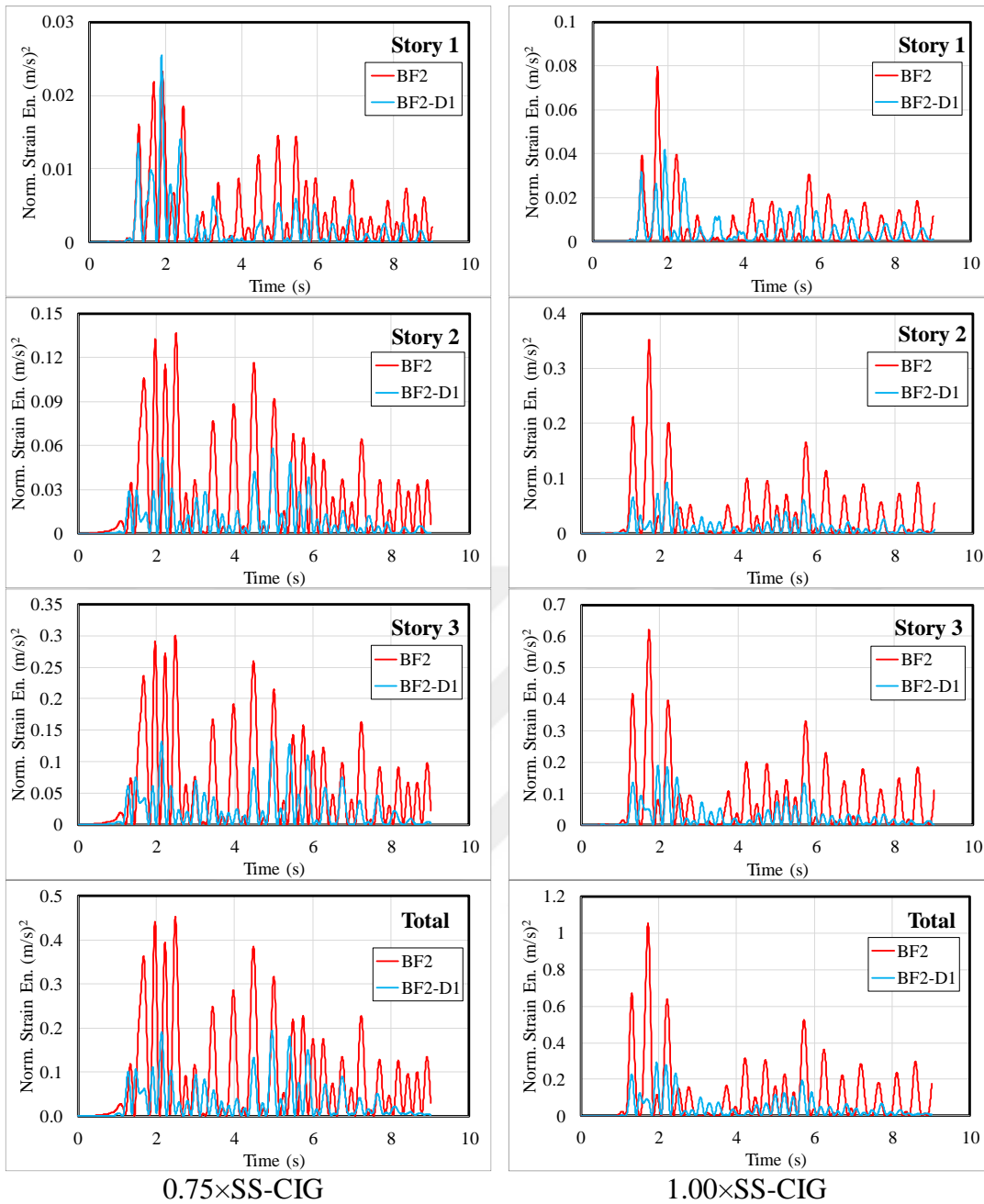


**Figure 2.89 :** Comparison for elastic strain energies of *BF2* and *BF2-D1*.

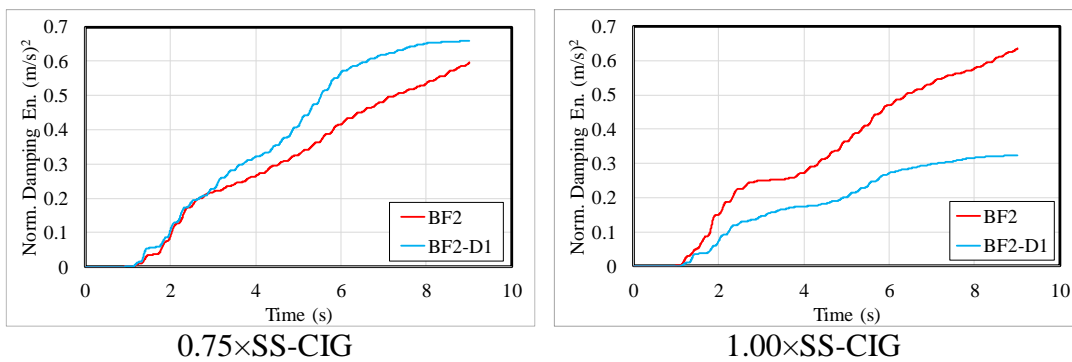


**Figure 2.90 :** Comparison for damping energies of *BF2* and *BF2-D1*.

The normalized plastic energy of the retrofitted case (*BF2-D1*) is relatively smaller than that of the bare frame (*BF2*), Figure 2.91. Also the main part of the plastic energy is generated by the damper in the retrofitted case.

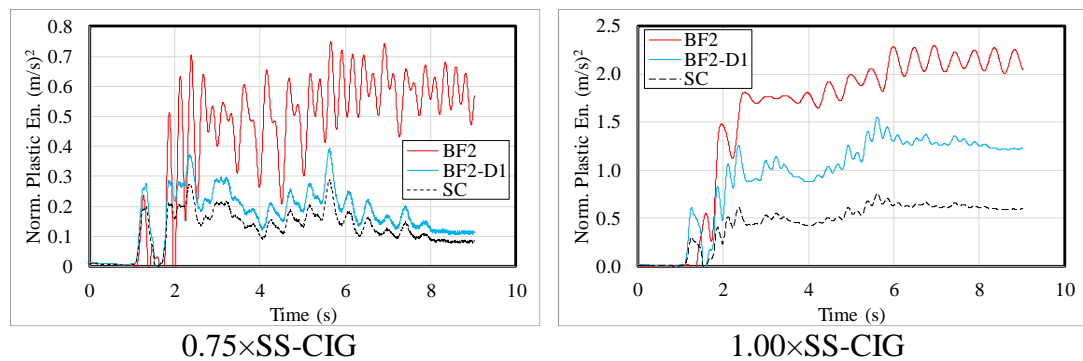


**Figure 2.91 :** Comparison for plastic energies of *BF2* and *BF2-D1*.

#### 2.4 Representation of MDOF response through SDOF system responses

Uang and Bertero (1990) proposed two types of energy equations in their pioneer study. They are relative and absolute input energies and are calculated by using the relative and absolute storey responses.

They performed shake table tests on a 0.3 scaled, six-storey, steel braced frame to determine the energy terms experimentally, Figure 2.92. The results were compared with the analytical predictions made on the equivalent *SDOF* system, see Figure 1.1. The comparative results displayed a quite satisfactory consistency. They concluded that the absolute input energy of an *MDOF* system can be predicted by means of the absolute input energy spectra of a *SDOF* system for the tested specimen.

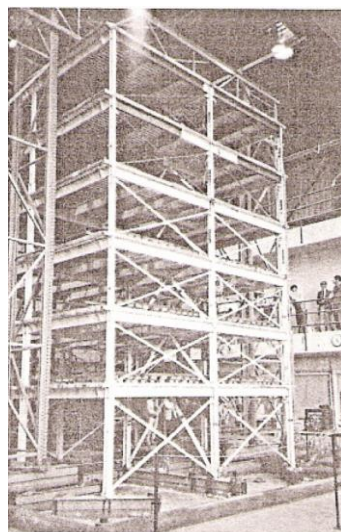


**Figure 2.92 :** Testing specimen of the Uang and Bertero (1990).

On the opposite side, Shen and Akbaş (1999) investigated seismic input energy demand of steel moment resisting frames (3, 6, 10 storeys and 4, 8 spans). The numerical analyses were performed by using 6 *EQ* record. The results of the numerical analyses were compared with the various input energy estimations made for the *SDOF* systems. The study results that the usage of *SDOF* systems to predict seismic energy intensities of *MDOF* systems has some limitations when the concept extended to the realistic structural systems. Correlation between the results of time history analyses and the methods based on *SDOF* systems fluctuates intensely.

Since there is a lack of available experimental data on relative seismic input energies of *SDOF* and *MDOF* systems in the literature, results of the experimental studies performed in this thesis are valuable in enabling the comparisons.

1.00×*SS-CIG* was utilized in the comparative study. The algorithm given in Chapter 4.2.2 is used to generate relative normalized input energy spectra for the specific damping ratios in *SDOF* systems. The damping ratio of the *SDOF* specimens is about 0.3% whereas the bare (*BF1* and *BF2*) and retrofitted (*BF1-D1* and *BF2-D1*) frames show about 3 and 5% damping, respectively. The experimental results are symbolized by circle, square and triangular dots on the analytically generated input energy spectra. There is good consistency between the experimental and analytical results, Figure 2.93.

Although the dominant periods of *SDOF* and *MDOF* specimens are very close to each other, it may not be possible to make a comparison between the experimental results because the systems had quite different damping ratios (*SDOF* systems 0.3%, *MDOF* systems 3 to 5%).

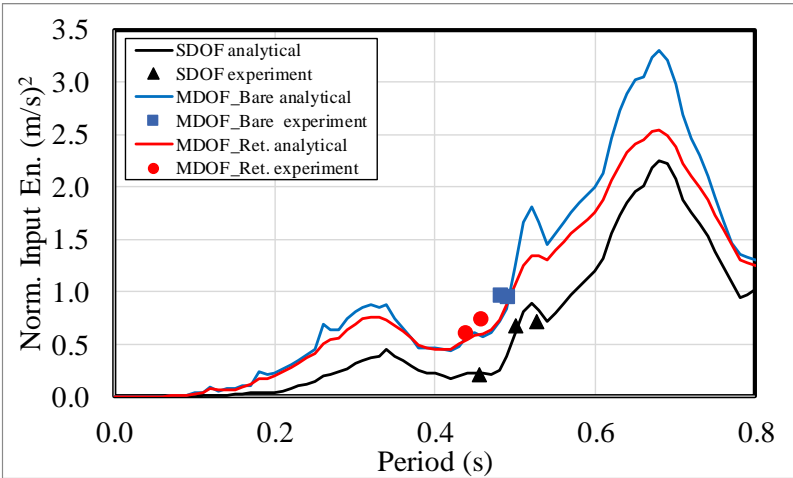


**Figure 2.93 :** The relative seismic input energy comparisons for *MDOF* and *SDOF* specimens.

Depending on the experimental results, the input seismic energy of *MDOF* system may be estimated from the proposed energy spectrum generated for *SDOF* system with the specific damping ratio.





### 3. NUMERICAL MODELS

The numerical *SDOF* and *MDOF* models of the tested specimens were generated and utilized in two different stages of the study. They are the ‘blind’ prediction phase and the evaluation of the test results. Henceforth, the refined models were utilized for the systems that were not be tested in the experimental part.

The numerical models were generated in Perform 3D software, since this has an interface for the definition of energy components. The program computes the seismic input energy and its components in the global scale. Hence, to reach the storey-based energy components, it is necessary to utilize a simple post-processing code by using the relative storey response histories produced by Perform 3D. The plastic energy component is displayed for the user selected member groups that is one of the crucial steps in the data preparation.

#### 3.1 Modelling Strategy

The specimens were represented by the frame elements in Perform 3D, Figure 3.1. Both of the frames are supported to the outside by the fixing supports. The self and supplementary masses of the specimens are represented by the masses concentrated on the frame joints.

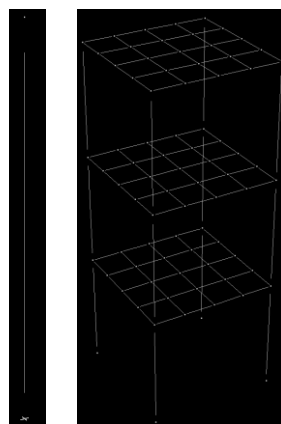


**Figure 3.1** : The generated numerical models.

The material tests results given in Table 2.2 were adopted to the numerical models. The material models of the structural members (beams and columns) are represented by symmetrical three parts linear force–displacement relation with strength decrement, Figure 3.2a. However, material behavior of the *SCs* are represented by the elastic perfectly plastic response model as it was proposed by Yüksel et al. 2018, Özkaynak et al. 2018, Güllü et al. 2015, Figure 3.2b.

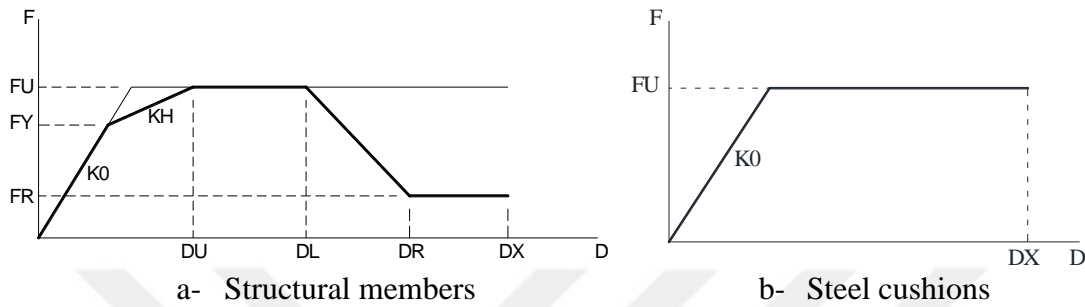


**Figure 3.2 :** Material models used for the tested elements.

Nonlinear behavior of the tested specimens was represented by the plastic hinge theory. The plastic hinges are assigned at both ends of the members. The hinge properties are defined by *fiber hinge* option of the program. The length of the plastic hinges is selected as  $2 \times h$ , where  $h$  is the sectional height, Figure 3.3a. Two representative examples are given here for the definition of sectional properties of beam (Figure 3.3b) and column type members (Figure 3.3c).

Geometric wise non-linearity is considered in the generated numerical models by using the “*P-Delta effect*” option of Perform 3D.

*SCs* that are used as metallic dampers in the study were represented in the numerical models by using *the rubber type isolater model* that is one of the available models in Perform 3D to represent the isolation and dissipative systems. The force-displacement response curves of *SCs* in the longitudinal and transversal directions are identical to *the rubber type isolater model*. The initial stiffness, the ultimate load and displacement capacities in the longitudinal direction are 0.1726 kN/mm, 0.7755 kN and 65 mm for the used *SCs*, respectively (Yüksel et al. 2018, Özkaynak et al. 2018). Initial stiffnesses in the transversal direction were defined as 0.5724 and 0.0438 kN/mm for compressive and tensile directions. Definition of these properties in the Perform 3D is depicted in Figure 3.4.

No.	Component Type	Component Name	Length	Propn
1	Column, Inelastic Fiber Section	ColInFib40/60/3		0.05
2	Column, Steel Type, Nonstandard Section	ColNss40/60/3		0.9
3	Column, Inelastic Fiber Section	ColInFib40/60/3		0.05

a- Assigning the fiber plastic hinges on a structural element (Compound)

No.	Type	Material Name	Area	Axis 2 Coord
1	Steel	InSt40/60/3	60	29.25
2	Steel	InSt40/60/3	60	27.75
3	Steel	InSt40/60/3	54	22.5
4	Steel	InSt40/60/3	54	13.5
5	Steel	InSt40/60/3	54	4.5
6	Steel	InSt40/60/3	54	-4.5
7	Steel	InSt40/60/3	54	-13.5
8	Steel	InSt40/60/3	54	-22.5
9	Steel	InSt40/60/3	60	-27.75
10	Steel	InSt40/60/3	60	-29.25

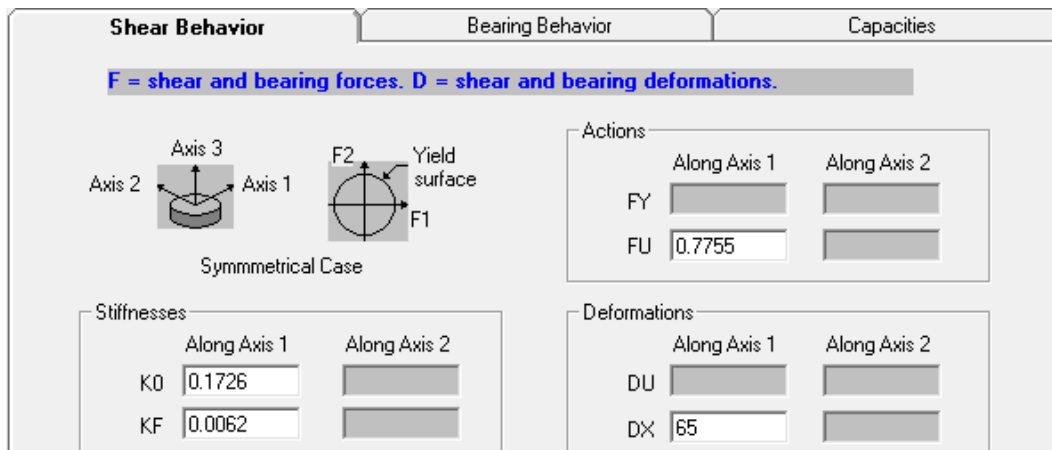
b- Fiber definition for a typical beam section

STRUCTURAL FIBER LIST (MAX 60) Click to highlight row for Insert, Replace or Delete.					
No.	Type	Material Name	Area	Axis 2 Coord	Axis 3 Coord
33	Steel	InSt40/60/3	13.5	-13.5	17.75
34	Steel	InSt40/60/3	13.5	-13.5	19.25
35	Steel	InSt40/60/3	13.5	-22.5	-19.25
36	Steel	InSt40/60/3	13.5	-22.5	-17.75
37	Steel	InSt40/60/3	13.5	-22.5	17.75
38	Steel	InSt40/60/3	13.5	-22.5	19.25
39	Steel	InSt40/60/3	2.25	-27.75	-19.25
40	Steel	InSt40/60/3	2.25	-27.75	-17.75
41	Steel	InSt40/60/3	15	-27.75	-12
42	Steel	InSt40/60/3	21	-27.75	0
43	Steel	InSt40/60/3	15	-27.75	12
44	Steel	InSt40/60/3	2.25	-27.75	17.75
45	Steel	InSt40/60/3	2.25	-27.75	19.25
46	Steel	InSt40/60/3	2.25	-29.25	-19.25
47	Steel	InSt40/60/3	2.25	-29.25	-17.75
48	Steel	InSt40/60/3	15	-29.25	-12
49	Steel	InSt40/60/3	21	-29.25	0
50	Steel	InSt40/60/3	15	-29.25	12
51	Steel	InSt40/60/3	2.25	-29.25	17.75
52	Steel	InSt40/60/3	2.25	-29.25	19.25

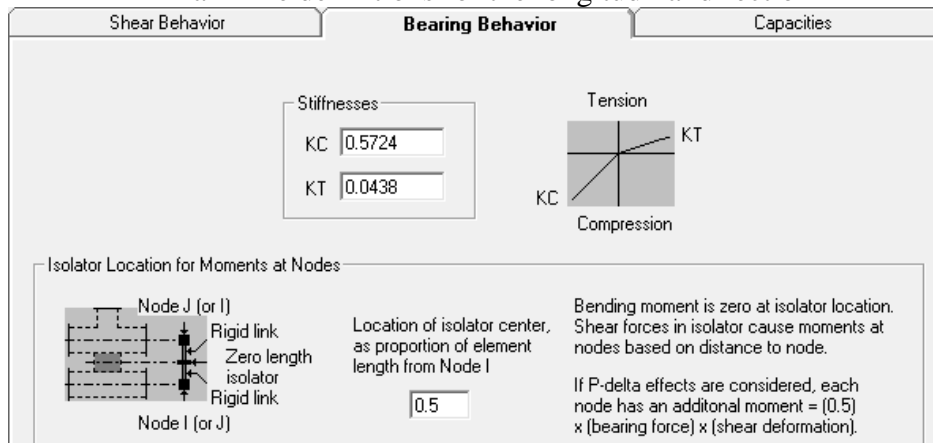
c- Fiber definition for a typical column section

**Figure 3.3** : Definition of the sectional properties in Perform 3D.

In the nonlinear time history analyses, the acceleration records gathered on the shake table were utilized to simulate the effect of *EQ*.



a- The definitions for the longitudinal direction



b- The definitions for the transversal direction

**Figure 3.4 : Modelling SCs in Perform 3D.**

## 3.2 Comparison of the Response Parameters

### 3.2.1 Response of the *SDOF* specimens

The comparisons between numerical and experimental responses of elastic *SDOF* specimens with the natural periods of 0.385, 0.526 and 0.667 s are illustrated to evaluate the success of the generated numerical models. The relative top acceleration, velocity and displacement histories obtained from the experimental and numerical works are presented in Figures 3.5 and 3.6 for two specific *EQs*.

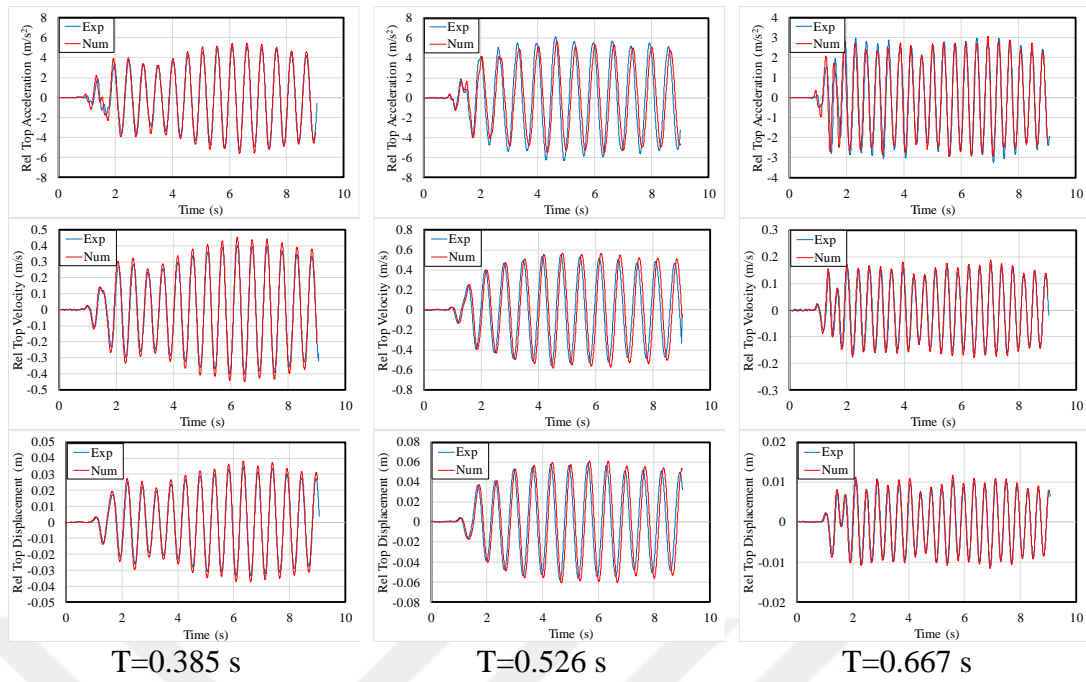


**Figure 3.5 :** Experimental and numerical response comparisons for  $0.25 \times SS-CIG$ .

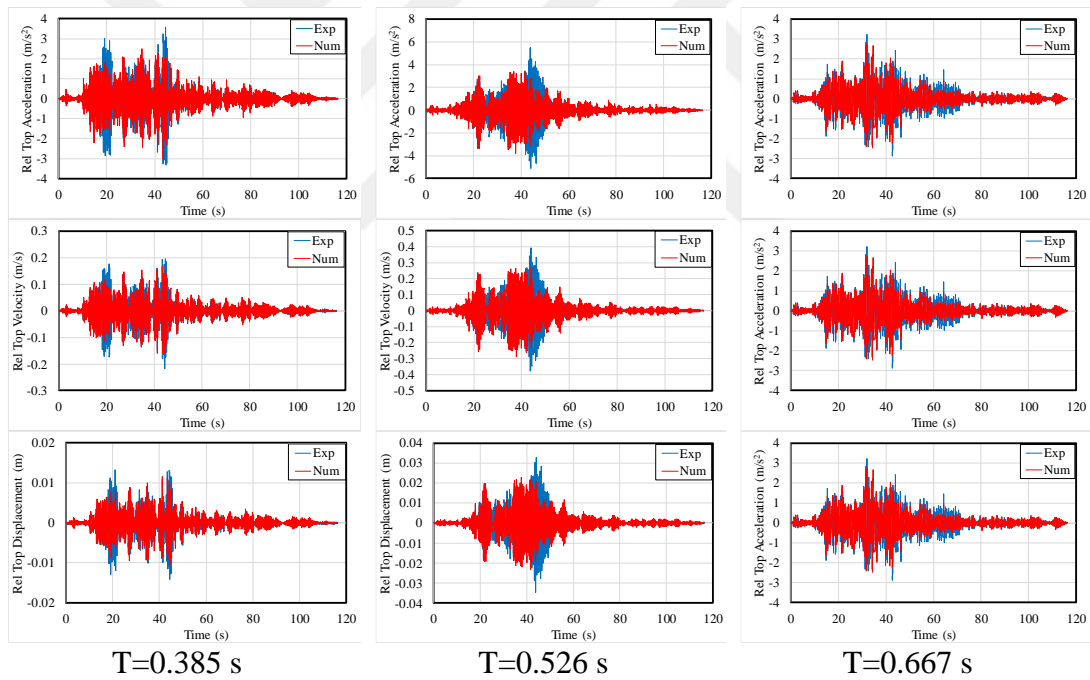


**Figure 3.6 :** Experimental and numerical response comparisons for  $0.25 \times CH-N10E$ .

Although there is a solid consistency between the numerical and experimental results for  $SS-CIG$ , partial deviations may be obtained in  $CH-N10E$ . It may be attributed to the unusual frequency content of  $CH-N10E$ , see Figure 2.26.

The similar comparisons were performed for the specimens running in the inelastic range. Some extent of discrepancy was observed between the experimental and

numerical results, Figures 3.7 and 3.8. It is understandable that the attached safety rope had some effects on the structural response components, Chapter 2.2.3.

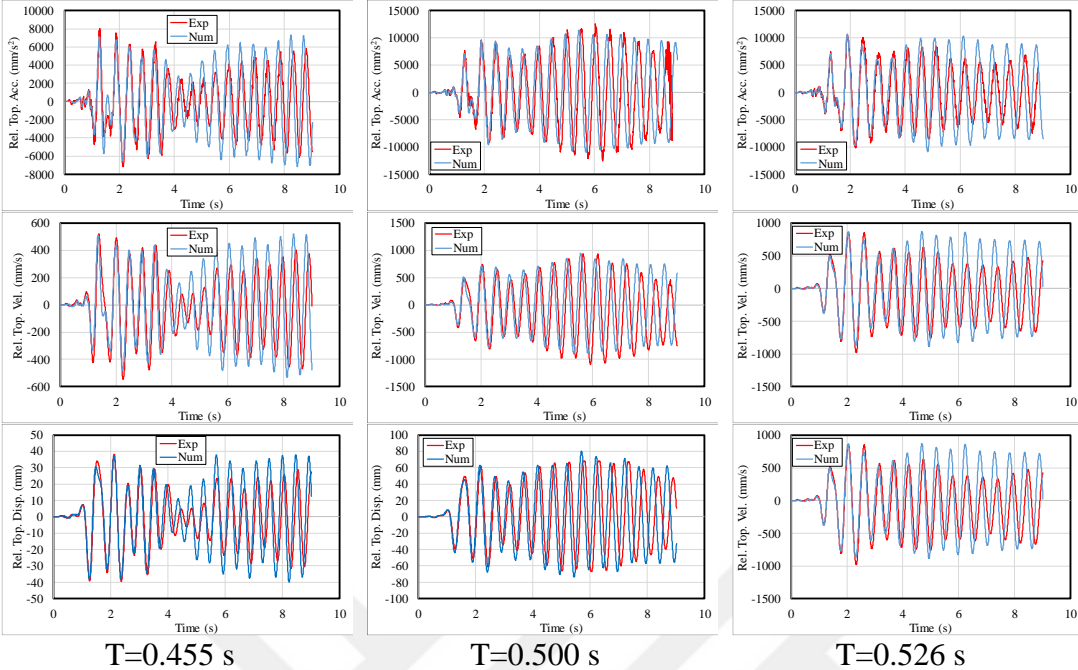


**Figure 3.7 :** Comparisons of the relative response components.

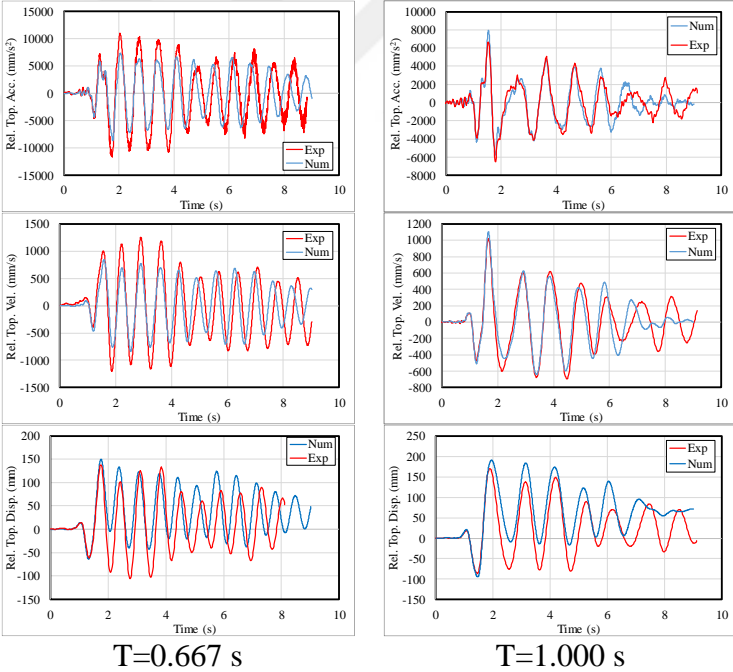


**Figure 3.8 :** Comparisons of the relative response components.

The inconsistency is more remarkable for the specimen with longer periods.

### 3.2.2 Response of the *MDOF* specimens

The relative response components of each *MDOF* specimens are compared between the experimental and numerical results.

The storey response components of *BF1* are compared with the numerical results in Figures 3.9 and 3.10.

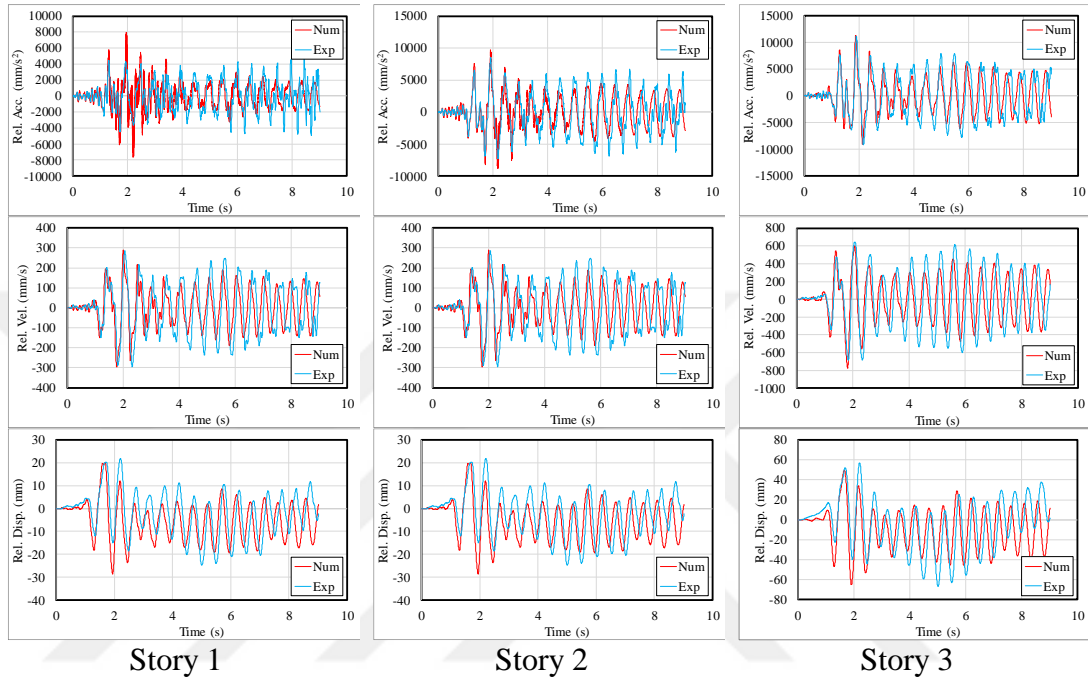


**Figure 3.9 :** Comparison of the storey responses of *BF1* for  $0.75 \times SS-CIG$ .

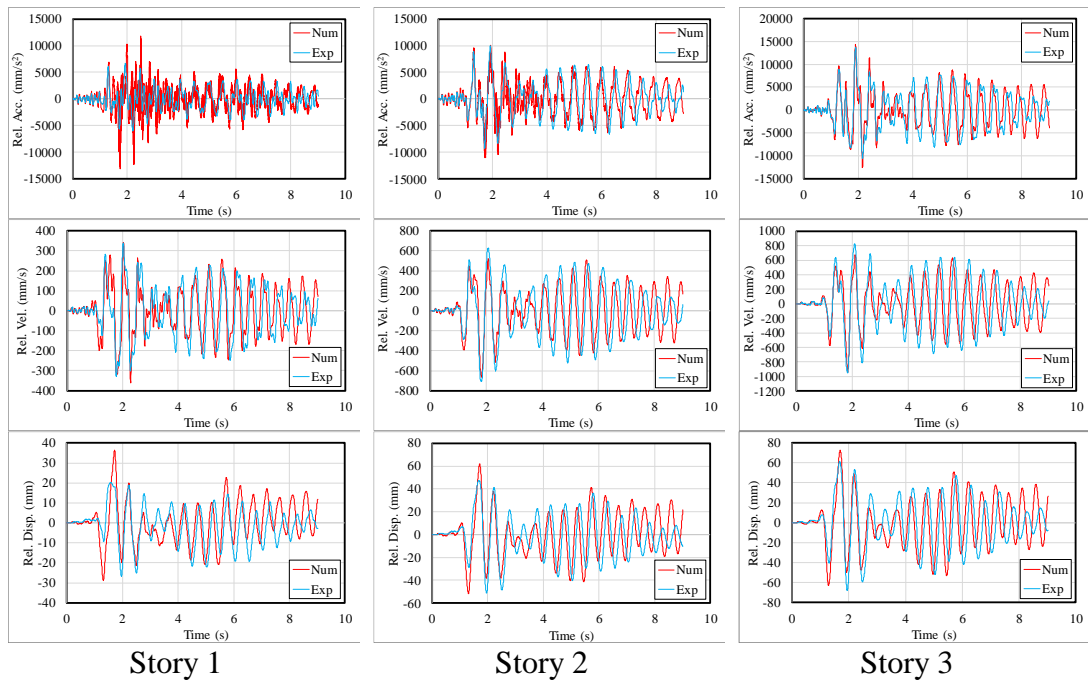


**Figure 3.10 :** Comparison of the storey responses of *BF1* for  $1.00 \times SS-CIG$ .

Subsequently, experimentally and numerically obtained storey responses of *BF1-D1* are compared with each other, Figures 3.11 and 3.12. Displacement of the 1<sup>st</sup> storey could not be obtained.

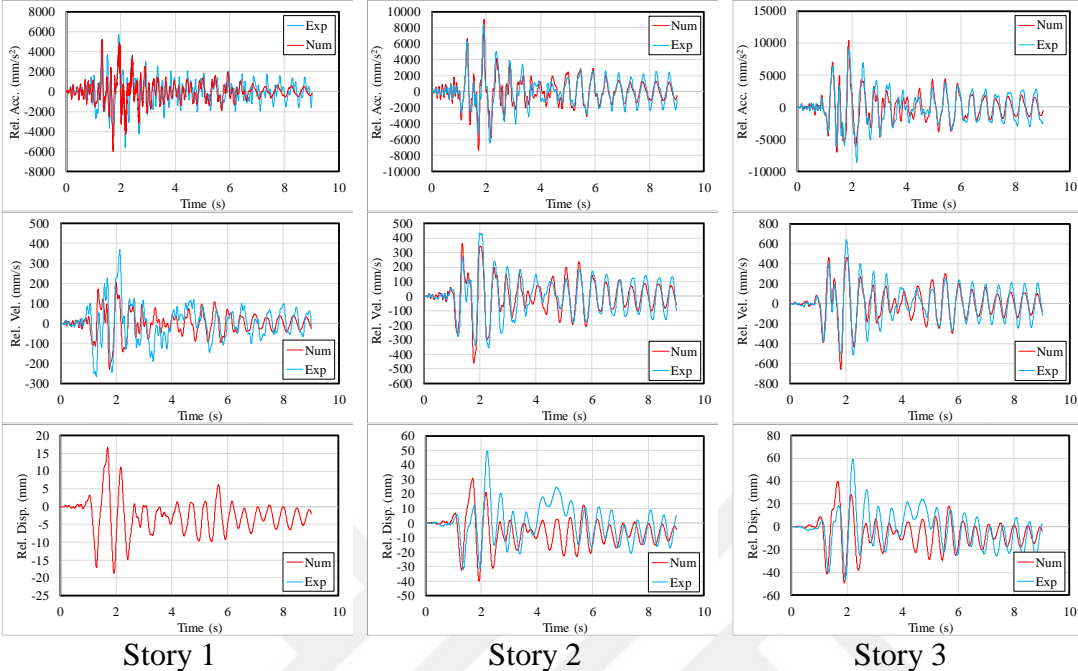


**Figure 3.11 :** Comparison of the storey responses of *BF1-D1* for 0.75×SS-CIG.

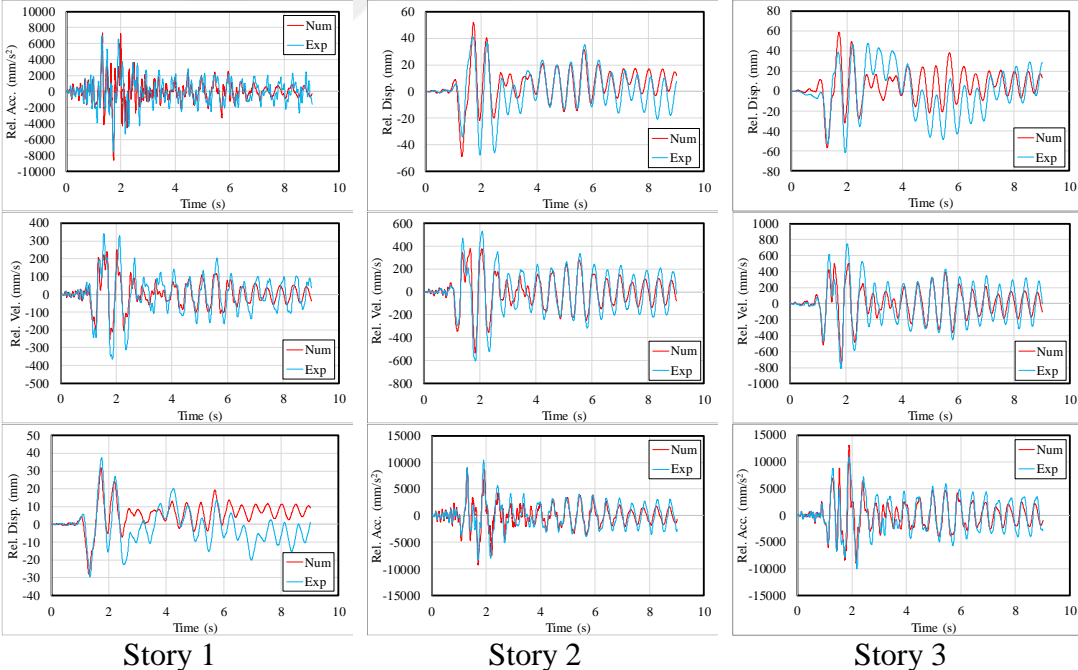


**Figure 3.12 :** Comparison of the storey responses of *BF1-D1* for 1.00×SS-CIG.

Numerical analyses performed for *BF2* are compared with the experimental results, in Figures 3.13 and 3.14. Similar to the previous specimens, displacement of the 1<sup>st</sup> storey could not be computed.

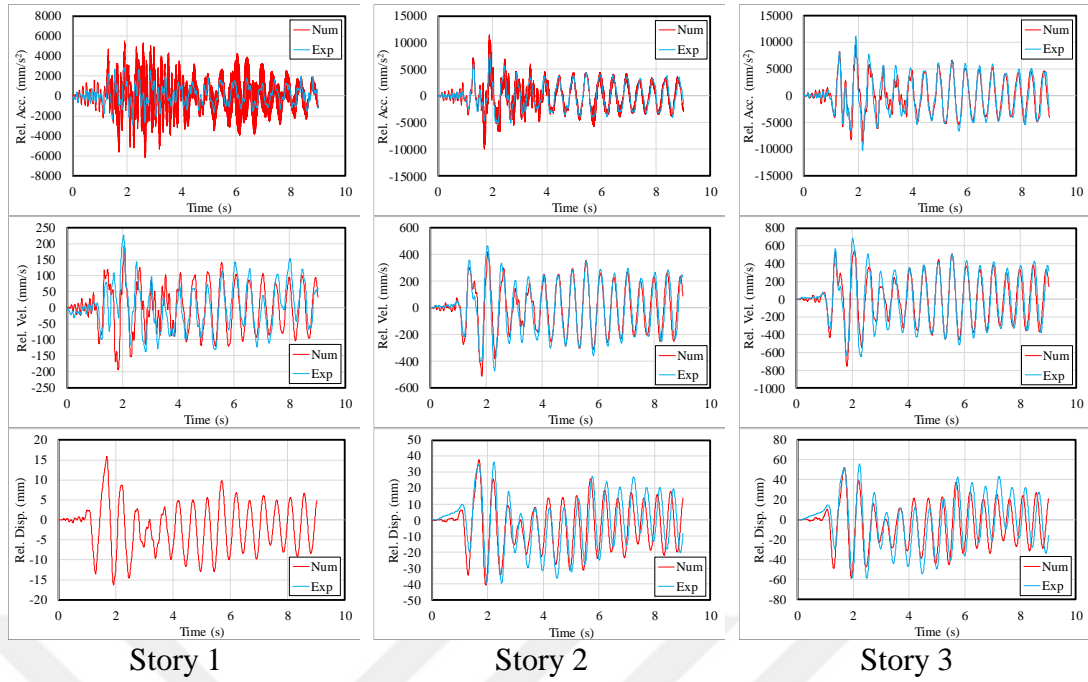


**Figure 3.13 :** Comparison of the storey responses of *BF2* for  $0.75 \times SS-CIG$ .

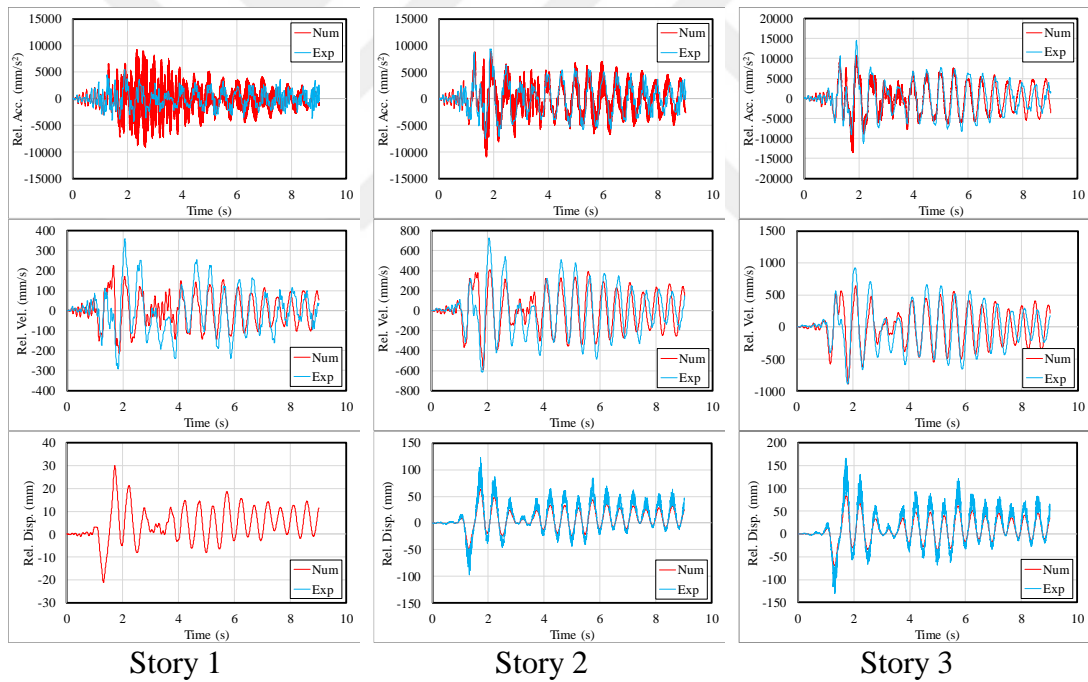


**Figure 3.14 :** Comparison of the storey responses of *BF2* for  $1.00 \times SS-CIG$ .

Finally, the results of *BF2-DI* are compared in Figures 3.16 and 3.17.

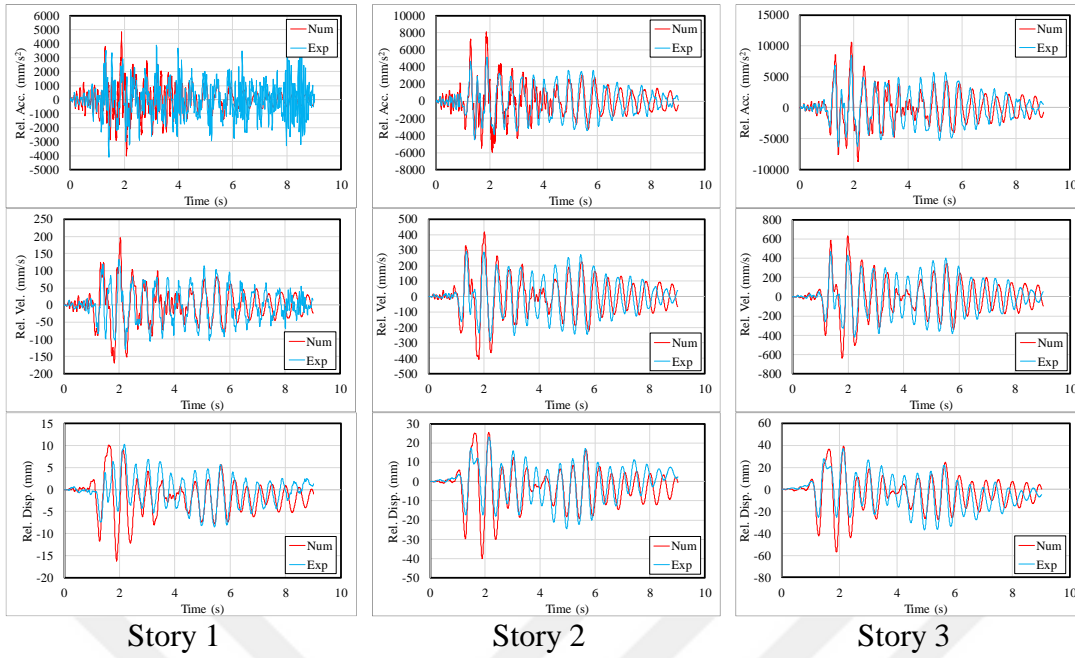


**Figure 3.15 :** Comparison of the storey responses of *BF2-D1* for  $0.75 \times SS-CIG$ .

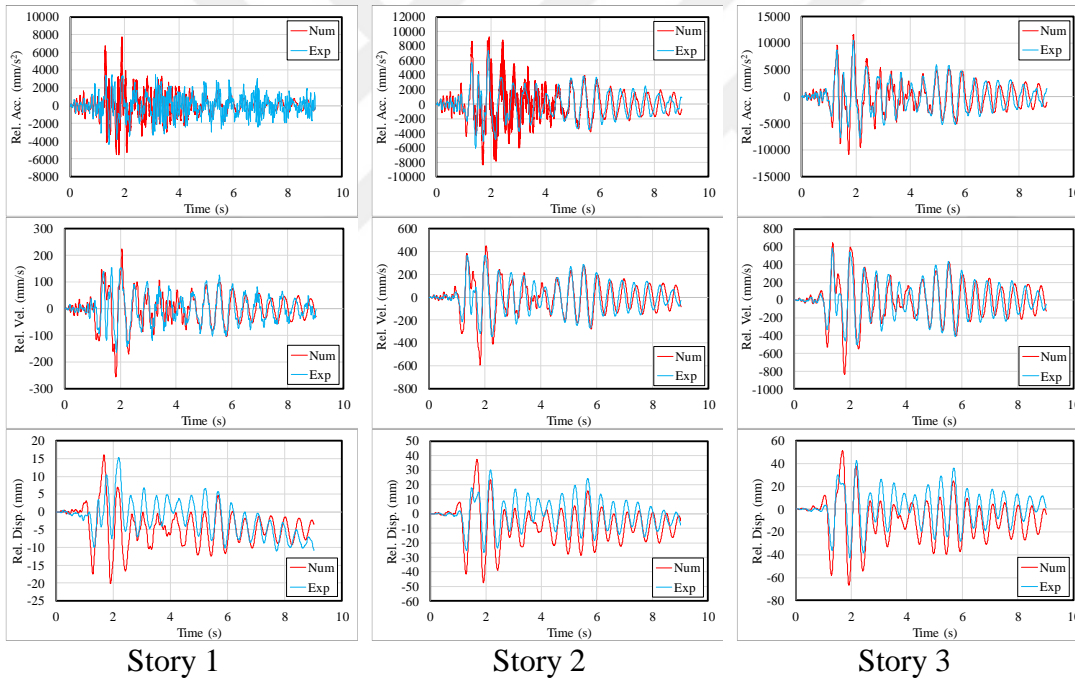


**Figure 3.16 :** Comparison of the storey responses of *BF2-D1* for  $1.00 \times SS-CIG$ .

All the experimental responses are reproduced quite satisfactorily by the generated numerical models. Although there are some inconsistencies in some graphics, the general pathways are substantially reliable. Consequently, the generated numerical models are sufficiently reliable to be employed in further studies.

### 3.3 Comparison of the Seismic Energy Components

It has been taken considerable effort to compare the seismic energy components reached in the experimental and numerical studies for the specimens. It should be defined that, since the energy terms are quadratically depended to the structural response components, the uneven form of the experimental response quantities may cause larger discrepancies in the seismic energy components.

#### 3.3.2 Energy components of the *SDOF* specimens

Seismic energy terms of elastic *SDOF* specimens are compared in Figures 3.17, 3.18 and 3.19. Since the specimen remained in the elastic range, total seismic input energy consists of damping, kinetic and elastic strain energy components. The comparisons were made for the specimens with 0.385, 0.526 and 0.667 s natural periods.

The experimental results were satisfactorily reproduced by the numerical models for both *EQ* records. The contribution of kinetic and elastic strain energies to total seismic input energy is larger for 0.25×*SS-CIG*, whereas the damping energy was the major energy component for 0.25×*CH-N10E*. The contribution of the elastic energy terms are relatively smaller for 0.25×*CH-N10E*.

Even though some discrepancies exist for the elastic energy terms of *CH-N10E*, relatively good correlation is obtained for the damping and input energies. Similar to the preceding case, elastic strain energy and kinetic energy are dominant for 0.25×*SS-CIG* and damping energy is the leading term for 0.25×*CH-N10E*.

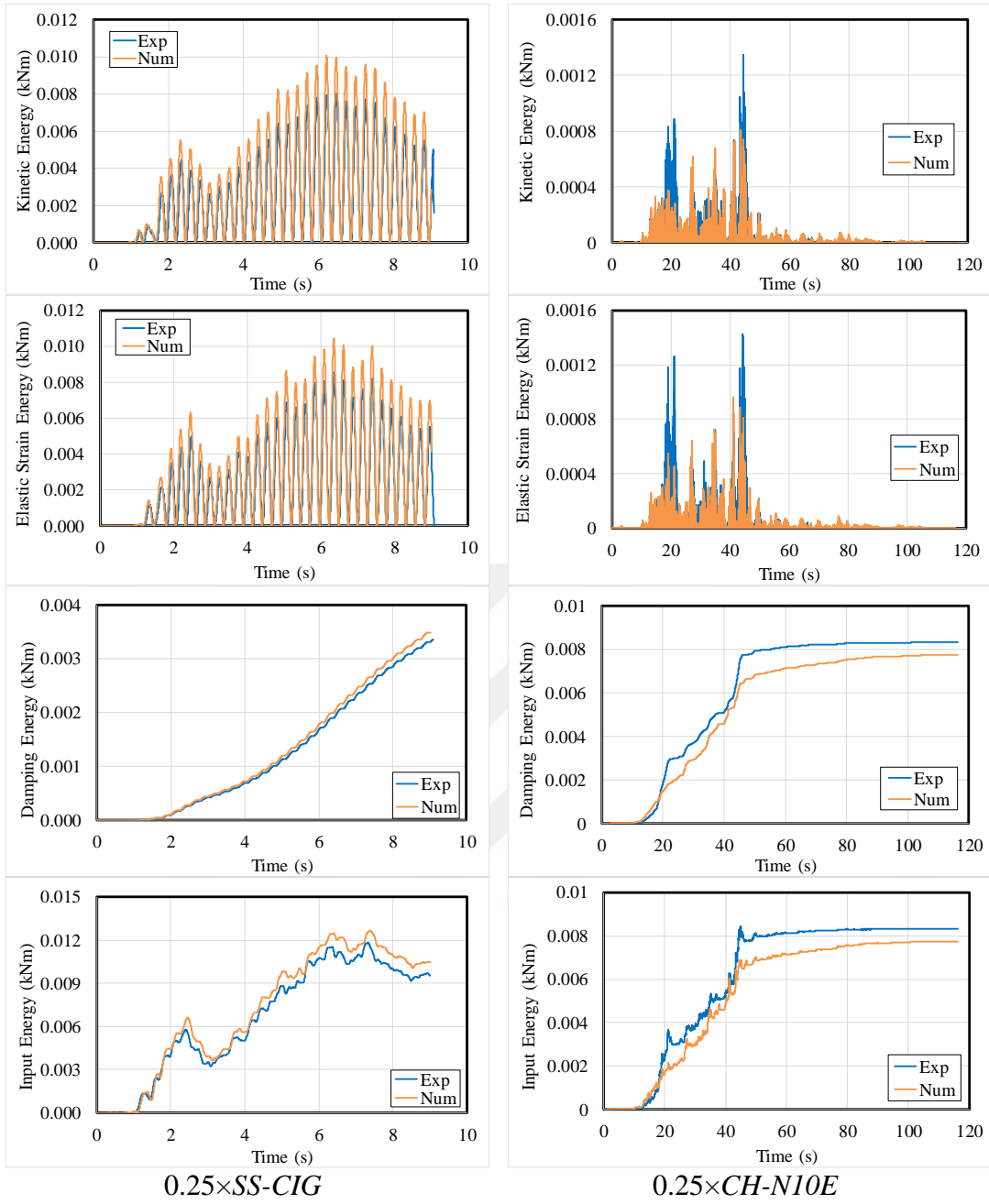


**Figure 3.17** : Energy comparisons for *SDOF* specimen having 0.385 s period.

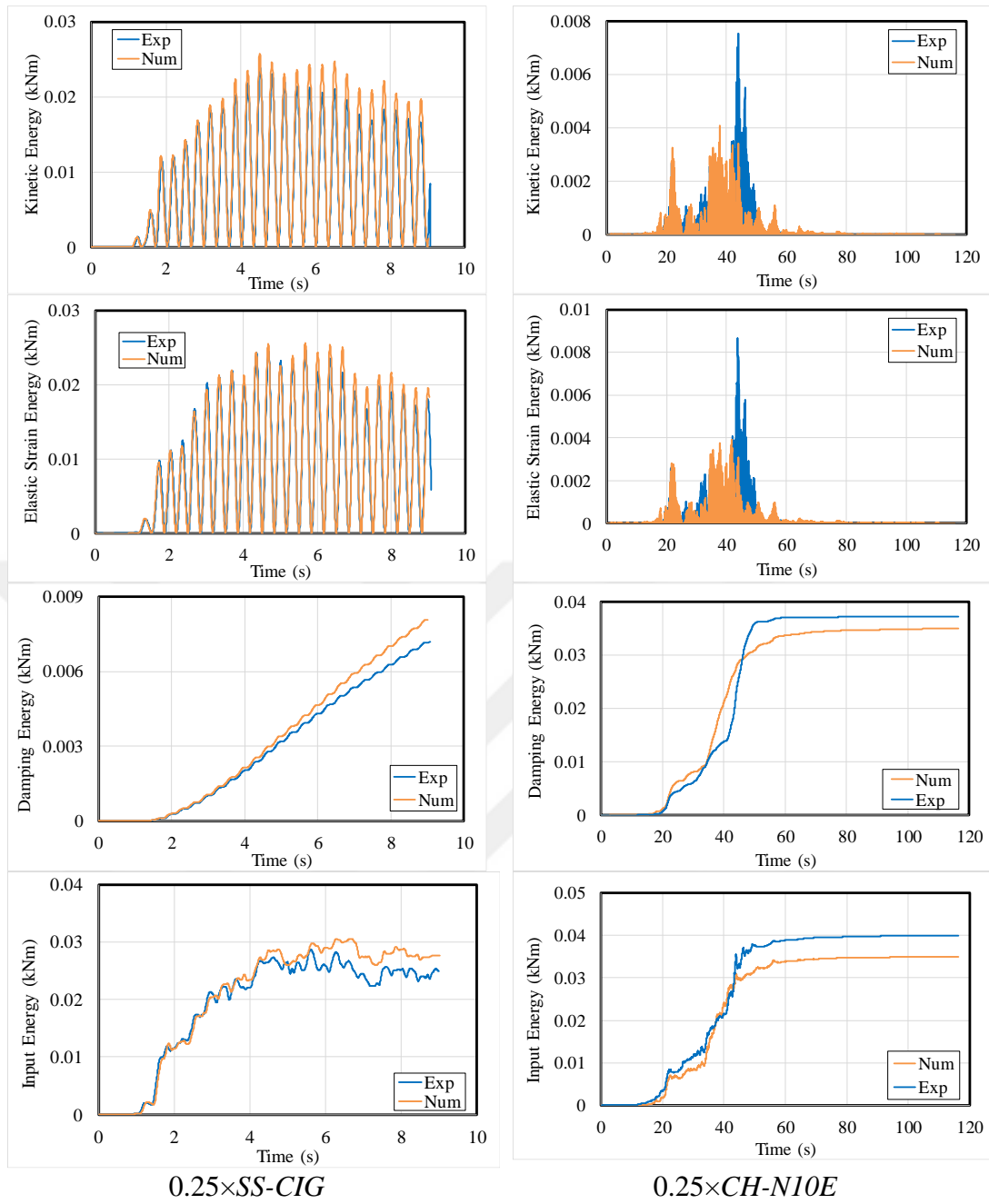


**Figure 3.18** : Energy comparisons for *SDOF* specimen having 0.526 s period.

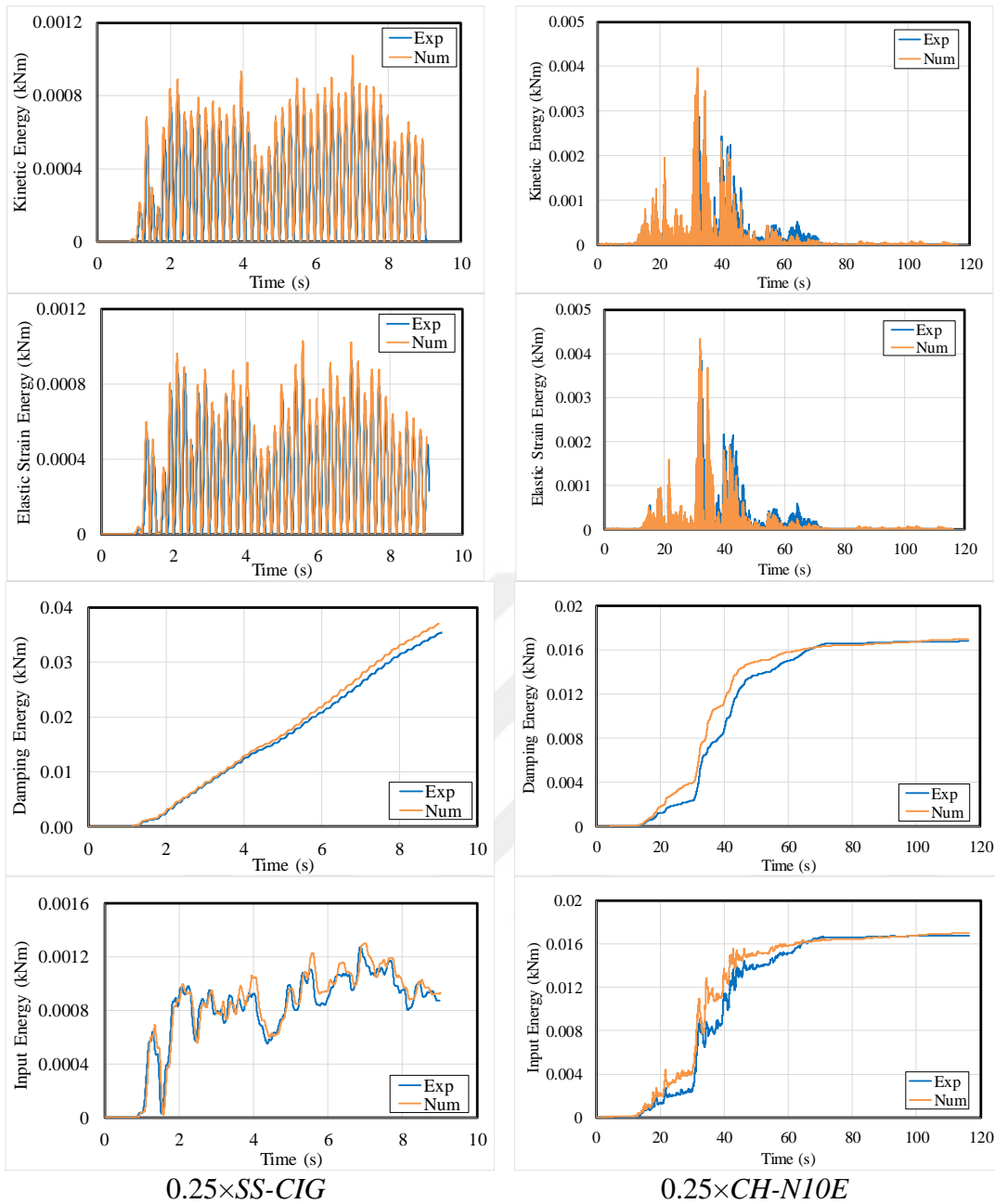


**Figure 3.19** : Energy comparisons for *SDOF* specimen having 0.667 s period.

For both of the *EQ* records, the greater part of the input energy is balanced by the damping energy component.

It may also be considered that the total seismic input energy is greater for the specimen with 0.385 s period for the 0.25×*SS-CIG* record. Conversely, *CH-N10E* produced higher energies for the other specimens. Therefore, not only the *EQ* record but also the period of the specimen have an effect on the intensity of the seismic input energy.

Similar energy comparisons are also presented for the specimens tested in the inelastic range. Seismic input energy and the other energy components of the specimens with 0.500, 0.526 and 0.667 s periods are represented in Figure 3.20.

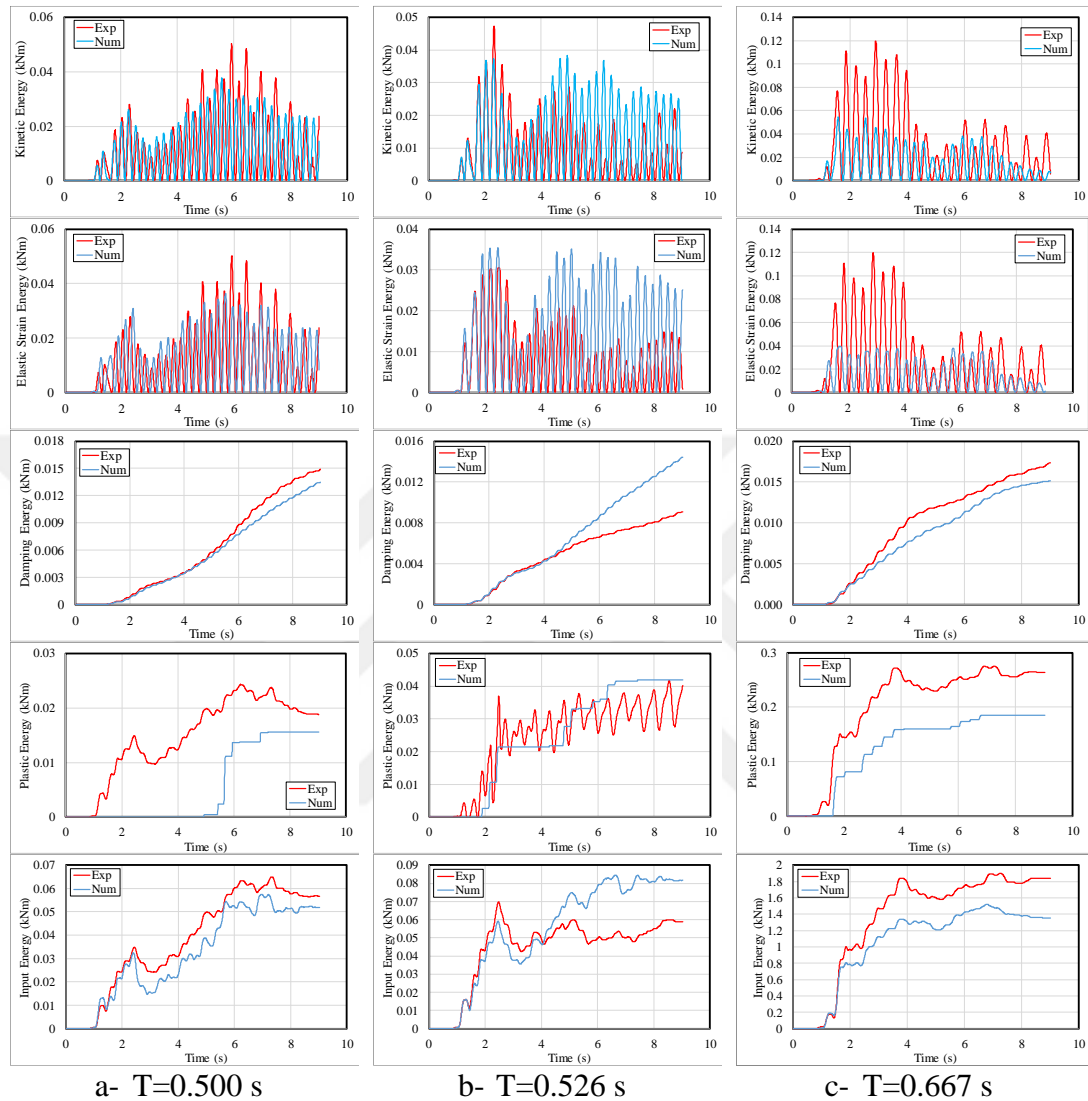


**Figure 3.20** : Seismic energy plots for *SDOF* specimen tested in inelastic range.

The energy terms are satisfactorily matched with each other. The differences in some storey response components reproduce to some extent of the discrepancies in the energy terms.

### 3.3.1 Energy components of the *MDOF* specimens

The energy components of the *MDOF* specimens are compared here. Since *Perform 3D* computes energy terms for the global structure, the total energy comparisons will be achieved.

Initially, mass-normalized energy components belonging to *BF1* are illustrated in Figure 3.21. The numerical results satisfactorily match with the experimental ones.

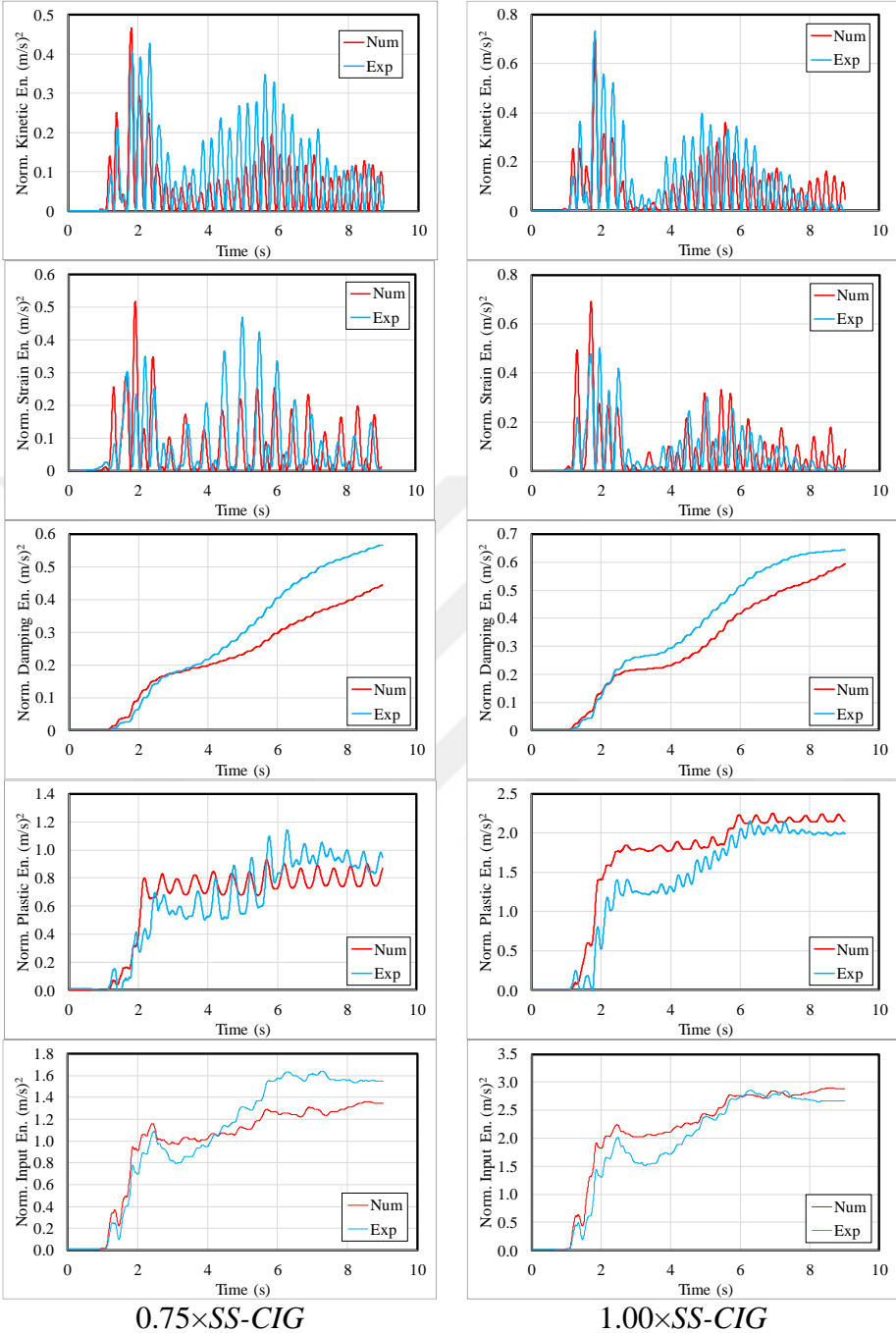


**Figure 3.21** : Energy comparisons for *BF1*.

Similar comparisons are also made for *BF1-D1*. Prediction of the numerical modes in terms of seismic energy shows good agreement with the experimental results, Figure 3.22.

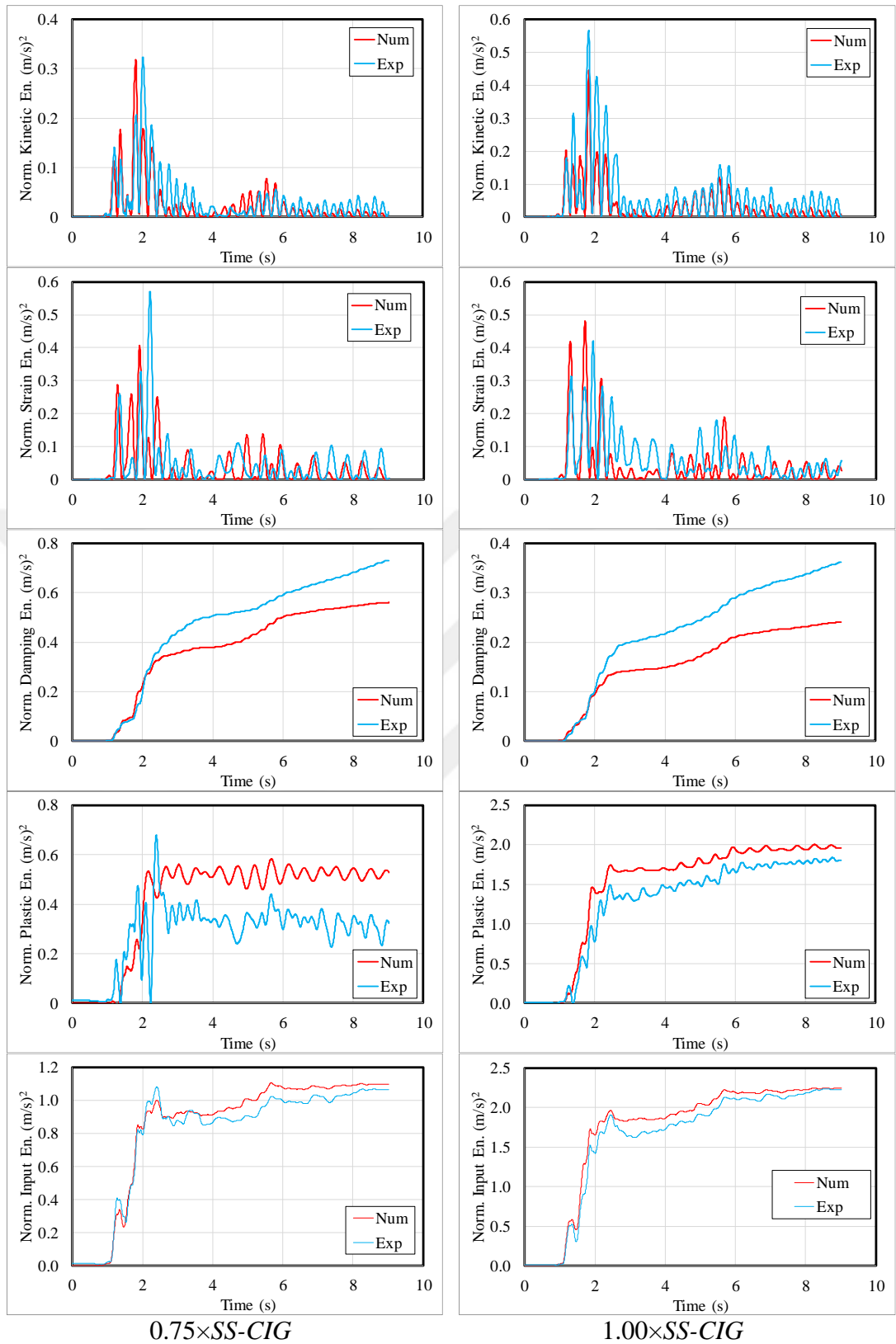


**Figure 3.22** : Energy comparisons for *BF1-D1*.

Energy plots for *BF2* are illustrated in Figure 3.23. Similarly, experimentally obtained energy terms are predicted reasonably closely by the generated numeric models.

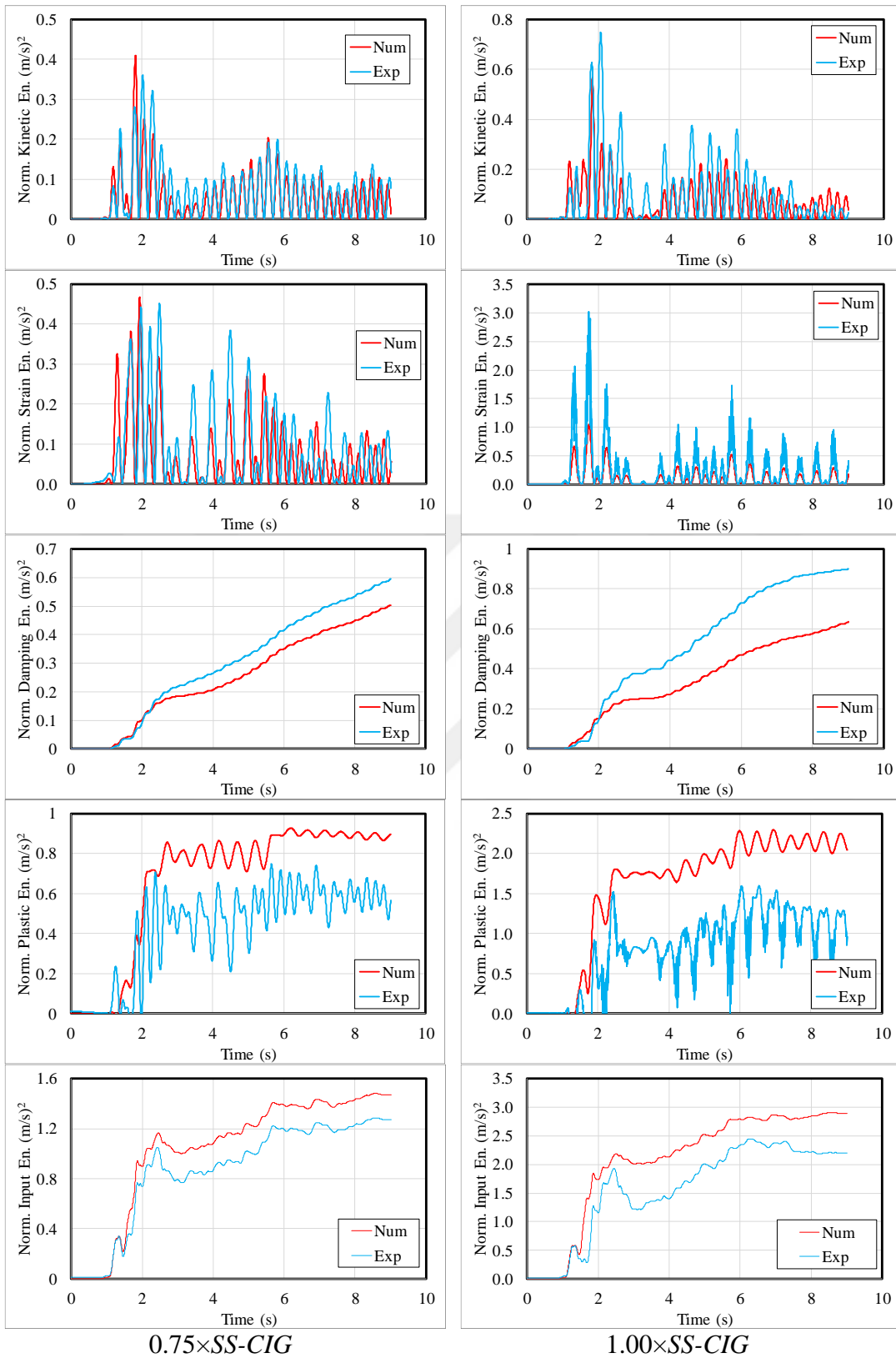


**Figure 3.23 :** Energy comparisons for *BF2*.

Finally, experimentally and numerically generated seismic energy components of *BF2-D1* are compared with each other. Again, the numerical models satisfactorily predicted the experimental behavior, Figure 3.24.

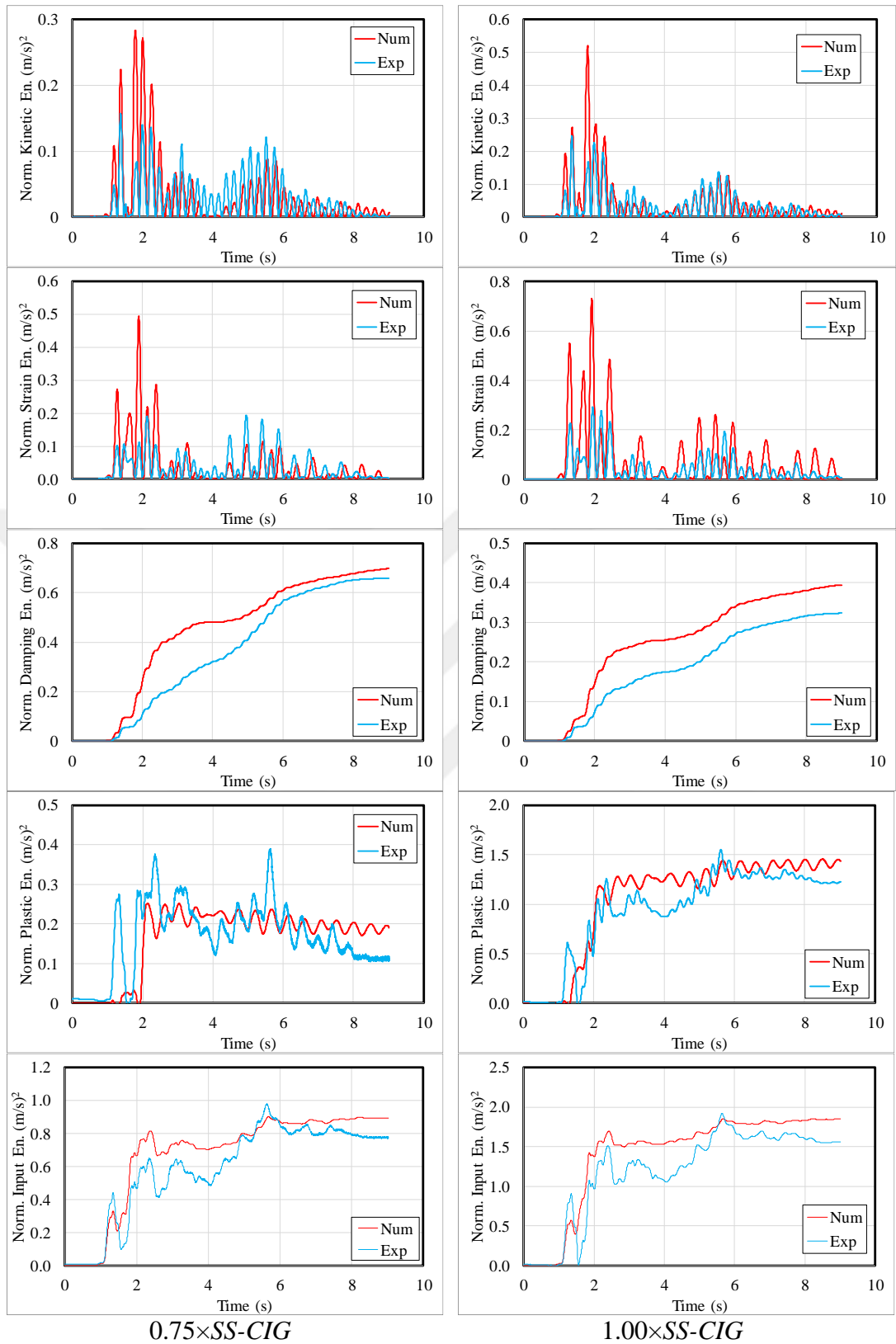


**Figure 3.24** : Energy comparisons for *BF2-D1*.

### 3.4 The Response Control of *MDOF* Systems by Alternative Implementation of *SCs*

Since the generated numerical models reasonably predict the experimental response parameters and energy components, some supplementary numerical analyses were performed to illustrate the response control of *MDOF* systems. Additionally, the *SCs* used as a metallic damper in this study were implemented in three different ways. The first one has two *SCs* at the first storey that is the most closely similar one to the tested specimen. The second one has three *SCs* in the same location. The last one has one additional *SCs* at second and third storeys. The structural configurations of the numerical models are illustrated in Figure 3.25.

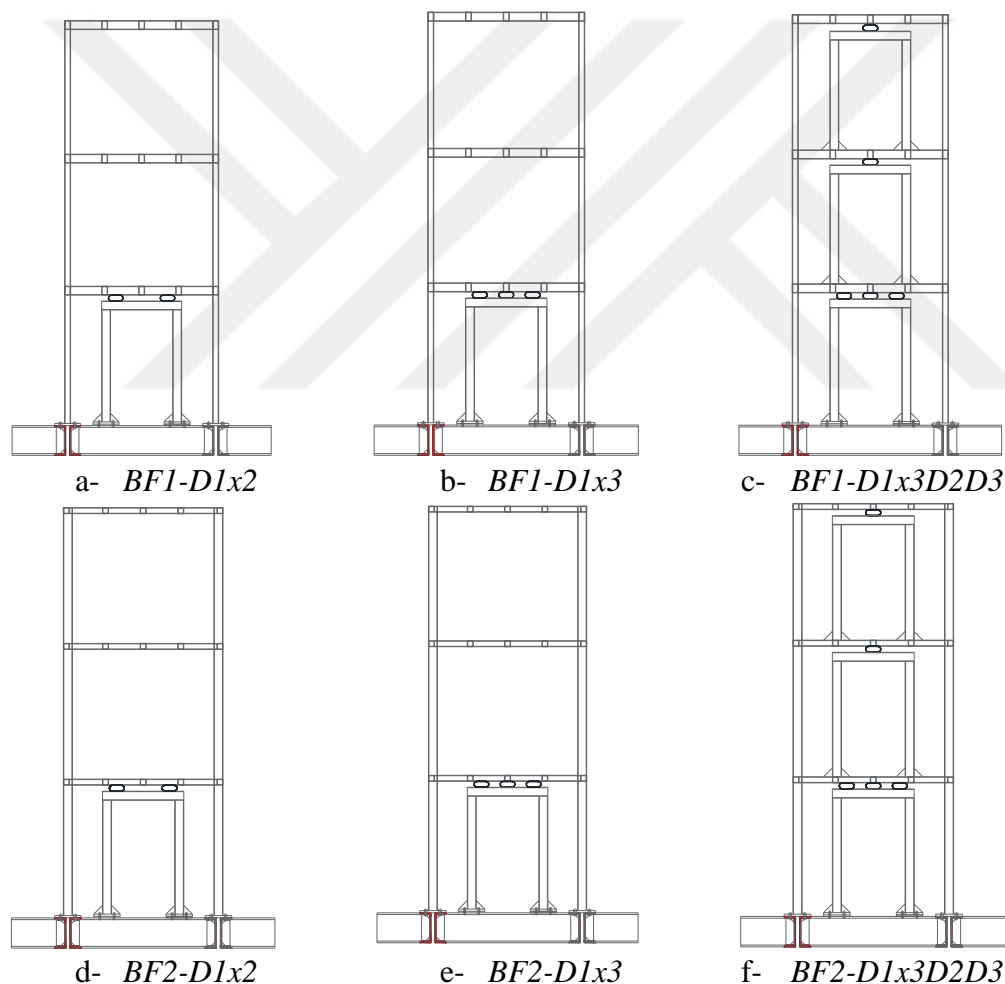


**Figure 3.25 :** Some alternative *SC* implementations for the response control.

Natural vibration periods obtained from free vibration analyses of the frames are listed in Table 3.1. The aim was to keep the natural frequencies close to those of the bare

frame. However, some amount of decrement is indispensable for the systems retrofitted at the second and third floors.

**Table 3.1 :** Natural vibration periods of the alternative *MDOF* systems.

#	Specimen	Natural period (s)
1	<i>BF1</i>	0.477
2	<i>BF1-D1</i>	0.449
3	<i>BF1-D1x2</i>	0.434
4	<i>BF1-D1x3</i>	0.424
5	<i>BF1-D1x3D2D3</i>	0.376
6	<i>BF2</i>	0.475
7	<i>BF2-D1</i>	0.452
8	<i>BF2-D1x2</i>	0.434
9	<i>BF2-D1x3</i>	0.431
10	<i>BF2-D1x3D2D3</i>	0.365

The damping ratio of 5% was assumed in the nonlinear time history analyses of all the retrofitted specimens. Nevertheless, higher damping ratios are expected with the increment of the number of *SCs*.

The numerically obtained seismic energy components for the retrofitted systems are given in Table 3.2.

**Table 3.2 :** The energy components of the retrofitted frames.

Record scaling	$E_k$ (kNm)		$E_{es}$ (kNm)		$E_d$ (kNm)		$E_p$ (kNm)		$E_l$ (kNm)	
	0.75	1.00	0.75	1.00	0.75	1.00	0.75	1.00	0.75	1.00
<i>BF1-D1x2</i>	0.002	0.004	0.005	0.005	0.423	0.582	0.465	1.251	0.895	1.842
<i>BF1-D1x3</i>	0.002	0.004	0.005	0.006	0.396	0.546	0.379	1.050	0.783	1.606
<i>BF1-D1x3D2D3</i>	0.002	0.003	0.005	0.007	0.317	0.419	0.460	1.020	0.783	1.447
<i>BF2-D1x2</i>	0.002	0.004	0.008	0.008	0.402	0.565	0.441	1.198	0.852	1.775
<i>BF2-D1x3</i>	0.002	0.003	0.008	0.009	0.394	0.545	0.355	1.058	0.758	1.613
<i>BF2-D1x3D2D3</i>	0.000	0.000	0.012	0.014	0.462	0.360	0.260	0.977	0.733	1.351

The elastic energy terms  $E_k$  and  $E_{es}$  are independent from the structural configuration. The systems having the similar dominant periods have similar intensities of input ( $E_l$ ) and plastic ( $E_p$ ) energies. The intensity of  $E_p$  decreases with the increment of *SC* number. Also, the ratios of  $E_p/E_l$  are in the same range for each *EQ*.

The plastic energy distributions between members of the frames are shown as bar diagrams, Figure 3.26. Where the terms of *C*, *B*, *D* stand for column, beam and damper, respectively, while 1,2 and 3 represent the storey numbers.

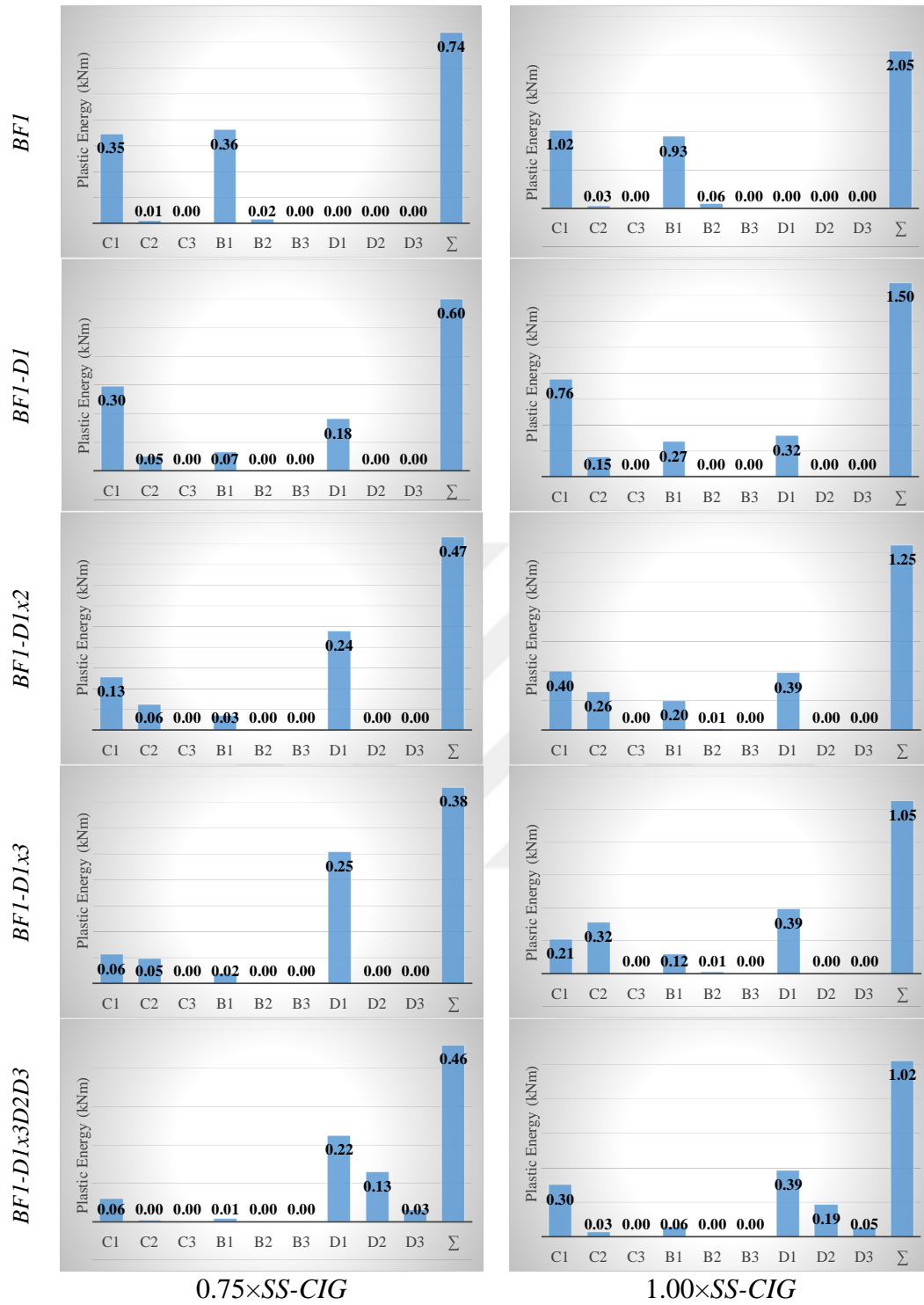


**Figure 3.26 :**  $E_p$  distribution of the strong beam – weak column type frames.

For strong beam - weak column type frames a major part of the input energy is transformed to plastic energy at the metallic dampers. In  $BF1-D1x3D2D3$  frame, about 85% and 60% of the input energy is dissipated by  $SCs$  for  $0.75 \times SS-CIG$  and  $1.00 \times SS-CIG$ , respectively.

Thanks to the implemented supplementary metallic devices, the plastic energy intensities on the structural members decreased to 0.073 kNm (*BF1-D1x3D2D3*) from 0.227 kNm (*BF1-D1x2*). The quantity was 0.7372 kNm for the bare frame (*BF1*) for 0.75×*SS-CIG*. Similarly, the plastic energy dissipated by the structural members was reduced to 0.390 kNm (*BF1-D1x3D2D3*) from 2.046 kNm (*BF1*) by the use of *SCs* for 1.00×*SS-CIG*.

Similar comparisons were performed for the strong column - weak beam type frames. The plastic energy distributions on the structural members are given as bar diagrams, Figure 3.27.

The plastic energies on the structural members are significantly reduced by the addition of the metallic dampers. Two *SCs* implemented to the first storey (*BF2-D1x2*) are almost sufficient to keep the columns in the elastic range. The plastic energy dissipated by the first-storey beams decreased to 0.08 kNm (*BF2-D1x3D2D3*) from 0.50 kNm (*BF2*) for 0.75×*SS-CIG*.

In the bare frame (*BF2*), 73% of seismic input energy is transformed to plastic energy by the plastic deformations of 1<sup>st</sup> and 2<sup>nd</sup> storey beams and 1<sup>st</sup> storey columns. The plastic deformations at the second storey beams are increased after the implementation of *SCs* to 1<sup>st</sup> storey. Alternatively, when the additional dampers are implemented to the upper floors, the plastic energy dissipated by 1<sup>st</sup> and 2<sup>nd</sup> storey beams is reduced to 0.23 and 0.18 kNm (*BF2-D1x3D2D3*) from 0.99 and 0.68 kNm (*BF2*), respectively, for 1.00×*SS-CIG*.

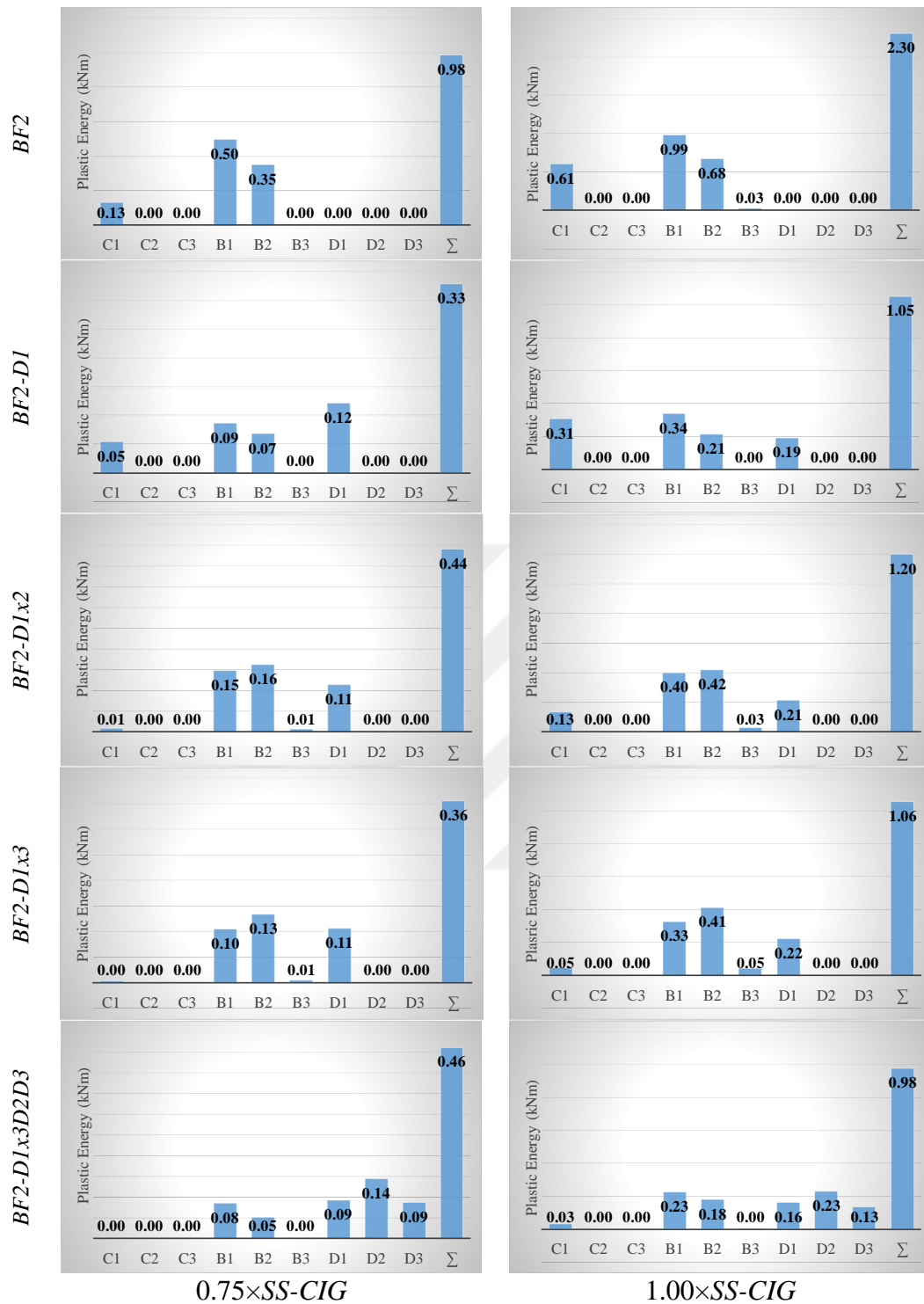


**Figure 3.27** : Ep distribution of the strong beam – weak column type frames.

The lateral storey displacements of the bare frames (*BF1* and *BF2*) are presented together in Figure 3.28 for  $1.00 \times SS-CIG$ . The relative storey displacements are calculated as 20.1, 26.13 and 14.5 mm for *BF1* and 16.3, 24.6 and 14.9 mm for *BF2*, respectively. The storeys where the maximum relative storey displacements exist, are the proper locations for the implementations of *SCs*. Although the 1<sup>st</sup> storey was

selected in the experimental case due to the simplicity of the application, the suitable storeys for implementing *SCs* are the 1<sup>st</sup> and 2<sup>nd</sup> ones.

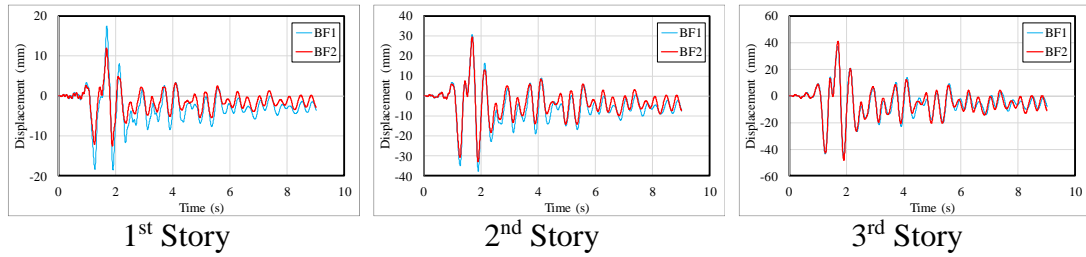


**Figure 3.28 :** The storey displacement histories of the bare frames.

The ratio of plastic energy to seismic input energy can be presented in two different forms. The first one represents global plastic energy dissipated by the structural members and metallic dampers, Figure 3.29a. However, the second one represents only the plastic energy dissipated by the structural members, Figure 3.29b. *Frame IDs* used in the horizontal axes of the graphics represent the frame types defined in Table 3.1.

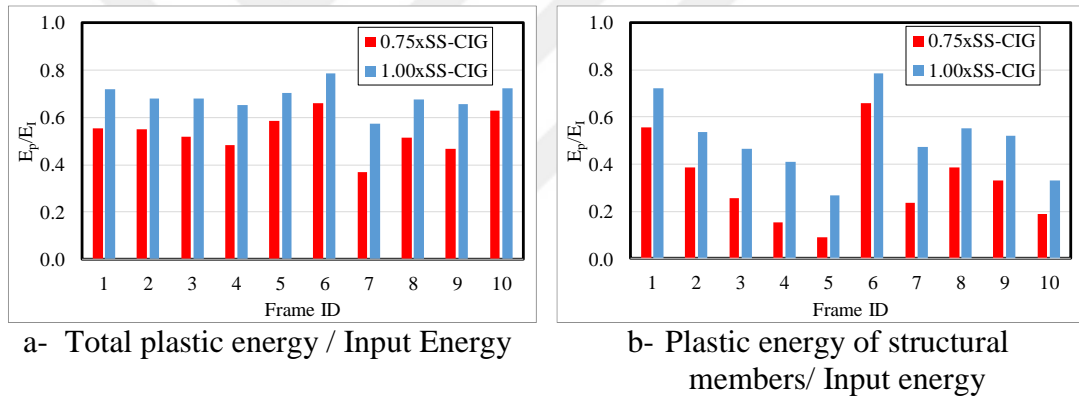


**Figure 3.29 :** Plastic energy to input energy ratios.

Average global plastic energy ( $E_p$ ) to input energy ( $E_i$ ) ratios of the *MDOF* systems are calculated as 0.54 and 0.70 for 0.75×*SS-CIG* and 1.00×*SS-CIG*, respectively, Figure 3.29a. The ratio is almost constant for each *EQs*, whereas the average structural member plastic energy ( $E_p$ ) to input energy ( $E_i$ ) ratios are significantly reduced by the addition of more *SCs* to the system.



#### 4. ESTIMATION OF THE SEISMIC INPUT ENERGY

There are several prediction equations and attenuation relations to compute seismic input energy in the current literature, for which see Chapter 1.2. The existing equations and the attenuation models are evaluated by the experimental and numerical works performed in the content of the thesis. Success of the existing equations was found to be limited, especially for the near-fault type *EQs*.

Two discrete approaches were accomplished to estimate the seismic input energy in this thesis. These are:

- A novel spectral prediction equation that distinguishes the structural damping is suggested.
- The closed form equation based on piece-wise exact method proposed by Aydınoglu and Fahjan (2002) is developed to obtain the seismic input energy spectra for a specific *EQ*.

##### 4.1 The Existing Seismic Input Energy Equations vs. Experimental Results

The existing equations about the seismic input energy prediction are classified into three groups: bilinear design equations, prediction equations and attenuation relations. The input energy equations were evaluated from the results of the elastic *SDOF* tests performed in this thesis. In the shake table test, *SS-CIG* and *CH-NIOE* records were utilized with a scale factor of 0.25, see Chapter 2.2.2. The mass normalized experimental spectral input energies are given together with discrete estimation formulae given in the literature, Figure 4.1.

The bilinear design equations are found to be quite conservative. Although there is a specific descending branch in the experimental results after the corner period ( $T_c$ ) of *EQ*, the bilinear design equations do not contain such a response. However, the equations suggested by Kuwamura and Galambos (1989) and Fajfar et al. (1989) made the best predictions for *SS-CIG* and *CH-NIOE* respectively, except for the corner period.

Similarly, Dindar et al. (2015) and Decanini and Mollaioli (2001) produced reasonable results for *SS-CIG* except for the corner period. The spectral equations suggested by Akiyama (1985) and Mezgebo and Lui (2017) are more conservative ones for both of the records.

The attenuation relations proposed by Chapman (1999) and Alici and Sucuoğlu (2016) predicted *absolute input energy* better especially for *SS-CIG*. However, the input energy at the corner period for *CH-N10E* was predicted to be somewhat smaller by all the attenuation equations.

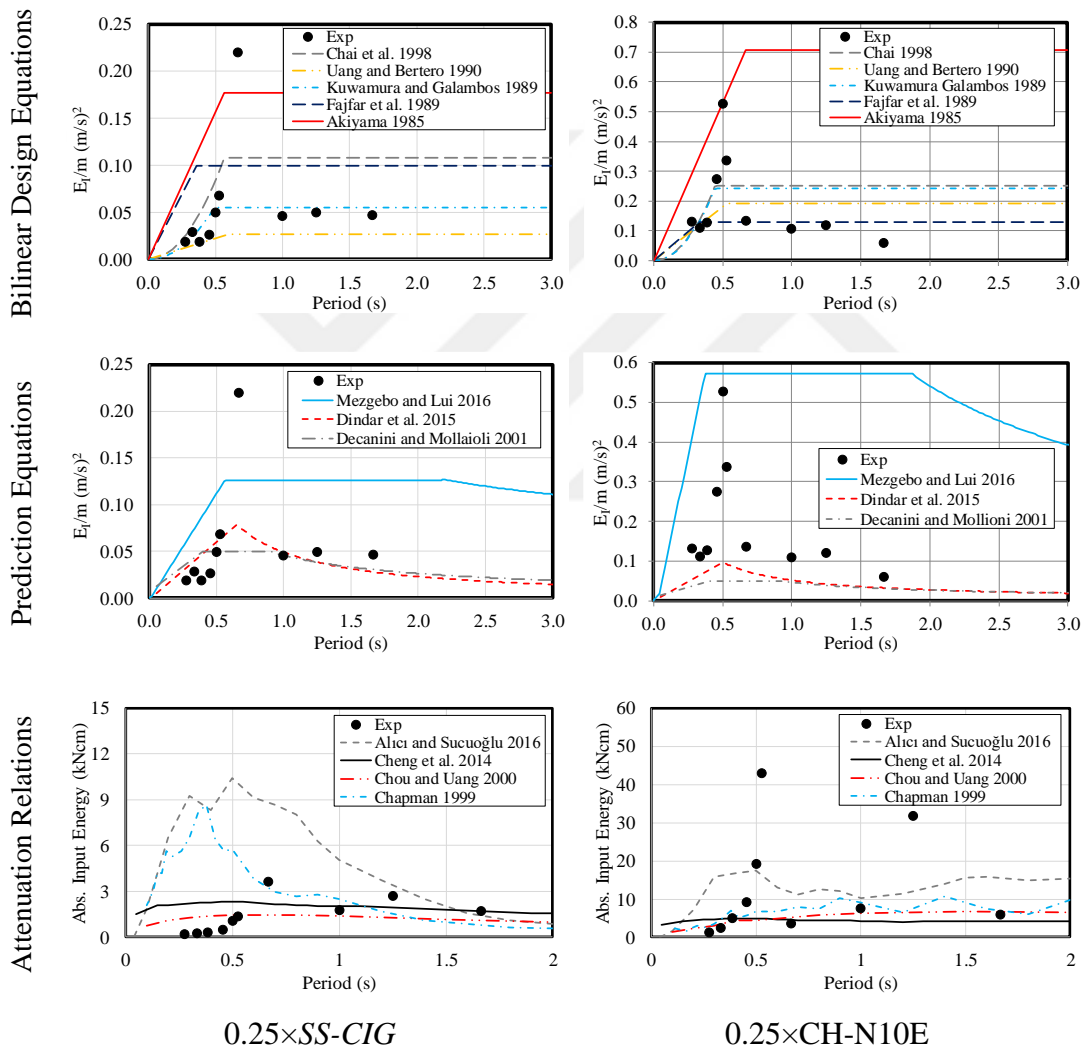


**Figure 4.1 :** Comparison of the existing equations with the experimental results.

Depending on the results, most of the existing equations to predict the seismic input energy have limited success, particularly around the corner period of the *EQ* record. Although most of the existing studies declare that damping has a minor effect on seismic input energy, divergence between the experimental and the estimated values

might be related to the damping effect (Güllü et al. 2018). Consequently, there is a necessity to describe a *damping modification factor* to be applicable for the existing input energy equations.

Moreover, the concave-shaped descending branch beyond the corner period is more realistic than that given by the bilinear spectral relations.

## 4.2 New Seismic Input Energy Relation Proposals

Shen and Akbaş (1999) made a comparison between the numerically obtained input energy intensities for *MDOF* steel frames. They used the spectral relations proposed by Housner (1956), Akiyama (1985), Fajfar et al. (1989), Kuwamura and Galambos (1989) and Uang and Bertero (1990). Since these equations consider only the characteristics of ground motion and disregard all of the structural properties, the assessment study resulted in significantly dissimilar results.

The results of the evaluative study obtained both in this thesis and Shen and Akbaş' study (1999) showed that the existing equations have some deficiencies. Consequently, there is a necessity to generate a novel relationship to predict seismic input energy. Therefore two discrete procedures have been suggested in this thesis. They are the spectral prediction equation and the closed form equation to determine seismic input energy.

### 4.2.1 A novel spectral prediction equation

A novel mass-normalized relative seismic input energy spectrum was developed through the dimensional analyses. The proposed spectrum consists of three parts, as shown in Figure 4.2. They are the ascending (1), plateau (2) and descending branches (3).

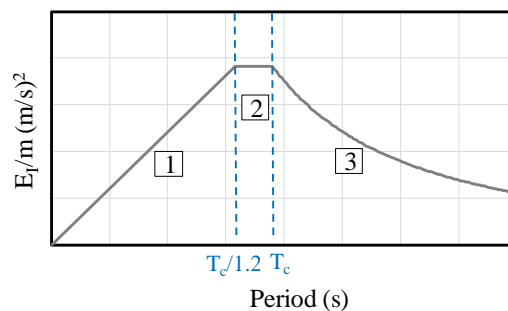


**Figure 4.2 :** The proposed mass normalized relative input energy spectrum.

The maximum  $E_I/m$  that corresponds to  $T_c$  is calculated by Equation 4.1, where  $T$  is the principal vibration period of the structure and  $B$  and  $k$  are the soil parameters (Dindar et al. 2015). The corner period of the  $EQ$  can be determined by either Fourier spectrum or undamped velocity spectrum of the  $EQ$  record, (Kuwamura et al. 1994). The initiation point of the plateau (partition 2) is determined by  $T_c/1.2$  to consider that plastic deformations lengthen the natural period and cause to increment in the seismic energy imparted to the system, (Akiyama 1985). The ascending brach (partition 1) is generated by connecting the points of origin and  $T_c/1.2$ . However, the descending branch (partition 3) is formed by the term of  $\left(\frac{T_c}{T}\right)^k$  in equation (4.1).

$$\frac{E_I}{m} = B \sqrt{SV(\xi)_{\max} SA(\xi)_{@SV_{\max}} T_c I_e t_e} \left(\frac{T_c}{T}\right)^k \quad (4.1)$$

Shen and Akbaş (1999) stated that seismic input energy responsive to frequency content, peaks of acceleration and velocity components, as well as duration of  $EQ$ . However, it was considered that a small number of parameters of the record is not sufficient for the accurate prediction of seismic input energy. Moreover, Sandikkaya and Akkar (2017) are also mentioned that the characterization of an  $EQ$  should be based on amplitude, frequency content and duration.

Subsequently, the novel empirical spectral equation to predict seismic input energy combines the parameters related with structure ( $T$ ), record ( $SA(\xi)$ ,  $SV(\xi)$ ), frequency content ( $T_c$ ), cumulative damage potential ( $I_e$ ) and effective duration ( $t_e$ ). The power of the considered parameters were obtained from the dimensional analyses. Structural damping is also considered in the suggested equation through the spectral acceleration and velocity. The dimension homogeneity of the empirical equation is exposed in equation (4.2) where the dimensions of force, length and time are represented by  $P$ ,  $L$  and  $T$ , respectively.

$$\frac{E_I}{m} = \frac{P \times L}{P \times T^2 / L} = \sqrt{\frac{L}{T} \times \frac{L}{T^2} \times T \times \frac{L^2}{T^3} \times T \times \frac{T}{T}} = \frac{L^2}{T^2} \quad (4.2)$$

The unitless terms  $B$  and  $k$  are given in Table 4.1. Moreover, the effective duration is considered to be a time interval between 5% and 75% of Arias intensity, (Bommer and Martinez-Pereira 1999, Dashti and Karimi 2017, Muin and Mosalam 2017).

**Table 4.1 :** B and k parameters, Dindar et al. (2015).

Parameters	Soil A	Soil B	Soil C	Soil D
	Rock	Stiff Soil	Soft Soil	Very Soft Soil
	$V_{s30} > 760$ m/s	$760 > V_{s30} > 360$ m/s	$360 > V_{s30} > 180$ m/s	$180$ m/s $> V_{s30}$
$B$	0.065	0.0705	0.077	0.085
$k$	0.910	1.095	1.456	1.658

The suggested seismic input energy equation is evaluated by the experimental results, firstly. The experimentally determined  $E_I/m$  values for *SS-CIG* and *CH-NIOE* are depicted, together with the proposed equation (equation 4.1) , Figure 4.3.

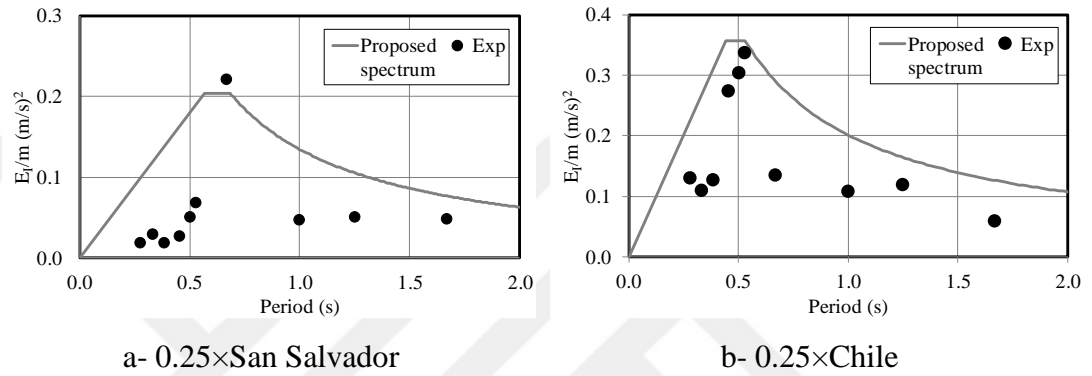
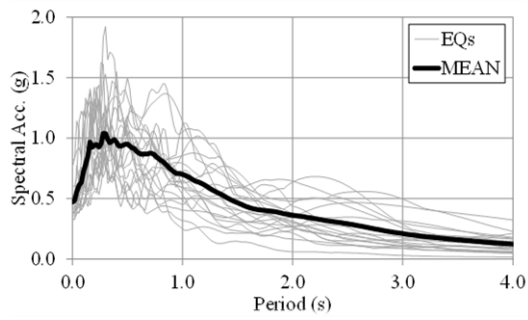


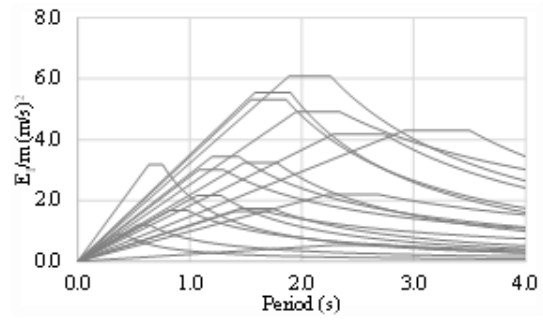
**Figure 4.3 :** Proposed seismic input energy spectra vs. the experimental results.

It can be seen that ultimate  $E_I/m$  values are closely estimated. Since the specimens were tested in the elastic range, the first partition of the spectrum is positioned on the conservative side for both of the records. It is a corollary of the decision about the initiation point of plateau ( $T_c/1.2$ ).  $E_I/m$  values corresponding to the periods longer than  $T_c$  was reasonably estimated for both of the records.

As a second attempt to evaluate the success of the proposed empirical equation, a comprehensive numerical study were accomplished for a set of historical *EQs*. The specific properties of the records are given in Table 4.2. The terms utilized to compute the empirical spectrum are listed in Table 4.3. Nineteen of the *EQ* records are near-fault and the remaining two (*LA270* and *TCU067*) are far-field types. Elastic acceleration spectra of the records for 5% damping ratio were generated by SeismoSignal, Figure 4.4a. Input energy spectra of the records obtained by the proposed equation is presented in Figure 4.4b. Though the plateau of the acceleration spectra set between 0.3 and 0.8 s, the placement of plateau in input energy spectra is affected by  $T_c$ .



a-Acceleration Spectra



b-EI/m Spectra

**Figure 4.4** : Spectra of the selected records.

The numerical model verified by the experimental results (see Chapter 3) was employed to generate input energy intensities for the selected twelve discrete periods. The proposed spectra are plotted with solid grey line. Black circles correspond to the numerical results, Figure 4.5.

**Table 4.2** : The *EQ* records utilized for numerical comparisons.

#	Record	Symbol	$M_s$	d (km)	PGA (cm/s <sup>2</sup> )	PGV (cm/s)
1	Chuetsu-Oki_Japan 2007 Joetsu Kakizakiki Kakizaki	65010EW	6.80	11.94	446.9	89.0
2	Irpinia_Italy-01 1980 Sturno	A-STU270	6.90	10.84	314.4	71.9
3	Duzce_Turkey 1999 Bolu	BOL090	7.14	12.04	790.3	65.8
4	Superstition Hills-02 1987 Parachute Test Site	B-PTS225	6.54	0.95	423.6	134.2
5	Montenegro_Yugoslavia 1979 Bar-Skupstina Opstine	BSO090	7.10	6.98	340.9	52.8
6	Cape Mendocino 1992 Centerville Beach_ Naval Fac	CBF360	7.01	18.31	468.5	51.2
7	Erzincan 03/13/1992 Erzincan S.	ERZ-EW	6.90	8.97	486.6	64.3
8	Imperial Valley 1979 El Centro Array #5	H-E05230	6.53	3.95	368.2	96.9
9	Darfield_ New Zealand 2010 Horc	HORCN18E	7.00	7.29	441.5	105.9
10	Northridge-01 1994 Jensen Filter Plant Administrative Bld.	JEN022	6.69	5.43	402.7	111.4
11	Niigata_Japan 2004 Nigh11	NIGH11EW	6.63	8.93	374.3	58.1
12	RSN3965_TOTTORI_TTR008EW	TTR008EW	6.61	6.86	383.9	54.2
13	Cape Mendocino 1992 Petrolia	PET090	7.01	8.18	648.9	88.5
14	Northridge-01 1994 La 00	LA0270	6.69	19.07	277.4	37.9
15	Imperial Valley 1979 El Centro Differential Array	H-EDA270	6.53	5.09	345.9	75.5
16	Loma Prieta 1989 Saratoga - Aloha Ave	STG000	6.93	8.50	302.0	41.6
17	Northridge-01 1994 Rinaldi Receiving Sta	RRS318	6.69	6.50	463.3	74.7
18	Chi-Chi, Taiwan 09/20/1999 CWB 99999 TCU067 S.	TCU067	7.62	28.70	318.8	66.6
19	Chi-Chi, Taiwan 09/20/1999 CWB 99999 TCU076 S.	TCU076	7.62	16.03	408.1	64.2
20	Northridge-01 1994 Pacoima Kagel Canyon	PKC360	6.69	7.26	424.6	51.4
21	Darfield_ New Zealand 2010 GDLC	GDLCN55W	7.00	1.22	750.0	116.0

**Table 4.3** : Parameters utilized for the proposed spectra.

#	Record	SA (m/s <sup>2</sup> )	SV (m/s)	T <sub>c</sub> (s)	I <sub>e</sub> (m <sup>2</sup> /s <sup>3</sup> )	t <sub>e</sub> (s)
1	65010EW	5.982	1.860	1.28	14.213	4.810
2	A-STU270	3.181	1.555	2.74	8.703	6.109
3	BOL090	11.624	2.019	0.98	15.176	1.500
4	B-PTS225	9.354	2.745	1.86	23.363	7.095
5	BSO090	5.989	1.808	1.30	18.964	7.800
6	CBF360	3.643	1.047	1.68	9.861	4.330
7	ERZ-EW	3.659	1.263	0.67	6.845	2.805
8	H-E05230	3.716	2.172	3.50	10.725	3.790
9	HORCN18E	6.462	2.088	1.90	19.966	6.475
10	JEN022	5.452	2.460	2.74	16.048	4.005
11	NIGH11EW	13.118	0.994	0.42	14.025	2.415
12	TTR008EW	8.914	1.896	1.28	11.233	4.630
13	PET090	16.225	2.033	0.76	23.862	2.720
14	LA0270	5.317	0.685	0.42	13.323	4.800
15	H-EDA270	2.505	1.210	2.68	10.940	3.700
16	STG000	3.657	1.174	1.74	9.128	3.740
17	RRS318	4.730	1.877	2.34	26.557	4.340
18	TCU067	5.880	1.495	0.76	16.341	7.595
19	TCU076	5.877	1.495	1.44	22.813	8.250
20	PKC360	1.070	1.131	0.64	11.202	5.630
21	GDLCN55W	6.668	2.314	2.26	28.120	5.630

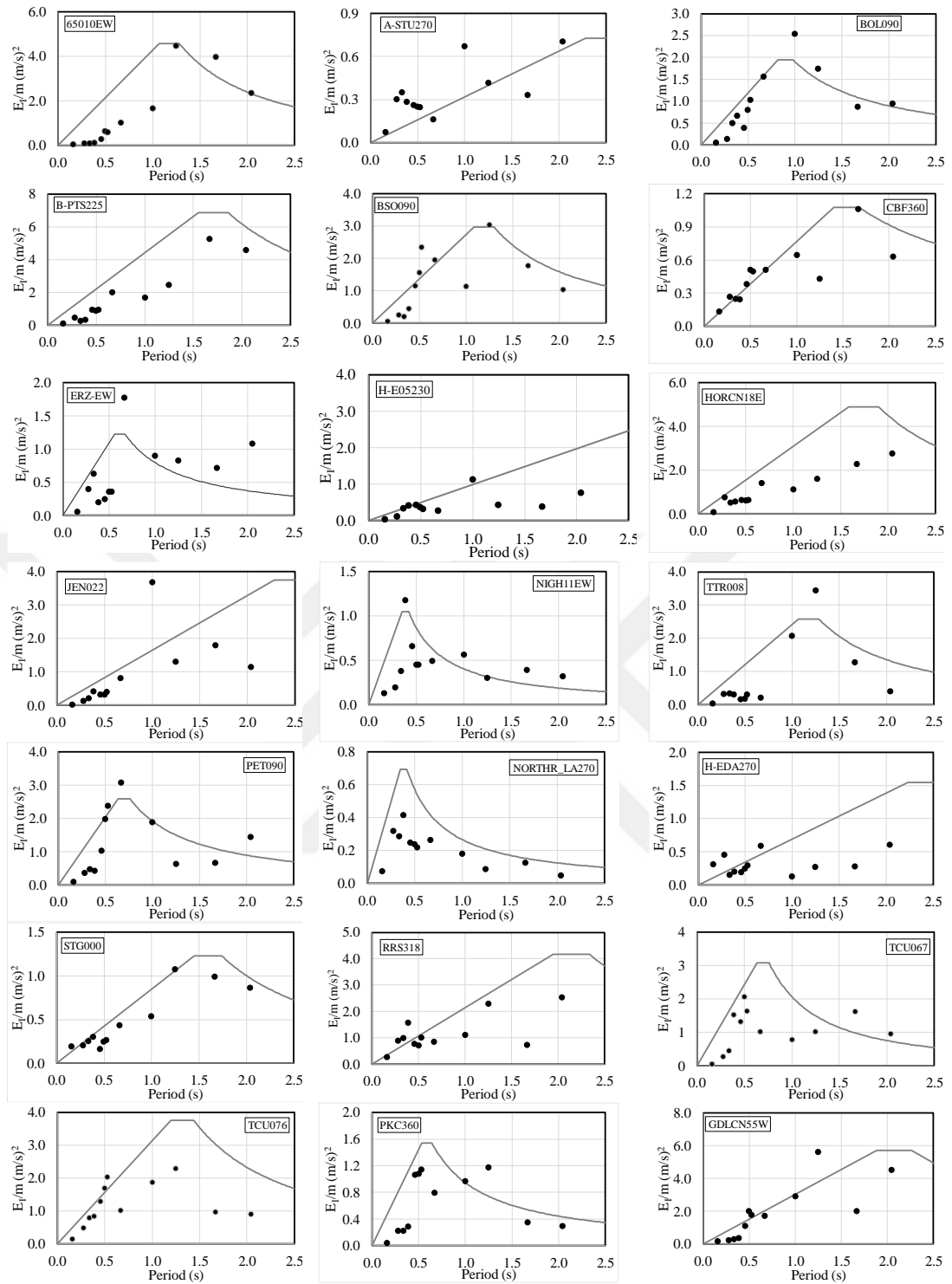


**Figure 4.5 :** Input energy spectra comparisons.

The suggested empirical formulae successfully predicted ultimate  $E_f/m$  intensities. Some discrepancies are experienced for *65010EW*, *A-STU270* and *ERZ-EW* records. The conceivable reason for the discrepancy is that these records had two or more peaks in their Fourier spectra. Extension of the plateau in the spectral shape of input energy may be a rational tactic for these type of records. In addition, the maximum input

energy of *H-E05230* is obtained at 2.73 s, that is longer than the maximum range (2.5 s) assigned for the energy graphics. Frequency contents of these records are presented in Figure 4.6.

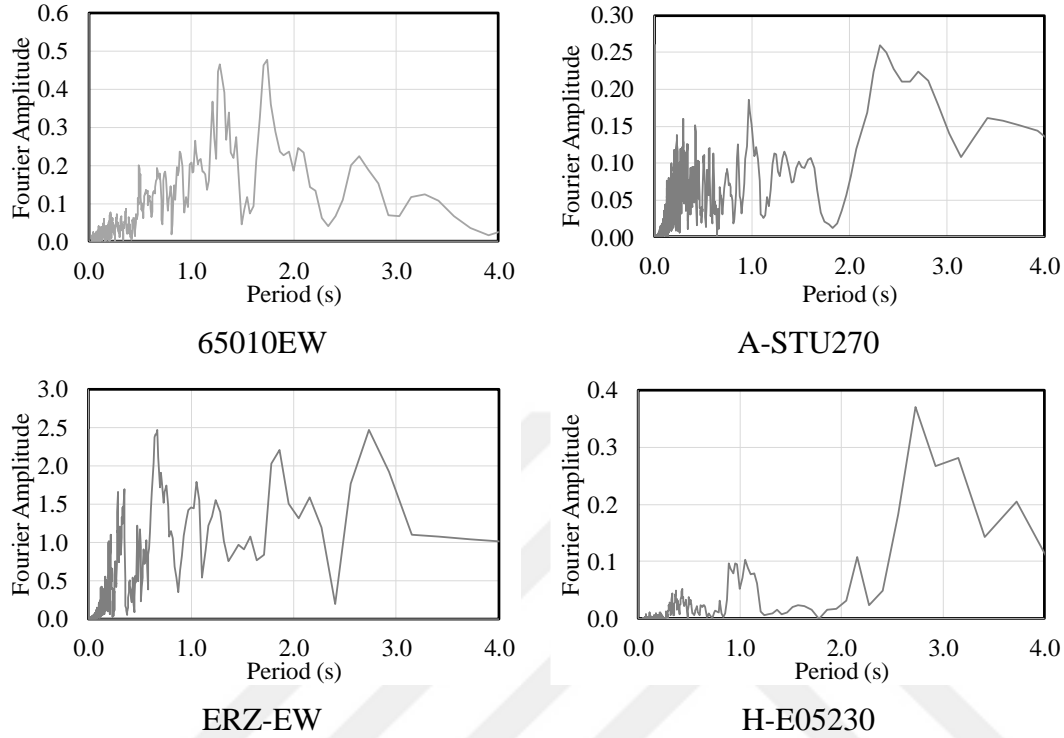


**Figure 4.6 :** Frequency content of some records.

The ascending branch ( $T < T_c$ ) is customarily successful. Additionally, the suggested spectrum is more capable for the estimation compared with the bilinear type spectra for most of the records.

From the analyses, it reveals that there is no direct correlation between input energy intensity and moment magnitude of the record.

The efficiency of the proposed spectral equation was investigated by way of *linear correlation coefficient* ( $\rho$ ), equation (4.3), where  $n$  is number of data;  $X$  and  $Y$  are two data series.

$$\rho = \frac{n\sum XY - (\sum X)(\sum Y)}{\sqrt{(n\sum X^2 - (\sum X)^2) \times (n\sum Y^2 - (\sum Y)^2)}} \quad (4.3)$$

The coefficient ( $\rho$ ) varies between -1.0 and 1.0 that means negative and positive full correlations, respectively. Here,  $\rho < 0.19$ ,  $0.2 < \rho < 0.39$ ,  $0.4 < \rho < 0.59$ ,  $0.6 < \rho < 0.79$  and  $\rho > 0.80$  were deliberated as *very weak*, *weak*, *intermediate*, *strong* and *very strong*

correlations, respectively. Correlations of the numerical results are displayed in Figure 4.7. Average of correlation coefficients for 21  $EQ_s$  were obtained as  $\rho=0.75$  for the proposed equation.

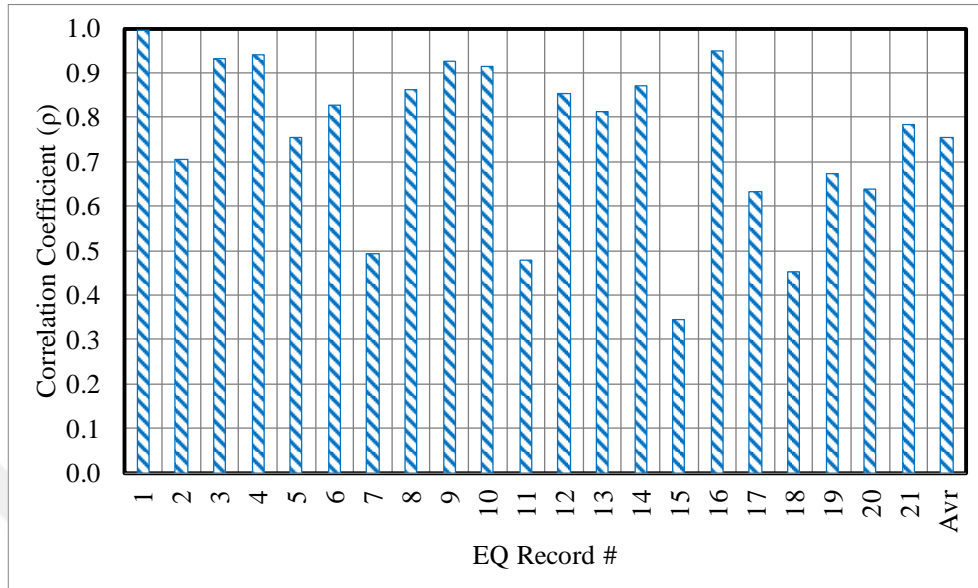


**Figure 4.7 :** Correlation analyses for the suggested input energy spectra.

The effects of some parameters on the proposed spectral seismic input energy equation were also investigated. The records are sorted from smaller to larger for the properties of intensity ( $I_e$ ), spectral acceleration, spectral velocity, peak ground acceleration, peak ground velocity, corner period, effective duration and moment magnitude. After that the records are linked to the sort of  $E_I/m_{max}$ . The graphics in which vertical and horizontal axes represent the variable and  $E_I/m$  are produced and number of points accumulated around the bisector (orange line) are counted, Figure 4.8.

None of the variables predicted the order adequately. Intensity, spectral velocity,  $PGV$  and moment magnitude have a stronger correlation against the others. Hence, their effect on the spectrum was investigated separately.

Figure 4.9 displays  $E_I/m$  spectra for the  $EQ_s$  with moment magnitude ( $M_s$ ) of 6.61~7.01.  $T_c$  and  $I_e$  of the records were presented in Table 4.3. The records with comparable  $M_s$  and  $T_c$  give similar spectra. When the sub-groups of  $EQ_s$  #9, #10, #17, #21 and  $EQ_s$  #2, #7, #16 were compared, it was realized that the effect of intensity ( $I_e$ ) varies between  $16 < I_e < 29$  and  $6 < I_e < 10$  for the first and second groups, respectively. Hence,  $M_s$  is not an unique determinant by itself, rather it should be accounted with  $T_c$  and  $I_e$  parameters. The records of  $EQ_s$  #9, #10, #17, #21 have the largest  $T_c$  and  $I_e$  values.

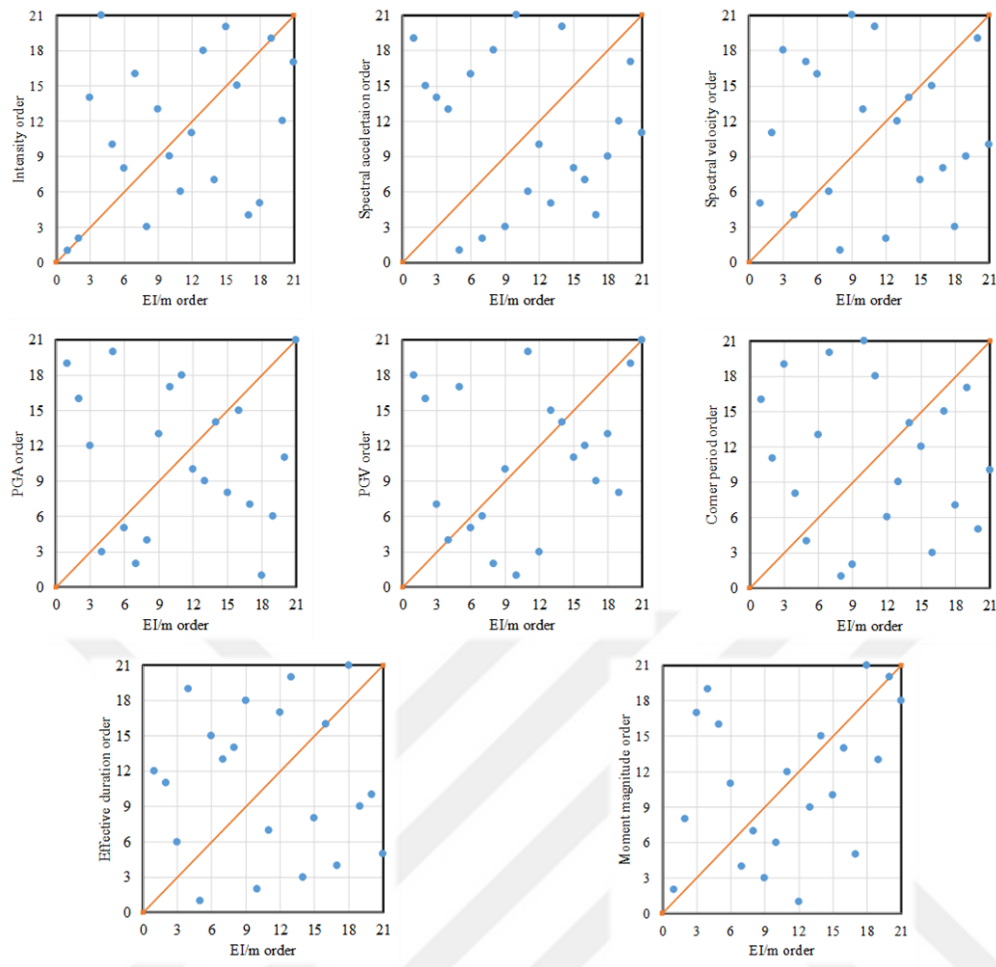


**Figure 4.8 :** Weightiness of the parameters on the seismic input energy.

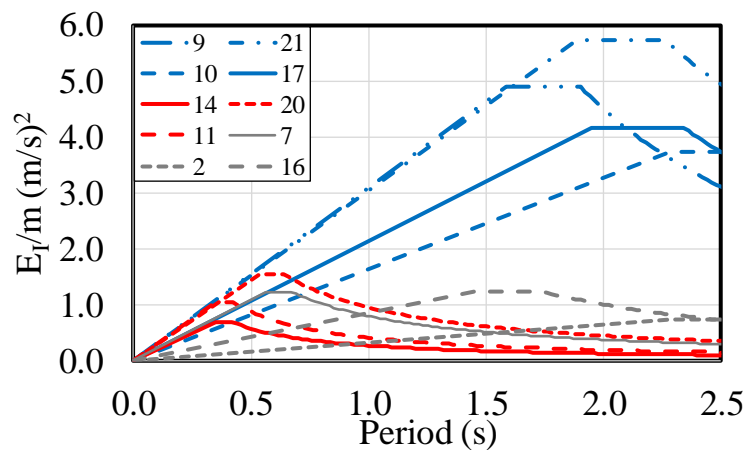


**Figure 4.9 :** Effect of moment magnitude on the seismic input energy.

Three groups of spectra were generated to evaluate the correlation between  $PGV$  and  $E_I/m$ . The  $PGV$  groups were set as 35-55, 65-75 and 100-135 cm/s, respectively. There is no direct correlation between  $PGV$  and  $E_I/m$ , Figure 4.10. However, the records having similar  $PGV$  and  $T_c$  produced similar input energy spectra.

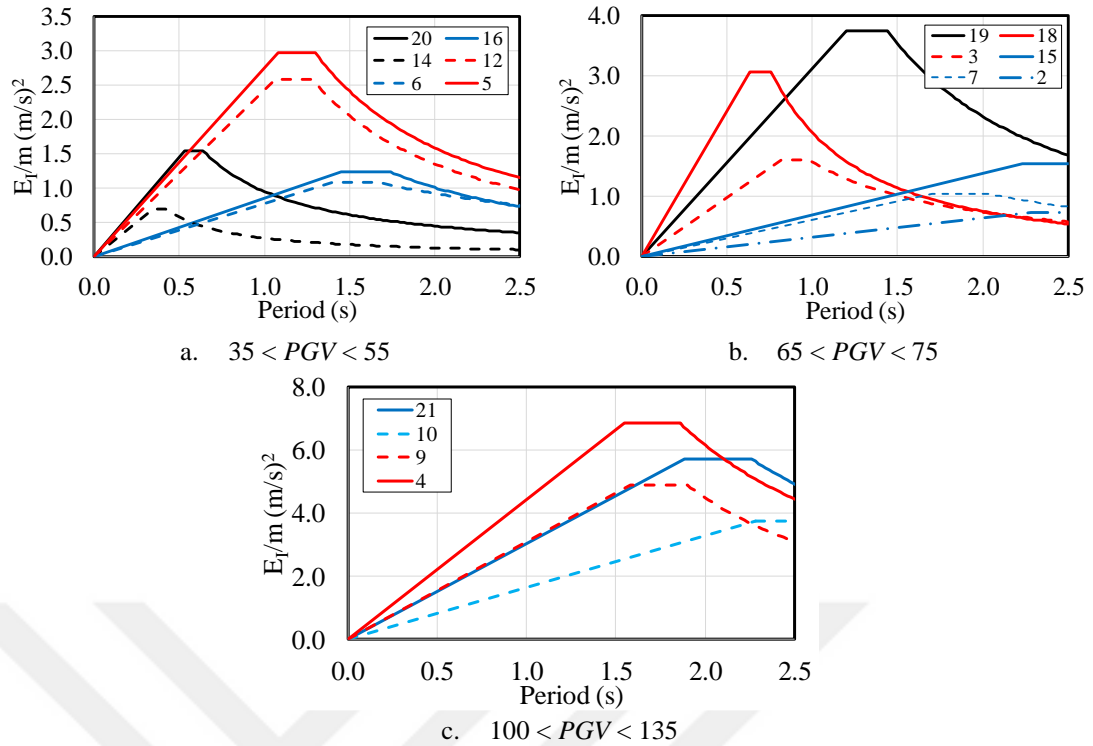


**Figure 4.10 :** Effect of PGV on the seismic input energy.

The intensity ( $I_e$ ) was found to be an efficient parameter on *Partition 1* of the proposed energy spectrum. Three sub-groups are able to be nominated for the *EQs*, Figure 4.11. When the intensity ( $I_e$ ) increases, the initial slope (Partition 1) also increases.

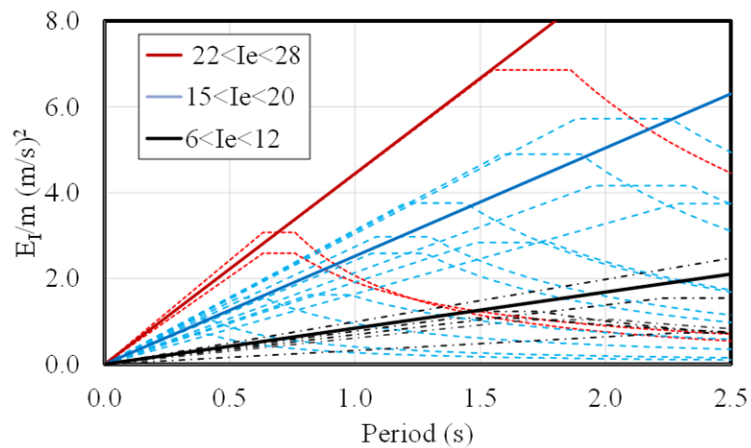


**Figure 4.11 :** Effect of intensity on the spectral shape.

#### 4.2.2 The closed form equation based on piece-wise exact method to calculate seismic input energy

Seismic input energy, as determined by equations 1.1 or 1.2, depends on the equation of motion of the *SDOF* system. Determination of the  $E_I/m$  spectrum necessitates vast and time consuming calculation efforts. However, some analyses techniques exists in the literature that enable the analysis of *SDOF* systems. One of them is the *piece-wise exact method* proposed by Aydinoglu and Fahjan (2003). It is capable of accounting for the geometric nonlinearity. The method that was originally proposed to obtain seismic response of *SDOF* systems, is utilized here as a tool in the determination of the  $E_I/m$  spectrum. The original method is able to consider two different constitutive equations. In the algorithm developed in this thesis, the *Elastic Perfectly Plastic (EPP)* response model has been utilized, depending on the conclusions that the hysteretic model type is ineffective on the seismic input energy (Benavent-Climent 2010, Dindar 2009).

The proposed piece-wise exact method initiates with the re-expression of the restoring force, as given in equation (4.4).

$$f_s(t) = f_s(t_i) + \beta_{ej}k[u(t) - u(t_i)] \quad (4.4)$$

where  $u(t_i)$  and  $f_s(t_i)$  are the displacement and the restoring force determined previously at a given time step  $t=t_i$ .  $\beta_{ej}k$  is the effective stiffness of the linear segment in terms of the initial stiffness ( $k$ ).  $\beta_{ej}$  equals 1 for the linear elastic case. The equation of motion of a *SDOF* system can be drawn by substituting equation 4.4 in it, equation (4.5) where  $u$ ,  $\dot{u}$  and  $\ddot{u}$  stand for displacement, velocity and acceleration respectively.

$$\ddot{u}(t) + 2\xi\omega\dot{u}(t) + \beta_{ej}\omega^2u(t) = -\ddot{u}^s(t) - \frac{f_s(t_i)}{m} + \beta_{ej}\omega^2u(t_i) \quad (4.5)$$

The ground acceleration is also re-expressed as a linear function between the time steps of  $t=t_i$  and  $t=t_{i+1}$ , equation (4.6).

$$\ddot{u}^s(t) = \ddot{u}^s(t_i) + \frac{\Delta\ddot{u}^s}{\Delta t} \tau \quad (4.6a)$$

$$\Delta\ddot{u}^s = \ddot{u}^s(t_{i+1}) - \ddot{u}^s(t_i) \quad (4.6b)$$

$$\Delta t = t_{i+1} - t_i \quad (4.6c)$$

$$\tau = t - t_i \quad (4.6d)$$

Equation 4.5 can be rewritten in the time span  $t_i \leq t \leq t_{i+1}$ , i.e.  $0 \leq \tau \leq \Delta t$  given as equation (4.7).

$$\ddot{u}(\tau) + 2\xi\omega\dot{u}(\tau) + \beta_{ej}\omega^2u(\tau) = -\ddot{u}^G(t_i) - \frac{\Delta\ddot{u}^s}{\Delta t}\tau \quad (4.7)$$

where the effective pseudo acceleration  $\ddot{u}^G(t_i)$  at  $t=t_i$  is expressed as shown by equation (4.8).

$$\ddot{u}^G(t_i) = \ddot{u}^s(t_i) + \frac{f_s(t_i)}{m} - \beta_{ej}\omega^2u(t_i) \quad (4.8)$$

The solution of equation 4.7 has two parts, namely a complementary solution, corresponding to free vibration response and a particular solution that satisfies the right hand side of the equation. The solutions were given for positive, negative and zero effective stiffnesses. The solutions for zero stiffness were generated for two different damping conditions. They are all given in equations (4.9), (4.10), (4.11) and (4.12).

*Positive effective stiffness of linear segment ( $\beta_{ej} > 0, \beta_{ej} > \xi^2 \geq 0$ )*

$$u(\tau) = \left[ C_1 \cos(\omega_D \tau) + C_2 \sin(\omega_D \tau) \right] \exp(-\xi\omega\tau) + C_3\tau + C_4 \quad (4.9)$$

*Negative effective stiffness of linear segment ( $\beta_{ej} < 0, \xi > 0$ )*

$$u(\tau) = \left[ C_1 \cosh(\omega_D \tau) + C_2 \sinh(\omega_D \tau) \right] \exp(-\xi\omega\tau) + C_3\tau + C_4 \quad (4.10)$$

*Zero effective stiffness of linear segment ( $\beta_{ej} = 0, \xi > 0$ )*

$$u(\tau) = C_1 \exp(-2\xi\omega\tau) + C_2 + C_3\tau^2 + C_4\tau \quad (4.11)$$

*Zero effective stiffness of linear segment ( $\beta_{ej} = 0, \xi = 0$ )*

$$u(\tau) = C_1\tau + C_2 + C_3\tau^3 + C_4\tau^2 \quad (4.12)$$

The intrinsic functions for the coefficients of  $C_k$  and to calculate the terms of  $A_{ij}$  and  $B_{ij}$  were given in the original paper (Aydınoglu and Fahjan 2003), equations (4.13) and (4.14).

$$u(t_{i+1}) = A_{11}u(t_i) + A_{12}\dot{u}(t_i) + B_{11}\ddot{u}^G(t_i) + B_{12}\Delta\ddot{u}^s \quad (4.13)$$

$$\dot{u}(t_{i+1}) = A_{21}u(t_i) + A_{22}\dot{u}(t_i) + B_{21}\ddot{u}^G(t_i) + B_{22}\Delta\ddot{u}^s \quad (4.14)$$

Since displacement (equation 4.13) and velocity (equation 4.14) responses of the *SDOF* system are determined for a specific time step, the acceleration response is attained through these responses.

Since the structural responses are determined, seismic input energy and its components are computed by equations (4.15), (4.16), (4.17) and (4.18). Since the *piece-wise exact*

*method* depends on the discrete data, the integration signs in equation 1.2 turn into the signs of summation. It was suggested that the time span selected for the calculation should be less than  $0.1 \times T$ , where  $T$  is predominant vibration period of *SDOF* system. The operations defined in equations 4.15 to 4.18 are generated through the *cumtrapz* function of MATLAB package that depends on the *trapezoidal numerical integration method*.

$$\frac{E_k}{m} = \sum_0^t \ddot{u} \dot{u} dt \quad (4.15)$$

$$\frac{E_D}{m} = 2\xi\omega \sum_0^t \dot{u}^2 dt \quad (4.16)$$

$$\frac{E_s}{m} = \omega^2 \sum_0^t u \dot{u} dt \quad (4.17)$$

$$\frac{E_I}{m} = -\sum_0^t \ddot{u}^g \dot{u} dt \quad (4.18)$$

The MATLAB based code (PW-SPECTs) is generated for the algorithm given above. The input data of the code are the vibrational period, damping ratio, time span and ground motion data. The code not only produces the responses and the energy histories but also their spectral counterparts.

The tested *SDOF* system with a 0.667 s vibrational period and 0.3% damping ratio are used for the verification of PW-SPECTs. The specimen was subjected to *SS-CIG* record. As an initial step; displacement, velocity and acceleration histories obtained from the experiment and PW-SPECTs are compared in Figure 4.12 where “*P-W*” and “*Exp*” stand for piece-wise exact method and experiment, respectively.

The obtained responses are quite consistent with each other. The few divergences observed at the peaks might be related to the assumption of damping made for the numerical analyses.

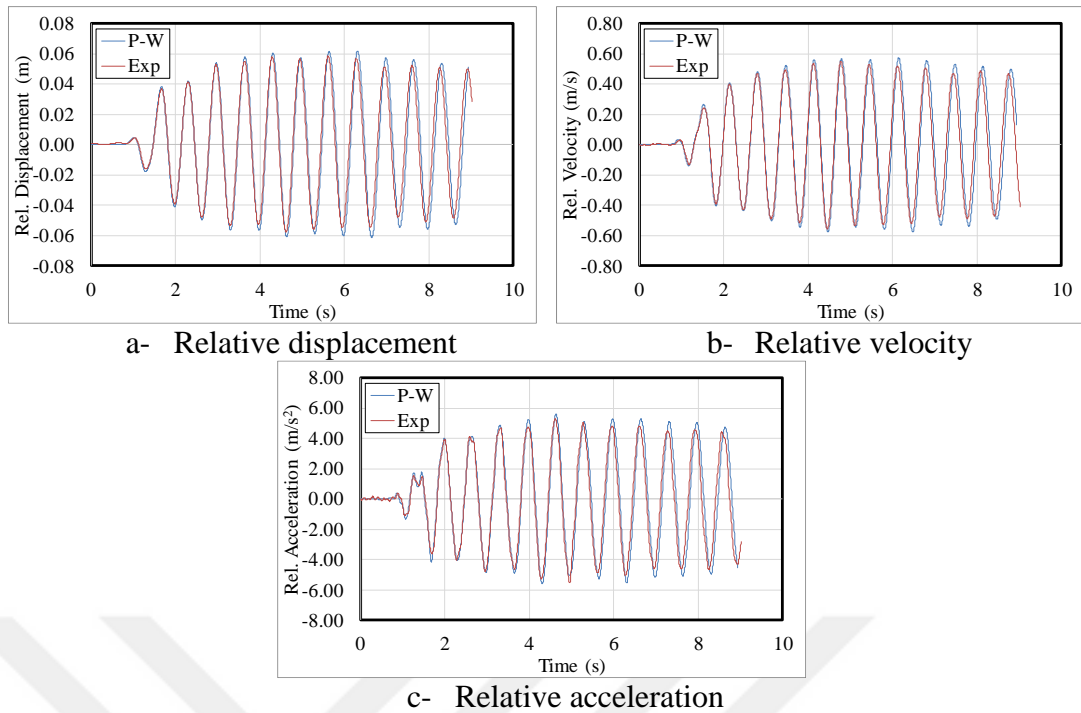


**Figure 4.12 :** Comparison of relative responses obtained by experiment and piece-wise exact method.

In the second step, the response spectra (*SD*, *SV* and *SA*) of the same record are generated by PW-SPECTs and SeismoSignal v16, which is one of the esteemed software packages in the field, Figure 4.13. The similar time span was ( $\Delta T=0.01$  s) used for both of the codes. The obtained results are almost the same.

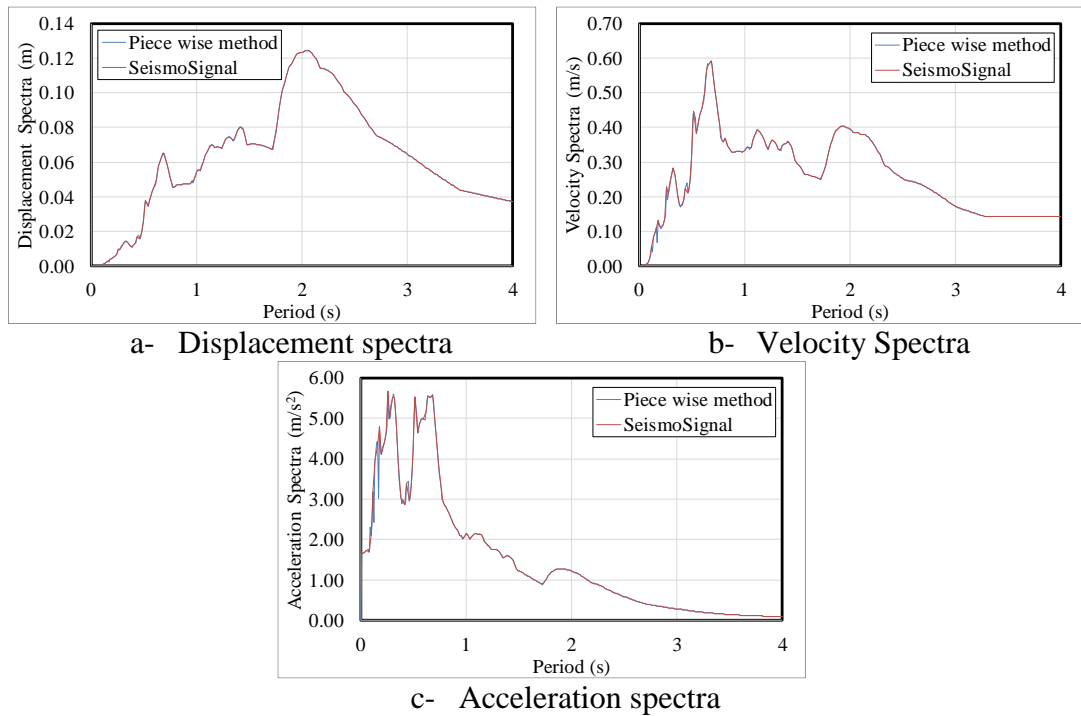


**Figure 4.13 :** Comparison for the spectra of the record and piece-wise exact method.

In the third step, mass normalized seismic input energy history of the specimen ( $T=0.667$  s and  $\xi=0.3\%$ ) is generated by PW-SPECTs and compared with the experimental result, Figure 4.14. The results are consistent with each other, except for the little time shift. It maybe related with the decision about the initiation point of the experimental data.

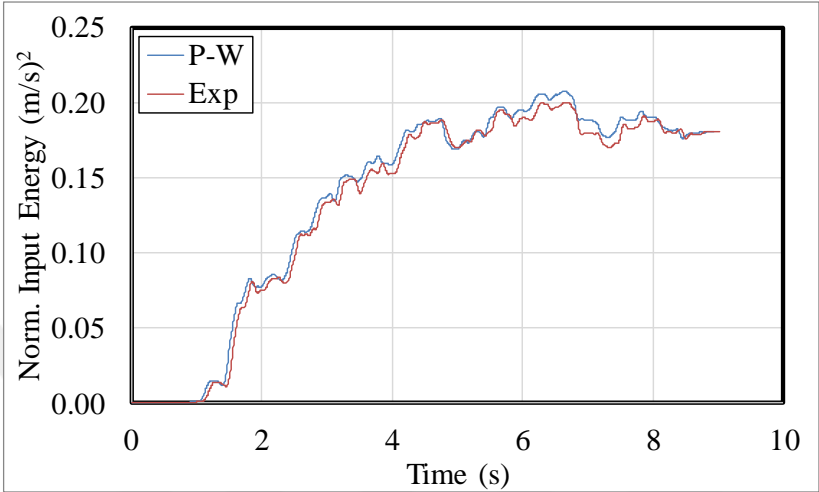


**Figure 4.14 :** Comparison of the mass normalized input energies obtained from experiment and piece-wise method.

After the evaluation phase of the  $E_I/m$  spectrum developed by PW-SPECTs is completed, some comparisons were achieved for *SDOF* and *MDOF* systems.

The elastic *SDOF* systems defined in Chapter 2.2.2 were used to generate experimental spectral values of  $E_I/m$ . Ten discrete systems were tested for  $0.25 \times SS-CIG$  record. The black dots in Figure 4.15 represent the couples of period vs.  $E_I/m_{max}$ . The corresponding  $E_I/m$  spectrum that was generated by PW-SPECTs by considering 0.3% damping ratio is also given in the same figure. The numerical spectrum makes relatively good estimations of the experimental results.

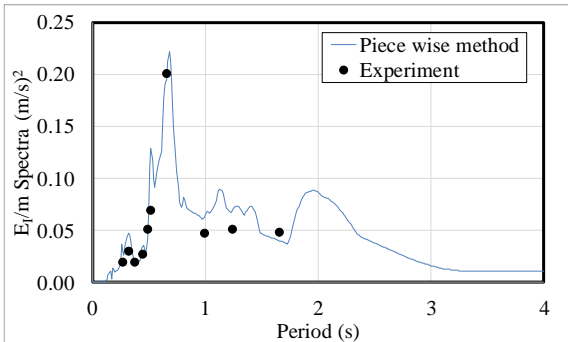


**Figure 4.15 :** Comparison of the  $E_I/m$  spectrum with elastic experimental results.

Subsequently the experimental spectral values of  $E_I/m$  obtained for the inelastic  $SDOF$  systems (Chapter 2.2.3) are compared with the numerical  $E_I/m$  spectrum, Figure 4.16. The experimental results represented by black dots in the figure are in good agreement with the numerical elastic spectrum generated by PW-SPECTs. This phenomena was proven numerically by Akiyama (1985), Lopez-Almansa (2013).

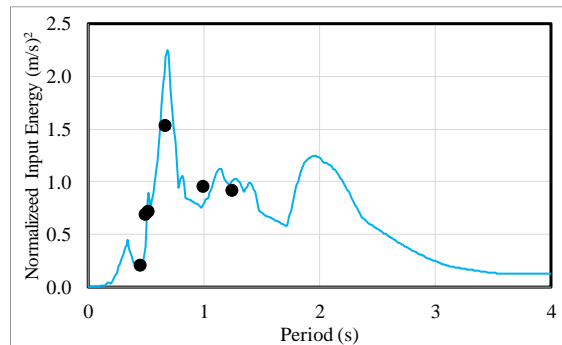


**Figure 4.16 :** Comparison of the  $E_I/m$  spectrum with inelastic experimental results.

In the final stage,  $E_I/m_{max}$  obtained from the  $MDOF$  system tests (Chapter 2.3) as well as the numerical analyses (Chapter 3.3.3) are compared with the numerical elastic spectrum generated for  $SS-CIG$  record, Figure 4.17. The comparisons are achieved for two specific cases in which the damping ratios are selected were 2 and 5%, depending on the experimental response.

Figure 4.17a consists of the results of  $BF1$  and  $BF2$ . In Figure 4.17b, the experimental results of  $BF1-D1$  and  $BF2-D1$ ; and the numerical results of  $BF1-D1x2$ ,  $BF1-D1x3$ ,  $BF1-D1x3D2D3$ ,  $BF2-D1x2$ ,  $BF2-D1x3$ ,  $BF2-D1x3D2D3$  are represented by black and red dots, respectively.

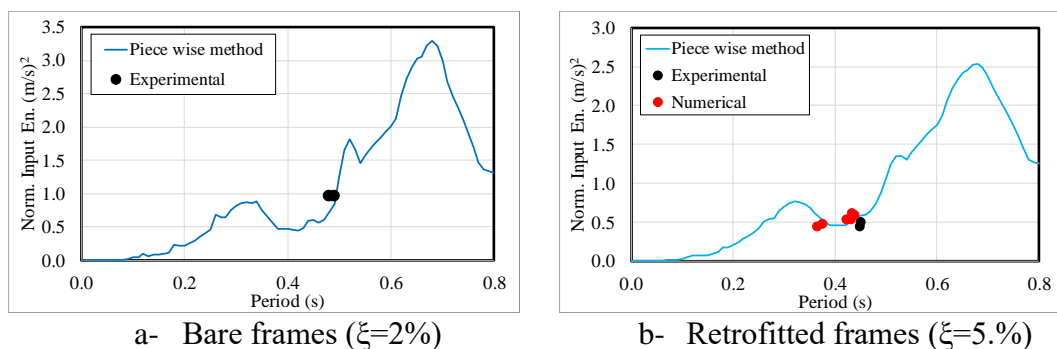


**Figure 4.17 :** Comparison of the proposed piece-wise method and  $MDOF$  specimen results.

The experimentally and numerically investigated  $MDOF$  systems generate the consistent  $E_I/m_{max}$  values with the spectra constructed for  $SDOF$  systems with  $\xi=2$  and

5%. This circumstance is in accordance with the conclusion of Uang and Bertero (1990).

### 4.3 Representation of Damping Effect on the Seismic Input Energy

Although seismic input energy ( $E_I/m$ ) imparted into a structure is a function of earthquake, soil and the structural characteristics; the damping properties of structure is currently assumed to be negligible. However, the seismic energy formulations (equations 1.1 and 1.2) are derived from the top responses of *SDOF* systems, where damping is a significant parameter. The spectral velocity and acceleration curves of *Erz-EW* (see Table 4.2) for 0, 2, 5 and 10% damping ratios are generated by PW-SPECTs, Figure 4.18. The spectra have dissimilar shapes, especially for some specific periods. For instance, there are substantial differences at periods of 0.30, 0.66 and 1.67 s that represent low- and mid-rise structures.

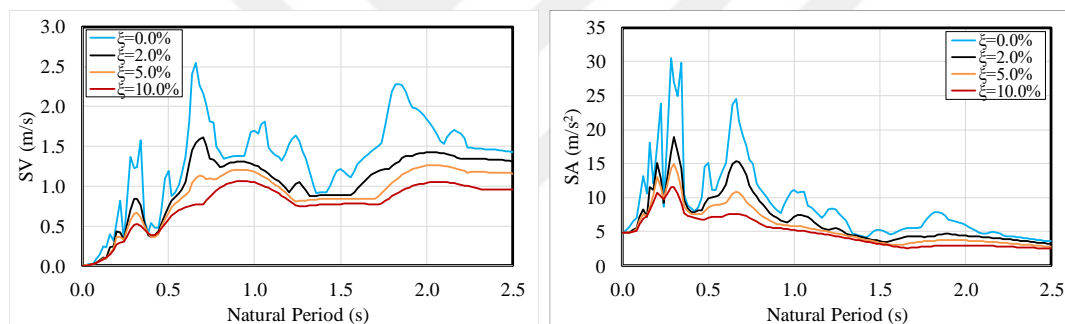


**Figure 4.18 :** Velocity and acceleration spectra of *Erz-EW*.

The damping effect on seismic input energy ( $E_I/m$ ) is investigated in both an experimental and numerical manner in this thesis, by using the *SDOF* systems described in Chapter 2. Their damping ratios were determined to be 0.3%. The second group of *SDOF* systems were tested with the displacement transducer positioned at the top of the specimen. The damping ratio was determined to be 3% for these specimens. *SS-CIG* record was utilized for all specimens with a scale factor of 0.25.

The experimentally validated numerical models were not utilized only to reproduce the experimental results, but also to produce the numerical results for different *EQ* records. The experimentally obtained top responses of the specimen ( $T=0.385$  s) are compared with the numerical results for 0.3% and 3.0% damping ratios, Figure 4.19.

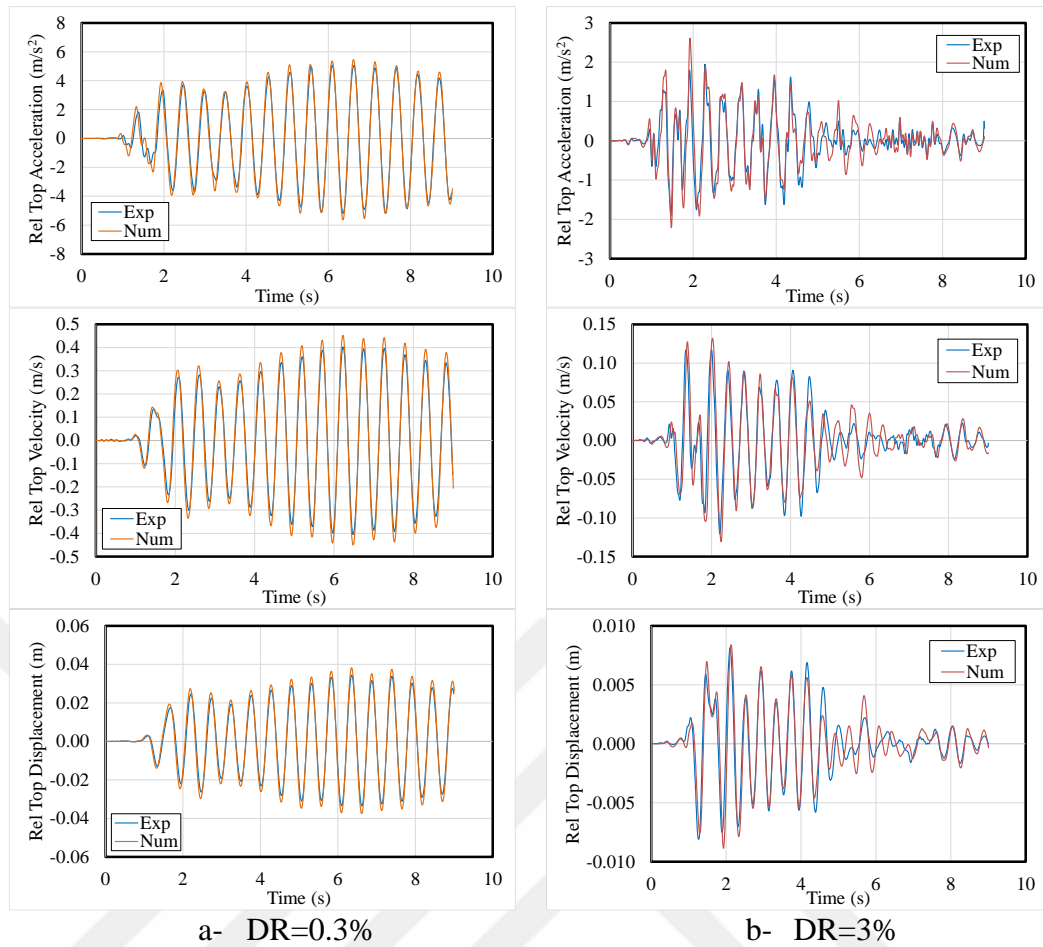


**Figure 4.19 :** The experimental and numerical responses of a *SDOF* system for  $0.25 \times SS-CIG$ .

It is seen that the general forms and intensities of the response parameters, those that are the base parameter of energy calculations, are quite different.

The experimental and numerical seismic energy graphics that were originally obtained in Chapters 2 and 3, are presented for two discrete cases of dampings (0.3 and 3.0%) in Figure 4.20.

From the graphics, it is seen that the damping ratio had an important effect not only the *energy cause to damage* ( $E_I - E_{elastic}$ ) but also the total input energy ( $E_I$ ). The system with 0.3% damping has 10 times greater input energy ( $E_I$ ). Similar distributions were observed for the other components.

The effect of damping ratio (0.3 and 3.0%) are discussed for the tested three discrete *SDOF* systems having vibrational periods of 0.385, 0.526 and 0.667 s in Figure 4.21. Total seismic input energy ( $E_I$ ) and its components are quite different for the systems with 0.385 and 0.526 s vibrational periods. Although the comparable seismic input

energies are obtained for the systems with 0.667 s vibrational periods, the other components are quite different.

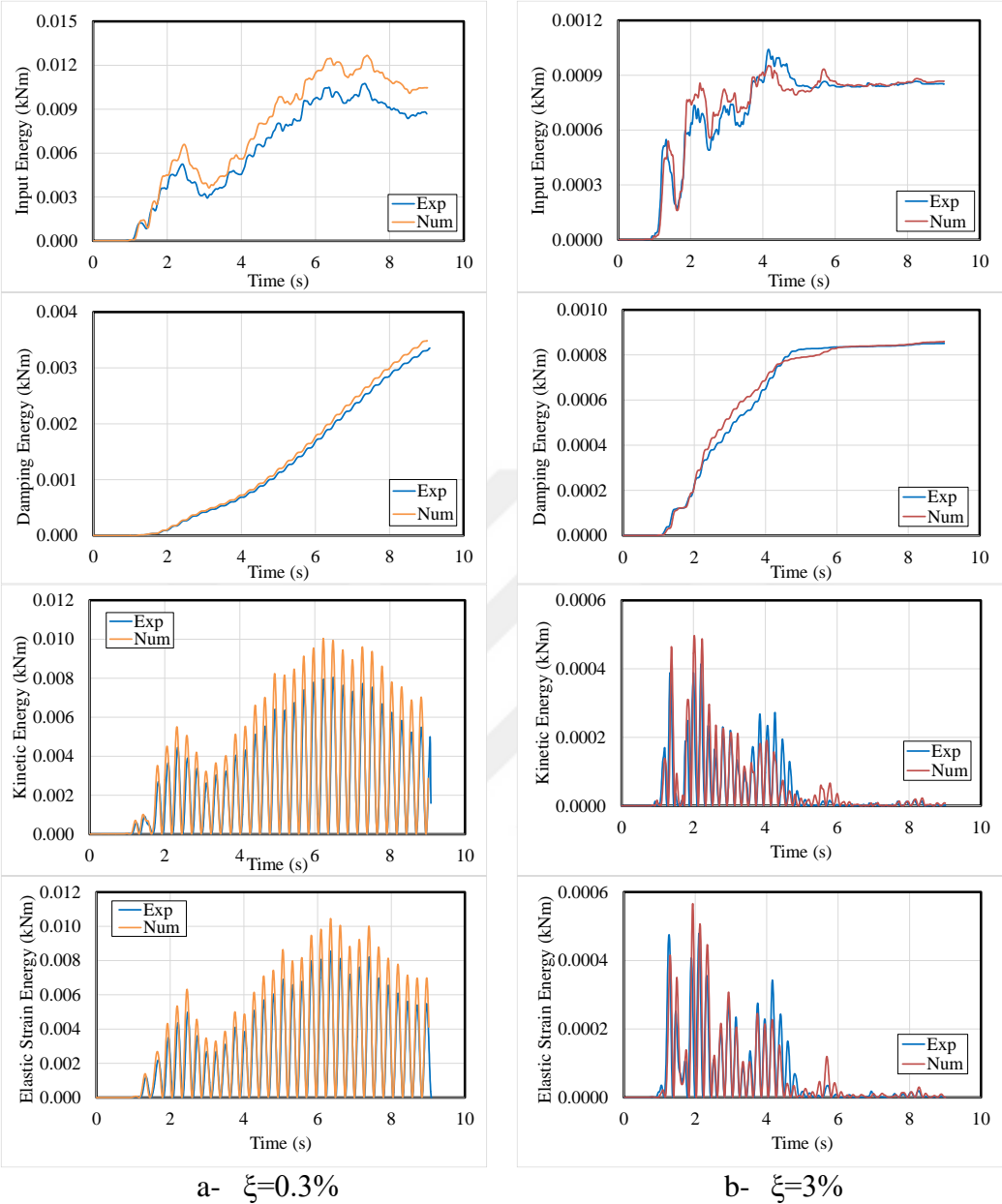


**Figure 4.20** : Seismic energy components of a *SDOF* system for  $0.25 \times SS-CIG$ .

Unexpectedly, the damping energy ( $E_d$ ) of 0.3% damped *SDOF* specimen having 0.385 s vibrational period is higher than the 3% damped one.

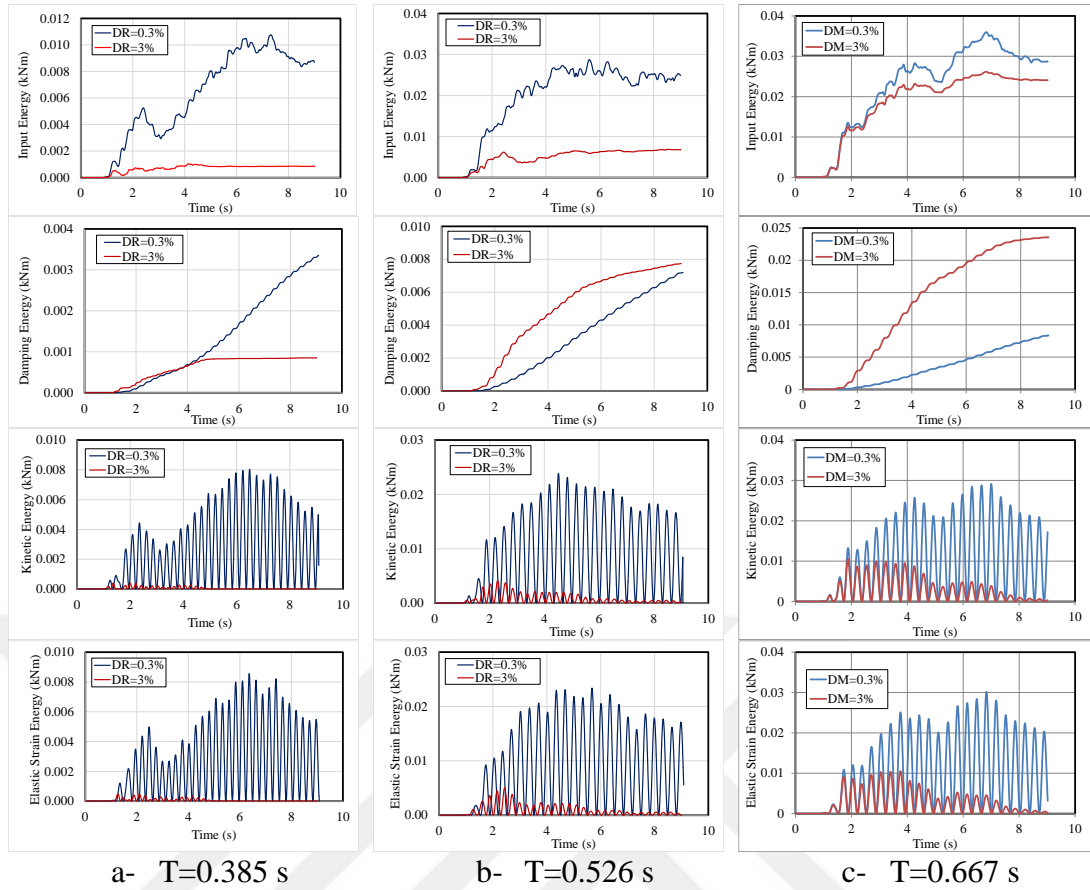


**Figure 4.21 :** Comparisons of experimentally obtained energy terms.

After validation of the numerical models, ten specific *SDOF* systems ( $T= 0.159, 0.277, 0.333, 0.385, 0.454, 0.500, 0.526, 0.667, 1.000, 1.250, 1.667$  and  $2.050$  s) having 0, 2, 5 and 10% damping ratios were analyzed for 7 *EQ* records and are given in Table 4.4.

The  $E_I/m$  intensities (10 periods  $\times$  4 damping ratio = 40 points) computed by means of the numerical model generated in Perform 3D are given together with the *power amplitude* of the *EQ* record, Figure 4.22. The graphics were produced by twin ordinates. The left one represent  $E_I/m$  intensity and the right one corresponds to power amplitude.

**Table 4.4 :** The selected ground motions for the evaluation of damping effect.

Record	Symbol	$M_s$	$d$ (km)	PGA ( $cm/s^2$ )	PGV ( $cm/s$ )
San Salvador 09/10/1986 (Experiment)	SS-E00W	5.40	9.00	857.4	59.3
Erzincan 03/13/1992 Erzincan S.	ERZ-EW	6.90	8.97	486.6	64.3
Duzce_Turkey 1999 Bolu	BOL090	7.14	12.04	790.3	65.8
Chi-Chi, Taiwan 09/20/1999 Cwb 99999 Tcu067 S.	TCU067	7.62	28.70	318.8	66.6
Darfield_ New Zealand 2010 GDLC	GDLCN55W	7.00	1.22	750.0	116.0
Kobe_ Japan 1995 Takatori	TAK090	6.90	1.47	658.3	122.9
Bam_Iran 2003 Bam	BAM-L	6.60	1.70	792.3	124.1
Northridge-01 1994 Sylmar-Converter Sta East	SYL360	6.69	5.30	827.3	129.3

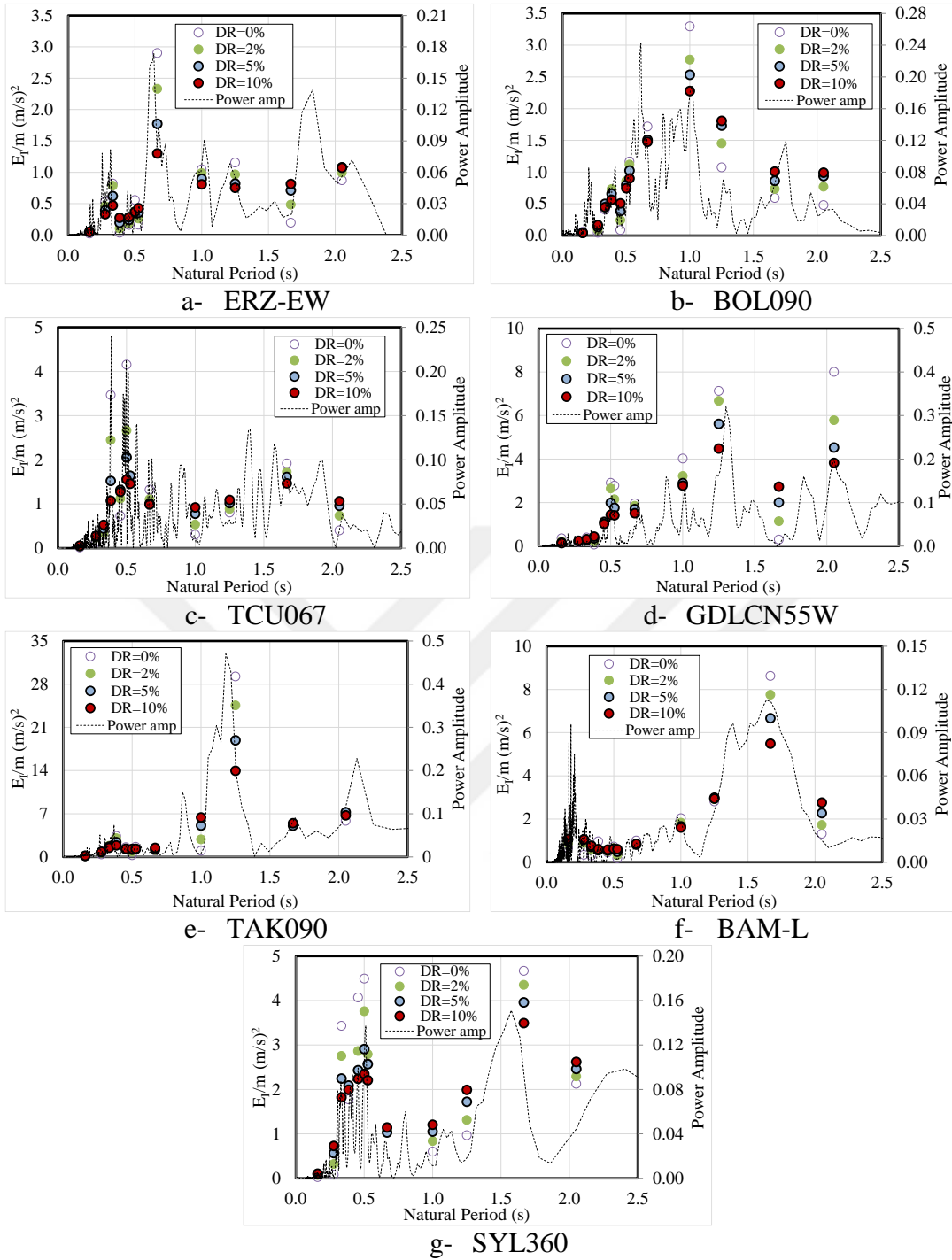


**Figure 4.22 :**  $E_I/m$  intensities and power spectra for the selected  $EQ$  records.

The following results might be driven from Figure 4.22.

- Damping has a significant effect on the seismic input energy ( $E_I$ ) for the systems having resonant periods of the  $EQ$  record.
- Seismic input energy ( $E_I$ ) is barely affected by damping except for the resonant periods of  $EQ$  record, that is the common understanding in the literature.

- Although the seismic input energy ( $E_I$ ) decreases by the increment of damping ratio at the main peaks of power spectrum of  $EQ$ , there is no direct correlation for the other periods. Hence, it will be more realistic to generate the input energy ( $E_I$ ) by considering the damping effect.

When the results of the experimental and numerical works are considered, it is clear that the damping ratio should be contemplated for determination of seismic input energy. Most of the seismic input energy equations given in the literature were generated for a 5% damping ratio. The damping modification factor ( $DMF$ ) is a valuable tool to convert an existing input energy spectrum to another form with a different damping property, (Güllü et al. 2018). However, there are a small number of studies in the literature. One of them is the paper written by Ye et al. (2009) in which the modification factor has been proposed for the spectra generated for 2% damping ratio, equations (4.19) and (4.20). Where  $\xi$  is the damping ratio,  $\mu$  is the displacement ductility and  $NE$  is the normalized seismic energy. However, most of the existing energy spectra given in the literature were produced for a 5% damping ratio. So, the chance of applicability of the equation is very limited.

$$\zeta = \frac{E_{I_{max,\xi,\mu}}}{E_{I_{max,\xi=0.02,\mu=1}}} = \left( 0.6845 - \frac{0.6393}{\mu} - 0.0882 \ln \xi - \frac{0.1517}{\mu} \ln \xi \right) \mu^{-0.57} \quad (4.19)$$

$$NE_{I_{max,\xi,\mu}} = (\zeta + 0.05) \times NE_{I_{max,\xi=0.02,\mu=1}} \quad (4.20)$$

A new, easily applicable damping modification factor ( $DMF$ ) for seismic input energy spectra is proposed in this thesis. The factor has different forms for the three damping ranges, equation (4.22). It can be applied to the input energy spectra generated for 5% damping ratio.

$$DMF = \begin{cases} \frac{1}{2} \times \left( \frac{2+\xi}{7} \right) \rightarrow \xi > \%5 \\ 1 \rightarrow \xi = \%5 \\ 2 \times \left( \frac{2+\xi}{7} \right) \rightarrow \xi < \%5 \end{cases} \quad (4.22)$$

Evaluation of the proposed damping modification factor ( $DMF$ ) is achieved by the comparisons with the factor proposed by Ye et al. (2009) and the specific points (orange dots) that were generated for 12 discrete  $SDOF$  systems for  $EQ$  records given

in Table 4.4. The spectra utilized for this purpose were generated by equation 4.1, Figure 4.23.

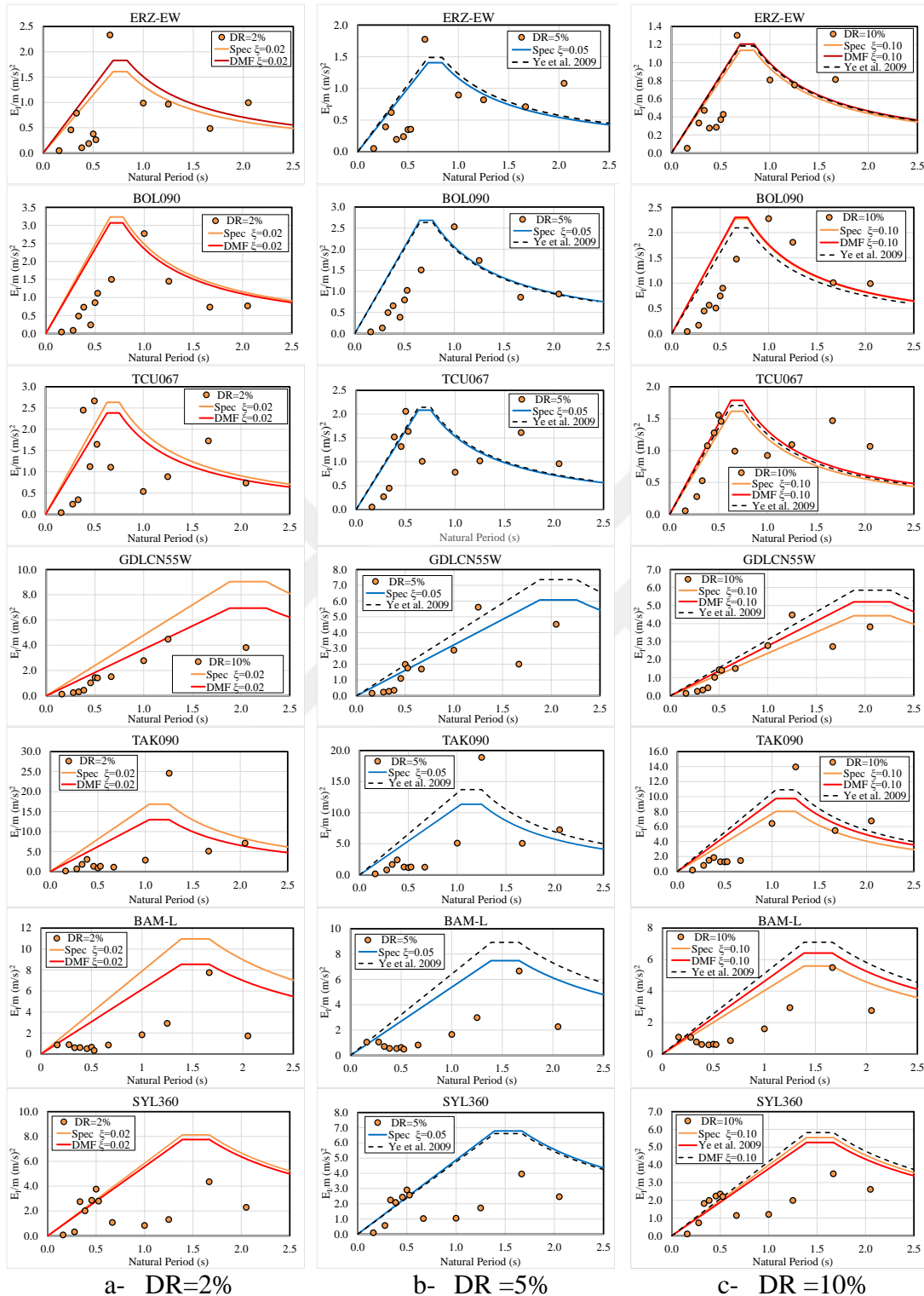


**Figure 4.23 :** Comparison of the damping modification factors with the spectral equation.

The proposed modification factor and the alternative one are based on 5% and 2% damping ratios, respectively. While the proposed factor is evaluated for 2 and 10%,

the other one is assessed for 5 and 10% damping ratios. It is clearly seen that the plateau of the seismic input energy spectra decreases by the increment of damping ratio.

Another evaluation process of the two *DMFs* is achieved by the comparison of peaks of “*original*” and “*converted*” spectra, Figure 4.24.

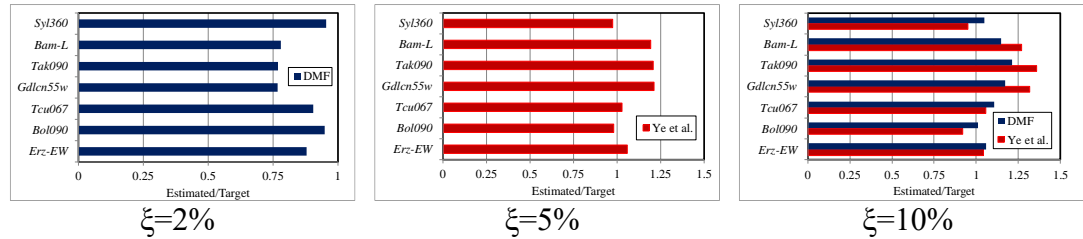


**Figure 4.24 :** The comparisons of the *DMFs*.

Maximum relative differences respect to the “*original*” one are 22% and 36% for the suggested and the other *DMFs*, respectively.

In the following step, the proposed *DMF* was applied to the input energy spectra based on *PSV* and  $V_{eq}$  suggested by Alıcı and Sucuoğlu (2016). The equation that was used for the calculation of input energy is given in equation (4.22). The parameters of the equation that were originally presented in the paper (Alıcı and Sucuoğlu, 2016) are summarized in Table 4.5.

$$V_{eq} / PSV = ae^{-bT} + c \quad (4.22)$$

The *ERZ-EW* record was utilized for this purpose. The pseudo spectral velocity (*PSV*) of the record was computed by PW-SPECTs. Hereafter,  $V_{eq}$  was extracted from equation 4.22. Then the mass-normalized input energies ( $E_1/m$ ) were computed by equation 1.3. Hence, three independent spectra were generated for 2, 5 and 10% damping ratios.

Subsequently, energy spectra corresponding to 2 and 10% damping ratios were estimated by using the spectrum generated for 5% damping ratio and the suggested *DMF*, Figure 4.25.

The spectra generated by the proposed *DMFs* are reasonably good agreement with the “*original*” spectra. The possible reason for the divergence for some periods is the differences between pseudo velocity spectra (*PSV*) having diverse damping ratios.

**Table 4.5 :** The parameters  $a$ ,  $b$  and  $c$  provided by Alıcı and Sucuoğlu (2016).

T	$\xi=2\%$			$\xi=5\%$			$\xi=10\%$		
	a	b	c	a	b	c	a	b	c
0.04	0.6662	9.8456	0.6913	0.7066	8.6722	0.7266	0.7321	7.9524	0.7493
0.1	0.9367	1.6342	0.9429	1.0832	0.1650	1.0750	1.1973	1.0100	1.174
0.2	0.9433	1.2842	0.9536	1.1458	0.2638	1.1178	1.3265	0.7183	1.2435
0.3	0.9300	1.234	0.9483	1.1501	0.4944	1.1097	1.3555	0.2593	1.234
0.4	0.9325	1.1691	0.9549	1.1598	0.5955	1.1055	1.3752	0.0035	1.219
0.5	0.9402	1.1199	0.9638	1.1831	0.6280	1.1087	1.411	0.1088	1.2077
0.6	0.9573	1.0712	0.9766	1.2082	0.6457	1.111	1.4459	0.1828	1.1932
0.7	0.971	1.0415	0.9856	1.2369	0.6524	1.113	1.4837	0.2275	1.1759
0.8	1.0037	0.9954	1.0016	1.273	0.6464	1.1158	1.5229	0.2559	1.1551
0.9	1.0296	0.9671	1.012	1.3155	0.6323	1.1178	1.5766	0.2511	1.1257
1.0	1.0552	0.9447	1.0203	1.3565	0.6211	1.1164	1.6276	0.2466	1.0891
1.1	1.0924	0.9157	1.0306	1.4106	0.5953	1.114	1.6896	0.2214	1.0344
1.2	1.1313	0.8897	1.0391	1.4566	0.5797	1.1065	1.7446	0.2203	1.002
1.3	1.1674	0.8695	1.0448	1.5068	0.5595	1.0955	1.7956	0.3269	1.1461
1.4	1.209	0.8475	1.05	1.557	0.5395	1.0804	1.847	0.317	1.1108
1.5	1.2509	0.8276	1.0534	1.6061	0.5204	1.0613	1.8981	0.3048	1.0685
1.6	1.3005	0.8039	1.0563	1.6614	0.4945	1.0354	1.9527	0.286	1.0146
1.7	1.342	0.7872	1.0562	1.7156	0.4697	1.004	2.0076	0.265	0.9492
1.8	1.4065	0.7556	1.0563	1.7741	0.4506	0.9811	2.1992	0.491	1.2982
1.9	1.4579	0.7336	1.0529	1.8255	0.515	1.0735	2.2743	0.4911	1.2947
2.0	1.5162	0.7071	1.047	1.884	0.4908	1.0477	2.3548	0.489	1.2922
2.2	1.639	0.6491	1.0246	2.0144	0.4259	0.9634	2.5288	0.4784	1.2888
2.4	1.7752	0.5871	0.9892	2.3087	0.5874	1.1859	2.6919	0.4666	1.2793
2.6	1.9016	0.5966	1.0219	2.4826	0.5719	1.1844	2.8431	0.4501	1.264
2.8	2.1786	0.6777	1.107	2.6554	0.5541	1.1805	2.9707	0.428	1.2383
3.0	2.3907	0.651	1.1119	2.8201	0.5319	1.1734	3.0649	0.3998	1.1945
3.5	2.8736	0.5813	1.1102	3.1056	0.4451	1.1053	3.1822	0.2616	0.8325
4.0	3.1446	0.4549	1.0317	4.6007	0.5093	1.1877	5.247	0.4583	1.2609

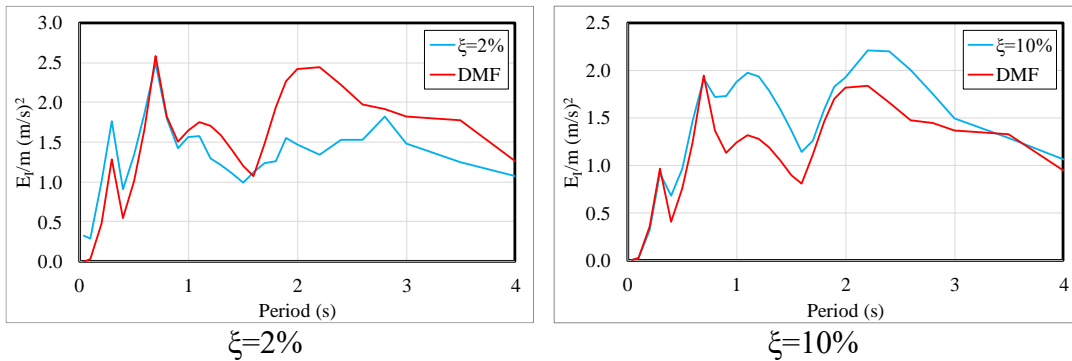


**Figure 4.25 :** Comparison of the input energy spectra constructed by using  $PSV$  values and proposed damping modification factor.

The proposed *DMFs* given in equation 4.21 are reasonably successful for the generation of energy input spectra and it may be utilized as an efficient tool in the calculations.

#### 4.4 Seismic Input Energy as an Earthquake Intensity Measure

The destructivity potentials of *EQs* can be estimated by using various parameters that are called *intensity measures*. They are rational tools which may be used to evaluate *EQs* prior to dynamic tests and nonlinear analyses with reducing computational costs and increasing confidence level (Avşar and Özdemir 2013). The optimum intensity measure will reduce the variability in the predicted response, (Dashti and Karimi 2017). Similarly, Kramer and Mitchell (2006) observed that by using an optimum intensity measure to select and scale *EQs* in the analyses, this will reduce variability and improve the confidence in the predicted engineering demand parameters. Bojorquez et al. (2017) also mentioned that intensity measures have some relationship with the structural demand parameters that is the key issue to reduce uncertainties on the estimation of seismic response.

Peak values of the records specifically peak ground acceleration (*PGA*), peak ground velocity (*PGV*) and peak ground displacement (*PGD*) were examined as intensity measures. Many researchers (Sucuoğlu and Nurtuğ 1995, Vamvatsikos and Cornell 2002) considered *PGV/PGA* ratio should be an independent intensity measure instead of peak values. They concluded that an increase of the ratio results in heavier damage to the structural members. Since the ratio reaches higher values for near-fault type records, it is considered as a separator for near-fault and far-field type *EQ* records.

Root mean squares (*RMS*) values of *EQ* record were suggested as an intensity measure since they much more effective to measure energy content of a seismic action (McCann 1980). The equations for acceleration, velocity and displacement data are given in equations (4.23), (4.24), (4.25).

$$a_{RMS} = \sqrt{\frac{1}{t} \int_0^t [a(t)]^2 dt} \quad (4.23)$$

$$v_{RMS} = \sqrt{\frac{1}{t} \int_0^t [v(t)]^2 dt} \quad (4.24)$$

$$d_{RMS} = \sqrt{\frac{1}{t} \int_0^t [d(t)]^2 dt} \quad (4.25)$$

Arias (1970) proposed an intensity measure that was named by his name. It considers total energy acting on the unit mass in an elasto-plastic systems, equation (4.26). The suggested formulation for *Arias intensity* ( $I_a$ ) is compatible with a variety of structural periods.

$$I_a = \frac{\pi}{2g} \int_0^{t_d} a^2(t) dt \quad (4.26)$$

The acceleration level corresponding to 95% of  $I_a$  is suggested as an intensity measure called the *A95* parameter (Sarma and Yang 1987).

*Characteristic intensity* ( $I_C$ ) is considered to be a more realistic measure to assess structural damage due of *EQ*. It deliberates acceleration *RMS* ( $a_{RMS}$ ) and the record duration ( $t$ ), equation (4.27), (Park et al. 1985).

$$I_C = a_{RMS}^{1.5} \sqrt{t} \quad (4.27)$$

*Cumulative absolute velocity* (*CAV*) was proposed by EPRI-NP-5930 (1988) and it was adopted for nuclear industry applications by Kramer (1996), equation (4.28). *CAV* was utilized as a local damage indicator for the instrumented buildings by Muin and Mosallam (2017). They concluded that, even though further research is necessary for assessing and quantifying the damage detection by *CAV*, it can be applied to the instrumented structures.

$$CAV = \int_0^t |a(t)| dt \quad (4.28)$$

Sarma (1971) proposed a velocity-based intensity measure called *specific energy density* (*SED*), equation (4.29).

$$SED = \int_0^t [v(t)^2] dt \quad (4.29)$$

*Acceleration and velocity spectrum intensities* (*ASI* and *VSI*) were proposed as the indicators for structural damages by Von Thun et al. (1988), Equations 4.30 and 4.31.

$$ASI = \int_{0.1}^{0.5} SA(\xi = 5\%, \tau) d\tau \quad (4.30)$$

$$VSI = \int_{0.1}^{2.5} SV(\xi = 5\%, \tau) d\tau \quad (4.31)$$

Housner (1952) demonstrated that maximum strain energy is related to the pseudo velocity spectrum. *Housner intensity (HI)* integrates a 5% damped pseudo velocity spectrum between  $T=0.1$  s and  $T=2.5$  s, alike to *VSI*, equation (4.32).

$$HI = \int_{0.1}^{2.5} PSV(\xi = 5\%, \tau) d\tau \quad (4.32)$$

Nutli (1979) utilized the third absolute extreme acceleration and velocity intensities in the histories as intensity measures. They are called the *sustained maximum acceleration* and *velocity (SMA and SMV)*.

Benjamin and Associates (1988) proposed an intensity measure called the *effective design acceleration (EDA)*. They filtered the original acceleration data by a low-pass filter with 9 Hz cut-off frequency. They considered the maximum acceleration in the revised data as the intensity measure.

Fajfar (1990) proposed an intensity measure to estimate possible damages on the structure after an *EQ*. *Fajfar intensity (IF)* is the product of *PGV* and  $t_d^{0.25}$ , equation (4.33).

$$IF = PGV \times t_d^{0.25} \quad (4.33)$$

Dashti et al. (2010) suggested the *shaking intensity rate (SIR)* as an intensity measure, equation (4.34). Numerical parametric studies were performed by Dashti and Karimi (2017) to assess the success of some intensity measures, including *SIR*, on liquefaction hazards on shallow-founded structures. They concluded that pseudo spectral acceleration at the first vibration period of the structure ( $PSA(T_1)$ ), *PGA* and *Ia* were found to be the best combination of efficiency, sufficiency and predictability.

$$SIR = I_{a_{5-75}} / t_{d_{5-75}} \quad (4.34)$$

Lin et al. (2013) exposed the importance of structural period on the intensity based assesment. Jager and Adam (2013) nominated a new intensity measure in which a 5% damped *PSA* at dominant period of equivalent *SDOF* system is utilized. Related to these studies, Tsantaki et al. (2017) suggested two alternative intensity measures given in equations (4.35) and (4.36). The first one is based on the geometric mean of *PSA* in

a certain period interval. Optimum lower and upper bounds for the period interval were suggested as the period of *SDOF* system and its 1.6 times, equation 4.35. The second intensity measure is a 5% damped *PSA* at the system period that is obtained by considering the second order effects. The period elongation of the system is computed through equation 4.36 where  $\theta$  is the stability coefficient.

$$PSA_{geo}(T_1, T_n) = \left( \prod_{i=1}^n PSA(T_i) \right)^{1/n} \quad (4.35)$$

$$T_{SDOF}^{P-\Delta} = T_{SDOF} \sqrt{1/(1-\theta)} \quad (4.36)$$

Bojorquez et al. (2017) proposed two independent intensity measures named as  $I_{Np}$  and  $I_B$ . The first one ( $I_{Np}$ ) considers nonlinear behavior of steel frame type structures through  $N_p$  parameter, equations (4.37) and (4.38). The second one ( $I_B$ ) accounts for the effect of the higher modes by  $R$  parameter, equation (4.39).  $R$  is ratio of  $i^{th}$  natural period ( $T_i$ ) to the first one ( $T_1$ ).

$$N_p = \frac{\prod (S(T_1), S(T_2), \dots, S(T_n))}{S(T_1)} \quad (4.37)$$

$$I_{Np} = Sa(T_1) N_p^{0.4} \quad (4.38)$$

$$I_B = S(T_1) N_p^{0.4} \prod_{i=2}^n R^{0.2} \quad (4.39)$$

Rathje et al. (1998) proposed the *mean period* ( $T_m$ ) as an effective and simple indicator for the frequency content characterization, equation (4.40).  $C_i$  and  $f_i$  are the amplitude and frequency corresponding to the discrete modes in the Fourier transform, respectively.

$$T_m = \frac{\sum C_i^2 / f_i}{\sum C_i^2} \quad (4.40)$$

Several different duration based intensity measures exist in the literature, such as *bracket duration* ( $t_b$ ), *uniform duration* ( $t_u$ ) and *effective duration* ( $t_e$ ). Additionally, Riddell (2007) pointed out that consideration of the duration increases the correlation between seismic intensity measure and engineering demand parameters.

Yakut and Yilmaz (2008) carried out a comprehensive numerical study to investigate the correlation between interstorey drifts of frame type structures and some existing intensity measures. It was concluded that spectrum based intensity measures are the most reliable ones between the period ranges of 0.2 and 1.1 s.

Most of the existing intensity measures generate the same results for the different structures because they are free from the structural properties. Lin et al. 2013 pointed out that more efficient and sufficient intensity measures should consider both structural and *EQ* characteristics. Moreover, Sandikkaya and Akkar 2017 declared that the characterization of an *EQ* should be based on amplitude, duration and frequency content.

Consequently, a novel intensity measure ( $I_{EQS}$ ) based on acceleration (*SA*) and velocity (*SV*) spectra, duration ( $t_d$ ) and frequency content ( $T_C$ ) of *EQ* as well as damping ( $\xi$ ) and vibrational characteristics ( $T$ ) of the structure is proposed here, equation (4.41). Where *cumulative damage potential* ( $I_e$ ) is calculated by equation 1.5.

$$I_{EQS} = \sqrt[3]{SA(\xi, T) \times SV(\xi, T) \times T_C \times I_e \times t_d} \quad (4.41)$$

Efficiency, sufficiency and predictability are essential criteria to evaluate the intensity measures (Tothong and Cornell 2008). The intensity measures given in the literature and the proposed one ( $I_{EQS}$ ) are correlated with the results of shake table tests. The intensity measures are classified into three main groups, Table 4.6.

**Table 4.6 :** The sub-groups for intensity measures

Record history based			Spectrum based	Duration or period based
Displacement	Velocity	Acceleration		
PGD	PGV	PGA	ASI	IF
d <sub>RMS</sub>	v <sub>RMS</sub>	a <sub>RMS</sub>	VSI	I <sub>C</sub>
	CAV	I <sub>a</sub>	HI	SIR
	SED	I <sub>C</sub>	PSA	t <sub>d</sub>
	IF	SIR	PSA <sub>P-Δ</sub>	t <sub>u</sub>
	SMV	SMA	PSA <sub>geomean</sub>	t <sub>b</sub>
		A95	I <sub>Np</sub>	t <sub>e</sub>
		EDA	I <sub>B</sub>	T <sub>m</sub>
		I <sub>EQS</sub>	I <sub>EQS</sub>	T <sub>p</sub>
				I <sub>EQS</sub>

The nonlinear relationship between the computed *intensity measures* (*IM*) and the *engineering demand parameters* (force, displacement etc.) can be defined by a standard power function obtained from the nonlinear regression analyses, equations (4.41). Where *EDP* and *IM* stands for *engineering demand parameter* and *intensity measure*, respectively. The relation can also be expressed in the logarithmic form as suggested by Mollaioli et al. (2013), equation (4.42).

$$EDP = \alpha(IM)^\beta \quad (4.41)$$

$$\ln(EDP) = \ln(\alpha) + \beta \ln(IM) \quad (4.42)$$

However, instead of the use of equations (4.41) and (4.42), *Pearson's linear correlation coefficient ( $\rho$ ) method* can also be utilized to show the efficiency, sufficiency and sensitivity of the intensity measure, equation (4.43) where  $n$  is the number of data points,  $X$  and  $Y$  are the data series. The coefficient “ $\rho$ ” varies between -1.0 and 1.0 that yields negative and positive correlations, respectively.

$$\rho = \frac{n\sum XY - (\sum X)(\sum Y)}{\sqrt{(n\sum X^2 - (\sum X)^2) \times (n\sum Y^2 - (\sum Y)^2)}} \quad (4.43)$$

The steel cantilever columns used in the experimental study (Chapter 2.2) with natural periods of 0.385, 0.526 and 0.667 s were subjected to *SS-CIG* and *CH-N10E* records with 0.25 scaling factor. The *engineering demand parameter (EDP)* is selected as the ratio of the maximum overturning moment to the yielding moment ( $M/M_y$ ), Figure 4.26a.

The proposed equation as an intensity measure ( $I_{EQS}$ ) gives the results shown in Figure 4.26b.

When Figures 4.26 a and b are compared, it can be seen that the order of  $IM$  ( $I_{EQS}$ ) is similar with  $EDP$  ( $M/M_y$ ).

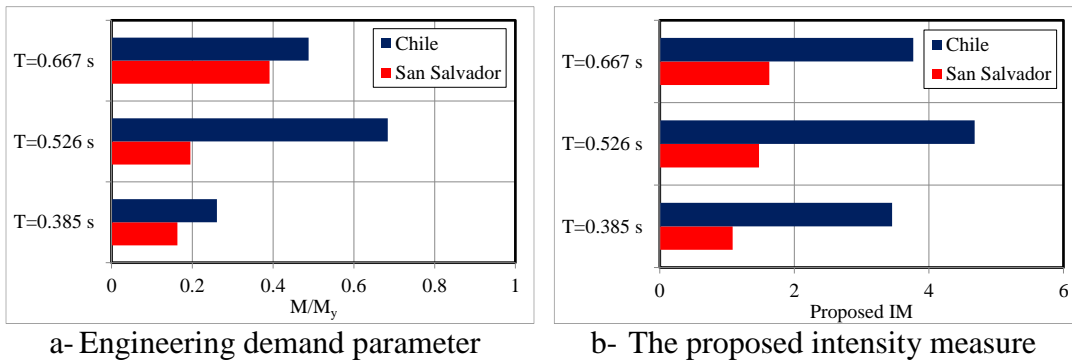


**Figure 4.26 :** Engineering demand parameter and proposed intensity measure results.

The comparison of the various intensity measure results are evaluated for the steel columns with 0.385, 0.526 and 0.667 s natural periods, Table 4.7. The comparisons are made for two specific *EQs* (*SS-CIG* and *CH-N10E*) that have relatively different energy contents, see Chapter 2.1.

**Table 4.7** : The comparisons of various intensity measures.

IM	T= 0.385 s		T=0.526 s		T=0.667 s	
	SS-CIG	CH-NH10E	SS-CIG	CH-NH10E	SS-CIG	CH-NH10E
PGA (m/s <sup>2</sup> )	1.726	1.197	1.726	1.197	1.726	1.197
PGV (m/s)	0.142	0.092	0.142	0.092	0.142	0.092
PGD (m)	0.026	0.025	0.026	0.025	0.026	0.025
PGV / PGA (s)	0.082	0.077	0.082	0.077	0.082	0.077
a <sub>RMS</sub> (m/s <sup>2</sup> )	0.313	0.177	0.313	0.177	0.313	0.177
v <sub>RMS</sub> (m/s)	0.038	0.015	0.038	0.015	0.038	0.015
d <sub>RMS</sub> (m)	0.010	0.004	0.010	0.004	0.010	0.004
I <sub>a</sub> (m/s)	0.142	0.583	0.142	0.583	0.142	0.583
I <sub>c</sub>	0.526	0.802	0.526	0.802	0.526	0.802
SED (m <sup>2</sup> /s)	0.013	0.028	0.013	0.028	0.013	0.028
CAV (m/s)	1.796	12.301	1.796	12.301	1.796	12.301
ASI (m/s)	1.312	1.117	1.312	1.117	1.312	1.117
VSI (m)	0.571	0.508	0.571	0.508	0.571	0.508
HI (m)	0.541	0.447	0.541	0.447	0.541	0.447
SMA (m/s <sup>2</sup> )	0.944	0.971	0.944	0.971	0.944	0.971
SMV (m/s)	0.107	0.088	0.107	0.088	0.107	0.088
EDA (m/s <sup>2</sup> )	1.728	1.197	1.728	1.197	1.728	1.197
A95(m/s <sup>2</sup> )	1.713	1.163	1.713	1.163	1.713	1.163
T <sub>p</sub> (s)	0.320	0.220	0.320	0.220	0.320	0.220
T <sub>m</sub> (s)	0.619	0.425	0.619	0.425	0.619	0.425
t <sub>d</sub> (s)	5.750	43.015	5.750	43.015	5.750	43.015
t <sub>u</sub> (s)	6.370	49.495	6.370	49.495	6.370	49.495
t <sub>b</sub> (s)	7.975	110.230	7.975	110.230	7.975	110.230
t <sub>e</sub> (s)	5.065	43.500	5.065	43.500	5.065	43.500
IF	0.128	0.197	0.128	0.197	0.128	0.197
SIR (m/s <sup>2</sup> )	0.061	0.014	0.061	0.014	0.061	0.014
PSA(T <sub>i</sub> ) (m/s <sup>2</sup> )	2.453	2.865	3.014	2.784	2.883	1.901
PSA <sub>P-Δ</sub> (T <sub>i</sub> ) (m/s <sup>2</sup> )	2.762	2.83	2.819	1.753	2.108	2.159
PSA <sub>geomean</sub> (m/s <sup>2</sup> )	2.659	2.733	2.725	2.278	2.166	1.775
I <sub>Np</sub> (m/s <sup>2</sup> )	5.797	7.734	6.587	6.847	5.260	3.170
<b>IEQS</b>	<b>1.081</b>	<b>3.451</b>	<b>1.473</b>	<b>4.679</b>	<b>1.626</b>	<b>3.766</b>

The success of various *IMs* might be evaluated by comparing their results with Figure 4.26a. From the comparisons, one can see that the *IMs* that account for the duration of *EQ* are more successful, since durations of *CH-NIOE* and *SS-CIG* records are quite different as 116.345 and 9.02 s, respectively. Those intensity measures are *I<sub>a</sub>*, *I<sub>c</sub>*, *SMA*, *CAV*, *SED* and *IF*.

The *IMs* that consider the spectral accelerations and structural period are the most successful when compared to the others, Table 4.7. Although; *PSA*, *PSA<sub>P-Δ</sub>*, *PSA<sub>geomean</sub>*

and  $I_{Np}$  consider only the structural periods,  $I_{EQS}$  accounts both structural period and damping. The comparisons of these  $IMs$  are made through the radar shaped graphics, Figure 4.27, where the numbers in the graphics represent the correlation coefficients.

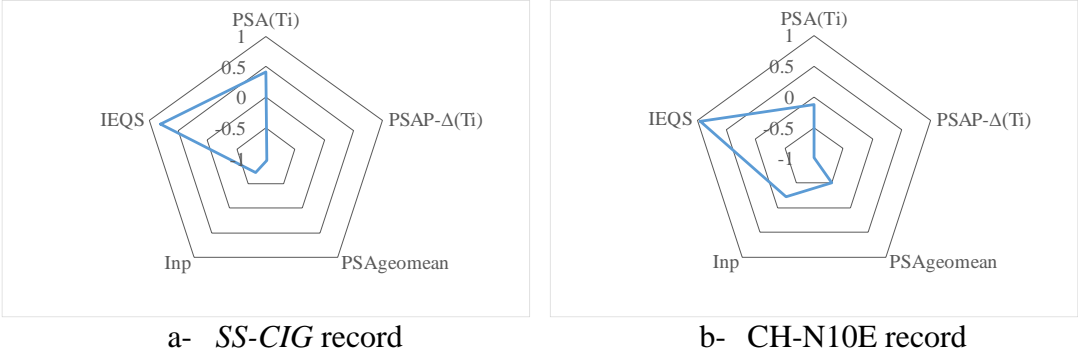


**Figure 4.27 :** Correlation coefficients of the existing and proposed intensity measures.

The proposed intensity measure ( $I_{EQS}$ ) has a very strong correlation ( $\rho=0.811$  and  $0.955$ ) with the experimental results.

From the numerical evaluations, the information can be obtained that  $EQ$  duration, period and damping property of the structural system are the crucial variables in the success of  $IM$ .

## 5. PREDICTION OF THE CRITICAL DISPLACEMENT

The estimation of the inelastic top displacement demand of a structural system is a crucial work for some nonlinear analyses procedures, Sürmeli and Yüksel (2015) and Chopra and Goel (2002).

The modal push-over analyses (*MPA*) technique requires a capacity curve consisting of modal displacement and modal acceleration, (*ADRS*). Subsequently, the displacement demand of the *MDOF* system is computed through nonlinear time history analyses and utilized in the nonlinear analysis procedure.

The *hybrid energy spectrum* depending on the energy equations is proposed here to estimate the storey displacements of *MDOF* systems. This can make the *MPA* procedures more desirable.

The procedure to determine the hybrid energy spectrum uses the *equivalent energy rule*. It can consider the *higher mode effect*. Initially, the mass-normalized relative seismic input energy spectrum ( $E_I/m$ ) is generated by the procedures described in Chapters 4.2.1 and 4.2.2. Secondly, the modal analysis should be performed to find out vibrational characteristics of the system.

The vertical axis of the hybrid energy spectrum ( $E_I/m$ ) represents summation of the mass normalized relative seismic input energies  $(E_I/m)_i$  corresponding to the sufficient number of vibrational modes.  $(E_I/m)_i$  values are combined by using the equation (5.1) where  $\Gamma_i$  is modal participation factors. Modal properties of the structure was also utilized in Leelataviwat et al. (2009), Benavent-Climent and Zahran (2010), Benavent-Climent (2011), Benavent-Climent et al. (2014) and Ke and Chen (2014).

$$EI / m = (EI / m)_1 \times \Gamma_1 + (EI / m)_2 \times \Gamma_2 + \dots + (EI / m)_n \times \Gamma_n \quad (5.1)$$

Horizontal axis corresponds to record specific spectral displacements (*SD*).

A special procedure is defined to determine the spectral displacement corresponding to the combined  $(E_I/m)$ . A definition for the angle of " $\alpha$ " is achieved for this purpose, see equation (5.2).

$$\alpha = \frac{SV(T_1, \xi)^2}{n \times SD(T_1, \xi)} \quad (5.2)$$

Where  $SV$  and  $SD$  are spectral velocity and displacement, respectively.  $T_1$  and  $\xi$  are the vibrational period and damping ratio corresponding to the dominant mode. “ $n$ ” is a variable that defines the relation between  $SV$  vs.  $(E_I/m)$  and it varies between the range of 0.5 and 2.0.

An inclined line is drawn on the hybrid spectrum by using the calculated “ $\alpha$ ” angle. The broken horizontal line (1) is initiated from the combined  $(E_I/m)$  and intersected with the inclined line. After that a vertical line (2) is drawn from the point to determine spectral displacement ( $SD$ ), Figure 5.1b.

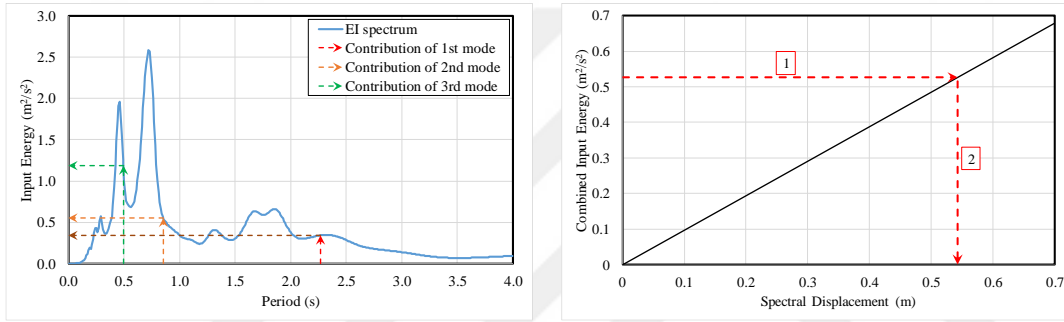


**Figure 5.1** : Application of the proposed method

The physical top displacements of the system are calculated from the spectral displacement ( $SD$ ) by equation (5.3) where  $j$  is mode number,  $N$  is the number of modes considered in the analyses,  $n$  is the storey number,  $\Gamma$  is modal participation factor and  $\Phi$  is modal displacement.

$$u_{jn} = \sum_{j=1}^N \Gamma_j \phi_{jn} SD \quad (5.3)$$

### 5.1 A Demonstrative Example

The inelastic displacement demands of 9- and 20-storey *SAC LA* benchmark steel frames (Figures 5.2 and 5.3) that designated as *MI* model (Gupta and Krawinkler 1999), were calculated by using the proposed procedure for a set of EQs, Table 5.1. The elastic spectral accelerations of the selected records and their arithmetic and geometric means are presented in Figure 5.4. The buildings have both perimeter and gravity frames. For the sake of simplicity, only the perimeter frames are modelled instead of whole 3D model (Sürmeli and Yüksel 2015).

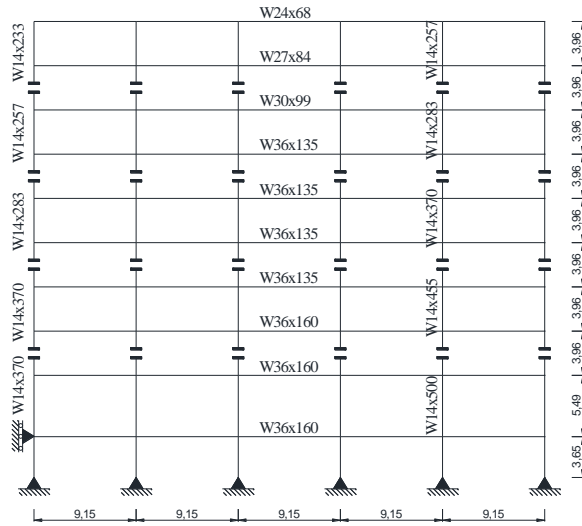


**Figure 5.2 : 9-Story SAC LA frame.**

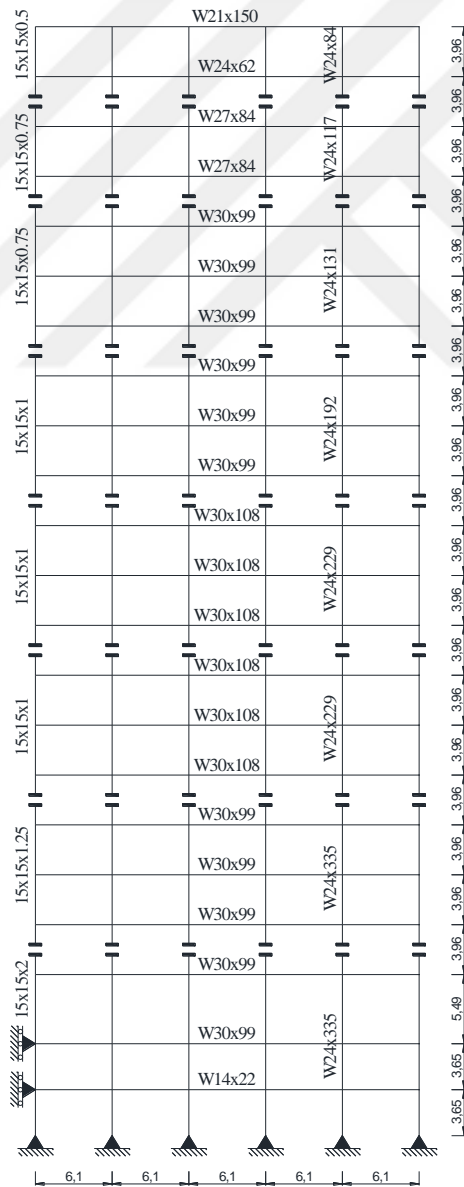


**Figure 5.3 : 20-Story SAC LA frame**

**Table 5.1** : Selected *EQ* records.

#	Record	Symbol	$M_s$	$d$ (km)	PGA	PGV
1	Landers 1992	CLW-TR	7.28	19.74	408.97	42.35
2	Kobe_Japan 1995	NIS090	6.90	7.08	493.20	36.62
3	Kobe_Japan 1995	SHI000	6.90	19.14	238.61	37.80
4	Kocaeli_Turkey	ARC090	7.51	13.49	147.05	39.57
5	Kocaeli_Turkey	DZC180	7.51	15.37	306.20	58.85
6	Chi-Chi_Taiwan	CHY101N	7.62	9.94	431.74	115.04
7	Friuli Italy-01 1976	A-	6.50	15.82	344.65	22.04
8	Duzce_Turkey 1999	BOL000	7.14	12.04	713.76	56.44
9	Imperial Valley-06	H-	6.53	22.03	344.45	33.00
10	Imperial Valley-06	H-E11140	6.53	12.56	357.06	34.44
11	Hector Mine 1999	HEC090	7.13	11.66	330.37	41.74
12	Sen Fernando 1971	PEL180	6.61	22.77	170.87	14.85
13	Superstation Hills-02	B-ICC000	6.54	18.20	351.05	46.36
14	Superstation Hills-02	B-	6.54	11.16	437.85	35.71
15	Loma Prieta 1989	CAP090	6.93	15.23	434.87	29.21
16	Loma Prieta 1989	GO3000	6.93	12.82	544.47	35.68
17	Landers 1992 Yermo	YER270	7.28	23.62	240.15	51.41
18	Northridge-01 1994	LOS000	6.69	12.44	402.25	42.97
19	Chi-Chi Taiwan	TCU045-	7.62	26.00	465.34	36.70

The inelastic behavior of the systems are defined by using plastic hinge theory and the bilinear hysteretic model. 5% damping ratio is considered for both of the systems. The masses, natural periods, modal participation factors are listed in Table 5.2.

**Table 5.2** : The dynamic properties of 9- and 20- storey SAC LA buildings

Mode	Period (s)		Effective mass (%)		Total mass (kNs <sup>2</sup> /m)		Participation Factor ( $\Gamma$ )	
	9-St	20-St	9-St	20-St	9-St	20-St	9-St	20-St
1	2.27	3.82	83.1	80.0			61.24	66.53
2	0.85	1.32	10.9	11.8			22.14	25.50
3	0.49	0.77	3.7	3.5	4500	5538	12.95	13.89
4		0.54		1.8				9.86
5		0.41		1.0				7.38
		$\Sigma=$	97.7	98.1				

Mass-normalized relative seismic input energy terms ( $E_I/m$ ) were computed by equation 4.1 and equation 4.18 for the set of *EQs*, see Table 5.1. The  $E_I/m$  values resulted from the numerical model generated in Perform 3D (squares in Figure 5.4) and the calculated combined input energies (circles in Figure 5.4) are depicted on the graphics corresponding to vibrational periods of the frames.

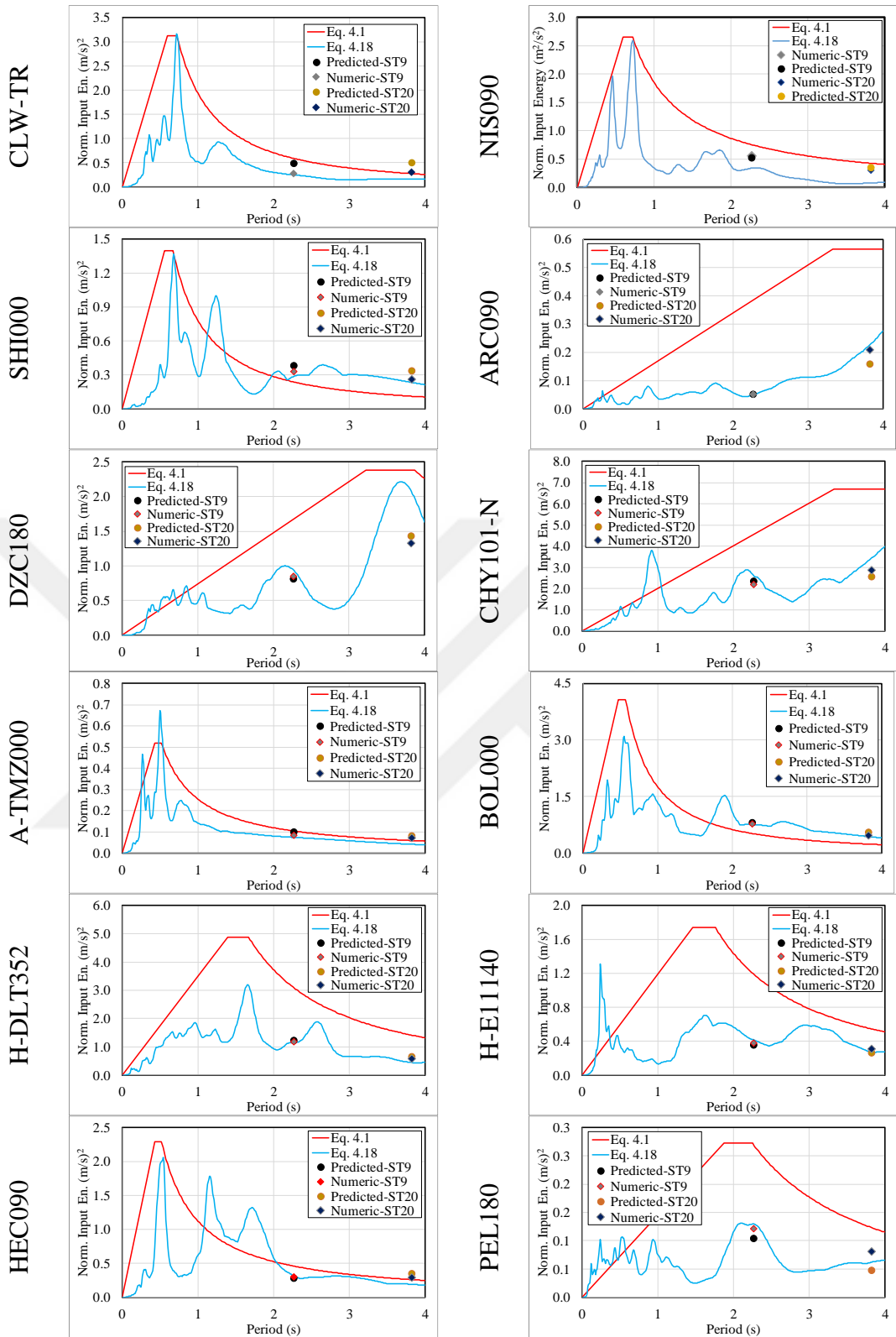


**Figure 5.4 :** Seismic input energy predictions for 9- and 20-story SAC frames.

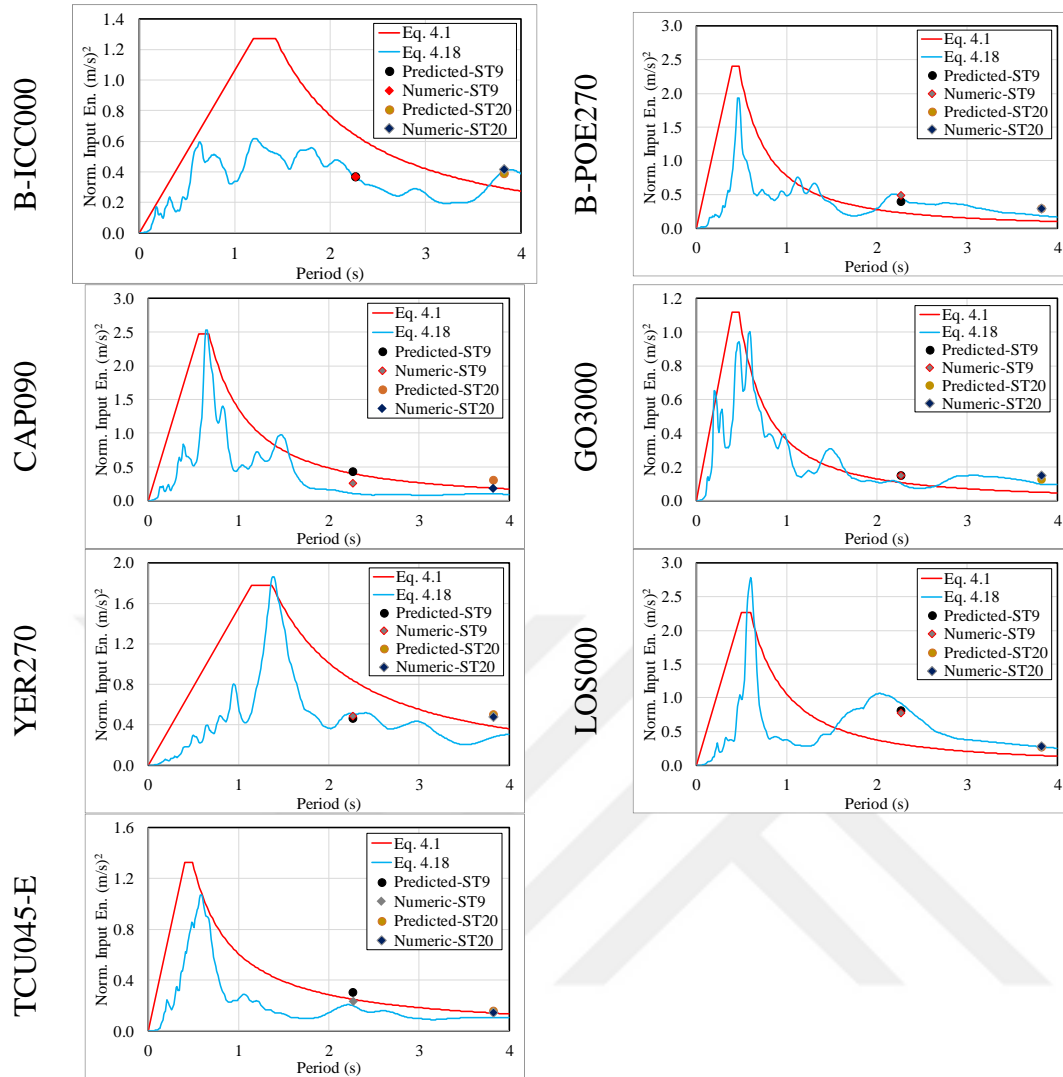


**Figure 5.4 (continued)** : Seismic input energy predictions for 9- and 20-story SAC frames.

The spectral combined input energies  $(E_I/m)_{pre}$  were calculated for 9- and 20-storey SAC LA buildings by using equation 5.1. The estimated combined energies  $(E_I/m)_{pre}$  through equation 4.18 and the “true” one calculated by Perform 3D  $(E_I/m)_{num}$  are presented in columns (2) and (3) of Tables 5.3 and 5.4 for 9- and 20-storey SAC LA buildings, respectively. The *relative percentage differences* between the estimated and “true” input energies are calculated by using the general rule given in equation (5.4).

$$\text{Relative Difference} = \frac{\mathcal{E}_{pre} - \mathcal{E}_{num}}{\left(\mathcal{E}_{pre} + \mathcal{E}_{num}\right) / 2} \quad (5.4)$$

The calculated relative percentage differences are listed in column (4) of Tables 5.3 and 5.4 for arithmetic and geometric means, as well as standard deviations for the data are calculated and given at the bottom of the tables.

The calculated the *covariances* for 9- and 20-storey SAC LA buildings are 0.258 and 0.370. These results represent that there are direct proportionality between  $(E_I/m)_{pre}$  and  $(E_I/m)_{num}$ . The correlation coefficients for the two systems in terms of input energies were calculated as 0.99 for both of the systems.

The spectral displacements (*SD*) are determined through the hybrid spectrums as defined in Figure 5.1. They are given in column (5) of Tables 5.3 and 5.4 for 9- and 20-storey SAC LA buildings, respectively. The procedure is exemplified for *GO3000 EQ* in Figure 5.5.

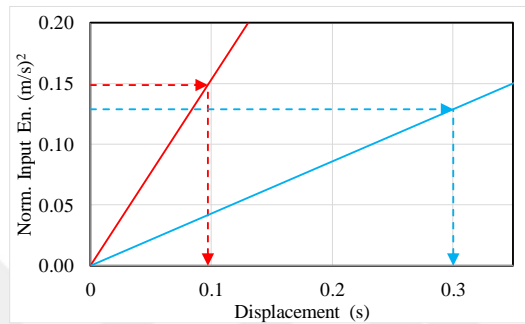


**Figure 5.5 :** Determination of the spectral displacement (*SD*) for 9 (red) and 20 (blue) SAC LA buildings.

The nonlinear displacement demands calculated from the numerical models generated in Perform 3D are presented in column (6) of the Tables 5.3 and 5.4. Arithmetic and geometric means as well as standard deviations for the data are calculated and given at the bottom of the tables. The *relative percentage differences* between the estimated and “*true*” inelastic top displacement demands are computed in column (7) of the tables by using equation (5.4).

The calculated *covariances* for the inelastic top displacement demands of 9- and 20-storey SAC LA buildings are determined as 0.027 and 0.106, respectively. Hence, there are direct proportionality between  $\delta_{pre}$  and  $\delta_{num}$ . The *correlation coefficients* for the inelastic top displacement demands are calculated as 0.900 and 0.853 or 9- and 20-storey SAC LA buildings, respectively.

**Table 5.3 :** Input energy and top displacement predictions for 9-storey frame.

#EQ	$(EI/m)_{pre}$ m <sup>2</sup> /s <sup>2</sup>	$(EI/m)_{num}$ m <sup>2</sup> /s <sup>2</sup>	$\varepsilon_{EI}$ %	$\delta_{pre}$ m	$\delta_{num}$ m	$\varepsilon_{\delta}$ %
(1)	(2)	(3)	(4)	(5)	(6)	(7)
1	0.491	0.283	53.7	0.159	0.142	11.1
2	0.554	0.527	5.0	0.642	0.527	19.7
3	0.381	0.327	15.3	0.411	0.284	36.5
4	0.051	0.052	2.8	0.161	0.123	27.0
5	0.809	0.849	4.8	0.759	0.496	41.9
6	2.335	2.178	7.0	0.699	0.591	16.7
7	0.098	0.083	17.1	0.099	0.096	3.1
8	0.803	0.777	3.2	0.465	0.386	18.7
9	1.214	1.169	3.8	0.585	0.306	62.7
10	0.353	0.378	6.8	0.269	0.347	25.3
11	0.276	0.296	7.0	0.303	0.284	6.5
12	0.104	0.121	15.4	0.200	0.174	14.4
13	0.366	0.365	0.3	0.305	0.291	4.6
14	0.391	0.485	21.5	0.342	0.262	26.8
15	0.428	0.253	51.5	0.216	0.123	54.7
16	0.149	0.150	1.2	0.104	0.102	1.9
17	0.463	0.484	4.6	0.264	0.288	8.7
18	0.814	0.770	5.6	0.327	0.390	17.7
19	0.301	0.230	26.9	0.187	0.173	7.9
Geo. Mean	0.379	0.355	7.1	0.290	0.246	14.9
Ar. Mean	0.546	0.515	13.3	0.342	0.283	21.3
Std	0.523	0.498	15.2	0.201	0.147	16.7
COV		0.258			0.027	
COR		0.990			0.900	

**Table 5.4 :** Input energy and top displacement predictions for 20-storey frame.

#EQ	$(EI/m)_{pre}$	$(EI/m)_{num}$	$\epsilon_{EI}$	$\delta_{pre}$	$\delta_{num}$	$\epsilon_{\delta}$
	$m^2/s^2$		%	m		%
(1)	(2)	(3)	(4)	(5)	(6)	(7)
1	0.511	0.307	49.7	0.262	0.240	8.9
2	0.349	0.233	39.8	0.230	0.209	9.6
3	0.334	0.257	25.8	0.277	0.306	10.1
4	0.159	0.209	27.4	0.400	0.401	0.2
5	1.432	1.329	7.5	1.247	0.916	30.6
6	2.559	2.853	10.9	1.482	1.488	0.4
7	0.081	0.070	14.1	0.155	0.096	47.2
8	0.547	0.463	16.5	0.449	0.428	4.7
9	0.651	0.591	9.6	0.964	0.357	91.8
10	0.260	0.312	18.2	0.598	0.444	29.4
11	0.350	0.290	18.8	0.590	0.317	60.1
12	0.048	0.081	51.2	0.213	0.205	3.5
13	0.390	0.416	6.4	0.961	0.502	62.7
14	0.293	0.291	0.8	0.465	0.281	49.2
15	0.304	0.185	48.6	0.379	0.165	78.9
16	0.129	0.149	14.2	0.319	0.262	19.6
17	0.502	0.481	4.4	0.886	0.481	59.3
18	0.269	0.278	3.0	0.123	0.341	93.9
19	0.158	0.143	9.9	0.173	0.248	35.4
Geo. Mean	0.321	0.302	13.2	0.418	0.334	16.9
Ar. Mean	0.491	0.470	19.8	0.535	0.405	36.6
Std	0.585	0.639	15.9	0.393	0.316	30.3
COV	0.370		0.106			
COR	0.990		0.853			

## 5.2 Discussion on the Results

Depending on the results of the demonstrative example, the following results can be concluded.

- The hybrid spectrum concept ( $SD$  vs. the combined  $E_I/m$ ) yields reasonable results in terms of seismic input energies and inelastic top displacement demands. The obtained correlation coefficients are relatively strong.
- The arithmetic and geometric means will be possibly smaller if the  $EQ$  records are scaled with respect to a specific target spectrum.

- It is considered that the energy spectra formulation given in equation 4.1 can also be utilized for practical purposes.
- The shape of the energy spectrum constructed by equation 4.18 is a good indicator for deciding the number of modes for the analyses.



## 6. CONCLUSIONS AND RECOMMENDATIONS

A comprehensive study to determine the seismic energy components and its application to calculate the inelastic top displacement of skeleton type steel frames has been completed. The study consists of the experimental works performed on *SDOF* and *MDOF* systems and the numerical works on the tested and the supplementary systems.

The energy equations were utilized to evaluate the effect of structural configuration, stiffness, mass and damping on the response control of steel frames.

The results obtained in the study can be classified into four groups. They are given in the following chapter.

### 6.1 Conclusions

#### 6.1.1 General

1. Two equations representing two discrete approaches are proposed to calculate seismic input energy and its components. The equations produce relatively successful results for both far-field and near-fault type *EQs*. Moreover, the damping effect on the seismic input energy can also be considered through the proposed equations.
2. An energy-based procedure was developed to predict the nonlinear top displacement of *MDOF* skeleton type steel structures. The proposed procedure is examined through 9- and 20-story SAC LA frames. It produced about 20% disagreement with the results of the nonlinear time history analyses.
3. The evaluation studies on the structural response control yield the following results:
  - Mass-tuning practice should be applied by considering the frequency content of the *EQ* record.

- Structural damping is effective on the seismic input energy. The maximum effect of damping is expected around the dominant frequencies of the *EQ* record.
  - Mass-normalized seismic input energy is independent from the lateral stiffness of the specimens.
4. A damping modification factor is proposed for seismic input energy spectrum. It can be utilized to convert a specific spectrum to another form for an altered damping ratio.
  5. An *EQ* intensity measure based on the energy equations is suggested. It is assessed through the discrete shake table test results. It showed a strong correlation between the experimental results and the predictions of the suggested new intensity measure.
  6. Since it was not possible to experimentally compare *MDOF* and *SDOF* systems with the same damping ratio, the experimental results obtained for *MDOF* systems are compared with the input energy spectrum produced by PW-SPECTs. It reveals that the seismic input energy imparted into *MDOF* skeleton type steel frames can be estimated by using *SDOF* systems. It makes it possible to easily account for the contribution of higher modes.

### 6.1.2 Experimental study

1. The steel cantilever column tests (*SDOF* systems) result that mass-normalized seismic input energy ( $E_I/m$ ) is not directly proportional to the mass of the system. Frequency content of *EQ* record have a significant effect on  $E_I/m$ .
2. The input energy spectra and attenuation relations that are available in the literature are compared with results of the performed elastic *SDOF* tests. The comparisons display that they are not successful in the estimation of  $E_I/m$  especially around corner period of the *EQ* record.
3. Although the seismic input energy intensities of *BF1* and *BF2* frames are alike due to their similar dominant frequencies, they have quite different plastic energy intensities.

4. The metallic dampers increased the global damping ratio of the system from 2-3% to 5% for *BF1-D1* and *BF2-D1*. Seismic input energy ( $E_I/m$ ) and plastic energy ( $E_p/m$ ) might be decreased by the increment of supplementary damping.
5. The steel cushions used as metallic dampers in this study dissipate a considerable amount of plastic energy ( $E_p/m$ ).
6. Steel cushions were more effective in *BF1*.

### **6.1.3 Numerical studies**

1. The experimental results obtained from the *SDOF* and *MDOF* system tests are represented successfully by the developed numerical models.
2. The plastic energy accumulated from the damages of the primary structural members was reduced considerably by the addition of more steel cushions at upper storeys.
3. The numerical model that has three steel cushions at the first and one at the upper storeys experienced almost zero-damage to the primary structural members.
4. The behavior of steel cushions should be represented in the numerical model not only by the longitudinal stiffness but also the transversal one.

### **6.1.4 Measurement and others**

1. The connection of the displacement transducers to relatively slender specimens resulted in relatively high structural damping.
2. Production of the lateral floor displacements from the acceleration measurements was not successful. Therefore, a non-contact displacement measuring system based on the vision-based algorithm was utilized in the study.
3. The acceleration histories derived from the vision-based displacement history are in good agreement with the results of using accelerometers.
4. The effect of pixel density and *Frame Per Second (fps)* on the quality of vision-based data were discussed by comparing the diverse records. It was realized that the higher resolution is more important for the strain measurements; thus a higher *fps* rate is better for capturing the displacement history in a dynamic test.

5. A simple procedure is developed to generate elastic top displacement history of *SDOF* system through the strain gauge measurements at the bottommost section. The comparisons yield very successful results.

## 6.2 Recommendations

- 1- The ideal *SDOF* and *MDOF* specimens with similar damping properties should be prepared and tested on the shake table to generate the experimental data to be used in the comparison of seismic input energies.
- 2- The storeys, having relatively higher lateral drifts in a *MDOF* system, are the proper positions for the placement of steel cushions. More than one steel cushion could be used at that storey to generate higher supplementary damping. More experimental data should be prepared for the discrete systems.
- 3- The methods proposed in this PhD thesis should be extended to the reinforced concrete frames.

## REFERENCES

- Akbaş, B., Shen, J., Hao, H.** (2001). Energy approach in performance-based seismic design of steel moment resisting frames for basic safety objective. *Structural Design of Special and Tall Buildings*, 10:193-217.
- Akiyama, H.** (1985). *Earthquake-Resistant Limit-State Design for Buildings*. University of Tokyo Press.
- Alemdar, Z.F., Browning J.A., Olafsen J.** (2011). Photogrammetric measurements of RC bridge column deformations. *Engineering Structures*, 33(8):2407-2415.
- Alıcı, F.S., Sucuoğlu, H.** (2016). Prediction of input energy spectrum: attenuation models and velocity spectrum scaling. *Earthquake Engng Struct. Dyn.*, 45(13):2137-2161.
- Amiri, G.G., Darzi, G.A.** (2007). Damping effect on elastic input energy. Proceedings of the *4th International Conference on Earthquake Geotechnical Engineering*, Thessaloniki, Greece.
- Arias, A.** (1970) *A measure of earthquake intensity*. In: Hansen RJ (ed) *Seismic design for nuclear power plants*, MIT Press, Cambridge.
- Aydınoğlu, N., Fahjan, Y.M.** (2003). A unified formulation of the piecewise exact method for inelastic seismic demand analysis including the P-delta effect. *Earthquake Engng Struct. Dyn.*, 32:871-890.
- Avşar, Ö., Özdemir, G.** (2013) Response of seismic-isolated bridges in relation to intensity measures of ordinary and pulse-like ground motions. *ASCE Journal of Bridge Engineering*, 18(3):250-260.
- Bazzurro, P., Cornell, A.A.** (2002). Vector-valued probabilistic seismic hazard analysis. Proceedings of the *7th US national conference on earthquake engineering*, Boston (MA).
- Benavent-Climent, A., Pujades, L.G., Lopez-Almansa, F.** (2002). Design energy input spectra for moderate-seismicity regions. *Earthquake Engineering and Structural Dynamics* 31:1151–1172 doi: 10.1002/eqe.153
- Benavent-Climent, A., Zahran, R.** (2010) An energy based procedure for the assessment of seismic capacity of existing frames: application to RC wide beam systems in Spain. *Soil Dynamics and Earthquake Engineering*, 30:354-367
- Benavent Climent, A.** (2011). An energy based method for seismic retrofit of existing frames using hysteretic dampers. *Soil Dynamics and Earthquake Engineering*, 31:1385-1396.
- Benavent-Climent, A., Escobedo, A., Donaire-Avila, J., Oliver-Saiz, E., Ramirez-Marquez, A.L.** (2014). Assessment of expected damage on buildings

subjected to Lorca earthquake through an energy-based seismic index method and nonlinear dynamic response analyses. *Bull Earthquake Eng*, 12:2049-2073.

- Benavent-Climent, A., Mota-Paez, S.** (2017). Earthquake retrofitting of R/C frames with soft first story using hysteretic dampers: energy-based design method and evaluation. *J Eng Struct* 137:19-32.
- Bertero, V.V., Uang, C.M.** (1988) *Implications of recorded earthquake ground motions on seismic design of building structures*. Earthquake Engineering Research Report UCB/EERC-88-13, University of California Berkeley, C.A.
- Bruneau, M., Wang, N.** (1996). Some aspects of energy methods for the inelastic seismic response of ductile SDOF structures. *J Eng Struct*, 18(1):1-12.
- Boore, D.M., Joyner, W.B., Fumal, T.E.** (1993). *Estimation of response spectra and peak accelerations from western north american earthquakes*. Open File Report No. 93-509, US Geological Survey, Menlo Park, CA.
- Bojorquez, E., Iervolino, I.** (2011). Spectral shape proxies and nonlinear structural response. *Soil dynamics and Earthquake Engineering*, 31(7):996-1008
- Bojorquez, E., Chavez, R., Reyes-Salazar, A., Ruiz, E.S., Bojorquez, J.** (2017). A new ground motion intensity measure IB. *Soil Dynamic and Earthquake Engineering*, 99:97-107
- Bommer, J.J., Martinez-Pereira, A.** (1999). The effective duration of earthquake strong motion. *Journal of Earthquake Engineering*, 3:127-172.
- Börekçi, H.** (2018). Analytical and experimental investigation of inelastic SDOF steel structures using energy-based principles (Master's thesis). Boğaziçi University, ISTANBUL (ongoing).
- Chai, Y.H., Fajfar, P., Romstad, K.M.** (1998). Formulation of duration-dependent inelastic seismic design spectrum. *ASCE Journal of Structural Engineering* 124(8):913-934.
- Chapman, C.M.** (1999). On the use of elastic input energy for seismic hazard analyses. *Earthquake Spectra*, 15(4):607-635.
- Chang, C.C., Ji, F.Y.** (2007) Flexible videogrammetric technique for three-dimensional structural vibration measurement. *Journal of Engineering Mechanics*; 133(6):656-664.
- Cheng, Y., Lucchini, A., Mollaioli, F.** (2014). Proposal of new ground motion prediction equations for elastic input energy spectra. *Earthquakes and Structures*, 7(4):485-510.
- Chopra, A.K., Goel R.K.** (2002). A modal pushover analysis procedure for estimating seismic demands for buildings. *Earthq Eng Struct Dyn* 31:561-582.
- Choi, H.S., Cheung, J.H., Kim, S.H., Ahn, J.H.** (2011). Structural dynamic displacement vision system using digital image processing. *NDT&E Int*, 44:597-608.
- Chou, C.C., Uang, C.M.** (2000). Establishing absorbed energy spectra – an attenuation approach. *Earthquake Engineering and Structural Dynamics*, 29(10):1441-1455.

- Chou, C.C., Uang, C.M.** (2003). A procedure for evaluating seismic energy demand of framed structures. *Earthquake Engineering and Structural Dynamics*, 32:229-244.
- CSI Inc.**, Perform 3D Performance based design software.
- D'Ambrissi, A. Mezzi, M.** (2015). An energy-based approach for nonlinear static analysis of structures. *Bull Earthquake Eng*, 13:1513–1530
- Dashti, S., Braj, J., Pestana, J., Riemer, M., Wilson, D.** (2010) Mechanisms of seismically induced settlements of buildings with shallow foundations on liquefiable soil. *J. Geotech. Geoenviron. Eng.* 136:151:164 doi:10.1061/(ASCE).GT.1943-5606.0000179
- Dashti, S., Karimi, Z.** (2017). Ground motion intensity measures to evaluate I: the liquefaction hazard in the vicinity of shallow-founded structures. *Earthquake Spectra*, 33(1):241-276.
- Decanini, L.D., Mollaioli, F.** (2001). An energy based methodology for the assessment of seismic demand. *Soil Dynamics and Earthquake Engineering*, 21:113-137.
- Deniz, D., Song, J., Hajjar, J.** (2017). Energy-based seismic collapse criterion for ductile planar structural frames. *Engineering Structures*, 141:1-13.
- Dindar, A.A., Yalçın, C., Yüksel, E., Özkaynak, H., Büyüköztürk, O.** (2015). Development of earthquake energy demand spectra. *Earthquake Spectra*, 31(3):1667-1689.
- Electrical Power Research Institute (EPRI)** (1988). *A criterion for determining exceedance of the operating basis earthquake*, Report No. EPRI NP-5930, Palo Alto, CA
- Fajfar, P., Vidic, T., Fischinger, M.** (1989) Seismic demand in medium- and long period structures. *Earthquake Engineering and Structural Dynamics*, 18:1133-1144.
- Fardis, M.** (2018) *From force- to displacement- based seismic design of concrete structures and beyond*. Recent Advances in Earthquake Engineering in Europe, Springer Press, pp:101-122.
- Gökçe, T., Orakdoğan, E., Yüksel, E.** (2017). Seismic protection of high voltage bushings by using polyuretan springs. Proceedings of the *16th World Conference on Earthquake Engineering*, Santiago, Chile.
- Gupta, A., Krawinkler, H.** (1999). *Seismic demands for performance evaluation of steel moment resisting frame structures (SAC Task 5.4.3)*. Report No. 132, The John A. Blume Earthquake Engineering Center, Stanford, CA.
- Güllü, A., Ozkaynak, H., Khajehdehi, A., Gokce, T., Azizisales, F., Bal, I.E., Smyrou, E., Yuksel, E., Karadogan, H.F.** (2015). Derivation of the closed form equations for the energy dissipative steel cushions. Proceedings of *14th world conference on seismic isolation, energy dissipation and active control of structures*, San Diego, USA
- Güllü, A., Yüksel, E., Khajehdehi A., Karadoğan, H.F. and Özkaynak, H.** (2016), Experimental and analytical evaluation of the axial behaviour of energy

dissipative steel cushions, Proceedings of 2016 NZSEE Conference, Christchurch, New Zeland, April.

- Güllü, A., Yüksel, E., Yalçın, C., Dindar, A.A., Özkaynak, H.** (2017). Experimental verification of the elastic input energy spectrum and a suggestion. Proceedings of *Interdisciplinary Perspectives for Future Building Envelopes Conference*, Istanbul, Turkey.
- Habibi, A., Chan, R.W.K., Albermani, F.** (2013). Energy-based design method for seismic retrofitting with passive dissipation systems. *Engineering Structures*, 46:77-86.
- Housner, G.W.** (1952). Spectrum intensities of strong motion earthquakes. Proceedings of the *symposium on earthquake and blast effect on structures*, Earthquake Engineering Research Institute, Los Angeles (CA)
- Housner, G.W.** (1956). Limit design of the structures to resist earthquakes. Proceedings of the *1st World Conference on Earthquake Engineering*. Berkeley: California.
- Husid, L.R.** (1969). Caractericas de terremotos analisis general. *Revista del IDEM* 8:21-42
- IEEE Standard 693** (2005). *Recommended practice for seismic design of substations*. Piscataway, NJ, IEEE Standard Department.
- Jager, C., Adam, C.** (2013). Influence coefficients for collapse capacity spectra. *Journal of Earthquake Engineering*, 17:859-878.
- Karadoğan, H.F., Yüksel, E., Yüce, S.Z., Taşkın, K., Saruhan, H.** (2006). *Experimental study on the original and retrofitted prefabricated RC columns*. Technical report, ITU, Istanbul.
- Karameşe, G.K.** (2018). *Yapı sistemlerinde yerdeğiştirme ve şekildeğiştirme büyüklüklerinin özel bir görüntü işleme yöntemiyle belirlenmesi* (Master's thesis). Istanbul Technical University, Institute of Science and Technology, ISTANBUL.
- Karayel, V.** (2016) *Çapraz yay gruplarını kullanan yeni bir sismik yalıtım sistemi* (PhD Dissertation), Istanbul Technical University, Institute of Science and Technology, ISTANBUL.
- Ke, K., Chen, Y.** (2014). Energy-based damage-control design of steel frames with steel slit walls. *Structural Engineering and Mechanics*, 52(6):1157-1176.
- Khashaee, P., Mohraz, B., Sadek, F., Lew, H.S., Gross, J.L.** (2003). *Distribution of earthquake input energy in structures*. Technical Report NISTIR 6903, National Institute of Standards and Technology, Gaithersburg, MD 20899.
- Kramer, S.L.** (1996) *Geotechnical earthquake engineering*. Prentice-Hall, New Jersey.
- Kramer, S.L., Mitchel, R.A.** (2006) Ground motion intensity measures for liquefaction hazard evaluation. *Earthquake Spectra*, 22:413-438

- Kuwamura, H., Galambos, T.V.** (1989) Earthquake load for structural reliability. *ASCE Journal of Structural Engineering* 115(6).
- Kuwamura, H., Kirino, Y., Akiyama, H.** (1994). Prediction of earthquake energy input from smoothed Fourier amplitude spectrum. *Earthquake Engineering and Structural Dynamics*, 23(10):1125-1137.
- Lee, S.S., Goel S.C.** (2001). *Performance based design of steel moment frames using a target drift and yield mechanism*. Research Rep. No. UMCEE 01-17, Dept. of Civil and Environmental Engineering, Univ. of Michigan, Ann Arbor, Mich.
- Leelatavivat, S., Subhash, C.G., Stojadinovic, B.** (2002). Energy based seismic design of structures using yield mechanism and target drift. *ASCE J. Struct. Eng.*, 128:1046-1054.
- Leelatavivat, S., Saewon, W., Subhash, C.G.** (2009). Application of energy balance concept in seismic evaluation of structures. *ASCE J. Struct. Eng.*, 135:113-121.
- Lin, T., Haselton, C.B., Baker, J.W.** (2013). Conditional spectrum based ground motion selection. Part II: intensity based assessment and evaluation of alternative target spectra. *Earthquake Engineering and Structural Dynamics* 42(11):1867-1884.
- Lopez-Almansa, F., Yazgan, A.U., Benavent-Climent, A.** (2013). Design energy input spectra for high seismicity regions based on Turkish registers. *Bull Earthquake Eng*, 11:885-912 doi 10.1007/s10518-012-9415-2.
- Luco, N.** (2002). *Probabilistic seismic demand analyses, SMRF connection fractures and near source effects*. PhD Dissertation, Stanford University.
- Lukas, B.D., Takeo, K.** (1981). An iterative image registration technique with an application to stereo vision. Proceedings of the 7<sup>th</sup> International Joint Conference on Artificial Intelligence, Vancouver, BC, Canada, August 24-28, 1981.
- Mathworks Inc.**, MATLAB 2016 available at [www.mathworks.com](http://www.mathworks.com).
- Manoukas, G., Athanatopoulou, A., Avramidis, I.** (2011). Static-pushover analysis based on an energy-equivalent SDOF system. *Earthquake Spectra*, 27(1):89-105
- McCann, M.** (1980). *RMS acceleration and duration of strong ground motion*. The Jhon A Blume Earthquake Engineering Center, Report No: 46, Stanford University.
- Mezgebo, M., Lui, E.M.** (2016). Hysteresis and soil site dependent input and hysteretic energy spectra for far-source ground motions. *Advances in Civil Engineering*, 2016:1548319
- Mollaioli, F., Lucchini, A., Cheng, Y., Monti, G.** (2013). Intensity measures for the seismic response prediction of base-isolated buildings. *Bull Earthquake Eng*, 11:1841-1866 doi: 10.1007/s10518-013-9341-x
- Morlier, J., Salom, P., Bos, F.** (2007). New image processing tools for structural dynamic monitoring. *Key Engineering Materials*, 347:239-244.

- Muin, S., Mosalam, K.M.** (2017). Cumulative absolute velocity as a local damage indicator of instrumented structures. *Earthquake Spectra*, 33(2):641-664.
- Nayerloo, M., Chase, J.G., Millane, A., Muller, C., Malharbe, A., Chen, X.Q., MacRae, G.A.** (2011). Seismic structural displacement measurement using a line-scan camera: camera-pattern calibration and experimental validation, *Journal of Civil Structural Health Monitoring*, 1(3-4):113-124.
- Nogueira, F.M.A, Barbosa, F.S., Barra L.P.S.** (t.y.). *Evaluation of structural natural frequencies using image processing*. Retrieved February 23, 2018 from [http://www.ufjf.br/lrm/files/2009/04/evaces\\_imagem.pdf](http://www.ufjf.br/lrm/files/2009/04/evaces_imagem.pdf).
- Nuttli, O.W.** (1979). *The relation of sustained maximum ground acceleration and velocity to earthquake intensity and magnitude*. US Army Engineer Waterways Experiment Station. Miscellaneous Paper S-76-1 Report 16:74.
- Okuyan, S.** (2017). *Scaling of input seismic energy of sdof systems through experimental and analytical investigation* (Master's thesis). Boğaziçi University, ISTANBUL.
- Ozkaynak, H., Gullu, A., Gokce, T., Khajehdehi, A., Mahdavi, M., Azizisales, F., Bal, I.E., Smyrou, E., Yuksel, E., Karadogan, H.F.** (2014). Energy dissipative steel cushions. *Proceedings of 2nd European conference on earthquake engineering and seismology*, Istanbul, Turkey.
- Özkaynak, H., Khajehdehi, A., Güllü, A., Azizisales, F., Yüksel, E., Karadoğan, F.** (2018). Uni-axial behavior of energy dissipative steel cushions. *Steel and Composite Structures*, 27(6), 661-674.
- Park, J.W., Lee, J.J., Jung, H.J., Myung, H.** (2010). Vision-based displacement measurement method for high-rise building structure using partitioning approach. *NDT&E Int*, 43:642-647.
- Park, Y.J., Ang, A.H.S., Wen, Y.K.** (1985). Seismic damage analysis of reinforced concrete buildings. *ASCE Journal of Structural Engineering*, 111(4):740-757.
- Pappas, A., Sextos, A., da Porta, F., Modena, C.** (2017). Efficiency of alternative intensity measures for the seismic assessment of monolithic free-standing columns. *Bull Earthquake Eng*, 15:1635:1659
- PEER Ground Motion Database, NGA-West2.** <http://ngawest2.berkeley.edu/>
- Rathje, E.M., Abrahamson, N.A., Bray, J.D.** (1998). Simplified frequency content estimates of earthquake ground motions. *Journal of Geotechnical and Geoenvironmental Engineering*, 124(2):150-159.
- Riddell, R.** (2008). On ground motion intensity indices. *Earthquake Spectra*, 23(1):147-173.
- Sandikkaya, M.A., Akkar, S.** (2017). Cumulative absolute velocity, Arias intensity and significant duration predictive models from a pan-European strong-motion dataset. *Bull Earthquake Eng*, 15:1881-1898

- Sarma, S.K.** (1971). Energy flux of strong earthquakes. *Tectonophysics* 11:159-& ISSN: 0040-1951
- Sarma, S.K., Yang, K.S.** (1987). An evaluation of strong ground motion records and a new parameter A95. *Earthquake Engineering and Structural Dynamics*, Vol. 15(1):119-132
- Savitzky, A., Golay, M.J.E.** (1964). Smoothing and differentiation of data by simplified least-squares procedures. *Analytical Chemistry*, 36:1627-1639.
- SeismoSoft** (2016) SeismoSignal.
- Shen, J., Akbaş, B.** (1999). Seismic energy demand in steel moment frames. *Journal of Earthquake Engineering*, 3(4):519-559.
- Smyrou, E., Gullu, A., Yuksel, E., Ozkaynak, H., Karadogan, H.F.** (2014). Modeling of an energy dissipater for precast RC cladding systems. *Proceedings of 2nd European conference on earthquake engineering and seismology*, Istanbul, Turkey
- Structural Engineers Association of California (SEAOC) VISION 2000 Committee.** Performance Based Seismic Engineering of Buildings 1995; vol 1.
- Sucuoğlu, H., Nurtuğ, A.** (1995). Earthquake ground motion characteristics and seismic energy dissipation. *Earthquake Engineering and Structural Dynamics*, 24(9):1195-1213
- Sürmeli, M., Yüksel, E.** (2015). A variant of modal pushover analyses (VMPA) based a non-incremental procedure. *Bull Earthquake Eng*, 13:3353-3379.
- Sütçü, F., Inoue, N., Hori, N.** (2006). Damper design of a structure with a displacement controlled soft-story. *Journal of Structural Engineering* (in the transactions of AIJ), 52B:255-260.
- Trifunac, M.D. and Brandy, A.G.** (1975). A study on the duration of strong ground motion. *Bulletin of the seismological society of America*, 65(3):585-626
- TS 138 EN 10002-1** (2004). *Metallic materials-tensile testing part 1: Method of test (at ambient temperature)*. Türk Standart Enstitüsü.
- Tsantaki, S., Adam, C., Ibarra, L.F.** (2017). Intensity measures that reduce collapse capacity dispersion of P-Delta vulnerable simple systems. *Bull Earthquake Eng*, 15:1085-1109 doi: 10.1007/s10518-016-9994-4.
- Tothong, P., Cornell, C.A.** (2008). Structural performance assessment under near-source pulse-like ground motions using advanced ground motion intensity measures. *Earthquake Engineering and Structural Dynamics*, 37(7):1013-1037
- Uang, C.M., Bertero, V.V.** (1988). *Implication of recorded earthquake ground motions on seismic design of building structures*. Report No: UBC/EERC-88/13, College of Engineering, University of California at Berkeley.
- Uang, C.M., Bertero, V.V.** (1990) Evaluation of seismic energy in structures. *Earthquake Engineering and Structural Dynamics*, 19:77-90.

- Url-1** <<http://www.tml.jp/e/product/transducers/general/displacement/cdp.html>> date retrieved 13.05.2018
- Url-2** <[http://www.tml.jp/e/product/strain\\_gauge/gauge\\_list/yf\\_list.html](http://www.tml.jp/e/product/strain_gauge/gauge_list/yf_list.html)> date retrieved 13.05.2018
- Vamvatsikos, D., Cornell, C.A.** (2002). Incremental dynamic analyses. *Earthquake Engineering and Structural Dynamics*, 31(3):491-514
- Von Thun, J.L., Rochim, L.H., Scott, G.A., Wilson, J.A.** (1988) Earthquake ground motions for design and analysis of dams. *Soil Dynamics and Earthquake Engineering II- Recent advances in ground motion evaluation, geotechnical special publication 20:463-481*
- Wilson, E.L., Habibullah, A.** (1987) Static and dynamic analyses of multi-story buildings including P-Delta effects. *Earthquake Spectra*, 3(2):289-298.
- Ye, L., Cheng, G., Qu, Z.** (2009). Study on energy-based seismic design method and the application for steel braced frame structures. Proceedings of the 6th International Conference on Urban Earthquake Engineering, Tokyo, Japan.
- Yüksel, E., Karadoğan, F., Özkaynak, H., Khajehdehi, A., Güllü, A., Smyrou, E., Bal, I.E.** (2018). Behavior of steel cushions subjected to combined actions. *Bulletin of Earthquake Engineering*, 16, 707-729.
- Zahrah, T.F., Hall, W.J.** (1998). Earthquake energy absorption in SDOF systems. *ASCE Journal of Structural Engineering*, 128(3):308-317.
- Zelachi, C., Monteiro, R., Pinho, R.** (2017). Critical assessment of intensity measures for seismic response of Italian RC bridge portfolios. *Journal of Earthquake Engineering*, DOI: 10.1080/13632469.2017.1342293

## CURRICULUM VITAE



**Name Surname** : Ahmet Güllü  
**Place and Date of Birth** : 17/04/1987 – Keçiören/Ankara  
**E-Mail** : ahmgullu@gmail.com

### EDUCATION

- **B.Sc.** : 2010, Yıldız Technical University, Faculty of Civil Engineering, Civil Engineering Department
- **M.Sc.** : 2012, Istanbul Technical University, Faculty of Civil Engineering, Civil Engineering Department

### PROFESSIONAL EXPERIENCE AND REWARDS:

- 2010-2014 Structural design engineer for several companies.
- 2014-2018 Research assistant at civil engineering department of ITU.

### PUBLICATIONS, PRESENTATIONS AND PATENTS ON THE THESIS:

- **Güllü A.**, Yüksel E., Yalçın C., Dindar A. A., Özkaynak H., Büyüköztürk O. 2018: An Improved Input Energy Spectrum Verified by the Shake Table Tests. *Earthquake Engineering and Structural Dynamics*. DOI: 10.1002/eqe.3121. Accepted on August 06, 2018.
- Yüksel E., Karadoğan F., Özkaynak H., Khajehdehi A., **Güllü A.**, Smyrou E., Bal I. E. 2018: Behavior of Steel Cushions Subjected to Combined Actions. *Bulletin of Earthquake Engineering*, 16, 707-729.
- Özkaynak H., Khajehdehi A., **Güllü A.**, Azizisales F., Yüksel E., Karadoğan F. 2018: Uni-axial Behavior of Energy Dissipative Steel Cushions. *Steel and Composite Structures*, 27(6), 661-674.

- **Gullu A.**, Yuksel E., Yalcin C. 2018: Seismic Energy Based Design: Numerical Evaluation of Diverse MDOF Systems *16th European Conference on Earthquake Engineering (16ECEE)*, June 18-21, 2018, Thessaloniki, Greece.
- **Gullu A.**, Yuksel E., Yalcin C., Dindar A. A, Ozkaynak H. 2017: Experimental Verification of the Elastic Input Energy Spectrum and a Suggestion. *Interdisciplinary Perspectives for Future Building Envelopes (ICBEST 2017)*, May 2017, Istanbul, Turkey.

#### **OTHER PUBLICATIONS, PRESENTATIONS AND PATENTS:**

- **Güllü A.**, Smyrou E., Khajehdehi A., Özkaynak H., Bal İ.E., Yüksel E., Karadoğan F. Numerical Modelling of Energy Dissipative Steel Cushions. *International Journal of Steel Structures*, Submitted: September 3, 2018, under review.
- Karadoğan F., Yüksel E., Khajehdehi A., Özkaynak H., **Güllü A.**, Şenol E. 2018: Cyclic Behavior of RC Cladding Panels Connected with Energy Dissipative Steel Cushions. *Engineering Structures*, Submitted: July 19, 2018, under review.
- Yuksel E., Durgun Y., **Gullu A.**, Saruhan Y. “Yapısal Kaplama Betonuna Uygulanan Önüretim Boşluklu Döşeme Sistemlerin Eğilme Davranışı” November 2017, *Beton Prefabrikasyon* 124-5:16.
- Yuksel E., Soydan C., **Gullu A.**, “Tek yönlü ve çevrimsel yükler etkisindeki önüretimli elemanların mafsallı bağlantılarının kayma davranışı”, *Beton Prefabrikasyon Dergisi*, 29(116):9-20, 2015. *Translated from* “Ioannis N. Psycharis, Harris P. Mouzakis, Shear resistance of pinned connections of precast members to monotonic and cyclic loading, *Engineering Structures* 41:413-427 (2012)” after getting permission.
- **Güllü A.**, Durgun Y., Senol E., Sahin F., Nobakhtjoo A., Saruhan H., Yüksel E., Özden B., Ölçer B., Özcan A.İ., “Flexural performance of slab tracks designed for high speed railway lines” *The Fourth International Conference on Railway Technology (Railways 2018)*, Sitges, Barcelona, Spain, September, 2018.
- **Gullu A.**, Saghayesh A.M., Yuksel E., “In-plane behavior of sandwich roof panels”, *7th Conference on Advances in Experimental Structural Engineering (7AESE)*, Pavia, Italy, September, 2017.
- Durgun Y., **Gullu A.**, Gokce T., Yuksel E., “Shake table tests of a special raised floor system”, *7th Conference on Advances in Experimental Structural Engineering (7AESE)*, Pavia, Italy, September, 2017.
- **Gullu A.**, Yuksel E., Karadogan H.F., “Energy dissipator steel cushions: Closed form equations for the combining actions”, *16th World Conference on Earthquake Engineering (16 WCEE)*, Santiago, Chile, January 2017, Paper No: 2122.
- **Gullu A.**, Yuksel E., Khajehdehi A., Karadogan H.F., Özkaynak H., “Experimental and analytical evaluation of the axial behavior of energy dissipative steel cushions”, *New Zealand Society for Earthquake Engineering Conference, Christchurch*, New Zealand, April 2016.
- **Gullu A.**, Ozkaynak H., Khajehdehi A., Gokce T., Azizisales F., Bal İ.E., Smyrou E., Yuksel E., Karadogan H.F., “Derivation of the closed form equations for the

energy dissipative steel cushions”, *14<sup>th</sup> World Conference on Seismic Isolation, Energy Dissipation and Active Vibration Control of Structures (14WCSE)*, San Diego, CA, USA, September 2015.

- Ozkaynak H., **Gullu A.**, Khajehdehi A., Gokce T., Azizisales F., Bal I.E., Smyrou E., Yuksel E., Karadogan H.F., “Bi-directional loading tests of steel cushions”, *14<sup>th</sup> World Conference on Seismic Isolation, Energy Dissipation and Active Vibration Control of Structures (14WCSE)*, San Diego, CA, USA, September 2015.
- Ozkaynak H., **Gullu A.**, Gokce T., Khajehdehi A., Mahdavi M., Azizisales F., Bal I.E., Smyrou E., Yuksel E., Karadogan H.F., “Energy dissipative steel cushions”, *2<sup>nd</sup> European Conference on Earthquake Engineering and Seismology (2ECEES)*, Istanbul, Turkey, August 2014.
- Smyrou E., **Gullu A.**, Yuksel E., Ozkaynak H., Karadogan H.F., “Modeling of an energy dissipater for precast RC cladding systems”, *2<sup>nd</sup> European Conference on Earthquake Engineering and Seismology (2ECEES)*, Istanbul, Turkey, August 2014.
- Khajehdehi A., **Gullu A.**, Gokce T., Ozkaynak H., Yuksel E., Karadogan H.F., “Cyclic test of the precast panels equipped with steel cushions”, *2<sup>nd</sup> European Conference on Earthquake Engineering and Seismology (2ECEES)*, Istanbul, Turkey, August 2014.
- Soydan C., **Gullu A.**, Hepbostanci O.E., Yuksel E., Irtem E., “Design of a special lead extrusion damper” *15<sup>th</sup> World Conference on Earthquake Engineering (15WCEE)*, Lisbon, Portugal, September 2012
- **Gullu A.**, Yuksel E., Karadogan H.F., “Experimental and analytical evaluation of the energy dissipater cushions under effect of combined loading” *Türkiye Abaqus Kullanıcıları Toplantısı (TAKT)*, Istanbul, Turkey, November 2016.
- **Gullu A.**, Yuksel E., Karadogan H.F., “Experimental and analytical evaluation of the energy dissipater cushions under effect of axial loading” *Türkiye Abaqus Kullanıcıları Toplantısı (TAKT)*, Istanbul, Turkey, November 2015.
- Ozkaynak H., **Gullu A.**, Gokce T., Khajehdehi A., Azizisales F., Mahdavi M., Bal I.E., Smyrou E., Yuksel E., Karadogan H.F., “Enerji sönmüleyici yastıkların çevrimsel davranışı” *Ulusal Yapı Mekaniği Laboratuvarları Toplantısı (YMLT)*, Kayseri, Turkey, May 2015.
- **Gullu A.**, Yuksel E., Karadogan H.F., “Experimental and analytical evaluation of the energy dissipater cushions” *Türkiye Abaqus Kullanıcıları Toplantısı (TAKT)*, Istanbul, Turkey, November 2014.

## RESEARCH PROJECTS

- Yeni nesil ön üretim travers ve travers plağı geliştirilmesi. *İTÜ NOVA TTO*.
- Determination of in-plane behavior of the sandwich roof panels, *İTÜ NOVA TTO*.
- Investigation on bonding between topping concrete and precast hollow-core voided slabs, *İTÜ NOVA TTO*.

- Improved Fastening Systems of Cladding Wall Panels of Precast Buildings in Seismic Zones (SAFECLADDING), *FP7*.
- A new methodology for energy based seismic design, *İTÜ BAP, PhD*.
- Experimental evaluation of a special energy dissipater in various frequency ranges, *İTÜ BAP, MSc*.
- 

#### **ATTENDED CONFERENCES AND WORKSHOPS**

1. MISTI MIT-BU-ITU Energy Based Design Workshop, *Boston, MA USA*, May **2018**.
2. Sanayi tesislerinin sismik tehlike ve risk değerlendirmesi, *Kocaeli, Turkey*, March **2018**.
3. 6. Yapı Mekaniği Laboratuvarları Toplantısı, *Trabzon, Turkey*, November **2017**.
4. 15. Türkiye ABAQUS Kullanıcıları Toplantısı, *İstanbul, Turkey*, November **2017**.
5. 7<sup>th</sup> Conference on Advances in Experimental Structural Engineering, *Pavia, Italy*, September **2017**.
6. MISTI MIT-BU-ITU Energy Based Design Workshop, *İstanbul, Turkey*, June **2017**.
7. Interdisciplinary Perspectives for Future Building Envelopes, *İstanbul, Turkey*, May **2017**.
8. 16th World Conference on Earthquake Engineering, *Santiago, Chile*, February **2017**.
9. Türkiye ABAQUS Kullanıcıları Toplantısı, *İstanbul, Turkey*, November **2016**.
10. New Zealand Society for Earthquake Engineering Conference, *Christchurch, New Zealand*, April **2016**.
11. Japan-Turkey Cooperative Program on Resilience Engineering for Energy and Urban Systems, *Tokyo, Japan*, **2016**.
12. Türkiye ABAQUS Kullanıcıları Toplantısı, *İstanbul, Turkey*, **2015**.
13. 14th World Conference on Seismic Isolation, Energy Dissipation and Active Vibration Control of Structures, *San Diego, CA, USA*, **2015**.
14. Safecladding Meeting, *Ispira, Italy*, **2015**.
15. ITU MIT Energy Based Design Workshop, *İstanbul, Turkey*, **2015**.
16. 5. Yapı Mekaniği Laboratuvarları Toplantısı, *Kayseri, Turkey*, **2015**.
17. Türkiye ABAQUS Kullanıcıları Toplantısı, *İstanbul, Turkey*, **2014**.
18. 2nd European Conference on Earthquake Engineering and Seismology, *İstanbul, Turkey*, **2014**.